The Analysis and Prediction of Jet Flow
and
Jet Noise about Airframe Surfaces

Matthew J. Smith

Contents:

Thesis submitted to the Faculty of the
Virginia Polytechnic Institute and State University
in partial fulfillment of the requirements for the degree of

Master of Science
in
Aerospace Engineering

Christopher R. Fuller, Chair
Steven A.E. Miller
William J. Devenport
Craig A. Woolsey

September 26, 2013
Blacksburg, Virginia

Keywords: Propulsion Airframe Aeroacoustics, Jet Noise, Ray Theory, Diffraction

The Analysis and Prediction of Jet Flow
and
Jet Noise about Airframe Surfaces

Matthew J. Smith

(ABSTRACT)

Aircraft noise mitigation has been an ongoing challenge for the aeronautics research community. In response to this challenge, aircraft concepts have been developed in which the propulsion system is integrated with the airframe to shield the noise from the observer. These concepts exhibit situations where the jet exhaust interacts with an airframe surface. Jet flows interacting with nearby surfaces exhibit a complex behavior in which acoustic and aerodynamic characteristics are altered. The physical understanding and accurate modeling of these characteristics are essential to designing future low-noise aircraft. In this thesis, an alternative approach is created for predicting jet mixing noise that utilizes an acoustic analogy and the solution of the steady Reynolds-Averaged Navier-Stokes (RANS) equations using a two equation turbulence model. A tailored Green's function is used in conjunction with the acoustic analogy to account for the propagation effects of mixing noise due to a nearby airframe surface. The tailored Green's function is found numerically using a newly developed ray tracing method. The variation of the aerodynamics, acoustic source, and far-field acoustic intensity are examined as a large flat plate is moved relative to the nozzle exit. Steady RANS solutions are used to study the aerodynamic changes in the field-variables and turbulence statistics. To quantify the propulsion airframe aeroacoustic (PAA) installation effects on the aerodynamic source, a non-dimensional number is formed that can be used as a basic guide to determine if the aerodynamic source is affected by the airframe and if additional noise produced by the airframe surface is present. The aerodynamic and noise prediction models are validated by comparing results with Particle Image Velocimetry (PIV) and far-field acoustic data respectively. The developed jet noise scattering methodology is then used to demonstrate the shielding effects of the Hybrid Wing Body (HWB) aircraft. The validation assessment shows that the acoustic analogy and tailored Green's function provided by the ray tracing method are capable of capturing jet shielding characteristics for multiple configurations and jet exit conditions.

This work received support from the National Aeronautics and Space Administration (NASA) Fundamental Aeronautics Program (FAP) High Speed Project (HSP) through the National Institute of Aerospace (NIA) cooperative agreement number NNL09AA00A.

Acknowledgments

I owe a tremendous debt of gratitude to Dr. Steve Miller of NASA Langley Research Center for dedicating his time and going out of his way to provide me with an extraordinary opportunity. His mentorship has helped me grow as an aerospace engineer and as a person.

I would like to gratefully thank my academic advisor Dr. Chris Fuller for his guidance and advice. Working under his supervision was an honor and a privilege.

The Aeroacoustics Branch at NASA Langley has been an exceptional working environment. I thank Dr. Charlotte Whitfield and everyone in the Aeroacoustics Branch for always offering support and making me feel at home.

I would like to thank Dr. William Devenport and Dr. Craig Woolsey for serving on my committee and for being two of the best teachers I have ever had. I would also like to thank the faculty and staff of the National Institute of Aerospace for providing a truly unique educational experience.

Thank you to my parents Henry and Mary Ann Smith for always supporting me in everything. Your words of encouragement have helped me get through the toughest times.

Finally, I cannot express how much I thank my fiancée, Beth, for her love, support, and patience. Her devoted support has been essential to my success and overall well being throughout my academic career, especially during this last very difficult year.

“**WIN** - **W**hats **I**mportant **N**ow: To make change; To influence; To use this moment to be better than the last; To achieve greatness in all aspects of your life;

WIN at home. **WIN** at school. **WIN** at business. **WIN** at life.”

— Bud Foster

Contents

List of Figures

List of Tables

Nomenclature

Abbreviations

AMELIA	Advanced Model for Extreme Lift and Aeroacoustics
ANOPP	Aircraft Noise Prediction Program
BBSAN	Broadband Shock-Associated Noise
BEM	Boundary Element Method
BVP	Boundary Value Problem
CFD	Computational Fluid Dynamics
CJES	Compact Jet Engine Simulator
DNS	Direct Numerical Simulation
EPNL	Effective Perceived Noise Level
ERA	Environmentally Responsible Aviation
ESM	Equivalent Source Method
FSC	Fast Scattering Code
*FUN*3*D*	Fully Unstructured Navier-Stokes Three-Dimensional Solver
HBPR	High Bypass Ratio
HWB	Hybrid Wing Body
JSIT	Jet-Surface Interaction Test
LBPR	Low Bypass Ratio
LEE	Linearized Euler Equations

LES	Large Eddy Simulation
NPR	Nozzle Pressure Ratio
$OASPL$	Overall Sound Pressure Level
PAA	Propulsion Airframe Aeroacoustics
PIV	Particle Image Velocimetry
PSD	Power Spectral Density
$RANS$	Reynolds-Averaged Navier-Stokes
$SHJAR$	Small Hot Jet Acoustic Rig
SMC	Small Metal Chevron
SPL	Sound Pressure Level
SST	Shear Stress Transport
TKE	Turbulent Kinetic Energy
TTR	Total Temperature Ratio
UCD	Unstructured Cell Data

English Symbols

A	Empirical constant
C	Diffraction coefficient for corner-diffracted rays
c	Speed of sound
c_∞	Free-stream speed of sound
c_l	Empirical constant associated with turbulent length scale
c_τ	Empirical constant associated with turbulent time scale
D	Diffraction coefficient for edge-diffracted rays
D	Nozzle exit diameter
D_j	Fully expanded jet diameter
D_m	Diffraction coefficient for creeping rays

$\boldsymbol{E}^0$	First end point of edge segment
$\boldsymbol{E}^F$	Second end point of edge segment
f_1	First damping function of discontinuity correction
f_2	Second damping function of discontinuity correction
k	Wave number
k_s	Turbulent kinetic energy associated with fine-scale mixing noise
L	Length of plate used for point source validation
l_s	Turbulent length scale
M_a	Acoustic Mach number
M_d	Design Mach number
M_j	Fully expanded Mach number
M_∞	Free-stream Mach number
$\boldsymbol{N}$	Axis of the diffraction cone and unit vector of edge
$\boldsymbol{O}$	Observer location
$\hat{p}$	Complex spatially dependent pressure amplitude
p	Static pressure
p_a	Acoustic pressure
$\hat{p}_D$	Complex pressure amplitude of diffracted ray
$\hat{p}_I$	Complex pressure amplitude of incident ray
p_j	Fully expanded static pressure
p_o	Stagnation pressure
$\hat{q}_s$	Statistical source term
r	Distance of edge to observer location
$\boldsymbol{S}$	Source location
S	Spectral density of acoustic pressure

St	Strouhal number
T	Lighthill stress tensor
T	Transfer function used for creeping rays
t	Proportionate distance along edge segment
T_0	Stagnation temperature
T_j	Fully expanded static temperature
$\overline{u}$	Mean streamwise velocity component
u_j	Fully expanded jet velocity
$\boldsymbol{V}$	Diffraction location
W	Width of plate used for point source validation
$\boldsymbol{x}$	Vector observer position
x_I	Estimate of jet impingement location
x_p	Axial distance to the plate trailing edge
$\boldsymbol{y}$	Source vector
y_p	Radial distance from the plate to the jet centerline

Greek Symbols

β	Wedge angle
δ	Damping coefficient of discontinuity correction
δ_{ij}	Kronecker delta function
∇	Vector differential operator
ν	Wedge index
ω	Radial frequency
ϕ_o	Polar angle to diffracted ray
ϕ_s	Polar angle to incident ray
ψ	Observer angle from the upstream axis

ρ	Density
ρ	Distance of source to observer location
τ	Eikonal
τ	Viscous stress
τ_s	Turbulent time scale
θ	Oblique angle between the edge and incident ray
δ_η	Spreading angle of the jet
Γ	Non-dimensional number
γ	Ratio of specific heats

Chapter 1

Introduction

1.1 Problem Definition and Motivation

Since the beginning of commercial jet powered aviation, the effect of aircraft generated noise has been a significant issue to passengers and the surrounding communities. Aircraft noise certification regulations and airport noise restrictions have been implemented to mitigate the noise problem. These regulations and restrictions have contributed to motivating the research and development of noise reduction technology. The aircraft noise research community has significantly reduced aircraft noise over the past five decades through the development of advanced bypass ratio fans, advanced jet nozzles, and airframe noise reduction technologies[1,2]. The historical reduction in commercial aircraft noise is shown Figure 1.1. The Effective Perceived Noise Level (EPNL) at the sideline certification point for various aircraft versus the year of initial service is shown. The most significant contribution of noise reduction was primarily due to the introduction of low bypass ratio (LBPR) and then high bypass ratio (HBPR) turbofan engines. However, progress since those technologies were introduced has not been as dramatic and a slower rate of noise reduction is observed.

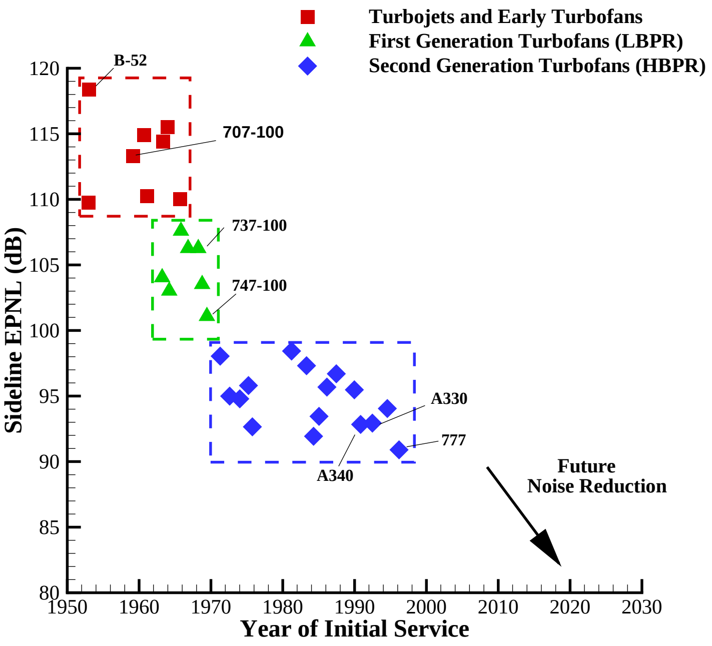

Figure 1.1: The historic trend of aircraft noise reduction[2]. The advancement in the bypass ratio technology of turbofan engines was a large contribution to the reduction of aircraft noise. EPNL is normalized to $100,000\ lb$ thrust.

Although current production aircraft meet certification requirements, continued growth in air traffic, the limited development of new airports, and increased limitations on existing airports, such as curfews, results in strong demand for the continued advancement of noise reduction technology[1]. As advances in engine noise technology with acceptable performance become more challenging, the reduction of aircraft noise becomes increasingly more difficult and it is necessary to examine other technologies to achieve further noise reduction. NASA's Environmentally Responsible Aviation (ERA) project was developed to address these current and future anticipated issues. Among goals for decreasing nitrogen oxide emissions and increasing fuel efficiency, the ERA targets a goal of 42 dB cumulative reduction below current Federal Aviation Administration noise levels for aircraft in the 2020 time frame and 71 dB cumulative reduction in the 2030 time frame[3].

To achieve the next generation of aircraft noise reductions, the aircraft noise research community must search beyond traditional airframe and engine noise reduction technologies. One such method is to shield the engine noise using the flight vehicle airframe. These shielding effects, of propulsion airframe aeroacoustics (PAA), can be utilized as a significant technology for noise reduction[2]. PAA is defined as the noise sources that are created or modified when the engine is integrated into the airframe. Airframe shielding is one such reduction technology included in the Hybrid Wing Body (HWB) concept aircraft proposed by the Boeing Company and the Advanced Model for Extreme Lift and Aeroacoustics (AMELIA) developed by the California Polytechnic State Institute. Both unconventional aircraft concepts, shown in Figure 1.2, introduce the fundamental change of installing the engines on top of the airframe. The shielding effect of the HWB is described by Thomas *et al.*[4] and Czech *et al.*[5] Acoustic characteristics of AMELIA are described by Horne *et al.*[6] The amount of jet noise reduction depends on the location of the engine nozzle relative to the trailing edge of the airframe and the distribution and directivity of noise sources within the jet plume. Thus, the location of the engine relative to the airframe trailing edge is a critical aspect of the design. If the engine is too close to the airframe surface and the engine exhaust flow impinges upon the airframe, then low-frequency "scrubbing" and trailing edge noise will be created.[7] This result mitigates some of the noise reduction potential of the shielding concept. Therefore, depending on the configuration, the surface effects can lead to either increases or decreases in noise relative to an engine operated in isolation.

Supersonic aircraft configurations, such as those developed by Welge *et al.*[8,9] for the 2020 to 2035 time frame or by Morgenstern *et al.*[10] for the 2035 time frame and beyond, demonstrate complicated nozzle and engine placement designed to reduce sonic boom and jet noise. Advanced low bypass ratio engines, as shown by Sokhey and Kube-McDowell[11], can be integrated into the airframe while potentially reducing jet noise. These concepts could also


(a) Hybrid Wing Body (b) AMELIA

Figure 1.2: Advanced aircraft designs exemplifying aeroacoustic shielding technology

create situations where the jet exhaust interacts directly with an airframe surface resulting in additional noise sources and a complicated scattered field. The ability to accurately predict the noise created, altered, or shielded by interactions between the jet flow and the airframe surfaces is essential to reducing the overall noise produced by the aircraft. However, modern jet noise prediction methods were generally developed to predict the noise of an isolated jet and are not applicable when the aircraft surfaces are included in the prediction. New jet noise prediction methodologies need to be developed to address these complicated configurations and advanced nozzle designs.

Several techniques have been developed to predict the scattered noise from the engine. Some of these techniques include the Boundary Element Method[12], the Equivalent Source Method used in NASA's Fast Scattering Code[13], and the ray tracing method.[14] There are relative advantages and disadvantages for each technique and only a limited number of source models have been developed for use with scattering methodologies. Currently, there is no first principle analytic prediction approach for jet noise, let alone for the resultant noise scattering by the airframe. Recently developed acoustic analogies such as those by Morris and Farrasat[15] or Miller[16] provide prediction capabilities based on physical principles but a high accuracy Green's function solver is required to account for the propagation effects. The ray tracing method is a candidate Green's function solver because of its low computational cost and accuracy at high frequencies.[14]

Jet-surface interactions can also produce a change in the noise sources associated with the aerodynamics of the jet flow. There have been several studies that examined the aerodynamic effects of nearby and impinging surfaces on jet flows. Donaldson and Snedeker[17] and Lamont and Hunt[18] showed that jets impinging on oblique and perpendicular surfaces significantly affect the turbulence and shock cell structure of supersonic jets. Studies involving jets not directly impinging on surfaces include those by Sawyer[19] and Al-Qutub and Budair,[20] among others. Capturing the effect on the acoustic source due to the changes in the aerodynamic characteristics of the jet flow-field is essential for accurate predictions of jet noise.

This work aims to address challenges associated with PAA predictions. Specifically, this work includes the development of prediction codes and an assessment of surface effects on the aerodynamic noise source generated by a jet and the acoustic propagation around arbitrary objects. The codes are validated using existing experimental data. The goals of this research are:

1. Validate an aerodynamic model using steady Reynolds-Averaged Navier-Stokes (RANS) solutions from a Computational Fluid Dynamics (CFD) solver and Menter SST turbulence model.
2. Examine the aerodynamic changes in the field-variables and turbulence statistics of a jet in the presence of a nearby surface.
3. Quantify the effect of the surface on the aerodynamic noise source based on the jet operating condition and surface location.
4. Develop an advanced scattering method that can be utilized in conjunction with an acoustic analogy approach.

5. Demonstrate calculations of jets integrated with the airframe using an acoustic analogy approach.

1.2 Thesis Overview

The remainder of this thesis is organized as follows. First, a literature review is presented that includes jet noise prediction methodologies, descriptions of noise sources, and current scattering techniques. Next, an aerodynamic analysis is presented. Steady RANS solutions are examined to study the aerodynamic changes in the field-variables and turbulence statistics. To validate the aerodynamic models, results are compared with Particle Image Velocimetry (PIV) data obtained by Bridges and Wernet[21]. The variation of the aerodynamic quantities, acoustic source, and far-field acoustic intensity are examined as a large flat plate is positioned relative to the nozzle exit. Predictions from various jet conditions and flat plate configurations are compared with an isolated jet. To quantify the propulsion airframe aeroacoustic installation effects on the aerodynamic noise source, a non-dimensional number is formed that contains the flow-conditions and airframe installation parameters. Following the aerodynamic and acoustic source analyses, an assessment of an acoustic analogy for the mixing noise component of jet noise in the presence of a scattering surface is presented. First, a ray tracing approach is derived, implemented, and validated against experimental data of a point source near a flat plate. The ray tracing methodology is then used in conjunction with an acoustic analogy to predict far-field mixing noise generated from a jet shielded by a flat plate. These predictions are validated by comparing with experimental far-field data. The prediction approach is then used to demonstrate the shielding capabilities of the HWB concept. Lastly, the conclusions of the analyses and future work are presented.

Chapter 2

Literature Review

In this chapter, a brief history of jet noise prediction methodologies is presented. The acoustic sources generated by subsonic and supersonic jets are described along with additional sources created due to jet-surface interactions. Lastly, current acoustic scattering techniques are discussed.

2.1 Jet Noise

Sir James Lighthill pioneered the physical understanding and first principles mathematical modeling of jet noise in 1952[22,23]. To identify the acoustic sources within a jet, he rearranged the Navier-Stokes equations of motion into an inhomogeneous wave equation. Inhomogeneous terms were arranged on the right side of the equation and designated as the equivalent sources. This resulted in an inhomogeneous wave equation of the form,

$$\frac{\partial^2 \rho}{\partial t^2} - c_\infty^2 \nabla^2 \rho = \frac{\partial^2 T_{ij}}{\partial x_i \partial x_j}, \tag{2.1}$$

where ρ is density, c_∞ is the ambient sound speed, and $T_{ij} = \rho v_i v_j + (p - \rho c_\infty^2)\delta_{ij} - \tau_{ij}$ is known as the Lighthill stress tensor. The variables v_i, p, and τ_{ij} are the velocity, pressure and viscous stresses, and δ_{ij} is the Kronecker delta function. Lighthill viewed the double divergence of T_{ij} as analogous to convecting quadrupoles. Through this formation, Lighthill implied that the quadropoles were related to small turbulent eddies, or the fine-scale motion of the turbulent flows. An important result of Lighthill's acoustic analogy is the noise scaling law. Using the free-space Green's function of the wave equation in R^3, Lighthill determined a solution to Eqn. 2.1 which revealed that the acoustic power radiated by a jet varies as the eighth power of the jet velocity.

Since the introduction of Lighthill's acoustic analogy, there have been multiple attempts to modify and improve the theory. The first two notable modifications were the inclusion of source convection and refraction effects.[24]. The source convection effects were first investigated by Ffowcs-Williams[25]. The quadrupoles are convected downstream by the mean-flow resulting in additional radiated noise in the direction of motion. Since the mean-flow of the jet is highly nonuniform, the radiated sound that is generated within the jet plume undergoes refraction as it propagates through the jet to reach the far-field. These effects likely cause the cardioid directivity observed in the far-field.

Lilley[26] proposed using a third order ordinary differential equation to account for refraction effects similar to the Pridmore-Brown operator[27]. Linearization is performed over the mean-flow of the jet. The mean-flow shear terms are shifted to the left side of the equation as wave propagation operators, thus refraction effects are taken into account. It is argued that Lilley's equation better describes the physical noise generation process; the right hand side of the equation is the source and the left hand side is interpreted as locally enforcing the appropriate wave propagation of the sources.[28] This is unlike Lighthill's[22,23] approach that included the propagation and source within T_{ij}.

Several methods for the prediction of jet noise are based on Lighthill's or Lilley's acoustic analogy. To make predictions of the radiated noise it is necessary to describe the statistics of the turbulence. In all of the approaches, some assumptions must be made concerning the statistical properties of the turbulent sources. Because a complete simulation of the jet turbulence and the noise it generates using Direct Numerical Simulation (DNS)[29] or Large Eddy Simulation (LES)[30] are too computationally expensive for high Reynolds number jet flows, noise predictions are often based on the solution of the RANS equations using a two equation turbulence model. RANS solutions have been used in methodologies by Tam and Auriault[31], Morris and Boluriaan[32], Morris and Miller[33], and Miller[16] among others.

One challenge when using the acoustic analogy approach is determining the acoustic source terms. This is due to a lack of understanding of the physics of turbulence. It has been observed that the noise characteristics of subsonic and supersonic jets include multiple components.[34] Turbulent mixing noise is the sole component for static subsonic and supersonic jets that are perfectly expanded. The noise of most supersonic jets, which are imperfectly expanded, comprise of three basic components: (i) turbulent mixing noise, (ii) broadband shock-associated noise,(iii) and screech tones. Additional noise components are also present when a subsonic or supersonic jet is in the proximity of a surface.

2.1.1 Mixing Noise

The jet mixing noise is created by the turbulent mixing of a jet with the ambient air. The mixing initially occurs in the shear layer, separating the potential core and ambient medium, and grows with distance from the nozzle. The mixing region gradually fills the entire jet plume multiple diameters from the nozzle through the transition region into what is known as the fully developed region. These regions of the turbulent mixing are shown in Figure 2.1

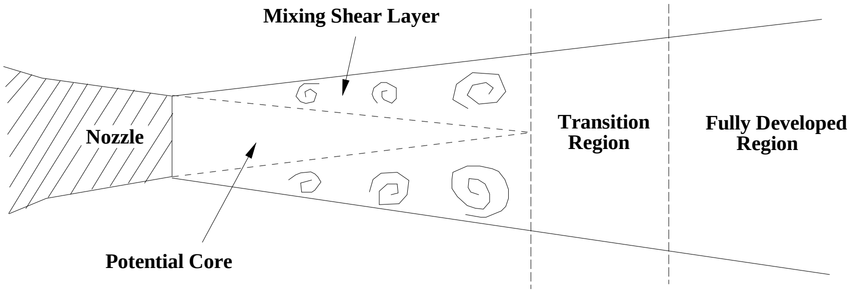

Figure 2.1: Turbulent mixing regions of a jet

Mixing noise is dominant at the downstream angles from the nozzle exit. It has been shown by Tam *et al.*[35] and Viswanathan[36] among others that turbulence in jets and free shear layers is made up of large coherent turbulent structures as well as fine-scale turbulence. Noise radiation is produced by both the large and fine-scale turbulence. The noise radiation produced by the large turbulent structures is more-so deterministic than the sound radiation produced by fine-scale turbulence. The former dominates the dynamics and overall mixing of jets and free shear layers. The large-scale structures radiate noise principally in the downstream direction. The fine-scale mixing noise component has a relatively uniform directivity and is dominant in the sideline and upstream directions.[34] A semi-empirical fine-scale mixing model by Tam and Auriault[31] has shown good agreement with experimental measurements, especially in the sideline direction. Morris and Farassat[32] have achieved similar results using their acoustic analogy approach.

Mollo-Christensen[37] was the first to show that large scale structures exist in jet flows. A statistical description of the large turbulent structures in free shear flows by means of a stochastic instability wave mode was used by Tam and Chen[38]. The stochastic instability wave model is based on the observation that the spreading rate of high-speed jets is very small, inferring that the flow variables as well as the turbulent statistics change slowly in the downstream direction. The turbulent statistics are nearly constant locally, implying a system in dynamical equilibrium.[34] The large-scale fluctuations of the system can then be mathematically represented by a linear superposition of its normal modes, as described by Tam and Chen[38].

2.1.2 Shock Noise

Shock cell structures within an imperfectly expanded jet are formed by oblique or normal shocks and expansion fans. An expansion fan is a continuous expansion region composed of an infinite number of Mach waves. Because of the large difference in static pressure inside and outside of the jet, an expansion fan is formed at the lip of the nozzle of an underexpanded jet and an oblique shock is formed for an overexpanded jet. The expansion fan decreases the pressure, expanding the flow, to the ambient conditions. The flow passing through oblique shocks abruptly increases in static pressure to match the ambient conditions. Since the flow outside of the jet is either typically stationary or subsonic, the shock waves impinge on the mixing layer of the jet and reflect within the jet plume to create a nearly periodic shock cell structure.[34] The shock cell structure creates additional noise sources.

Broadband Shock-Associated Noise

Broadband shock-associated noise (BBSAN) is generated from the interaction between the turbulent structures and the shock-cell structure as the turbulence convects through the jet plume. This can occur for either convergent or convergent-divergent nozzles. The first prediction method for BBSAN was developed by Harper-Bourne and Fisher[39]. Shock associated noise is observed as a broad spectral peak, with additional peaks at lower intensities and higher frequencies, at relatively large angles from the jet downstream axis. The interaction between the downstream traveling instability waves and the nearly periodic shock-cell structure results in an interference pattern of traveling waves. The phase velocity of these waves can be higher than that of the instability waves alone and gives rise to noise radiation at large angles to the jet downstream axis, including the upstream direction.[34] Since there is a random set of instability waves interacting with the shock cells, the resulting radiation pattern involves broad lobes rather than sharply directional radiation. A recent BBSAN prediction model developed by Morris and Miller[33] uses a RANS CFD solution for the properties of the flow-field and is based on an acoustic analogy.

Screech Tones

Screech tones are the least understood and least predictable component of supersonic jet noise. This is due to their sensitivity to changes in the surrounding environment[31]. In the same manner as the BBSAN, the instability wave interacts with the shock cells in the jet plume and the unsteady interaction generates acoustic radiation in the upstream direction. This leads to an acoustic feedback phenomenon. The feedback acoustic waves propagate upstream within the jet mixing layer and excite the shear layer in the nozzle lip region. The excitation of the shear layer closes the feedback loop as new instability waves are formed which travel downstream.[31]

2.1.3 Jet-Surface Interaction Noise

The preceding jet noise theories and source descriptions correspond to a static jet in which no solid boundaries are present. When a jet is integrated with a surface such as an airframe, noise can be altered or additional noise may be created. Scattering, jet scrubbing, and jet impingement are three ways that jet flows and surfaces interact. Impingement occurs when the jet flow is directly stagnating on an airframe or surface. Jet scrubbing occurs when the jet flow-field is altered due to the surface but isn't stagnating. Scattering occurs when the jet flow is not significantly altered due to the presence of a surface. However, the noise propagation is altered due to the presence of an airframe.

Previous studies[40,41,42,43,44] have suggested that the most dominant source of interaction noise is generated by the turbulence within the free shear layer of the jet convecting downstream past the trailing edge of the wing or airframe. There are potentially two noise generating mechanisms. The first is due to unsteady loadings on the airframe surface within the boundary layer, which produces dipolar noise, as described by Curle's[40] formulation for acoustically compact surfaces. Curle's[40] dimensional analysis of the equations showed that the far-field sound level related to a jet traveling along a surface scales with the sixth power of convection velocity.

The second mechanism, as first discovered by Ffowcs Williams and Hall[41], comes as a result of diffraction of the jets turbulent flow about the trailing edge. He concluded that the edge scattered field is proportional in intensity to the fifth power of flow velocity. As such it is likely to be the dominant sound source at sufficiently low flow speeds.

Crighton and Leppington[42] expanded this work to show that the scaling exponent varies between 5 and 6 depending on the relative stiffness of the surface. Later, Amiet[44] modified these theories to use the surface pressure from the convecting eddies upstream of the trailing edge to determine the strength of the trailing edge noise source. Since both the scrubbing and trailing edge noise mechanisms result from convecting turbulence, their respective radiation frequency content is similar and difficult to separate. The spectral characteristics are apparent in the experimental results shown in Chapter 6.

2.2 Scattering Prediction Methods

Acoustic models for all jet-surface interactions are required for an accurate prediction. A prediction model for the interaction effects due to jet noise scattering is presented in this work. The acoustic analogies such as those by Morris and Farrasat[15] or Miller[16] can provide mixing-noise prediction capabilities based on physical principles but a numerical Green's function solver is required to account for propagation effects. Scattering techniques such as those described in the following sections can solve for the Green's function required in the acoustic analogies.

2.2.1 Boundary Element Method

The boundary element method (BEM) uses an integral equation to solve the Helmholtz equation. The solution at any point in the computational domain is represented by an integral over the outer-boundary of the scattering object. The boundary element method generally is a two step process. In the first step, the unknown acoustic variables on the object surface are determined. This is followed by a second step that computes acoustic variables for any field point. The boundary integral equation is reduced to a linear system of equations by representing the boundary as a set of "equivalent" sources.[45] Solving the linear system can become computationally expensive as the order of the matrix depends on the size of the object and the mesh needs to be fine enough to meet the Nyquist criteria. Also, the sources are restricted to monopoles and dipoles only. Assuming that the computational domain resolves the wavelength of sound, the BEM has shown to be an accurate scattering prediction technique. The BEM has been used by Agarwal and Dowling[45] in the shielding prediction of a monopole acoustic source for the Blended Wing Body configuration. The method has also been validated by Huang and Papamouchou[12]. At high acoustic frequencies, boundary element methods become prohibitively computationally expensive due to the requirement to resolve the acoustic wavelength. Thus, boundary element calculations are restricted to low frequencies.

2.2.2 Equivalent Source Method

The equivalent source method (ESM) follows the same approach as the BEM. The basic concept of the ESM is to replace the boundary value problem (BVP) with a distribution of point multipoles located inside the scattering body.[46] Each multipole is solved for in the system of equations by adjusting their strengths to satisfy the boundary condition. The method is used in NASA's Fast Scattering Code (FSC) by Tinetti *et al.*[13]. The fundamental advantage of the ESM over other boundary methods is that the resulting linear system can be considerably smaller than those arising from boundary element or boundary integral methods. However, for the same reason as the BEM, the calculations are restricted to low frequencies and the computational cost is dependent on the geometry size. Predictions of the FSC[47] are used for comparison in Chapter 5.

2.2.3 Ray Tracing Method

The ray tracing method, based on geometrical ray theory, is derived on the basis that energy is carried along defined paths through a medium. Under certain circumstances, energy along these defined paths can be approximated as rays rather than waves. The ray theory approximation is valid when the wavelength is much smaller than the shielding object and is therefore limited to high frequencies. Further details are described in Section 5.1. This approach offers several advantages for acoustic scattering problems if it satisfies certain criteria. The methods computational cost is frequency independent. The rays need to only be traced once for all frequencies of interest.[14] Also, it is not computationally dependent on the geometry size but only the complexity of the geometry. These are key advantages relative to other methods previously described, which have a high computational cost for high frequencies and large geometries. Another advantage of the ray theory approach is that it can provide a physical understanding of the sound propagation path at any location.

2.3 Summary

Since the understanding of jet noise is directly tied to the understanding of turbulence in jet flows, the prediction of jet noise is and will continue to be an extremely challenging problem. There have been many attempts to modify and improve Lighthill's classical acoustic analogy theory. Since the computation cost of direct simulations of high Reynolds number turbulence is impractical, noise predictions are often based on the solution of the RANS equations closed by a two equation turbulence model such as the methodologies by Tam and Auriault[31], Morris and Boluriaan[32], and Morris and Miller[33]. The methodology by Miller[16] uses an acoustic analogy approach in conjunction with a tailored Green's function to account for propagation effects.

Scattering techniques have been developed that can provide the Green's function required in the acoustic analogies. Boundary integral methods such as BEM and ESM have shown to yield accurate results but are restricted to low frequencies because of computation cost. The ray tracing method is computationally independent of frequency and geometry size. In light of these advantages, the ray tracing method is used in conjunction with an acoustic analogy approach in the following sections to study the shielding effects of a nearby surface on jet mixing noise.

The noise of supersonic jets may comprise of multiple components involving turbulent mixing noise and shock-associated noise. The analysis of turbulent mixing noise for subsonic and supersonic jets is the focus of study. The additional noise sources generated when a surface is in the proximity of jets are discussed in the following sections; however, the analyses are focused on the effects of the surface on the turbulent mixing of the jet.

Chapter 3

Aerodynamic Analysis

In this chapter, the aerodynamic analysis is presented. Steady Reynolds-Averaged Navier-Stokes (RANS) solutions are examined to study the aerodynamic changes in the field-variables and turbulence statistics as a large flat plate is positioned relative to the nozzle exit. The turbulence statistics and field-variables obtained from the steady RANS solutions of the isolated jet are used in the acoustic analogy to predict the associated mixing noise in Chapter 6. To validate the aerodynamic models, results of the isolated jet are compared with Particle Image Velocimetry (PIV) data. The variation of the aerodynamic quantities is examined by comparing predictions from various jet conditions and flat plate configurations with an isolated jet.

3.1 Steady RANS

The steady RANS equations are solved with a Computational Fluid Dynamics (CFD) approach using the NASA Fully Unstructured Navier-Stokes three-dimensional[48] (FUN3D) solver. The Menter[49] Shear Stress Transport (SST) turbulence model is used to close the

RANS equations. The model utilizes the strengths of the Jones and Launder k-ϵ model[50] and the Wilcox k-ω model[51,52]. It utilizes the k-ω model in the inner region of the boundary layer and switches to the k-ϵ model in the outer region and in free shear layers. The model also takes into account the transport of the principal turbulent shear stress within adverse pressure gradients. In this work, the noise source is dependent upon quantities obtained from the steady RANS solution.

The coordinate system and geometry of the nozzle and plate are illustrated in Fig. 3.1. Coordinates x, y, and z are normalized by the nozzle diameter. This normalized coordinate system is used to illustrate results in the following sections. The origin of the coordinate system used for the analysis is located at the nozzle exit. The positive x axis points in the jet principal direction, the y axis is normal to the plate, and the z axis is parallel to the plate. The plate is located at multiple cross-stream distances from the jet centerline axis to the plate surface, y_p, and multiple streamwise distances from the nozzle exit to the trailing edge, x_p.

The plate positions relative to the nozzle exit included in the analysis are shown in Table 3.1. The first column contains normalized streamwise distances from the nozzle exit to the edge of the flat plate and the second column shows normalized radial distances to the flat plate. Table 3.2 provides information regarding the jet operating conditions analyzed. The operating conditions include three subsonic jets, one of which is heated, and two cold supersonic jets, one of which is over-expanded and the other ideally-expanded.

Table 3.1: Plate Locations

Axial Distance to Trailing Edge (x_p/D)	Radial Distance to Jet Centerline (y_p/D)
4	1,2,4,6,8,10
10	1,2,4,6,8,10
20	1,2,4,6,8,10

The field variables and turbulent statistics are discretized on a mixed element (structured-

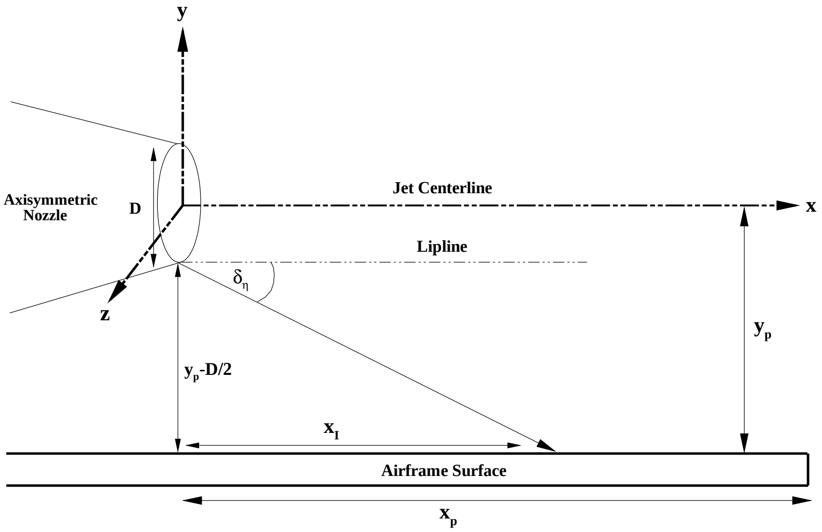

Figure 3.1: The coordinate system and distance parameters used throughout this study.

Table 3.2: Jet Operating Conditions

Nozzle	Setpoint	NPR	TTR	M_a	M_j
SMC000	3	1.197	1.000	0.5	0.513
SMC000	7	1.861	1.000	0.9	0.985
SMC000	27	1.357	1.926	0.9	0.678
SMC016	11606	2.748	1.000	1.128	1.29
SMC016	11610	3.670	1.000	1.31	1.5

unstructured) computational grid. An unstructured grid is used to resolve the jet flow when the plate is present while a structured grid is retained to resolve the jet plume. All calculations are fully three-dimensional and utilize symmetry. The nozzle geometries and flow conditions coincide with the PIV experiment of Bridges and Wernet[21]. Figure 3.2 shows an outline of the three-dimensional computational domain with the plate located two nozzle diameters, D, offset from the jet axis and parallel to the jet centerline. Values of p_o and T_o are specified by boundary conditions consisting of nozzle pressure and temperature ratios at the nozzle inlet and static pressure at the domain exit. A symmetric boundary condition is enforced on the x-y plane at $z = 0$. All other boundaries are defined with a free-stream condition of $M_\infty = 0.01$ and ambient pressure. The SMC000 nozzle profile and a portion of the computational domain are shown in Fig. 3.3. This portion of the domain represents a slice in the x-y plane at $z = 0$ normalized by D. The full computational domain extends $75D$ downstream, $50D$ cross-stream along the z axis, and $100D$ cross-stream along the y axis to form a rectangular prism. The number of grid points in the domain with a plate present is 2,195,937 and the number of elements is 2,827,906. The number of grid points in the domain without a plate present is 1,180,575 and the number of elements is 1,472,843. These represent typical values for the cases examined.

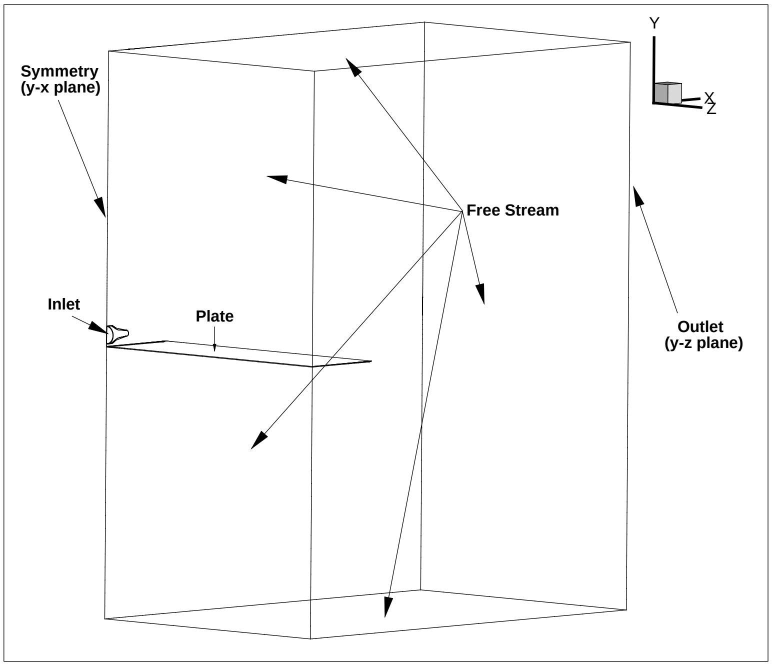

Figure 3.2: An outline of the computational domain used for the CFD calculations. The flow of the jet is in the positive x direction and the coordinate system is centered at the nozzle exit. The domain extends 75 nozzle diameters downstream, 100 diameters in the y direction, and 50 diameters in the z direction. The types of boundaries are labeled.

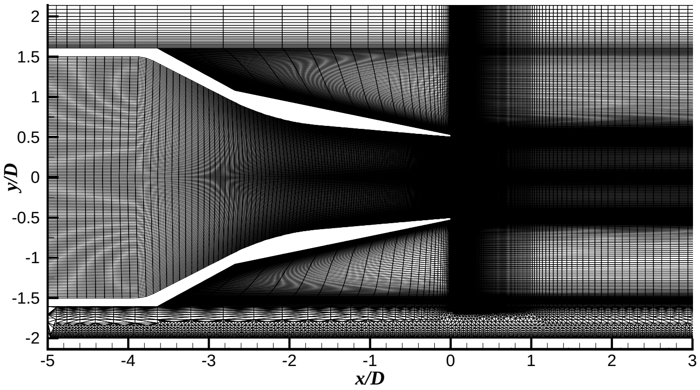

Figure 3.3: A portion of the computational domain on the x-y plane at $z = 0$ showing the structured/unstructured grid of the convergent nozzle and flat plate located $2D$ away from the centerline. The nozzle geometry matches the NASA Glenn Research Center SMC000 nozzle with an exit diameter of $D = 0.0508$ m. The coordinates are normalized by the nozzle exit diameter.

3.2 Aerodynamic Validation

Validation of the isolated jet steady RANS solution is performed by comparing the streamwise velocity component and Turbulent Kinetic Energy (TKE) with the PIV data from the isolated jet experiment of Bridges and Wernet[21]. The PIV dataset of Bridges and Wernet[21] was developed in part to support the validation of jet noise prediction methodologies and steady RANS solutions for a wide range of jet velocities and temperatures. Mean velocities, TKE, and Reynolds stresses are important parameters for statistical acoustic analogies. The first two are used for validation and subsequent analysis in this study.

Subsonic Jet

The first comparison of steady RANS solutions with measurement is performed with a subsonic cold jet operating at $M_j = 0.513$ from the convergent SMC000 nozzle. Contour plots of Fig. 3.4 show a qualitative comparison of the streamwise velocity component and TKE. The velocity and TKE are normalized by the fully expanded velocity and its square, respectively. The steady RANS solutions are shown on the top half planes and the corresponding PIV data are shown on the bottom half planes. The streamwise velocity component shown in Fig. 3.4(a) has noticeable variation from the PIV. The predicted thickness of the potential core past $6D$ is below measurement and the fall-off past $8D$ is higher. The predicted peak TKE occurs near $5.5D$ and the PIV peak TKE occurs further downstream at $6.25D$. Furthermore, the predicted magnitude of peak TKE is lower than measurement. However, the global qualitative agreement is favorable compared to other solutions produced by similar CFD codes (for example see Georgiadis *et al.*[53]).

Qualitative comparisons are conducted for the isolated jet by examining aerodynamic data along the centerline and axial locations at $x/D = 1, 4,$ and 16. Figure 3.5 shows the centerline

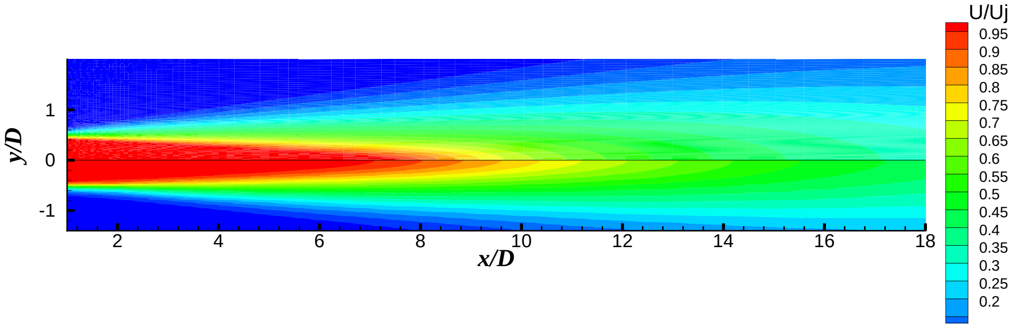

(a) Streamwise Component of Velocity

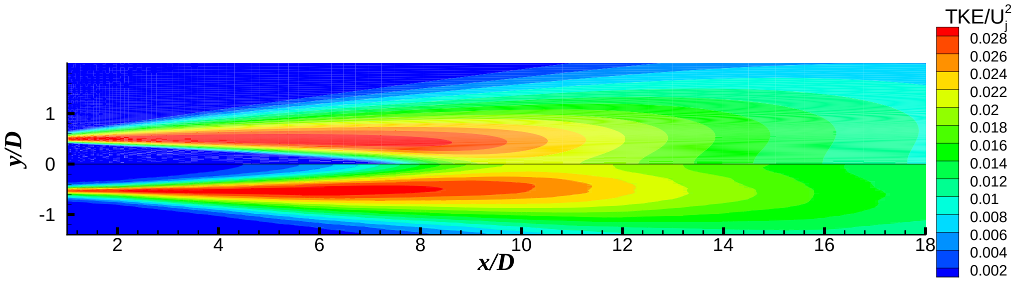

(b) Turbulent Kinetic Energy

Figure 3.4: Contours of the steady RANS solution and PIV data. The steady RANS solutions are shown on the top half planes and PIV data are shown on the bottom half planes. The jet operates at $M_j = 0.513$ and $TTR = 1.00$.

variation of the normalized streamwise velocity component and TKE of both the steady RANS solution and PIV data. Figure 3.6 shows radial profile comparisons of the same quantities. Figure 3.5(a) shows that the predicted jet potential core length is larger than measurement by $2D$. The predicted streamwise velocity component follows the same $\approx 1/x$ decay as the measured data along the centerline, shown in Fig. 3.5(a), and also matches the radial decay at $x/D = 1$ and $x/D = 4$, shown in Fig. 3.6(a). The predicted TKE along the centerline matches the experiment in terms of peak magnitude but the peak occurs one diameter further upstream than experiment. The peak magnitudes of TKE at $x/D = 1$ and

$x/D = 4$ are larger than measurement by 0.0015 and 0.001 $TKE/{U_j}^2$ respectively and are located $0.25D$ closer to the centerline than experiment. The solution under-predicts both the streamwise velocity component and TKE relative to measurement far downstream from the nozzle exit.

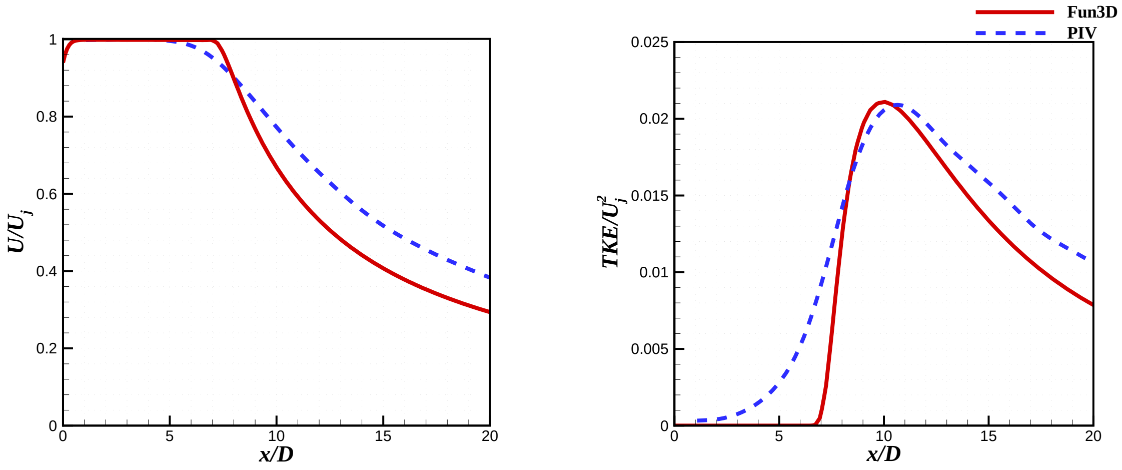

(a) $Velocity$

(b) TKE

Figure 3.5: The (a) steady RANS streamwise velocity component and (b) TKE along the jet centerline ($y/D = 0$ & $z/D = 0$) compared with PIV data from the experiment of Bridges and Wernet[21]. The jet operates at $M_j = 0.513$ and $TTR = 1.00$ from the convergent SMC000 nozzle.

Supersonic Jet

Qualitative comparisons are also conducted for the supersonic over-expanded jet operating at $M_j = 1.29$ from the $M_d = 1.5$ SMC016 nozzle. Again, the aerodynamic data is examined along the centerline and radial locations at $x/D = 1, 4,$ and 16. Figure 3.7 shows the centerline variation of the normalized streamwise velocity component and TKE of both the steady RANS solution and PIV data. Figure 3.8 shows radial profile comparisons of the same quantities. As seen in Fig. 3.7, the predicted potential core length is $2D$ larger relative

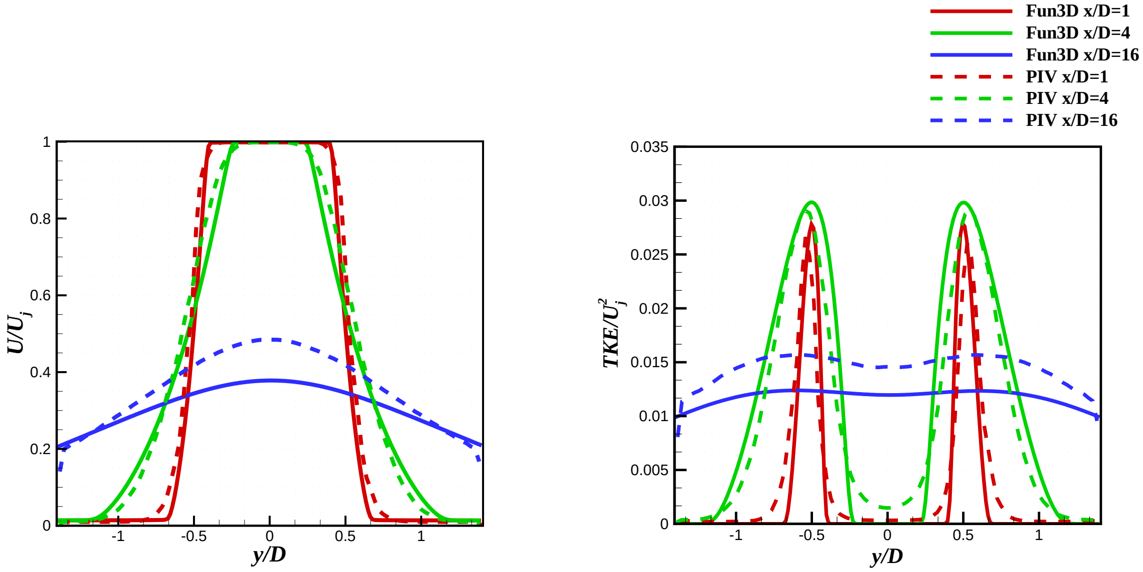

(a) $Velocity$

(b) TKE

Figure 3.6: The (a) steady RANS streamwise velocity component and (b) TKE at $x/D = 1$, $x/D = 4$, and $x/D = 16$ compared with PIV data from the experiment of Bridges and Wernet[21]. The jet operates at $M_j = 0.513$ and $TTR = 1.00$ from the convergent SMC000 nozzle.

to measurement. Within the potential core, the predicted shock cell structure locations compare favorably with the experiment. The steady RANS solution over-predicts the rate of decay along the centerline shown in Fig. 3.7(a) and matches the radial decay in the potential core region at $x/D = 1$ and 4 as shown in Fig. 3.8(a). The steady RANS solution under-predicts the radial decay through the shear layer greater than $0.5D$ from the centerline. In the fully developed region of the flow at $x/D = 16$, the steady RANS solution only slightly over-predicts the radial velocity profile. This is a favorable prediction relative to the TKE profile at $x/D = 16$ shown in Fig. 3.8(b) and the subsonic jet predictions shown at $x/D = 16$ in Fig. 3.6. On the centerline the peak $TKE/{U_j}^2$ is 0.03 below measurement and occurs $2D$ further downstream than measurement as shown in Fig. 3.7(b). The TKE predictions match the experiment in peak magnitude at $x/D = 4$ but over-predicts $TKE/{U_j}^2$

at $x/D = 1$ and $x/D = 16$ by 0.015 and 0.005, respectively. In concurrence with the subsonic cold jet comparisons of Fig. 3.6(b), the predicted TKE is lower than measurement further downstream from the nozzle. These trends are representative of all jet conditions shown in Table 3.2. Further steady RANS comparisons are shown in AppendixA. The predictions are favorable relative to experiment, for all jets examined, in the potential core region of the flow-field where inviscid terms dominate the equations of motion.

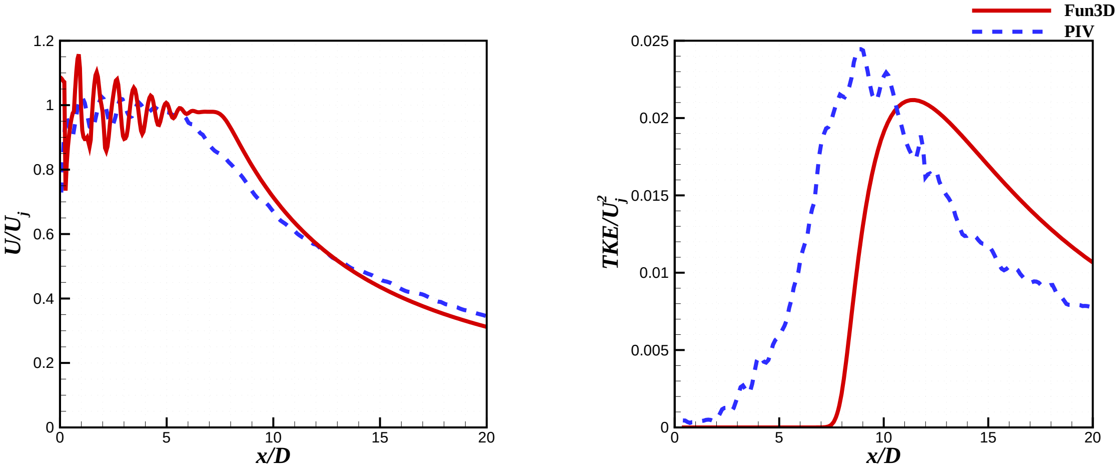

(a) $Velocity$ (b) TKE

Figure 3.7: The (a) steady RANS streamwise velocity component and (b) TKE along the jet centerline ($y/D = 0$ & $z/D = 0$) compared with PIV data from the experiment of Bridges and Wernet[21]. The jet operates at $M_j = 1.29$ and $TTR = 1.00$ from the SMC016 nozzle.

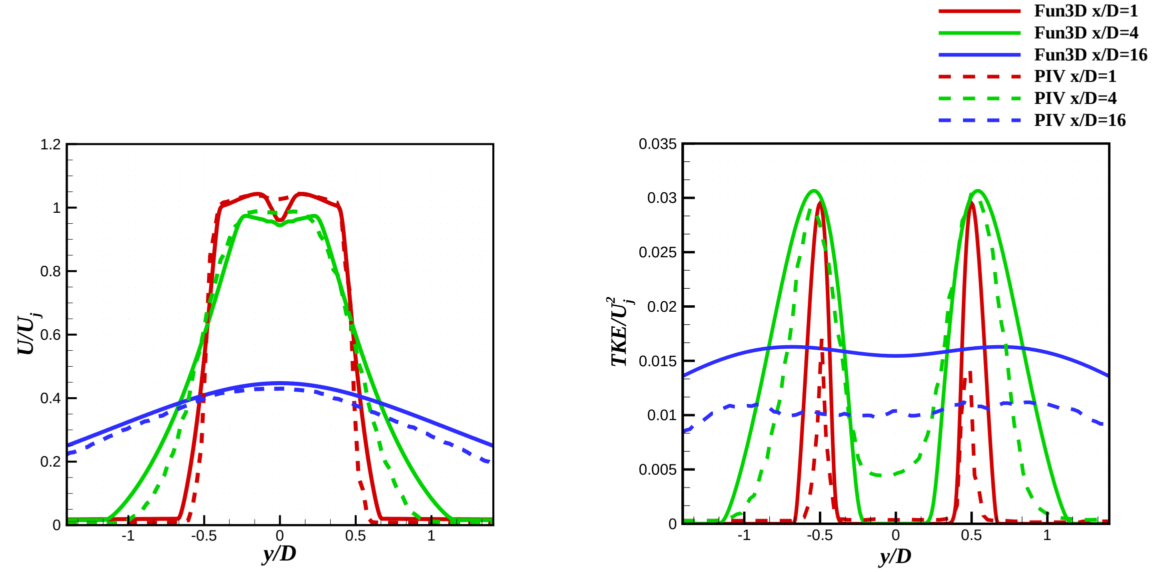

(a) $Velocity$

(b) TKE

Figure 3.8: The (a) steady RANS streamwise velocity component and (b) TKE at $x/D = 1$, $x/D = 4$, and $x/D = 16$ compared with PIV data from the experiment of Bridges and Wernet[21]. The jet operates at $M_j = 1.29$ and $TTR = 1.00$ from the SMC016 nozzle.

3.3 Jet-Airframe Analysis

The steady RANS solutions of a $M_j = 0.513$ and $TTR = 1.00$ jet from the convergent SMC000 nozzle in the presence of a flat plate are now compared with the isolated jet operating at the same conditions. Figure 3.9 shows radial profiles of TKE at $x/D = 10$ for multiple plate positions. The plate is located at $y_p/D = -1, -2, -4, -6, -8$, and -10 perpendicular to the jet centerline and extends to $x_p/D = 10$ and 20 downstream from the nozzle exit. Figure 3.9 shows that as the plate is moved closer to the jet the TKE distribution is increasingly deformed. The peak magnitude closest to the plate decreases and the peak magnitude furthest from the plate increases. This trend is amplified when increasing the x_p/D location from 10 to 20 for most of the cases examined. Furthermore, the jet plume is being deformed and is drawn toward the plate due to a coandă like effect. For example, in Fig. 3.9(a) the $x_p/D = 10$ and isolated jet case both have a TKE local minimum at $y/D = 0$. However, as the plate is moved closer as in Fig. 3.9(f) the local minimum of TKE for $x_p/D = 10$ is now located at $y/D = -0.16$. The effect of extending the plate from $x_p/D = 10$ to $x_p/D = 20$ amplifies the effect of the deformation of the jet plume as can be seen in Fig. 3.9(a). The peak TKE close to the plate is lower by 0.0005 $TKE/{U_j}^2$, and the peak TKE furthest from the plate is higher by 0.001 $TKE/{U_j}^2$. Similar changes of the TKE distribution are observed for all jet conditions examined. These numerical results show the changes in the aerodynamic characteristics of the jet plume induced by nearby surfaces. These changes affect the noise source amplitude and position as the plate location is altered.

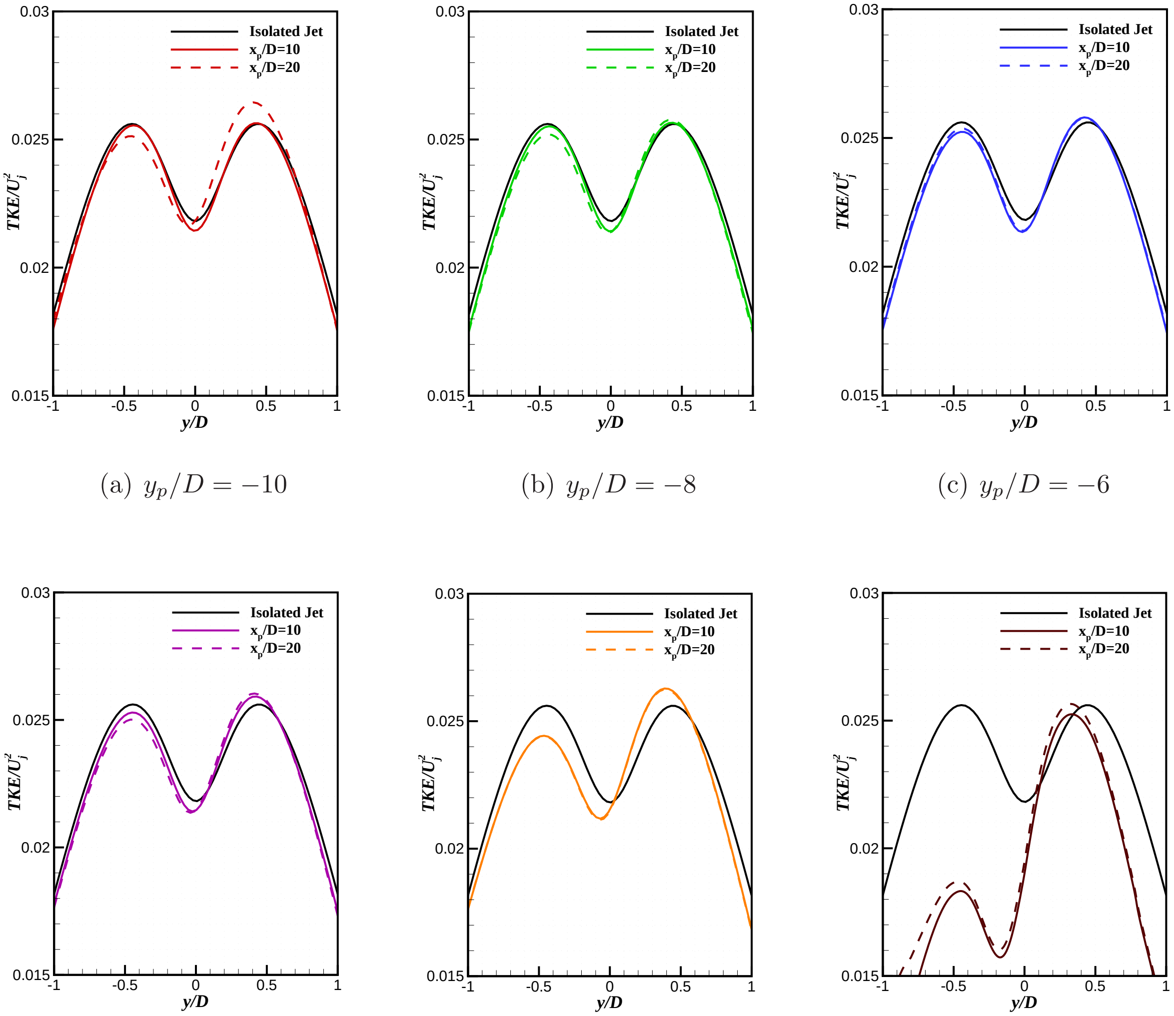

(a) $y_p/D = -10$

(b) $y_p/D = -8$

(c) $y_p/D = -6$

(d) $y_p/D = -4$

(e) $y_p/D = -2$

(f) $y_p/D = -1$

Figure 3.9: Radial variation of TKE at $x/D = 10$ downstream of the nozzle exit. The spatial coordinate is normalized by the nozzle exit diameter. Parts (a)-(f) show the steady RANS solution with the plate located at 10, 8, 6, 4, 2, and $1D$ from the jet centerline respectively and extending 10 and $20D$ downstream from the nozzle ($D = 0.0508$ m). The jet operates at $M_j = 0.513$ and $TTR = 1.00$ from the convergent SMC000 nozzle.

Chapter 4

Surface Interaction Effects on the Jet Acoustic Source

The results of the aerodynamic assessment of Chapter 3 show that nearby solid surfaces change the aerodynamic characteristics of the jet flow-field, even if the jet centerline is multiple diameters away from a solid surface. Thus, the method by which a jet engine is integrated with the airframe of a flight vehicle can have significant effect on the aerodynamic source of sound. This is a highly complicated problem that has received significant attention(See Czech[5] and Thomas[4,54] for example). It is characterized by a large number of parameters that are highly interdependent. In this chapter, a fine-scale mixing model informed by steady RANS solutions is used to qualify the relative effect of propulsion airframe aeroacoustic installation effects on the aerodynamic source. A non-dimensional number is formed that can be used as a basic guide to ascertain whether the aerodynamic source is affected by the airframe relative to the equivalent isolated jet aerodynamic source. The non-dimensional number has arguments involving the flow-conditions and jet position.

4.1 Non-dimensional Analysis

Parameters are identified that have a direct impact on the aerodynamic source of the jet based on the position of the airframe surface. These parameters are illustrated in Fig. 3.1. The first parameter is the fully expanded diameter of the jet,

$$D_j = D\sqrt{\frac{M_d}{M_j}\left(\frac{1+\frac{\gamma-1}{2}M_j^2}{1+\frac{\gamma-1}{2}M_d^2}\right)^{(\gamma+1)/4(\gamma-1)}}, \tag{4.1}$$

where D is the nozzle exit diameter, D_j represents the necessary equivalent nozzle exit diameter for a shock free flow, M_d and M_j represent the design Mach number and the fully expanded Mach number, respectively, and γ is the ratio of specific heats.

Additionally, x_p is the distance from the nozzle exit to the trailing edge of the airframe[1] parallel to the jet centerline. y_p is the characteristic length from the nozzle centerline to the nearest airframe surface. x_I is the shadow distance on the airframe surface from the nearest airframe surface point at which the jet first interacts with the airframe. This value is dependent on the problem geometry, the engine cycle condition, and $x_I = f(x_I)$. The simplest estimate for x_I is the jet impingement location, that is a function of the initial spreading rate of the jet. The parameter, x_I, is approximated as,

$$x_I = \frac{y_p - D/2}{\tan[\delta_\eta]}, \tag{4.2}$$

where δ_η is the spreading angle of the jet. Values of δ_η are not readily available without numerical calculations or measurement. An empirical model developed by Lau[55] is adopted

---

[1] We elect to use airframe and flat plate interchangeably in terms of the analysis.

for δ_η,

$$\delta_\eta = 0.177(1 - 0.294M_j^2)\left(1 + \frac{1}{2}(M_j^2 - 1)(T_j/T_o - 1.4)^2\right), \tag{4.3}$$

which is valid for a wide range of single-stream jet Mach numbers and temperature ratios. The flows of this investigation fall within the range of validity of Eqn. 4.3. Equation 4.3 is dependent on a wide range of parameters that do not explicitly appear. Using these parameters a non-dimensional number is proposed,

$$\Gamma = \left(\frac{D_j}{y_p}\right)\left(\frac{x_p}{x_I}\right). \tag{4.4}$$

Using the approximation of X_I from Eqn 4.2, Eqn. 4.4 can be written as,

$$\Gamma = \frac{D_j x_p \tan[\delta_\eta]}{y_p(y_p - D/2)}, \tag{4.5}$$

where $y_p > D/2$. Physically, Eqn. 4.5 is the ratio of the product of the jet and airframe length scales divided by the cross-stream length scale and interaction distance. Small values of Γ can suggest that airframe effects on the jet aerodynamic noise sources are negligible. Likewise, large values of Γ can suggest that the effects of the airframe on the aerodynamic noise sources of the jet are very large. In the following sections, Eqn. 4.5 is evaluated using different jet conditions and airframe surface positions, and compared with numerical predictions of the variation of the noise from the aerodynamic source.

4.2 Fine-Scale Mixing Model

To quantitatively assess the changes of the acoustic source, a statistical noise prediction approach is selected. Here, we choose the semi-empirical fine-scale mixing noise model of Tam and Auriault[31]. The expression for the spectral density of the acoustic pressure in the far-field, S, is given by,

$$S(\boldsymbol{x},\omega) = 4\pi\left(\frac{\pi}{\ln 2}\right)^{3/2}\int_{-\infty}^{\infty}\int_{-\infty}^{\infty}\int_{-\infty}^{\infty}\frac{\hat{q}_s^2 l_s^3}{\overline{c}^2\tau_s}\frac{|p_a(\boldsymbol{x};\boldsymbol{y},\omega)|^2\exp\left[-\frac{\omega^2 l_s^2}{\overline{u}^2 4\ln 2}\right]}{1+\omega^2\tau_s^2\left(1-\frac{\overline{u}}{c_\infty}\cos\theta\right)^2}d\boldsymbol{y} \tag{4.6}$$

where A is a constant coefficient, c is the speed of sound, $\overline{u}$ is the mean streamwise velocity component, $\boldsymbol{x}$ is the observer position, $\boldsymbol{y}$ is the source position, and ω is the radial frequency. $\hat{q}_s = (4/9)A^2\overline{c}^2\overline{\rho}^2 k_s^2$ is a statistical source term where k_s is the TKE associated with turbulence that produces fine-scale mixing noise. k_s is set equal to the TKE computed from the steady RANS solution.

If predictions are restricted to the sideline direction and it is assumed that sound refraction by the jet shear layer has negligible effect on S, then a simplified form of $p_a(\boldsymbol{x};\boldsymbol{y},\omega)$ can be constructed. As shown by Morris and Farassat[15] the adjoint acoustic pressure at $\psi = \pi/2$ (the jet sideline) is,

$$|p_a(x_2;\boldsymbol{y},\omega)|^2 = \frac{\omega^2}{64\pi^4 c_\infty^4 x^2} \tag{4.7}$$

This approach does not take into account propagation effects associated with sound waves interacting with surfaces such as the flat plate. This is advantageous because the effects of surfaces on the jet noise source are isolated.

The scales of turbulence in Eqn. 4.6 are related to the steady RANS solution of the jet by simple dimensional models. The length scale is $l_s = c_l k_s^{3/2}/\epsilon$ and the time scale is $\tau_s = c_\tau k_s/\epsilon$, where ϵ is the dissipation of TKE. The quantity, ϵ, is computed from the steady RANS solution as $\epsilon = 0.09 k_s \omega$. By relating the turbulent scales to the steady RANS solution, the predicted noise is dependent on the jet mean-flow. The mean flow is dependent on the boundary conditions, the nozzle geometry, and the position of the plate relative to the jet. The acoustic source strength and spatial distribution as a function of frequency is directly connected to the steady RANS solutions.

The coefficients A, c_l, and c_τ of Eqn. 4.6 are specified by comparing prediction with measurement, following the methodology of Tam and Auriault[31]. The coefficients are calibrated with the SMC000 nozzle operating at $M_j = 1.00$ and $TTR = 1.00$. The coefficients are constant irrespective of observer position, jet operating condition, or airframe geometry after calibration. The values are $A = 3548.0$, $c_l = 0.018$, and $c_\tau = 0.015$, that vary from those calculated by Tam and Auriault[31] because the steady RANS solver and turbulence model differ. Figure 4.1 shows the prediction compared with the experiment of Bridges and Brown[56]. The Sound Pressure Level (SPL) per unit St is represented on the y-axis, where $St = \omega D_j/u_j$ is the Strouhal number. The prediction captures the peak intensity and the nearly correct decay of intensity at high frequency. There is a slight discrepancy at lower frequencies where the decay of intensity is lower than measurement.

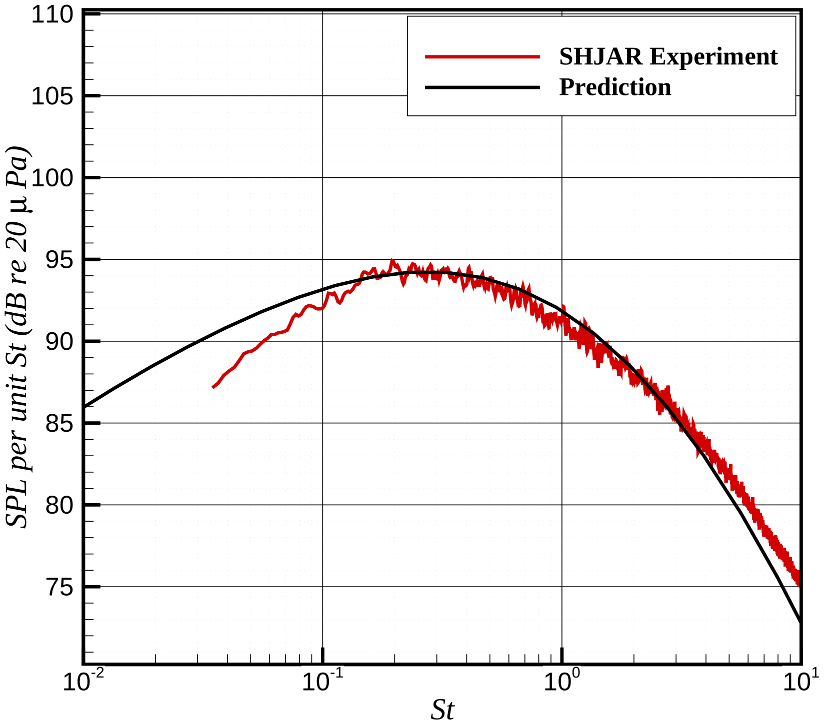

Figure 4.1: The free-field prediction at $R/D = 100$ and $\psi = 90$ degrees using the model of Tam and Auriault[31] compared with the experiment of Bridges and Brown[56]. The jet operates at $M_j = 1.00$ and $TTR = 1.00$ from the convergent SMC000 nozzle with $D = 0.0508$ m.

4.3 Noise Source Results

The effects that the flat plate has on acoustic intensity originating from the jet aerodynamic source are investigated by using the steady RANS solutions and Eqn. 4.6. The isolated jet predictions are subtracted from the installed jet predictions on a Power Spectral Density (PSD) basis for comparison. The first comparison consists of the cold subsonic jet at $M_j = 0.513$ and is presented in Fig. 4.2. In Fig. 4.2(a), the plate is located at $y_p/D = -1, -2, -4, -6, -8$, and -10 from the jet centerline and extends $x_p/D = 10$ downstream of the nozzle exit. In Fig. 4.2(b), the plate is located at $y_p/D = -1$ from the jet centerline and extends $x_p/D = 4, 10$, and 20 downstream of the nozzle exit. When the plate is extended to $x_p/D = 10$ downstream of the nozzle exit, the results from Fig. 4.2(a) show only a small effect on the noise spectrum as the plate approaches the centerline until the plate is at $y_p/D = -2$. The noise deviation from the isolated jet reaches a maximum of -1.5 dB at the lowest frequency and 0.75 dB at the highest frequency when the plate is located at $y_p/D = -2$. For all plate locations further than $2D$ away from the centerline, the noise deviations are within ± 0.75 dB from the isolated jet case. When the plate is located at $y_p/D = -1$, the noise intensity is -6.9 dB relative to the isolated jet case at the lowest frequency. The effect of varying the plate length relative to the nozzle exit is displayed in Fig. 4.2(b). At the lowest frequency, the noise intensity deviation from the isolated jet reaches a maximum of -6.5 dB, -6.9 dB, and -7.9 dB as the plate is extended to $x_p/D = 4, 10$, and 20 downstream from the nozzle exit, respectively. At the highest frequency, the maximum deviation for each plate extension does not exceed 0.75 dB.

Predictions of the over-expanded supersonic $M_j = 1.29$ jet from the convergent-divergent SMC016 nozzle are compared at various plate positions relative to the isolated jet. Figure 4.3(a) displays the effects of the surface as it approaches the jet centerline, and Fig. 4.3(b) shows the effects of the surface as the plate length is extended relative to the nozzle exit.

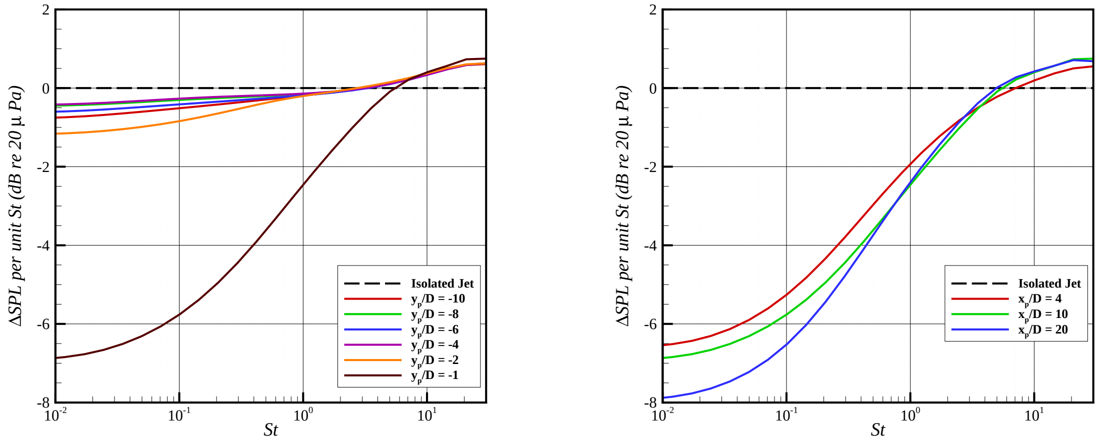

(a) $x_p/D = 10$

(b) $y_p/D = -1$

Figure 4.2: Attenuation plot of the free-field prediction at $R/D = 100$ and $\psi = 90$ degrees using the model of Tam and Auriault[31] for the isolated jet and plate cases. For part (a), the plate is located at 1, 2, 4, 6, 8, and $10D$ laterally from the jet centerline and extends $10D$ downstream from the nozzle. For part (b) the plate is located at $1D$ laterally from the jet centerline and extends 4, 10, and $20D$ downstream from the nozzle. The jet operates at $M_j = 0.513$ and $TTR = 1.00$ from the convergent SMC000 nozzle with $D = 0.0508$ m.

In Fig. 4.3(a), the noise intensity deviation from the isolated jet reaches a maximum of -1.0 dB at the lowest frequency and 0.1 dB at the highest frequency when the plate is located at $y_p/D = -2$. For all plate locations further than $2D$ away from the centerline, the noise deviations are within -0.6 dB from the isolated jet case at the lowest frequency and -0.02 dB at the highest frequency. When the plate is located at $y_p/D = -1$, the noise reaches a maximum -6.4 dB difference from the isolated jet case. From Fig. 4.3(b), the noise deviation from the isolated jet reaches a maximum of -5.7 dB, -6.4 dB, and -7.7 dB at the lowest frequency as the plate extends $x_p/D = 4, 10$, and 20 downstream from the nozzle exit, respectively. The maximum dB difference from the isolated jet for each plate position is slightly decreased in magnitude at lower frequencies when compared to the subsonic jet. There is no increase in noise intensity at high frequencies in contrast to the subsonic case.

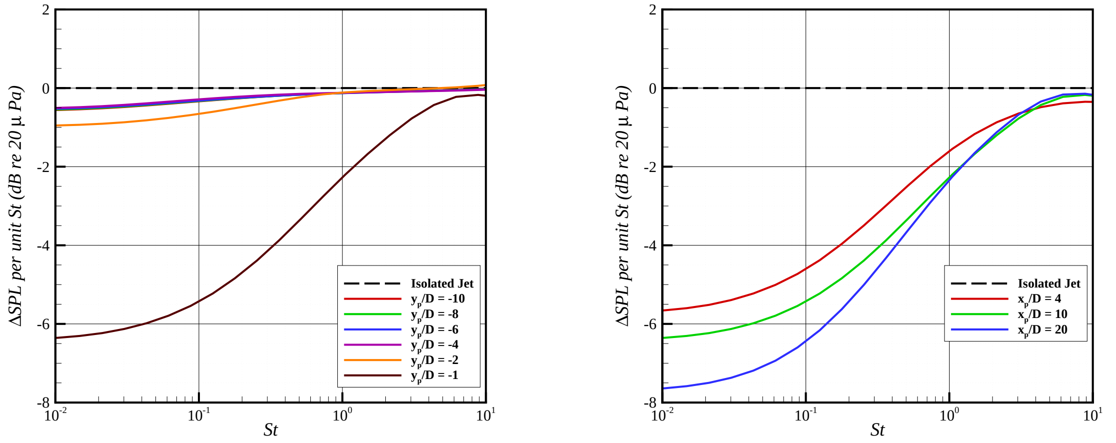

(a) $x_p/D = 10$

(b) $y_p/D = -1$

Figure 4.3: Attenuation plot of the free-field prediction at $R/D = 100$ and $\psi = 90$ degrees using the model of Tam and Auriault[31] for the isolated jet and plate cases. For part (a), the plate is located at 1, 2, 4, 6, 8, and $10D$ laterally from the jet centerline and extends $10D$ downstream from the nozzle. For part (b) the plate is located at $1D$ laterally from the jet centerline and extends 4, 10, and $20D$ downstream from the nozzle. The jet operates at $M_j = 1.29$ and $TTR = 1.00$ from the convergent SMC016 nozzle with $D = 0.0508$ m.

Fig. 4.4 shows comparisons of an on-design $M_j = 1.5$ cold jet. From Fig. 4.4(a), the noise intensity deviation from the isolated jet reaches a maximum of -1.0 dB at the lowest frequency and 0.1 dB at the highest frequency when the plate is located at $y_p/D = -2$ and $x_p/D = 10$. For all plate locations further than $2D$ from the centerline, the noise deviations are within -0.6 dB from the isolated jet case at the lowest frequency and -0.02 dB at the highest frequency. When the plate is located at $y_p/D = -1$, the noise reaches a maximum -6.4 dB difference from the isolated jet case at the lowest frequency. In Fig. 4.4(b), the noise deviation from the isolated jet reaches a maximum of -6.1 dB, -6.4 dB, and -8.1 dB as the plate extends to $x_p/D = 4, 10$, and 20 from the nozzle exit, respectively. In regards to the magnitude of the maximum difference and general trend of the spectra, the predictions of the jet and plate cases relative to the isolated jet case are in close agreement with the over-expanded jet. In Fig. 4.4(b), there is a 0.4 dB increase in magnitude of noise intensity deviation with the plate located at $y_p/D = -1$ and extending $x_p/D = 4$ and 20 downstream when compared to the over-expanded jet in Fig. 4.3(b) at lower frequencies. At the higher frequencies there is no notable difference from the over-expanded jet.

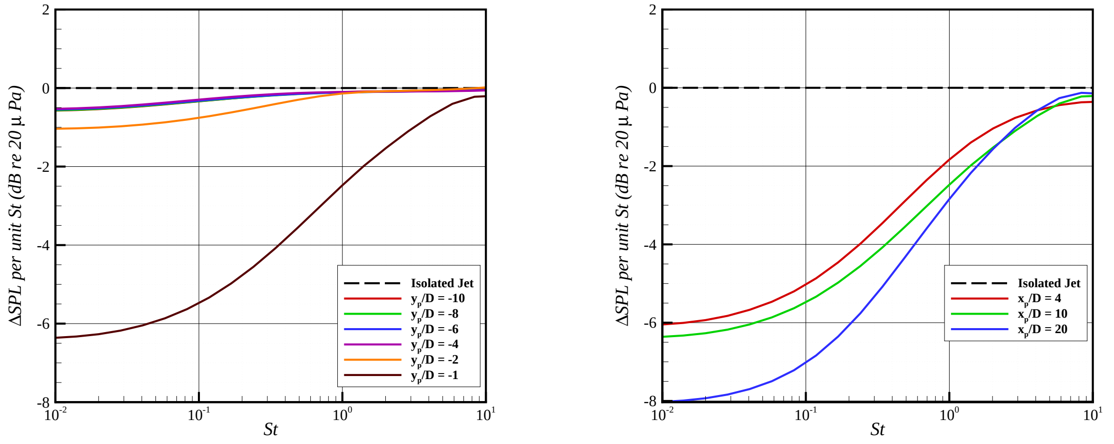

(a) $x_p/D = 10$

(b) $y_p/D = -1$

Figure 4.4: Attenuation plot of the free-field prediction at $R/D = 100$ and $\psi = 90$ degrees using the model of Tam and Auriault[31] for the isolated jet and plate cases. For part (a), the plate is located at 1, 2, 4, 6, 8, and $10D$ laterally from the jet centerline and extends $10D$ downstream from the nozzle. For part (b) the plate is located at $1D$ laterally from the jet centerline and extends 4, 10, and $20D$ downstream from the nozzle. The jet operates at $M_j = 1.50$ and $TTR = 1.00$ from the convergent SMC016 nozzle with $D = 0.0508$ m.

The comparisons described above are representative of the other jet conditions analyzed in this study. As the jet approaches the plate there is a consistently larger difference in the noise spectrum from the isolated jet at lower frequencies. This is due to the surface having a larger effect on the flow further downstream from the nozzle exit. It has been shown by Brooks *et al.*[57] and Podboy[58] that peak noise sources are located near the nozzle exit at higher frequencies and lower frequency peak noise sources are located multiple nozzle diameters downstream. The presence of the plate has a larger effect on the jet flow multiple diameters from the nozzle exit and therefore has a larger effect on the aerodynamic source at lower frequencies.

Next, the effect that the plate has on the acoustic source localization is examined by comparing noise source maps of the jet flow for various plate positions using the steady RANS solutions and the integrand of Eqn. 4.6 near the peak frequency. Contours of SPL per unit St for the cold subsonic $M_j = 0.513$ jet at a frequency of $1kHz$ ($St \approx 0.3$) are shown in Fig. 4.5. In this comparison the plate length extends to $x_p/D = 10$ and the plate is located at $y_p/D = -10, -6, -4, -2,$ and -1 from the jet centerline. When the plate is located at $y_p/D = -10$ in Fig. 4.5(a), the noise source distribution is unaffected by the presence of the plate. The two peak noise sources are located $9.5D$ downstream from the nozzle exit and are symmetric in magnitude about the jet centerline. There is no significant deformation of the source distribution due to the presence of the plate further than $2D$ from the jet centerline. As the plate approaches the jet at $y_p/D = -2$ shown in Fig. 4.5(d), the peak magnitude of the source closest to the plate is decreased by $\approx 1\ dB$ and the location is unchanged. When the plate is located at $y_p/D = -1$, shown in Fig. 4.5(e), the peak noise source furthest from the plate is decreased in magnitude by $\approx 1\ dB$ and is shifted $0.5D$ upstream relative to the $y_p/D = -10$ case shown in Fig. 4.5(a). The peak noise source distribution closest to the plate is significantly deformed. The peak magnitude is decreased by $\approx 6\ dB$ and is shifted $1D$ upstream relative to the $y_p/D = -10$ case. An additional strong noise source is also formed close to the plate further downstream at $x/D = 14$. This is a distinguishable difference from the other comparisons and could be explained by an observed increase in TKE past the trailing edge of the plate. Figure 4.5 shows that the magnitude of the peak acoustic source closest to the plate decreases as the plate surface approaches the jet centerline, and the magnitude of the peak acoustic source furthest from the plate is not significantly altered until the plate is located at $y_p/D = -1$ from the jet centerline. The location of the peak noise sources are unaltered until the plate is located at $y_p/D = -1$. These comparisons represent trends that are consistent for all jet conditions analyzed.

Overall, the results show that the plate has a larger effect on the acoustic source as it approaches the jet centerline and as the plate length extends further downstream. As the effective jet impingement area of the plate is increased, the acoustic intensity radiating from the jet decreases. Note, this result does not account for additional sources produced by the jet interacting with the surface. To quantify the effect of a nearby surface on the jet noise source, the non-dimensional number Γ is used, as described in Eqn. 4.5. The overall sound pressure level (OASPL) is predicted over a frequency range of $20Hz$ to $100kHz$ for all plate locations and jet conditions described in Tables 3.1 and 3.2 using the steady RANS solutions and Eqn. 4.6 at $\psi = \pi/2$. The installed jet predictions of OASPL are subtracted from the isolated jet predictions on a PSD basis. Figure 4.6 shows the absolute value of ΔOASPL as a function of Γ. The physics of the jet flow and airframe interaction dictate the value of Γ, and the value of Γ expresses how large an effect the jet airframe interaction has on the jet noise source. The data collapse shows a critical value of $\Gamma \approx 1$. As the cross-stream length scales $y_p(y_p - D/2)$ decrease to the equivalent of the product of the jet and airframe length scales $(D_j x_p \tan[\delta_\eta])$, Γ increases from 0 to 1. In the region, $0 < \Gamma \lesssim 1$, the cross-stream length scales are dominant and the physical quantities of the aerodynamic flow are not sufficiently altered to have a significant effect on the jet noise source. In Fig. 4.6, small values of Γ approaching ≈ 1 have ΔOASPL less than 0.5 dB and are considered negligible. As the jet spreading angle, fully expanded jet diameter, or surface length increases the product of the jet and airframe length scales surpasses the cross-stream length scales and Γ increases beyond unity. As a result of the dominance of the jet and airframe length scales in this region, $1 < \Gamma < \infty$, the physical quantities of the aerodynamic flow are sufficiently altered and have a large effect on the jet noise source. As shown in Fig. 4.6, values of $\Gamma > 1$ result in a range of ΔOASPL from 2.0 dB to 2.75 dB. It is observed that ΔOASPL increases as Γ increases.

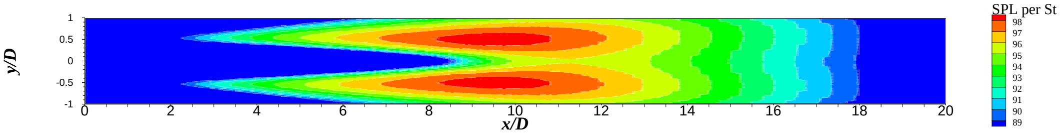

(a) $y_p/D = -10$

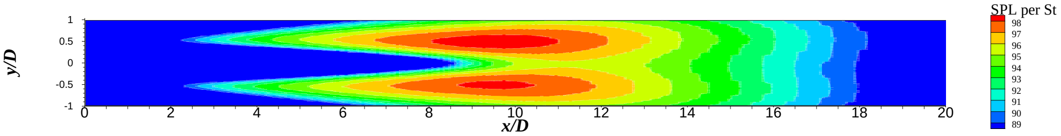

(b) $y_p/D = -6$

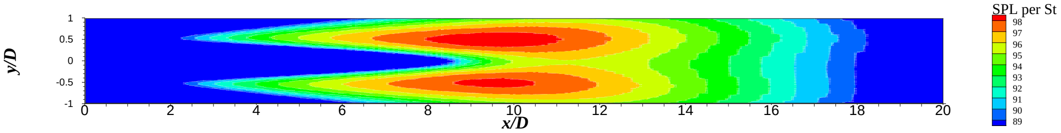

(c) $y_p/D = -4$

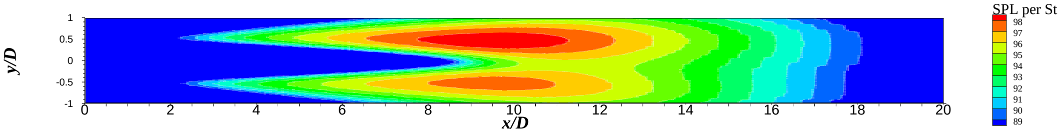

(d) $y_p/D = -2$

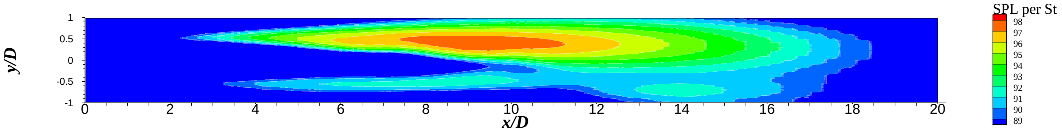

(e) $y_p/D = -1$

Figure 4.5: Contours of peak acoustic source downstream from the nozzle exit at $f = 1000Hz$ ($St \approx 0.3$). The spatial coordinates are normalized by the nozzle exit diameter. Parts (a)-(e) show the acoustic source with the plate located at $y_p/D = -10, -6, -4, -2$, and -1 respectively and extending $10D$ downstream from the nozzle. The jet operates at $M_j = 0.513$ and $TTR = 1.00$ from the convergent SMC000 nozzle with $D = 0.0508$ m.

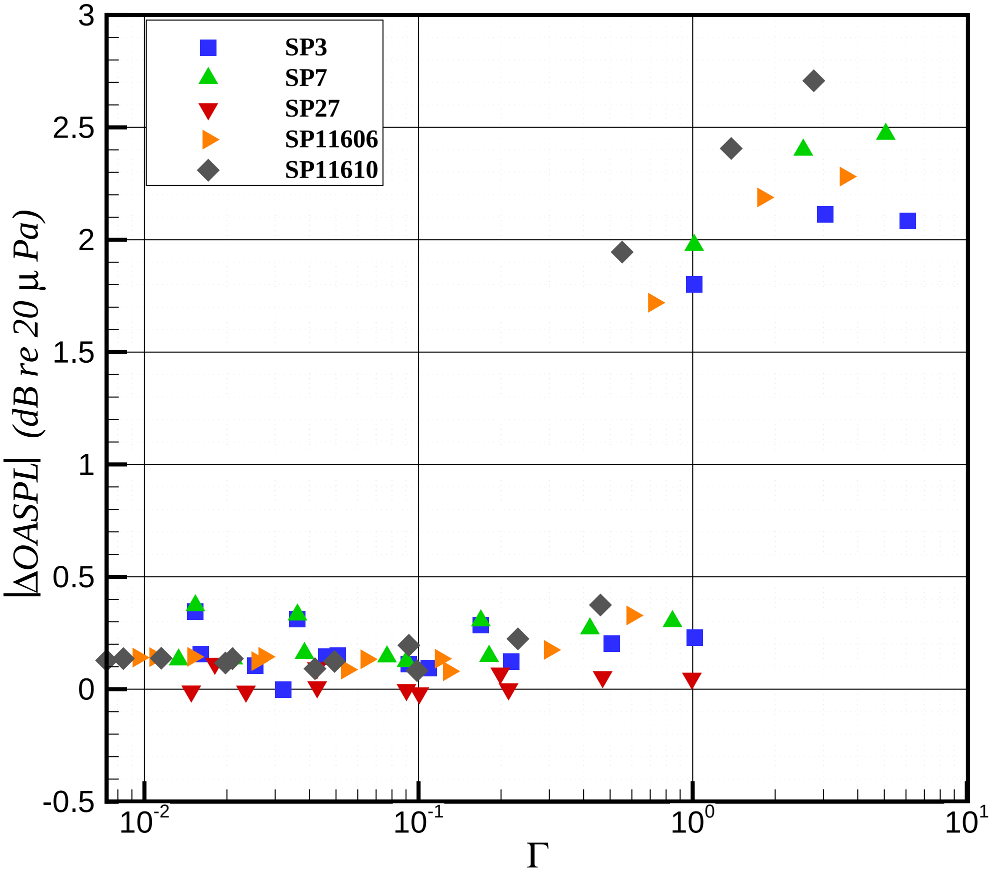

Figure 4.6: Results of $\Delta OASPL$ as a function of non-dimensional number Γ (Eqn. 4.5). $\Delta OASPL$ is calculated relative to the isolated jet case for each airframe configuration and jet condition as listed in Tables 3.1 and 3.2, respectively.

4.4 Summary

The parameter Γ is physically defined as the ratio of the product of the jet and airframe length scales divided by the cross-stream length scale and interaction distance. Calculation of the parameter Γ can be a useful tool when performing propulsion airframe aeroacoustics (PAA) analysis. When analyzing the noise propagation for a jet airframe interaction corresponding to $\Gamma << 1$, the airframe is expected to have a negligible effect on the jet noise source. For instance, a supersonic on-design $M_j = 1.5$ cold jet with an airframe surface located at $x_p/D = 20$ and $y_p/D = 4$ corresponds to $\Gamma = 0.099$ and ΔOASPL $= 0.083dB$ in Fig. 4.6. Since $\Gamma << 1$ and there is a negligible difference in the free-field jet noise source, the isolated jet aerodynamic source model along with a tailored Green's function can used for a prediction that includes propagation about the airframe. A $M_j = 0.985$ jet with an airframe surface located at $x_p/D = 4$ and $y_p/D = 1$ corresponds to $\Gamma = 5.063$ and ΔOASPL $= 2.47dB$ in Fig. 4.6. The large value of Γ results in a large difference from the free-stream noise prediction; therefore a separate aerodynamic source model is required for further analysis. An isolated jet aerodynamic source model can be used for a PAA analysis with small values of Γ. For large values of Γ, some noise reduction can be attributed to the change in the jet noise source and not to shielding effects. However, large values of Γ also suggest that additional noise sources may exist from jet-surface interaction such as scrubbing and trailing edge noise. Recent studies have investigated the effects of liners on propulsion airframe surfaces[54]. The effectiveness of airframe liners is associated with the location of the airframe relative to the jet flow. The implications of Γ could be useful in future PAA liner studies.

The parameter Γ can include additional terms involving multiple jet streams or account for the boundary layer thickness on the airframe. An equivalent parameter for the fully expanded jet diameter and jet spreading angle can be developed for a dual-stream jet. However, a new model would be required for the estimation of the jet spreading angle. Inclusion of boundary layer effects will increase the effect of the cross-stream length scales. The airframe boundary layer thickness can be subtracted from the cross-stream length scales. A model to estimate the boundary layer thickness would be required. The general effect of the airframe on the jet noise source as a function of Γ is expected to be consistent for these cases but may have a different critical value.

Chapter 5

Ray Tracing Analysis

In this chapter, an overview of the ray tracing method is presented. The method, based on geometrical ray theory, is derived on the basis that energy is carried along defined paths through a medium. Under certain circumstances, energy along these defined paths can be approximated as rays rather than waves.[59] The geometrical ray theory approach offers several advantages for acoustic scattering problems if it satisfies certain criteria.[60] The methods computational cost is frequency independent. The rays need to only be traced once for all frequencies of interest. Also, it is not computationally dependent on the geometry size but only the complexity of the geometry. These are key advantages relative to other methods such as the boundary element method used by Agarwal[45] or the equivalent source method used in NASA's Fast Scattering Code by Tinetti *et al.*[13], which carry a large penalty for high frequencies and large geometries. Throughout the rest of the chapter, ray theory and the geometrical theory of diffraction are derived. The implementation of the theory is then described, and the developed ray tracing solver is validated against experimental results. This scattering technique is useful for predicting diffraction effects such as jet noise diffracting from an airframe.

5.1 Ray Theory

The three dimensional wave equation is,[59]

$$\left(\nabla^2 - \frac{1}{c^2}\frac{\partial^2}{\partial t^2}\right) p(\boldsymbol{x}, t) = 0, \tag{5.1}$$

where c is the local speed of sound, ∇ is the vector differential operator, and $p(\boldsymbol{x}, t)$ is the acoustic pressure defined in three dimensional space, $\boldsymbol{x}$, and time, t. Assuming a solution for the acoustic pressure from a constant-frequency disturbance that is a complex function separable in space and time,

$$p(\boldsymbol{x}, t) = \hat{p}(\boldsymbol{x})e^{i\omega t}, \tag{5.2}$$

and substituting it into the wave equation results in the Helmholtz equation,

$$\nabla^2\hat{p}(\boldsymbol{x}) + \left(\frac{\omega}{c}\right)^2 \hat{p}(\boldsymbol{x}) = 0, \tag{5.3}$$

where $\hat{p}(\boldsymbol{x})$ is the complex spatially dependent amplitude of acoustic pressure and $\omega = 2\pi f$ is radial frequency. An assumed solution for the complex amplitude is,

$$\hat{p}(\boldsymbol{x}) = A(\boldsymbol{x}, \omega)e^{i\omega\tau(\boldsymbol{x})}, \tag{5.4}$$

where $\tau(\boldsymbol{x}) = T(\boldsymbol{x})/c_\infty$ is the quantity known as the eikonal[59] and c_∞ is the ambient speed of sound. Constant values of $T(x)$, with units of length, define surfaces of constant phase.

Substituting the assumed solution into the Helmholtz equation gives,

$$\nabla^2 A + i\omega\left(2\nabla A \bullet \nabla\tau + A\nabla^2\tau\right) - \omega^2 A\left[(\nabla\tau)^2 - \frac{1}{c^2}\right] = 0. \tag{5.5}$$

Equating the real and imaginary parts results in two equations that are coupled and nonlinear, which are difficult to solve. To simplify the problem for a high-frequency limit, it can be assumed that an asymptotic expansion of the pressure amplitude $A(x,\omega)$ exists as a power series (See Pierce[61] for details) in inverse powers of frequency ω,

$$A(\boldsymbol{x},\omega) = A_0(\boldsymbol{x}) + \frac{1}{\omega}A_1(\boldsymbol{x}) + \frac{1}{\omega^2}A_2(\boldsymbol{x}) + ... \tag{5.6}$$

After substituting Eqn. 5.6 into Eqn. 5.5 and eliminating all terms except those with the two highest orders of magnitude of ω, the equation simplifies to,

$$i\omega\left(2\nabla\tau\nabla A_0 + \nabla^2\tau A_0\right) - \omega^2 A_0\left[(\nabla\tau)^2 - \frac{1}{c^2}\right] = 0. \tag{5.7}$$

It is assumed that A_0 is a valid approximation for A with high ω $\left(\lim\limits_{\omega\to\infty} A(\boldsymbol{x},\omega) = A(\boldsymbol{x})\right)$. Separation of the real and imaginary terms and further simplification leaves,

$$(\nabla\tau)^2 = \frac{1}{c^2} \qquad \mathit{or} \qquad (\nabla T)^2 = \frac{c_\infty^2}{c^2} = n^2 \tag{5.8a}$$

$$2\nabla\tau\nabla A + \nabla^2\tau A = 0 \qquad \mathit{or} \qquad \nabla \bullet \left(A^2\nabla\tau\right) = 0. \tag{5.8b}$$

This result could also be derived directly from Eqn. 5.5 by setting the coefficients of ω and ω^2 to zero. Eqn. 5.8a is the eikonal equation, where $n = c_\infty/c$ is the index of refraction. The second part of Eqn. 5.8a is formed from multiplying through by A and using the mathematical relation $\nabla \bullet (\phi \vec{B}) = \phi \nabla \bullet \vec{B} + \nabla \vec{B} \bullet \phi$. Noting that a dot product of a vector with itself gives the magnitude squared of that vector, it can be shown from Eqn. 5.8a that,[59]

$$\nabla T = n\hat{s}, \tag{5.9}$$

where $\hat{s}$ is the unit vector that gives the local direction of propagation. Tracing the variation of $\hat{s}$ in space defines a ray path. If the local speed of sound is equal to the ambient speed of sound, then $n = 1$, and the ray path travels in a straight line. According to Eqn. 5.9, a ray path is perpendicular to the eikonal. This approximation implies that a ray is always normal to the local surface of constant phase, as shown in Figure 5.1.

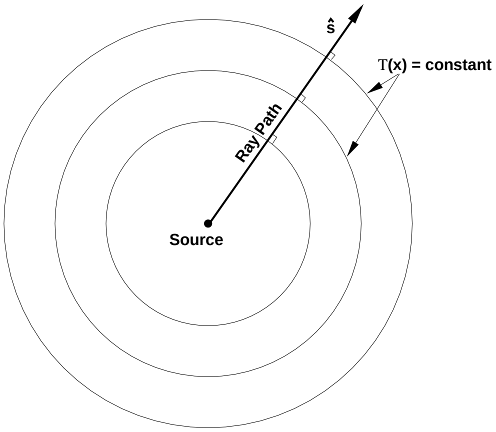

Figure 5.1: The wavefront and constant phase along a ray for a point source and $c = c_\infty$

To determine how the amplitude A varies along a ray, Eqn. 5.8b is solved using ray tube areas.[61] A ray tube consists of all rays passing through a small area $S(\boldsymbol{x}_0)$ at a point $\boldsymbol{x}_0$ to a point $\boldsymbol{x}$ with a cross sectional area $S(\boldsymbol{x})$, as shown in Figure 5.2.

By applying Gauss's theorem to the volume of the ray tube segment, the volume integral

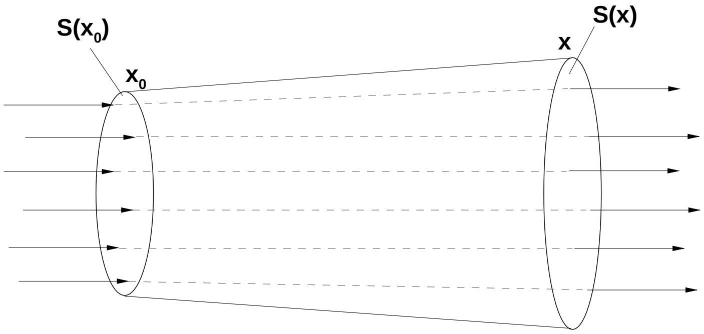

Figure 5.2: A ray tube consisting of all rays passing through an area S.

can be written as a surface integral,

$$\int\int\int \nabla \bullet \left(A^2 \nabla \tau\right) dV = \int\int \left(A^2 \nabla \tau \bullet \vec{\boldsymbol{n}}\right) dS, \tag{5.10}$$

where $\vec{\boldsymbol{n}}$ is the surface normal vector. Since the ray paths are in the direction $\nabla T = \hat{s}$, the rays only pass through the end caps and the integrals over the surfaces of the sides of the ray tube vanish. Integrating over surfaces of the end caps results in,

$$A^2(\boldsymbol{x}) S(\boldsymbol{x}) (\nabla \tau \bullet \vec{\boldsymbol{n}})_{\boldsymbol{x}} - A^2(\boldsymbol{x}_0) S(\boldsymbol{x}_0) (\nabla \tau \bullet \vec{\boldsymbol{n}})_{\boldsymbol{x}_0} = 0. \tag{5.11}$$

If the ray is passing through a homogeneous medium ($c = constant$), then $(\hat{s} \bullet \vec{\boldsymbol{n}})_{\boldsymbol{x}} = (\hat{s} \bullet \vec{\boldsymbol{n}})_{\boldsymbol{x}_0}$ and the pressure amplitude at some point $\boldsymbol{x}$ along the ray tube can be defined as,

$$A(\boldsymbol{x}) = A(\boldsymbol{x}_0) \left[\frac{S(\boldsymbol{x}_0)}{S(\boldsymbol{x})}\right]^{1/2}. \tag{5.12}$$

This solution shows that the energy within a ray tube (SA^2) remains constant within the limitation set forth by the eikonal equation. If the tube represents a single ray and the area ratio is known, Eqn. 5.12 relates the amplitudes at two points $\boldsymbol{x}$ and $\boldsymbol{x}_0$. In a spherical pressure wave of radius r, the energy of the wavefront is evenly distributed over the spherical surface area $4\pi r^2$. Thus, the energy per unit area of an expanding spherical pressure wave decreases as $1/r^2$. Using the ratio of spherical surface areas at two points $\boldsymbol{x}$ and $\boldsymbol{x}_0$ along a ray with $r = \|\boldsymbol{x} - \boldsymbol{x}_0\|$, the amplitude $A(x)$ decreases as $1/r$. Now, referring back to the assumed amplitude in Eqn. 5.4, the complex spatially dependent amplitude of acoustic pressure can be determined along a ray path through a homogeneous medium as,

$$\hat{p}(\boldsymbol{x}) = A(\boldsymbol{x}_0, \omega) \left[\frac{1}{\|\boldsymbol{x} - \boldsymbol{x}_0\|} \right] e^{i\omega\tau(\boldsymbol{x})}, \tag{5.13}$$

provided the amplitude A at some point $\boldsymbol{x}_0$ is known and all conditions satisfy the eikonal equation.

5.1.1 Geometrical Theory of Diffraction

The geometrical theory of diffraction for acoustics is an extension to geometrical ray theory that includes a solution to the diffracted field in the shadow region. The shadow region is where there is no direct line of sight from a source to observer. The theory, developed by Keller,[60] has been recently used in the area of propulsion airframe aeroacoustics to aid in the study of shielding effects (see Suzuki[62], Agarwal[14], Rens[63], and Lummer[64] for example). In compliance with the ray theory described previously, the geometrical theory of diffraction assumes that energy travels along straight or curved lines through a medium. Incident rays that hit surface edges, corners, or slightly graze the surface create diffracted rays that propagate to the shadow region. There are two possible solutions of diffracted rays supported by the theory that account for the diffracted field; edge-diffracted rays and creeping rays. Edge-diffracted rays are the focus of this study; however, creeping rays and other possible contributions to the diffracted field are discussed.

Edge-Diffracted Rays

The fundamental concepts of edge-diffracted rays are based on a modified form of Fermat's principle. Fermat's principle for edge diffraction states that an edge-diffracted ray from a point S to a point O is a curve that has stationary optical length among all curves from S to O with one point on the edge[60]. In other words, the curves correspond to paths that can be traversed in the least time. The ray paths from S to some point on the edge V and V to O are straight lines unless traveling through different media. If the two rays lie in different media, the ray paths are assumed to follow Snell's law of refraction.

Keller observed from Sommerfeld's[65] solution of diffraction by a semi-infinite screen with a straight edge that incident waves propagating in a direction normal to the edge create a cylindrical diffracted wave centered on the edge. This observation suggests that an incident ray normal to the edge creates diffracted rays propagating in all directions normal to the edge. The same observation is made for incident waves propagating at an oblique angle to the edge which create diffracted waves that form a conical section. The diffracted wave fronts produced by an oblique incident wave are parallel cones with a shared axis on the edge. Thus, incident rays at an oblique angle with the edge produce a cone of diffracted rays with the axis as the edge and the vertex at the point of diffraction. Following Fermat's principle for edge diffraction, the diffracted ray and the corresponding incident ray make equal angles with the edge at the point of diffraction, provided that they are both in the same medium. These principles of diffracted rays are geometrically illustrated in Figure 5.3.

After the ray diffracts, it has similar properties to the incident ray, but it is dependent on the field at the point of diffraction. The acoustic pressure field at the diffraction point on the edge is determined using the ray theory solution of Eqn. 5.13,

$$\hat{p}(\boldsymbol{V}) = \frac{A(\boldsymbol{S},\omega)}{\|\boldsymbol{V}-\boldsymbol{S}\|} e^{i\omega\tau(\boldsymbol{V})}, \tag{5.14}$$

where $\boldsymbol{S}$ is the source location and $\boldsymbol{V}$ is the diffraction location at the edge. The acoustic pressure field at the diffraction point determines the initial amplitude and phase of the diffracted ray. The phase along the diffracted ray is simply the eikonal, $\tau(\boldsymbol{O})$, along the diffracted ray added to the phase at the diffraction point. To determine the amplitude of the diffracted ray, the ray tube area relationship of Eqn. 5.12 is used. In contrast to the spherical spreading rate of the incident ray, the cross-sectional area of the diffracted ray tube is proportional to r because the wave is cylindrical. Therefore, the energy per unit area of the diffracted ray tube decreases as r^{-1} and the amplitude decreases as $r^{-1/2}$ in Eqn. 5.12. Using this result and assuming that the amplitude and phase on the diffracted ray is proportional to the field at the point of diffraction, the acoustic pressure of the diffracted ray is,

$$\hat{p}(\boldsymbol{O}) = D\hat{p}(\boldsymbol{V}) \left[\frac{\rho}{r(r+\rho)}\right]^{1/2} e^{i\omega\tau(\boldsymbol{O})}, \tag{5.15}$$

where D is the diffraction coefficient, r is the distance from the edge to observer ($\|\boldsymbol{O}-\boldsymbol{E}\|$), and ρ is the distance from source to observer ($\|\boldsymbol{O}-\boldsymbol{S}\|$). Keller[60] found that Eqn. 5.15 satisfies Sommerfeld's[65] exact solution for diffraction of a wave by a half-plane when it is asymptotically expanded for large frequencies. The resultant diffraction coefficient D is,

$$D = \frac{e^{i\frac{\pi}{4}}\sin\left(\frac{\pi}{n}\right)}{n\sqrt{2\pi k}\sin(\theta)} \left[\frac{1}{\cos\frac{\pi}{n} - \cos\frac{\phi_s-\phi_o}{n}} + \frac{1}{\cos\frac{\pi}{n} - \cos\frac{\phi_s+\phi_o+\pi}{n}}\right], \tag{5.16}$$

where $k = 2\pi f/c_\infty$ is wave number, ϕ_s is the polar angle to the incident ray, ϕ_o is the polar angle to the diffracted ray, and θ is the oblique angle between the edge and incident ray. Here, n is a parameter of the wedge angle, $\beta = n\pi$. The angles are illustrated in Figures 5.3 and 5.4. Analysis of a half-plane corresponds to $n = 2$. Adopting a simplification from Agarwal *et al.*[14], a wedge index $\nu = \pi/\beta$ is used to redefine the diffraction coefficient as,

$$D = \frac{\nu \sin(\nu\pi)\, e^{i\frac{\pi}{4}}}{\sqrt{2\pi k}\sin(\theta)} \left[\frac{1}{\cos(\nu\pi) - \cos(\nu(\phi_s - \phi_o))} + \frac{1}{\cos(\nu\pi) - \cos(\nu(\phi_s + \phi_o + \pi))} \right]. \tag{5.17}$$

The contribution to the acoustic field from a single diffracted ray can be calculated using Eqns. 5.15, and 5.17, and the geometric parameters illustrated in Figures 5.3 and 5.4.

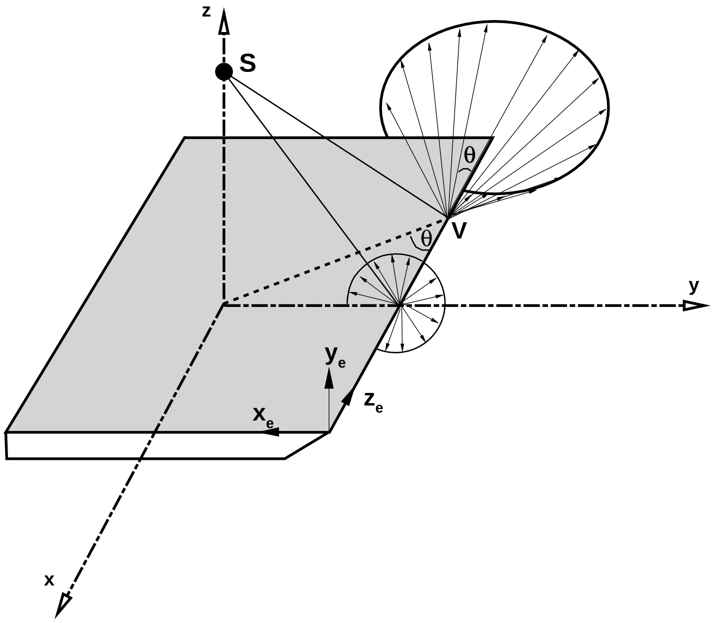

Figure 5.3: Parameters describing incident rays diffracting from the edge of a plate. Incident rays at an oblique angle to the edge form a cone of diffracted rays with an equivalent angle. Incident rays normal to the edge form a cylindrical distribution of diffracted rays corresponding to an angle of $\theta = 90°$.

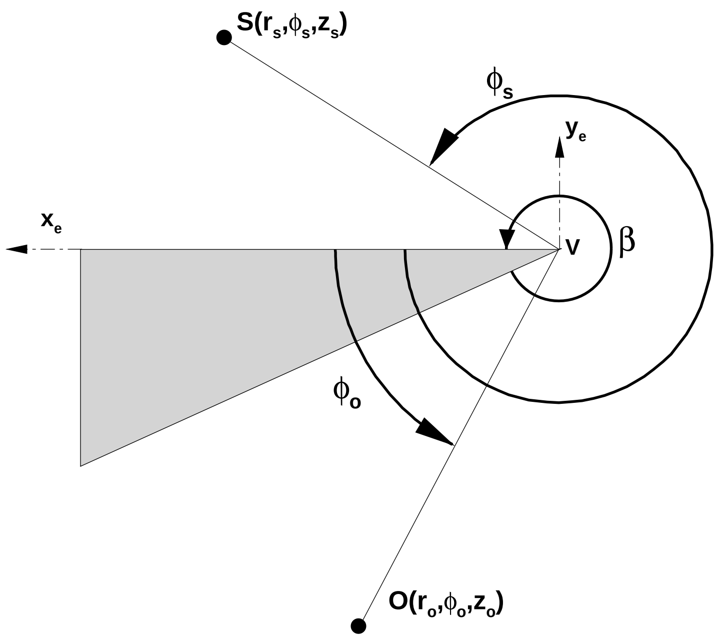

Figure 5.4: Parameters for diffraction from a sharp edge.

Creeping Rays and Corner Diffraction

Creeping rays, also known as surface diffracted rays, are produced when a ray is incident tangentially to a smooth boundary or interface[66]. After the incident ray grazes the tangent surface, it travels along the surface and continuously sheds a diffracted ray at every point on the surface, as shown in Figure 5.5. The diffracted rays travel at an incident angle tangent to the surface at the point from which it emitted. The concept of creeping rays also follows an alternate form of Fermat's principle that states that a surface diffracted ray from a point S to a point O is a curve that makes stationary the optical length among all curves from S to O having an arc on the boundary. This implies that S to S_T and O_T to O are straight lines tangent to the surface at S_T and O_T respectively, and S_T to O_T is a geodesic curve on the surface.

A solution to surface diffracted rays, similar to the edge-diffracted ray, is proposed by Levy

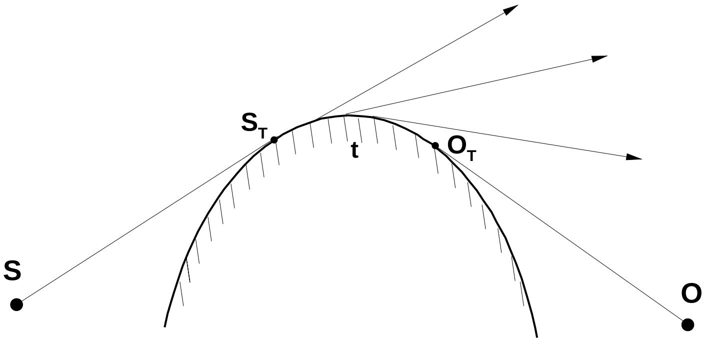

Figure 5.5: Incident ray diffracting from a smooth surface.

and Keller[66] as,

$$\hat{p}(\boldsymbol{O}) = T(\boldsymbol{S}_T, \boldsymbol{O}_T)\hat{p}(\boldsymbol{S}_T)\left[\frac{\rho}{r(r+\rho)}\right]^{1/2} e^{i\omega\tau(\boldsymbol{O})}, \tag{5.18}$$

where $T(\boldsymbol{S}_T, \boldsymbol{O}_T)$ is a transfer function that relates the diffracted field at the two tangent points $\boldsymbol{S}_T$ and $\boldsymbol{O}_T$.[67] The function $T(\boldsymbol{S}_T, \boldsymbol{O}_T)$ is given by,

$$T(\boldsymbol{S}_T, \boldsymbol{O}_T) = \sum_m D_m(\boldsymbol{S}_T)\left[e^{\left(ikt - \int_0^t \alpha_m(\tau)d\tau\right)}\sqrt{\frac{d\sigma(\boldsymbol{S}_T)}{d\sigma(\boldsymbol{O}_T)}}\right] D_m(\boldsymbol{O}_T). \tag{5.19}$$

Here, $D_m(\boldsymbol{x})$ is the diffraction coefficient at a point $\boldsymbol{x}$, α_m is the decay coefficient, t is the distance along the curve, and $[d\sigma(\boldsymbol{S}_T)/d\sigma(\boldsymbol{O}_T)]^{1/2}$ is the attenuation of the ray field due to the divergence of two nearby creeping rays. The values of these coefficients are problem specific and are based on the diffraction geometry, material properties, and wave number. These values have been evaluated for simple problems such as a cylinder and a sphere by Levy[66]. Eqn. 5.19 shows that the creeping ray transfer function exponentially decreases with the distance traveled along the curve. If $t << r$, where r is the distance to the observer, the creeping ray converges to the approximate solution of an edge-diffracted ray. If $t >> r$, the field along the ray decreases exponentially and has a negligible contribution to the diffracted field relative to any edge-diffracted rays. Thus, the use of only edge-diffracted rays is a valid approximation for problems involving sharp edges, as in the physical systems investigated in this work.

Corner-diffracted rays are derived following the same approach as the edge-diffracted rays, except the diffracted rays propagate in all directions from the corner. The wave fronts from corner-diffracted waves are spherical and centered at the corner, as described by Keller[68]. Since the cross-sectional area of the corner-diffracted ray tube is proportional to $1/r^2$, the amplitude along the diffracted ray decreases as $1/r$. The acoustic pressure field due to the corner-diffracted is,

$$\hat{p}(\boldsymbol{O}) = C\hat{p}(\boldsymbol{V}) \left[\frac{1}{\|\boldsymbol{O} - \boldsymbol{V}\|} \right] e^{i\omega\tau(\boldsymbol{O})}, \tag{5.20}$$

where C is the corner diffraction coefficient. Similar to D, the corner diffraction coefficient must depend on the geometric parameters, the directions of the incident and diffracted rays at the point of diffraction, and wave number. Since C must be proportional to γ or k^{-1}, the corner diffracted field decreases faster than edge-diffracted rays as k increases. The corner-diffraction problem is more complex than the edge or surfaces diffraction problem. Solutions have been proposed for specific problems such as corner-diffraction of an elliptical cone by Kraus[69] and a circular cone by Felsen[70] and Siegel[71]. At high frequencies, edge-diffracted rays have the largest contribution to the diffracted field in the shadow region. Due to the dominance of the edge-diffracted rays over the two other types of diffracted rays, only the edge-diffracted rays are applied in the ray tracing implementation in this work.

5.2 Implementation

In this thesis a ray tracing program is developed to calculate the edge-diffracted rays that account for the acoustic pressure field in the shadow region, where there is no direct line of sight between the source and observer. Accounting for the acoustic pressure field in the shadow region allows for complex aeroacoustic predictions such as airframe shielding. In this section, the methodology in which ray theory and the geometrical theory of diffraction is implemented is described. The description includes how the scattering geometry of the physical system under investigation is used as input to the computer program and how the edge-diffracted rays and incident rays are calculated. The implementation begins by reading a geometry, along with a source and observer location, into computer memory. The information from the geometry file is then used to find the three-dimensional projection and edge, or diffraction outline, relative to a source and observer location. The resulting diffraction outline is then used to determine if the observer is in the shadow region. Edge-diffracted rays are then determined from the diffraction outline and summed with any existing direct incident rays in the complex field. An outline of the implementation is described in the following steps:

1. Read the scattering geometry.
2. Find the three-dimensional projection of the geometry.
3. Find the edge of the geometry.
4. Test if the observer is in the shadow zone.
5. Find all diffracted rays associated with observer.
6. Sum the existing diffracted and incident rays in the complex field.

Each step is described in detail in the following subsections.

5.2.1 Read Geometry

In order to gain information about the scattering or shielding object, a grid generation of the geometry of the object is first stored in a readable file format. The size, configuration, and location of the geometry is essential to calculating the edge-diffracted rays. The geometry information can currently only be read from an Unstructured Cell Data (UCD) file format. UCD files consist of a data structure made up of cells and nodes. The cells can be points, lines, quadrilaterals, triangles, tetrahedrons, pyramids, prisms, or hexahedrons. Only the surface domains of the geometry are retained when the file is read. The type of cells compatible with the ray tracing solver include triangles and quadrilaterals only. Each cell has a corresponding number of nodes, that are described based on their three-dimensional location in Cartesian coordinates. An example UCD file format is shown in Figure 5.6. After the header lines in Figure 5.6(a), the number of nodes (214) and number of cells (238) are listed on line 4, respectively. The description of each nodes is then listed, starting with the node identification number then the x, y, and z location from left to right. The beginning of the cell listing is shown in Figure 5.6(b). On each cell line, the cell identification number, material identification number (not used), cell type ("quad" or "tri"), and cell vertices are listed from left to right.

The order in which the nodes are listed as vertices for each cell is important in subsequent steps of the solver and can vary depending on how the geometry is defined. The order of the listed vertices is dependent on the direction of the surface normal vector. The surface normal vector is the cross product of consecutive edges of a cell. For the order of nodes for each cell to be consistent, all surface domains of the three-dimensional geometry must be oriented with the surface normal directed outward from the geometry center.

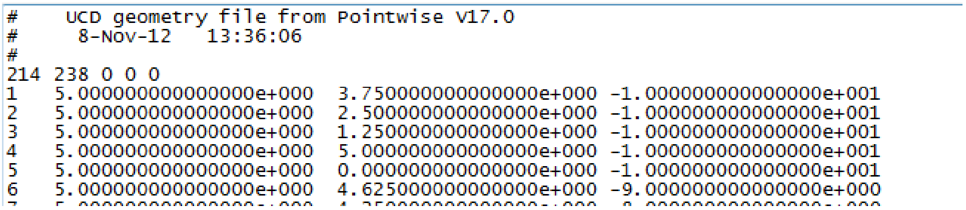

```
#    UCD geometry file from Pointwise V17.0
#     8-Nov-12   13:36:06
#
214 238 0 0 0
1    5.000000000000000e+000  3.750000000000000e+000 -1.000000000000000e+001
2    5.000000000000000e+000  2.500000000000000e+000 -1.000000000000000e+001
3    5.000000000000000e+000  1.250000000000000e+000 -1.000000000000000e+001
4    5.000000000000000e+000  5.000000000000000e+000 -1.000000000000000e+001
5    5.000000000000000e+000  0.000000000000000e+000 -1.000000000000000e+001
6    5.000000000000000e+000  4.625000000000000e+000 -9.000000000000000e+000
```

(a) Node Description

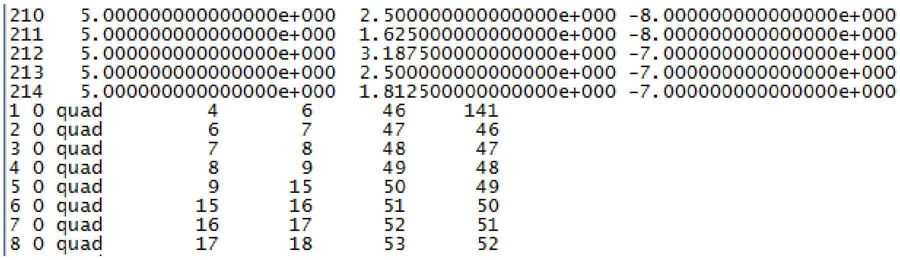

```
210    5.000000000000000e+000  2.500000000000000e+000 -8.000000000000000e+000
211    5.000000000000000e+000  1.625000000000000e+000 -8.000000000000000e+000
212    5.000000000000000e+000  3.187500000000000e+000 -7.000000000000000e+000
213    5.000000000000000e+000  2.500000000000000e+000 -7.000000000000000e+000
214    5.000000000000000e+000  1.812500000000000e+000 -7.000000000000000e+000
1 0 quad          4        6        46      141
2 0 quad          6        7        47       46
3 0 quad          7        8        48       47
4 0 quad          8        9        49       48
5 0 quad          9       15        50       49
6 0 quad         15       16        51       50
7 0 quad         16       17        52       51
8 0 quad         17       18        53       52
```

(b) Cell Description

Figure 5.6: Example UCD geometry file format.

5.2.2 Find Projection

After the scattering geometry is read by the computer program into memory, the three-dimensional projection of the scattering object based on the perspective of source to observer is found. This is an important step required for finding the diffraction line and shadow region. To find the projection, a rotation matrix is created to temporarily rotate the geometry coordinates to a new reference frame based on the vector direction from source to observer. The rotation matrix is formed as follows: The $\boldsymbol{z}'$ axis is formed based on the vector between the observer and the source location. $\boldsymbol{O} = [O_1, O_2, O_3]$ is the observer location and $\boldsymbol{S} = [S_1, S_2, S_3]$ is the source location,

$$\boldsymbol{z}' = \frac{\boldsymbol{S} - \boldsymbol{O}}{\|\boldsymbol{S} - \boldsymbol{O}\|}. \tag{5.21}$$

The x' and y' axes can be formed from an infinite number of solutions. Since the projection is only temporary to find the perspective three-dimensional edge in the original reference frame, the x' and y' axes are arbitrary as long as they are orthonormal and follow the right-hand rule convention. Following the rules of orthogonality,

$$\boldsymbol{z}' \bullet \boldsymbol{x}' = z'_1 \cdot x'_1 + z'_2 \cdot x'_2 + z'_3 \cdot x'_3 = 0. \tag{5.22}$$

Given $\boldsymbol{z}'$ from the source and observer location, a simple solution is,

$$\begin{aligned} \boldsymbol{x}' &= [z'_2, -z'_1, 0] \\ \boldsymbol{y}' &= \boldsymbol{z}' \times \boldsymbol{x}'. \end{aligned} \tag{5.23}$$

An example of the temporary reference frames is illustrated in Figure 5.7. Using the new axes, a rotation matrix is formed and multiplied by the node locations to determine the projected coordinates in the $\boldsymbol{x}' - \boldsymbol{y}'$ plane.

$$\begin{bmatrix} x_{proj} \\ y_{proj} \end{bmatrix} = \begin{bmatrix} x'_1 & x'_2 & x'_3 \\ y'_1 & y'_2 & y'_3 \end{bmatrix} \cdot \begin{bmatrix} x \\ y \\ z \end{bmatrix} \tag{5.24}$$

This method of mapping the three-dimensional points to a two-dimensional plane is used to find the total edge of the object and the shadow region.

5.2.3 Find Diffraction Outline

The edge, or diffraction outline, of the geometry is now determined based on the source and observer location. The diffraction outline of the geometry is found by determining

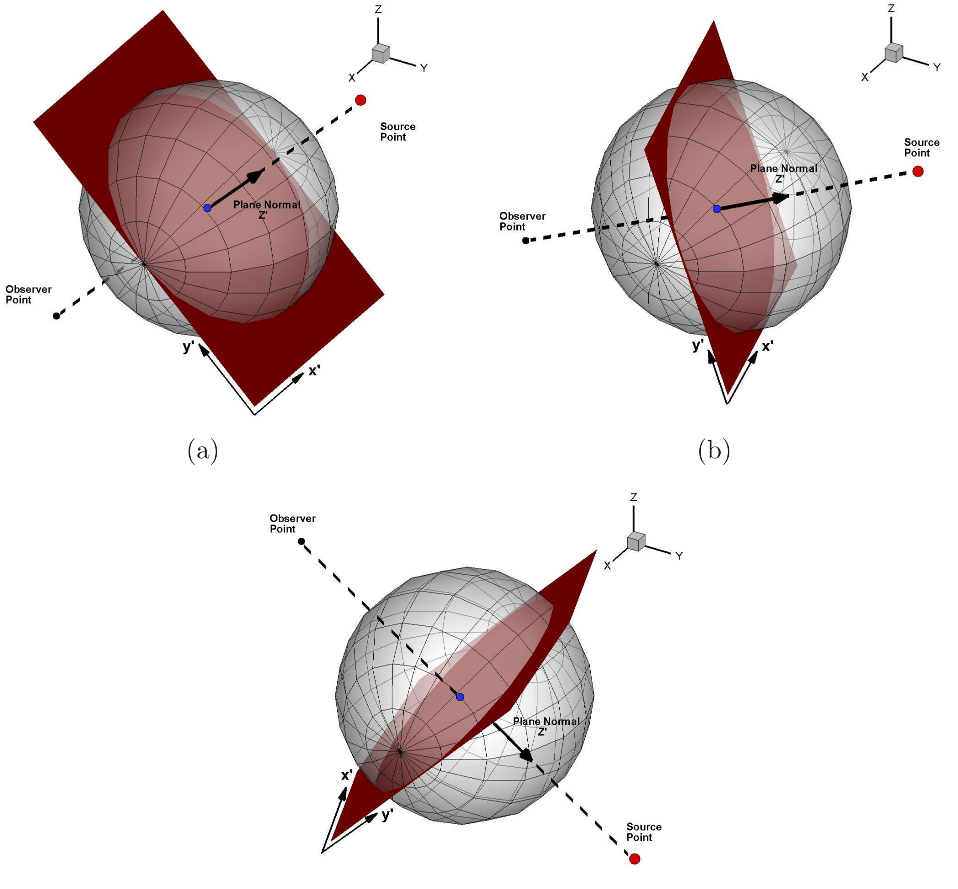

(a)

(b)

(c)

Figure 5.7: Example of reference frame based on source-observer projection.

the unique edges from the individual cells in the projected two-dimensional plane and then extracting the corresponding three-dimensional edge. Unique edges are on the boundary of the projected domain and are only specified once to describe a cell. For instance, if two cells share an edge, that edge is not unique and is therefore not an edge of the total geometry. In Figure 5.8(a), the unique edges are displayed in the projection and the corresponding three-dimensional edge is shown in Figure 5.8(b).

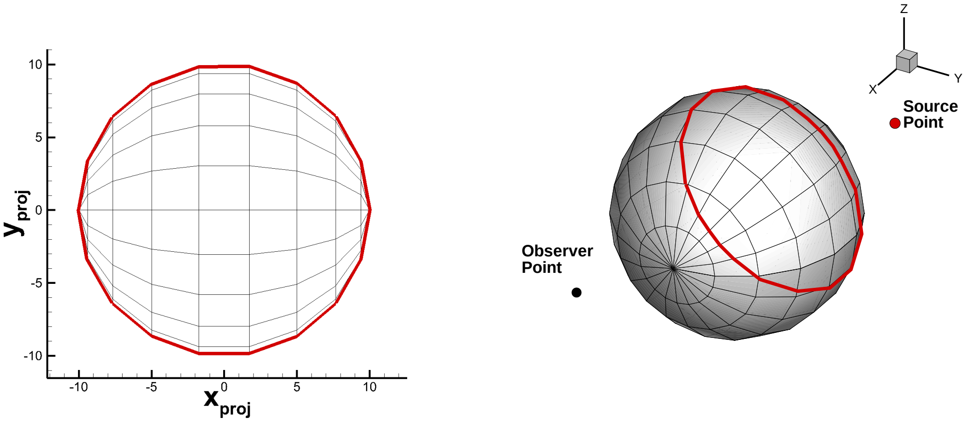

(a) Two-dimensional (b) Three-dimensional

Figure 5.8: The (a) unique edges from the projected plane and (b) the corresponding diffraction outline on the three-dimensional geometry.

5.2.4 Shadow Test

To test if the observer is shielded, or in the shadow region relative to the source location, an approach by Glassner[72] is adopted. The approach substitutes an equation of the ray into an equation of the object and determines if there is a real solution. If a real solution exists then there is an intersection and the observer is in the shadow zone. A simple test for an arbitrary object is to use the edge determined in the projected plane, as described in Section 5.2.3, which is represented as a two-dimensional polygon. Using the equation for the three-dimensional projected plane, the point of intersection can be determined. It can then be determined if the intersection point is within the boundaries of the edge on the two-dimensional plane. Figures 5.9 and 5.10 illustrate the process for a ray intersecting a spherical object.

A reference frame, $\hat{u}-\hat{v}$, is established with the origin at the point of intersection on the two-dimensional plane. Each edge segment is then tested to see if it crosses the positive $\hat{u}$-axis. If there is only one edge segment recorded crossing the positive $\hat{u}$ axis, the point is within

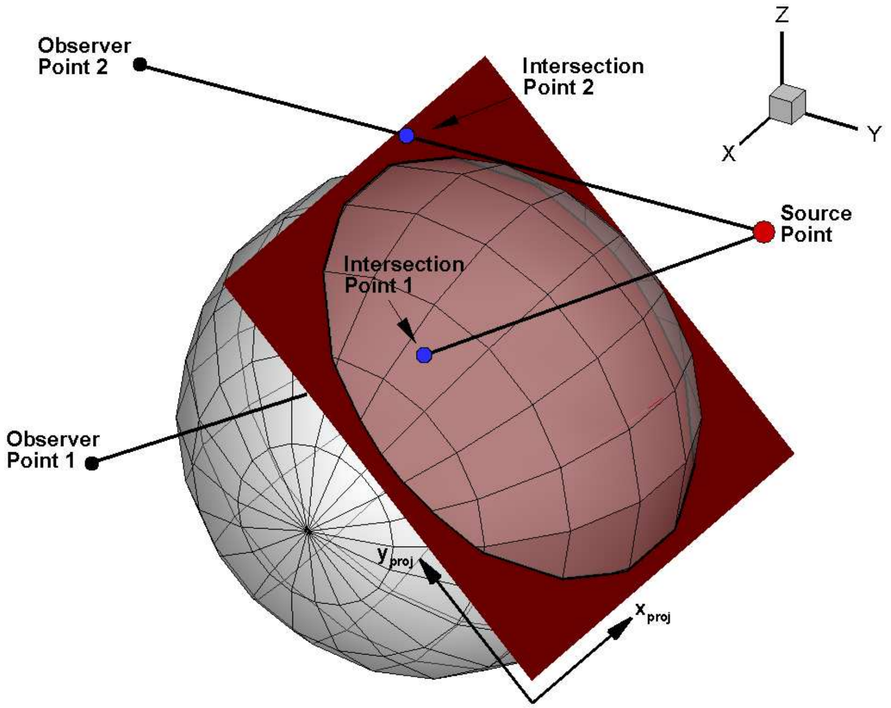

Figure 5.9: Example Ray-Object Intersection: three-dimensional representation

the two-dimensional boundary. If there are zero or two edge segments recorded crossing the positive $\hat{u}$-axis, the point is outside the two-dimensional boundary. For instance, in Figure 5.10, the first intersection point is shown to have one edge segment cross the positive $\hat{u}$-axis, where the second intersection point has zero edge segments crossing the positive $\hat{u}$-axis.

5.2.5 Find Diffracted Rays

The ray paths are now found based on the source, observer, and the edge of the geometry. According to the geometrical theory of diffraction described in the Section 5.1.1, incident rays diffract at an edge in the shape of a cone with the vertex concurrent with the point

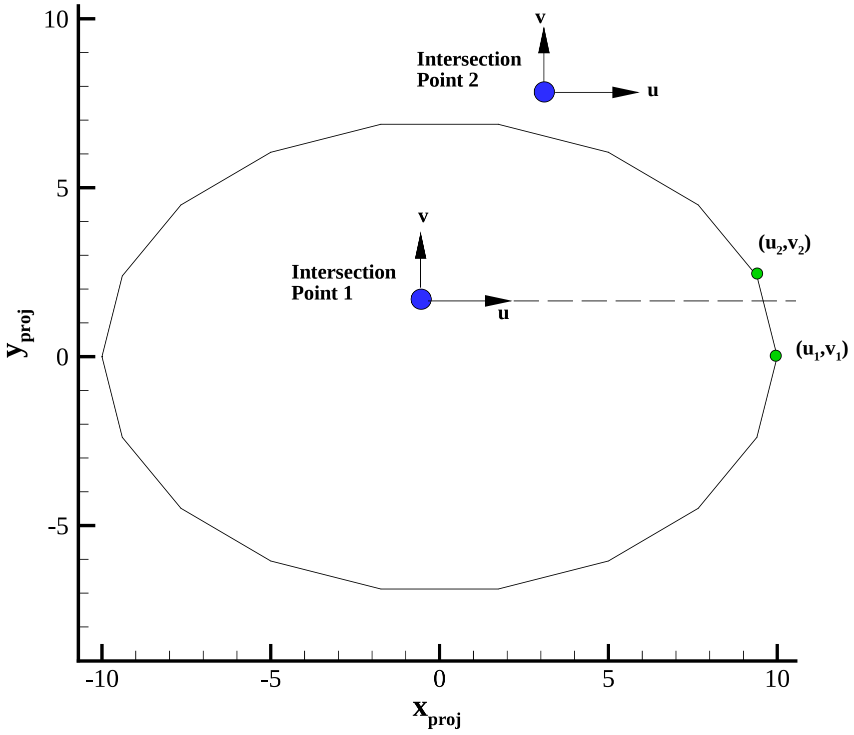

Figure 5.10: Example Ray-Object Intersection: three-dimensional representation

of diffraction and the axis aligned with the edge. The angle of the diffraction cone is equal to the oblique angle between the incident ray and the edge. These angles are displayed in Figure 5.3. For every combination of source, observer, and geometric location there may be multiple or zero diffracted rays. The generalized equation for a cone about an arbitrary axis is,

$$(\boldsymbol{O}-\boldsymbol{V})^T\boldsymbol{N}=(\boldsymbol{O}-\boldsymbol{V})^T(\boldsymbol{O}-\boldsymbol{V})\,cos(\theta), \tag{5.25}$$

where $\boldsymbol{O}$ is the observer location on the surface of the cone, $\boldsymbol{V}$ is the point of diffraction and vertex of the cone, $\boldsymbol{N}$ is the axis of the cone and unit vector of the edge, and θ is the angle of the cone. All observer points $\boldsymbol{O}$ that satisfy Eqn. 5.25 are on the surface of the cone, and have a diffracted ray edge point $\boldsymbol{V}$. The angle θ is,

$$\theta = cos^{-1}\left(\frac{[\boldsymbol{V} - \boldsymbol{S}] \bullet \boldsymbol{N}}{\|\boldsymbol{V} - \boldsymbol{S}\|}\right). \tag{5.26}$$

Combining Eqns. 5.25 and 5.26 yields an equation for the vertex location $\boldsymbol{V}$ that consists of three unknown spatial variables (V_1, V_2, V_3),

$$\begin{gathered} \sqrt{(V_1 - S_1)^2 + (V_2 - S2)^2}\,[N_1(O_1 - V_1) + N_2(O_2 - V_2) + N_3(O_3 - V_3)] = \\ \big[(V_1 - S_1)^2 + (V_2 - S_2)^2 + (V_3 - S_3\big]\,[N_1(V_1 - S_1) + N_2(V_2 - S2)]. \end{gathered} \tag{5.27}$$

Eqn. 5.27 is parameterized by t on a straight edge segment. The parameterized equations are,

$$\begin{aligned} V_1 &= E_1^0 + (E_1^F - E_1^0)t \\ V_2 &= E_2^0 + (E_2^F - E_2^0)t \\ V_3 &= E_3^0 + (E_3^F - E_3^0)t, \end{aligned} \tag{5.28}$$

where $\boldsymbol{E}^0$ and $\boldsymbol{E}^F$ are the first and second end point of the edge segment respectively, and t is the proportionate distance along the edge segment. Figure 5.11 shows these quantities and the cone parameters. Using the parameters in Eqns. 5.28 and 5.27, t is solved in the region $0 \leq t \leq 1$ using the secant method. If a real solution for t exists for $0 \leq t \leq 1$, the diffraction point, source location, and observer location are used to calculate all angle parameters required for the diffraction coefficient in Eqn. 5.17. The complex value of the acoustic pressure field from the diffracted ray can then be calculated using Eqn. 5.15. This process is repeated for each segment on the edge of the geometry.

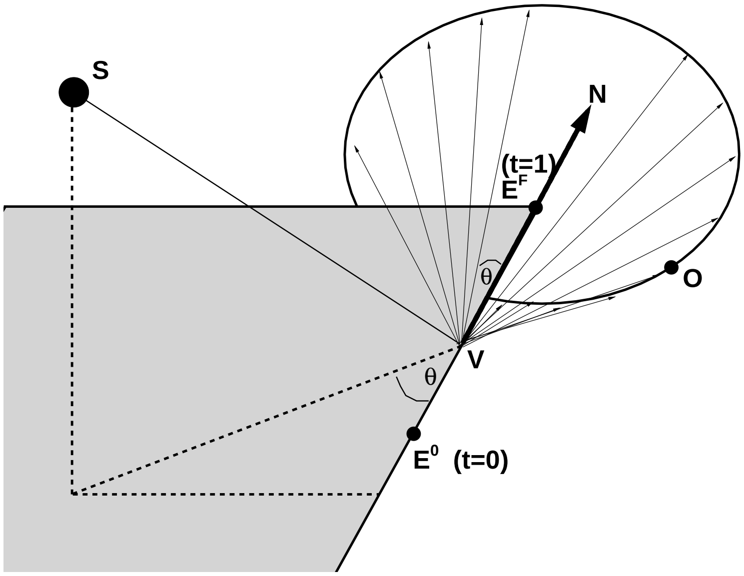

Figure 5.11: Parameterized quantities of diffracted cone on an edge segment

5.2.6 Summation of Rays

The final step in the ray tracing implementation consists of summing the complex values of all existing incident and diffracted rays. The complex expressions are added so the phase relationship of the individual rays can be preserved. Preserving the phase relationship between the rays allows for the diffraction patterns to form due to the constructive interference of the acoustic waves. For an observer location $\boldsymbol{O}$, the total complex amplitude of acoustic pressure from a constant-frequency disturbance at source $\boldsymbol{S}$ is calculated as,

$$\hat{p}(\boldsymbol{O}) = \hat{p}_I(\boldsymbol{O}) + \sum \hat{p}_D(\boldsymbol{O}), \tag{5.29}$$

where $\hat{p}_I(\boldsymbol{O})$ is the complex pressure amplitude of the incident ray and $\hat{p}_D(\boldsymbol{O})$ is the complex pressure amplitude of a single diffracted ray. If the observer is in the shadow region, there is no contribution from an incident ray, and the total diffracted field is just the sum of all diffracted rays.

5.2.7 Discontinuity Correction

A discontinuity exists in the diffraction coefficient for specific observer angles that has a large effect on the calculation. The last terms of the diffraction coefficient in Eqn. 5.17,

$$\ldots\left[\frac{1}{\cos\left(\nu\pi\right)-\cos\left(\nu\left(\phi_s-\phi_o\right)\right)}+\frac{1}{\cos\left(\nu\pi\right)-\cos\left(\nu\left(\phi_s+\phi_o+\pi\right)\right)}\right], \tag{5.30}$$

become discontinuous when $(\phi_s - \phi_o) = \pm\pi$ or $(\phi_s + \phi_o + \pi) = \pm\pi$, where ϕ_s and ϕ_o are the polar angles of the incident ray and the diffracted ray shown in Figure 5.4, respectively. Physically, the discontinuity arises when a diffracted ray is produced near the edge of the shadow region. For example, if $\phi_s = 3\pi/2$, the source is directly above the diffraction point. Thus, the denominator of the first term in Eqn. 5.30, decreases as ϕ_o approaches $\pi/2$ which is directly below the diffraction point. In this case, values of ϕ_o less than $\pi/2$ are in the shadow region and values greater than $\pi/2$ are not. To correct for the discontinuity, terms in Eqn. 5.30 are multiplied by a damping function to change the limit from $\pm\infty$ to 0^+ and 0^- respectively as the denominator approaches zero. The damping function does not alter the terms outside the region of the singularity, which allows for the behavior of the function away from the discontinuity to be unaffected. The proposed functions for the first and second term of Eqn. 5.30 are,

$$f_1 = 1 - e^{-\delta[\cos(\nu\pi) - \cos(\nu(\phi_o - \phi_s))]^2} \tag{5.31a}$$

$$f_2 = 1 - e^{-\delta[\cos(\nu\pi) - \cos(\nu(\phi_o + \phi_s + \pi))]^2}, \tag{5.31b}$$

where δ is a damping coefficient. When the terms in the exponent approach zero, the damping function approaches zero. For values not approaching zero in the exponent, the damping function is approximately equal to 1. Figure 5.12 shows the effect of multiplying the damping function f_1 by the first term in Eqn. 5.30. Values in the figure correspond to, $\phi_s = 3\pi/2$, $\nu = 2\pi/3$, and $0 \leq \phi_o \leq \pi$. As shown, the uncorrected function is discontinuous at $\phi_o = \pi/2$, and the corrected function is continuous and finite. However, there is no deviation between the two functions far from $\phi_o = \pi/2$. The narrow region affected by the damping function is dependent on the damping coefficient. Decreasing the value of δ increases the range of values affected by the damping function. A value of $\delta = 30$ yields results that are aligned with experimental observation. The coefficient is held constant for all other validation comparisons.

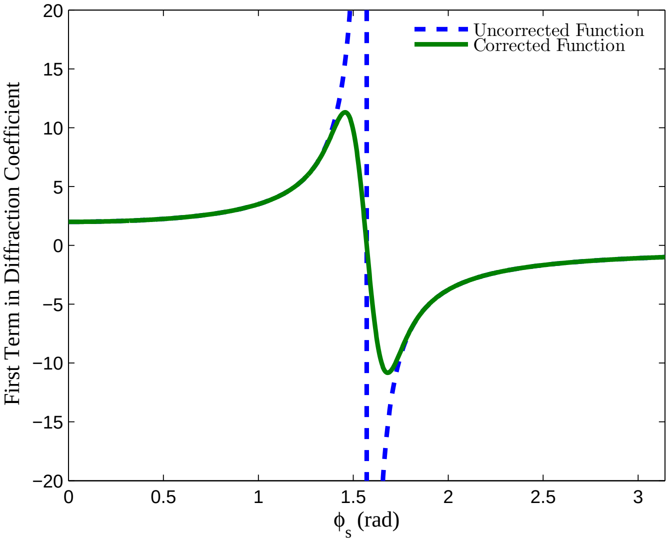

Figure 5.12: Example of the correction used to treat the discontinuity in the diffraction coefficient.

5.3 Point Source Validation

This section describes the comparisons of predicted and measured shielding of a point source by rectangular plates. Experimental data of Ahtye and McCulley[73] is used to validate the ray tracing method. The measurement data is digitized from multiple figures because it is not available in electronic form. Slight inaccuracies in amplitude and directivity of the experiment are due to digitization error. To further test the validity of the method, predictions are also compared with NASA's Fast Scattering Code (FSC) by Tinetti and Dunn[47].

5.3.1 Experimental Overview

Rectangular plates and circular cylinders were used to simulate airframe shielding effects. Only the experimental data from the rectangular plate cases are used to validate the edge-diffracted ray calculations. A schematic of the experimental test configuration is shown in Figure 5.13. A point source is simulated above the plate by an inverse tapered horn connected to a loud speaker. A microphone traverse is located below the plate along the x-axis. The location along the traverse is designated by the angle θ from the sound source, with $\theta = 0°$ directly below the sound source and θ measured in the positive x direction. Ahtye and McCulley[73] give a full description of the sound source and microphone, including directivity and amplitude calibration details. The aluminum rectangular plates have square and sharp tapered edges. The angles of the square and sharp edge are $\beta = 270°$ and $\beta = 340°$ measured clockwise from the to surface, respectively. The dimensions of the square and sharp edge are shown in Figure 5.14. The length and width of both plates is $L = 2.0\ m$ and $W = 0.5\ m$, respectively.

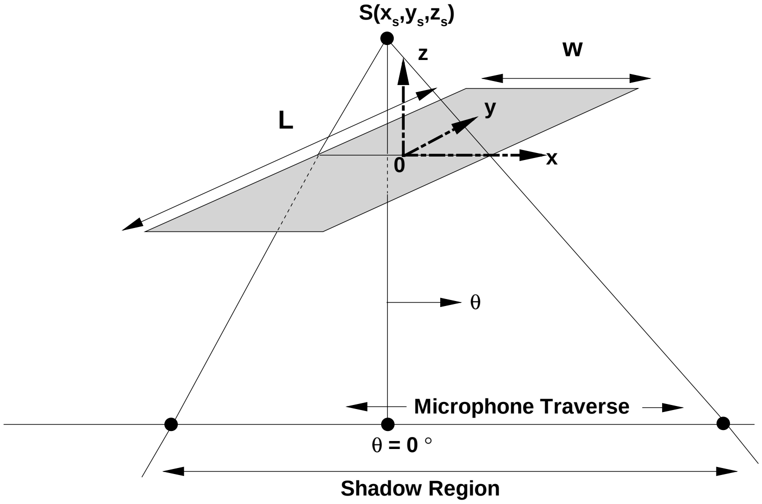

Figure 5.13: Coordinate system of point source validation experiment

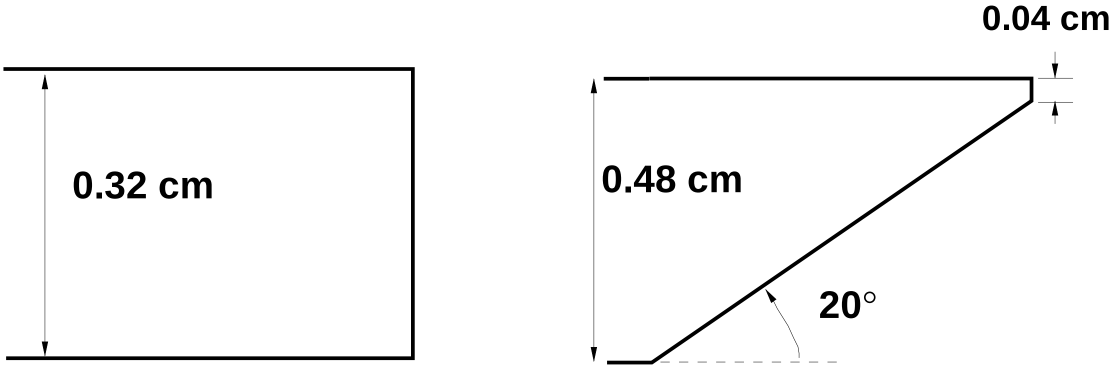

(a) Square Edge (b) Sharp Edge

Figure 5.14: Rectangular plate edge dimensions.

Ahtye and McCulley[73] explain in detail the limitations and difficulties of their experiment. Notable difficulties that can lead to potential reasons for discrepancies include:

- Simulating pure omni-directional sound source.
- Reflections from acoustic wedges lining the anechoic chamber walls.
- Possible error in simulated point source location.
- Impedance loading of the source by reflection from the plate.

The sensitivity of the point source location relative to the ray tracing method and additional difficulties will be discussed.

5.3.2 Results

A surface grid is generated for both plates that correspond to the dimensions of the experiment. However, the geometry of the sharp edge plate does not include the finite thickness of 0.04 *cm* as shown in Figure 5.14. Due to the simple shielding geometry, the number of grid points required is small. To demonstrate the use of multiple cells and nodes, the surface domain includes 80 nodes and 54 cells. Figure 5.15 shows the surface grid, the extracted edge, and the source location. The acoustic source used in the simulation consisted of a stationary monopole of unit strength located at $\boldsymbol{S} = [0.0,\ 0.0,\ 0.5W]$, where the width $W = 0.5\ m$. After finding the edge of the geometry using the approach in Section 5.2.3, the diffracted rays and the direct incident rays are found for each microphone location, as shown in Figure 5.16. The diffracted rays are summed for the total complex acoustic pressure and converted to sound pressure level (SPL). The corresponding free-field calculation of SPL is then subtracted from the diffracted field to determine the predicted shielding in ΔSPL.

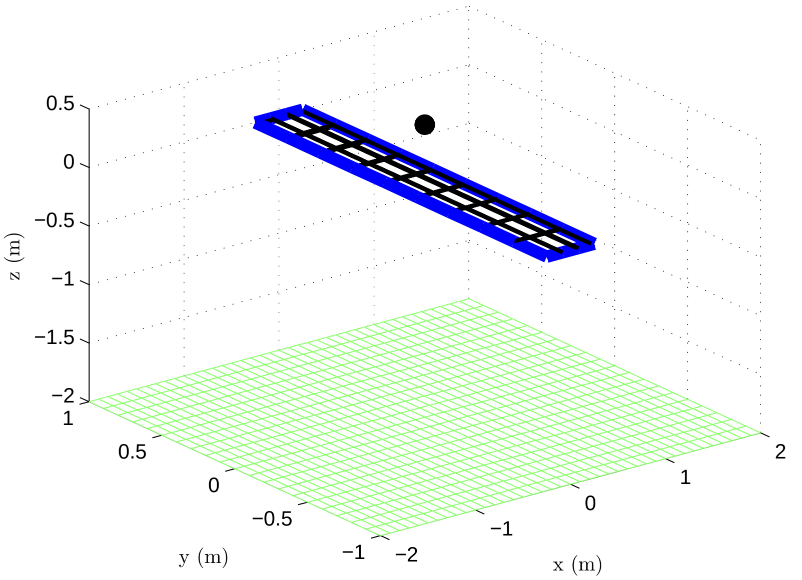

Figure 5.15: Example of acquiring plate edge from three-dimensional geometry.

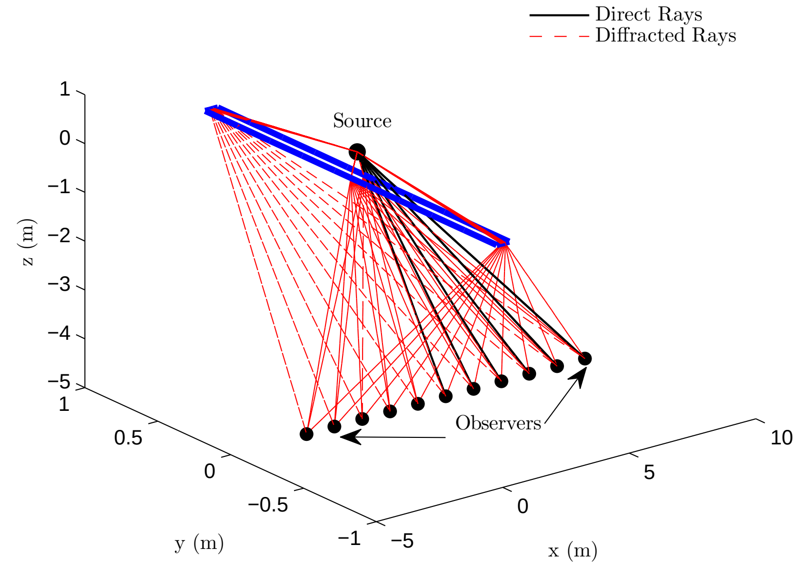

Figure 5.16: Incident and edge-diffracted acoustic rays emanating from point source above plate.

The predicted and measured ΔSPLs are plotted as functions of the traverse angle, θ, at various frequencies. Below the plate, the traverse is located at $z = 10W$, $y = 0$, and ranges from $-2\ m \leq x \leq 9\ m$. The corresponding range of angles is $-20 \leq \theta \leq 60$. The range of available data slightly varies case by case. The predicted ΔSPLs of the ray tracing method and FSC are compared beyond the range of the available experimental data. Due to the symmetric location of the point source, the angles $\theta = \pm 45°$ should correspond to the edge of the geometric shadow region. The value of the acoustic frequency is given in terms of cycles per second (Hz) and a non-dimensional frequency kW, where k is the wave number, and W is the width of the plate. The non-dimensional frequency (Helmholtz number $= kW$) is used to generalize the results so that comparisons can be made with other dimensional applications.

Comparisons of the square edge case, $\beta = 270°$, are shown in Figure 5.17. The source excitation frequencies are 1 kHz, 2 kHz, 4 kHz, 8 kHz, and 12 kHz. The results show that the nature of the sound and is captured by the ray tracing prediction. The maximums and minimums are generally coincident at all frequency ranges presented, with exception of the highest frequency. The captured pattern of the diffracted field resembles the constructive and destructive interferences between the multiple diffracted waves produced by the edges. Also, the predicted diffraction pattern is symmetric, matching the symmetry of the problem geometry. The slight asymmetry of the measured data could be due to the difficulty in placing the source. The ray tracing method consistently under-predicts the measured shielding for all frequencies, where FSC over-predicts the shielding for 1.0 kHz, 2.0 kHz, 4.0 kHz, and matches the experiment at 8.0 kHz. The largest deviation from the experiment at the peaks ranges from $4-7\ dB$, except near $\theta = 45°$. FSC over-predicts the experiment by $4-5\ dB$ and is within $\pm 1\ dB$ at 8.0 kHz. The discontinuous jump shown by the ray tracing prediction at $\theta = 45°$ is due to the addition of direct rays to the diffracted field outside of the shadow region. The sharp transition from the shadow region to the incident region is a result of the discontinuous distribution of rays inherent in the method. Slope discontinuities in the diffracted field were also seen by Agarwal[67]. It is possible that the inclusion of creeping rays and corner-diffracted rays will smooth out the slope discontinuities in the diffracted field.

The comparisons of the sharp edge case, $\beta = 340°$, are shown in Figure 5.18. Measured data for this case is shown at frequencies of 4 kHz, 8 kHz, and 12 kHz. Similar to the square edge case, the maximums and minimums generally coincide with the experiment, with exception to $f = 12\ kHz$. The discontinuity is again apparent at $\theta = 45°$, where the shadow region ends. In contrast to the square edge case, the ray tracing method predictions show improved agreement in terms of the shielding magnitude, especially at small angles. Within the range $-20° < \theta < 20°$, the ray tracing predictions are within $\pm 3\ dB$ of the experiment at the peaks and $\pm 4\ dB$ at the valleys. The ray predictions also agree well with the FSC prediction in this range. The larger deviation of the peaks and valleys ($> 5\ dB$) occur closer to the edge of the shadow region. Some of the deviation in this area can be partially attributed to the discontinuity correction explained in Section 5.2.7. At the lower frequencies, 1 kHz and 2 kHz, the ray tracing predictions are compared to the FSC predictions. At 1 kHz, the ray tracing prediction does not capture the same diffraction pattern as the FSC prediction but is in close agreement of the peak magnitude at $\theta = 0°$. This comparison, in which $kW = 9$, illustrates the low frequency limit of ray tracing. At 2 kHz, the prediction of the diffraction pattern agrees with the FSC prediction, except near the edge of the shadow zone. There is a 4 dB difference at the peaks and a much larger difference ($> 10dB$) at the valleys. The larger difference at the minimums is due to the higher phase sensitivity for destructive wave interference.

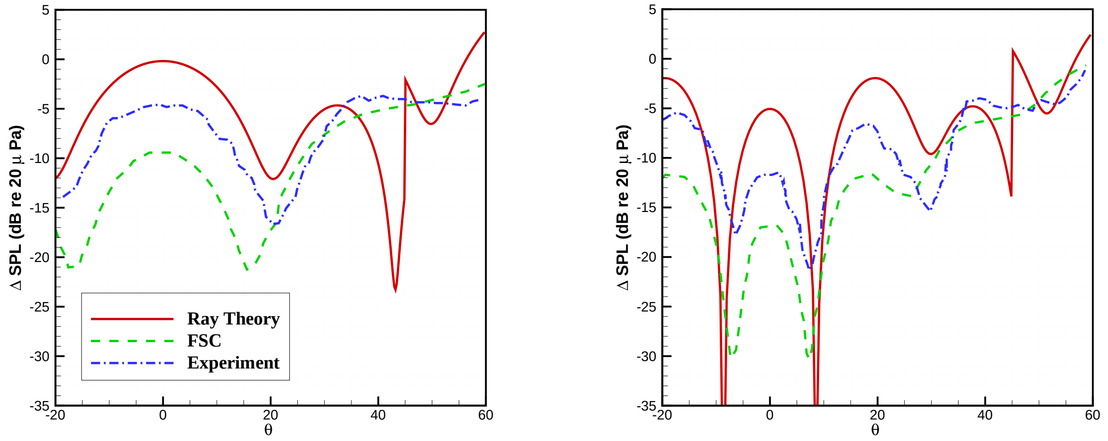

(a) $f = 1000\ Hz, kW = 9$

(b) $f = 2000\ Hz, kW = 18$

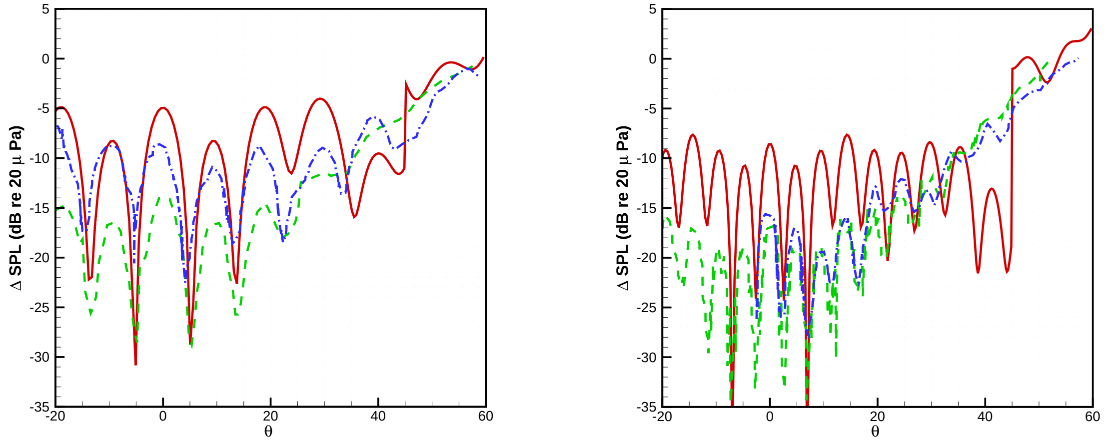

(c) $f = 4000\ Hz, kW = 37$

(d) $f = 8000\ Hz, kW = 73$

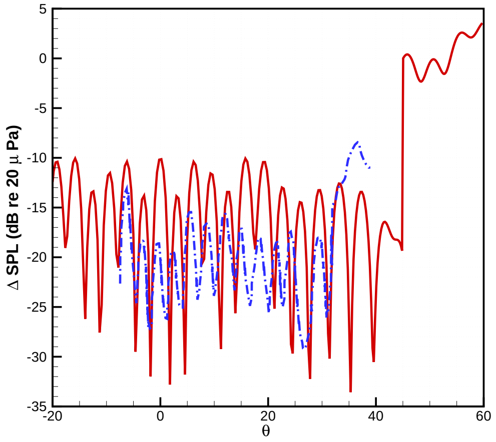

(e) $f = 12000\ Hz, kW = 110$

Figure 5.17: Square edge shielding predictions compared to experiment, S = [0, 0, 0.5W].

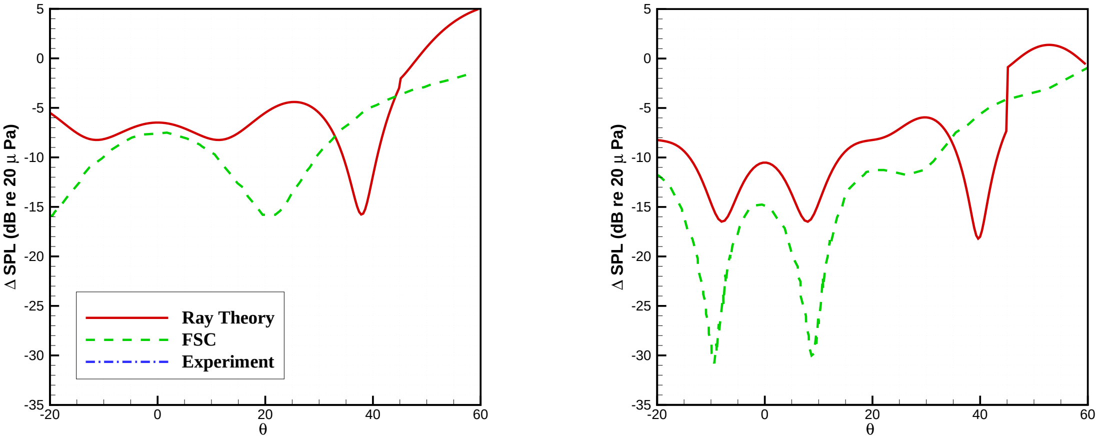

(a) $f = 1000\ Hz, kW = 9$ (b) $f = 2000\ Hz, kW = 18$

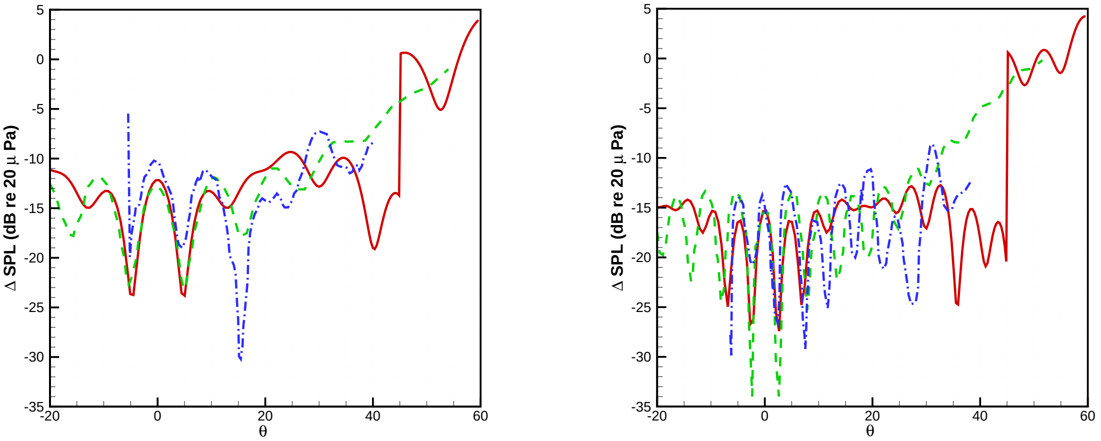

(c) $f = 4000\ Hz, kW = 37$ (d) $f = 8000\ Hz, kW = 73$

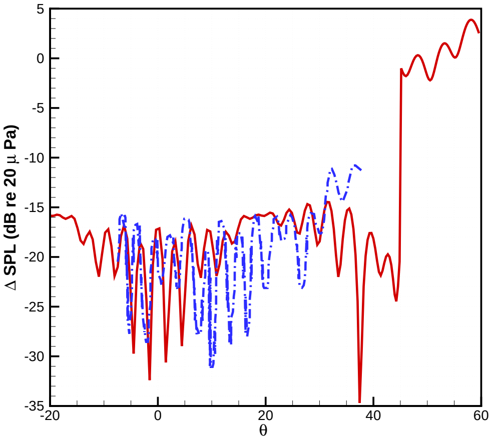

(e) $f = 12000\ Hz, kW = 110$

Figure 5.18: Sharp edge shielding predictions compared to experiment, S = [0, 0, 0.5W].

Effect of Edge Angle

To quantify the effect of the edge angle on the diffracted field, ray tracing predictions in the shadow region are compared with the same plate at various edge angles. The experiment and FSC are also compared at the two available angles, $\beta = 270°$ and $\beta = 340°$. The comparisons are shown in Figure 5.19 at a frequency of $f = 4000\ Hz$.

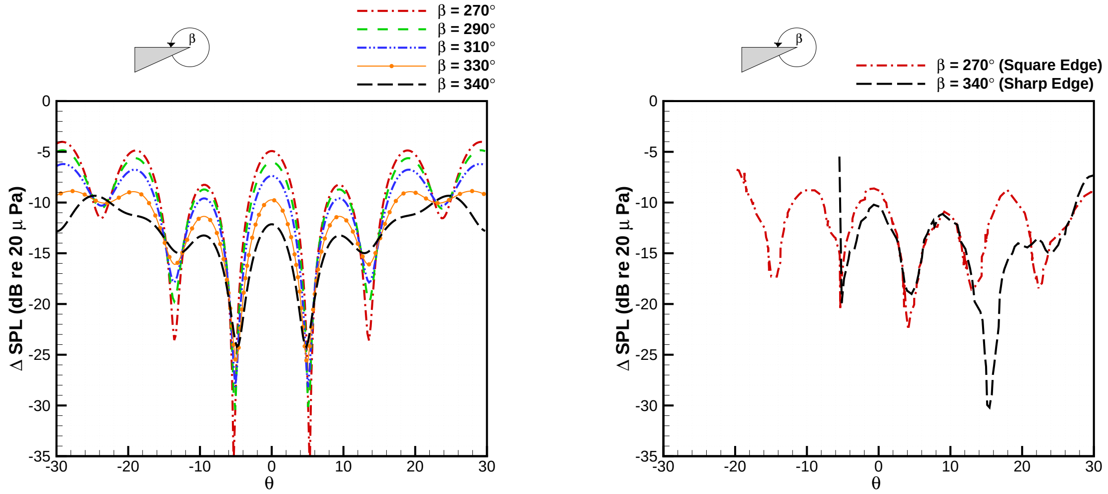

(a) Ray Tracing Method

(b) Experiment

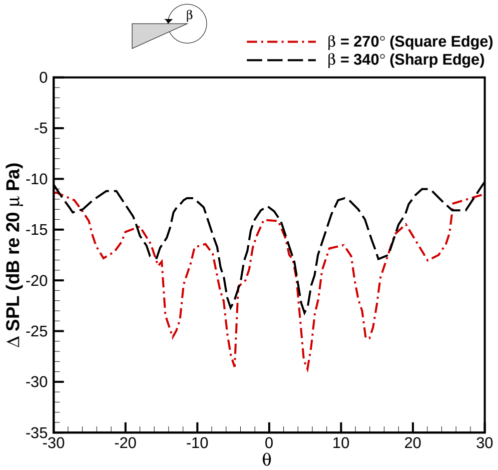

(c) Fast Scattering Code

Figure 5.19: Edge angle effect on noise attenuation in shadow region, $f = 4000\ Hz$

The ray tracing method shows a trend of decreasing magnitude as the edge angle increases. The magnitude of the constructive interference pattern decreases, and the amount of destruction decreases. The decrease and increase of the maximums and minimums illustrate a flattening effect as the edge angle increases. There is a maximum 7 dB decrease in magnitude as the edge angle increases from $\beta = 270°$ to $\beta = 340°$ at $\theta = 0°$, resulting in an average $0.1 dB/°$ decrease. The relative magnitude difference from crest to trough decreases as the angle increases from $\theta = 0°$, increasing the flattening trend. The experiment shows a small difference in attenuation from the two angles. This could be due to the finite thickness of the sharp edge, or creeping rays that are not accounted for in the ray tracing method. The FSC predictions do not follow the same trend as the ray tracing method. In contrast, there is an overall increase in magnitude for the sharp edge ($\beta = 270°$). The relative difference in magnitude from peak to trough does decrease, which slightly mimics the flattening trend of the diffraction pattern shown by the ray tracing method.

The ray tracing method shows a stronger sensitivity to the angle of the sharp edge than the experiment or FSC. The seclusion of other possible diffraction effects such as creeping rays in the ray tracing method can explain why the angle has a larger influence on the predicted diffraction field. The difference between the relative sensitivity to the edge angle can help explain some of the magnitude discrepancies between the ray tracing method and experiment. For instance, there is a difference in magnitude of 5 dB at the peaks when comparing the square edge case. This deviation in magnitude is within the $5 - 7$ dB range of magnitude difference for an edge angle of $\beta = 270°$ and $\beta = 340°$ seen by the ray tracing method.

Point Source Sensitivity

In the experiment of Ahtye and McCulley[73], the opening at the small end of the inverse tapered horn has a diameter of $D_T = 0.63\ cm$. This finite distance may lead to possible uncertainty in the location of the correct point source. At high frequencies the uncertainty produced by this finite distance may explain the deviation in the diffraction pattern of peaks and valleys shown in Figures 5.17(e) and 5.18(e). At the highest frequencies presented, 8 kHz and 12 kHz, the acoustic wave length is within one order of magnitude of the horn diameter. Thus, the source is not a point source, and is likely directional. Table 5.1, describes the range of frequencies and their acoustic wave length ratios relative to the diameter of the tapered horn.

$f\ (Hz)$	kW	k (m^{-1})	$\lambda\ (m)$	D_T/λ
1000	9	18	0.35	0.02
2000	18	36	0.17	0.04
4000	37	74	0.09	0.07
8000	73	146	0.04	0.16
12000	110	220	0.03	0.22

Table 5.1: Table of frequency ranges and wavelength ratios.

To assess the sensitivity of the simulated point source location at high frequencies, predictions are compared with the source location varied within the distance of the horn diameter. Along the x-axis, the simulated source is varied from $-0.5D_T$ to $0.5D_T$. Figure 5.20 describes the diffraction pattern in the shadow zone for the various source locations at 8 kHz and 12 kHz. Shifting the source half a horn tip diameter in either direction significantly changes the diffraction patterns constructive interference. At 8 kHz, the location of the maximums and minimums are out of phase for each source location. There is a consistent $2 - 3\ dB$ difference in magnitude due to the phase shift. The diffraction pattern from $-0.5D_T$ to $0.5D_T$ is symmetric about $\theta = 0°$ because of the symmetric geometry. At 12 kHz, the diameter of the horn tip is approximately a quarter of the wavelength, and the diffraction pattern shifts out of phase if the source shifts $0.5D_T$ in either direction. A full D_T shift in the source location results in a pattern that is out of phase with large deviations ($> 6dB$) in magnitude.

Based on ray tracing predictions, frequencies with wavelengths comparable to the radius used to simulate the point source can result in an out of phase diffraction pattern. The out of phase diffraction pattern can result in a large variation in magnitude. The sensitivity of the diffraction pattern to the simulated source location can explain some of the deviation observed when comparing with the measured data at high frequencies.

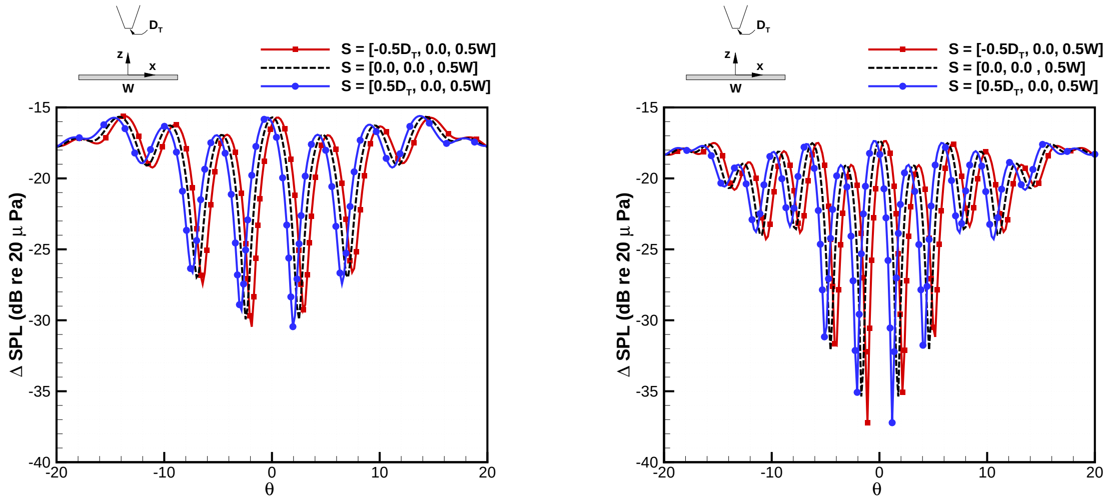

(a) $f = 8000\ Hz, kW = 73$

(b) $f = 12000\ Hz, kW = 110$

Figure 5.20: Source location sensitivity at high frequencies.

5.3.3 Summary

This section described the comparisons of predicted and measured shielding of a point source by a rectangular plate. Experimental data of Ahtye and McCulley[73] was used to validate the ray tracing method. Despite multiple discrepancies and possible sources of error, comparisons with experimental data over a wide range of frequencies demonstrate that the ray tracing method is capable of predicting the correct characteristics and trends of the diffraction pattern in the shadow zone. The method is therefore suitable for further airframe shielding analysis. Notable observations of the results include the following:

1. The predicted interference pattern is generally coincident with the experiment over most frequency ranges.
2. The ray tracing method consistently under-predicts the shielding of the square edge plate and demonstrates improved agreement for the sharp edge plate.
3. The FSC predictions are superior for the square edge case at higher frequencies, although the ray tracing predictions are within the same approximate dB error range at lower frequencies. Though, both the present theory and FSC are not formulated for square edge geometries.
4. The ray tracing method shows the largest discrepancies at the lowest frequency ($kW = 9$) and in regions near the edge of the shadow zone. The Helmholtz number of $kW = 9$ is identified as a lower frequency limit.
5. Apart from experimental error, discrepancies can be attributed to the uncertainty in the simulated source location and the effective edge angle. The shielding predictions and measurements at various edge angles show that the ray tracing method has a stronger sensitivity to the edge angle than the experiment or FSC predictions.
6. Predictions of the diffracted field from a source varied within the finite distance of the horn diameter show the diffraction pattern is sensitive within that distance at high frequencies.

Chapter 6

Jet-Airframe Noise Predictions

In this chapter, an assessment of an acoustic analogy for the mixing noise component of jet noise in the presence of a scattering surface is presented. The approach by Miller[16] allows for the acoustic source and propagation of the jet noise to be addressed separately. A model of the equivalent acoustic sources from the jet are informed by steady RANS solutions, where an augmented solution for the propagation is simplified to finding a tailored Green's function of the Helmholtz equation. The methodology of this approach is described in the following section. The limits of the approach are extended to predicting noise in the diffracted field by using the ray tracing method to determine the tailored Green's function. The acoustic analogy approach in conjunction with the developed ray tracing solver is used to demonstrate aeroacoustic predictions of jets integrated with the airframe. Experimental data from the Jet-Surface Interaction Test of Brown *et al.*[7](JSIT) are used to validate the predictions of jets configured near a flat plate. A general description of the JSIT experiment is given, and multiple comparisons are shown that include various jet conditions and plate configurations. Finally, the methodology is used to predict the shielding of jet noise from the next generation aircraft Hybrid Wing Body (HWB) configuration.

6.1 Methodology

6.1.1 Acoustic Analogy

An acoustic analogy is the rearrangement of the governing equations of motion into an operator that supports wave propagation and is equated to equivalent sources. The following methodology by Miller[16] is based on the acoustic analogy of Morris and Farassat[15]. Following their approach, the Euler equations are rearranged into the inhomogeneous linearized Euler equations (LEE) in which the acoustic propagation and equivalent sources are separated. A convolution integral of the vector Green's function of the LEE and the equivalent sources define the fluctuating pressure in the far-field. The spectral density is the Fourier transform of the autocorrelation of the fluctuating pressure. Using an approximation by Tam and Auriault[31], two closely placed source points in the jet are related, and the spectral density can be written in terms of the two-point cross-correlation of the equivalent sources and the vector green's function of the LEE.

Using the equivalent source models of Tam and Auriault[31] and Morris and Boluriaan[32], the spectral density can be written in terms of the vector Green's function of the LEE, π_g^n, as,

$$
\begin{aligned}
S(\boldsymbol{x},\omega) = \rho_\infty^2 c_\infty^4 \int_{-\infty}^{\infty}\int_{-\infty}^{\infty}\int_{-\infty}^{\infty} & \frac{2\pi^{3/2} c_\infty^2 l_x l_y l_z \tau_s x^2}{c_\infty^2 x^2 + (u x_1 + v x_2 + w x_3 + c_\infty x)^2 \tau_s^2 \omega^2} \\
\times \left\{ \pi_g^{*0}(\boldsymbol{x},\boldsymbol{y},\omega)\pi_g^{0}(\boldsymbol{x},\boldsymbol{y},\omega) A_s^2 \frac{(u_s/c_\infty)^4}{\tau_s^2} \right. & + \left. \sum_{n=1}^{3}\sum_{m=1}^{3} \pi_g^{*n}(\boldsymbol{x},\boldsymbol{y},\omega)\pi_g^{m}(\boldsymbol{x},\boldsymbol{y},\omega) B_s^2 \frac{(u_s/c_\infty)^2 u_s^4}{l_x^2} \right\} \\
& \times \exp\left[-\frac{\left(l_x^2 x_1^2 + l_y^2 x_2^2 + l_z^2 x_3^2\right)\omega^2}{4 c_\infty^2 x^2} \right] d\boldsymbol{y},
\end{aligned}
\tag{6.1}
$$

where A_s and B_s are constants, $\boldsymbol{x}$ is the observer location, $\boldsymbol{y}$ is the source location, and

ρ_∞ and c_∞ are the ambient density and speed of sound, respectively. The parameters u, v, and w represent the x, y, and z time averaged velocity components, respectively. Lastly, the parameters l_x, l_y, l_z, u_s, and τ_s, are the integral scales of turbulence that are required to describe the equivalent sources. Empirical models or unsteady CFD simulations can be utilized to find these parameters. Following the methodology of Tam and Auriault[31], the integral scales of turbulence are related to a steady RANS solution by,

$$l_x(\boldsymbol{y}) = c_l K(\boldsymbol{y})^{3/2}/\epsilon(\boldsymbol{y}), \tag{6.2}$$

$$\tau_s(\boldsymbol{y}) = c_\tau K(\boldsymbol{y})/\epsilon(\boldsymbol{y}), \tag{6.3}$$

and,

$$u_s(\boldsymbol{y}) = c_u \sqrt{2K(\boldsymbol{y})/3}, \tag{6.4}$$

where K is the turbulent kinetic energy and ϵ is the dissipation rate of turbulent kinetic energy. The coefficients $c_\tau = 0.30$, $c_u = 1.00$, and $c_l = 1.00$ are determined through calibration based on a reference jet operating at the sonic condition, $TTR = 3.20$, using a 0.0508 m convergent nozzle and observer at $R/D = 100$ in the sideline location. The calibrated values differ from those of Tam and Auriault[31] due to the use of a different acoustic analogy and steady RANS solver. The cross-stream integral length scales, l_y and l_z, are set to 3/10 of l_x, which corresponds to experimental observation. These coefficients are held constant regardless of the jet condition, nozzle geometry, or any other parameter variation.

The vector Green's function of the LEE (π_g^n) is related to the Green's function of Lilley's[26] equation by,

$$\pi_g^0(\boldsymbol{x},\boldsymbol{y},\omega) = \omega^2 g_l(\boldsymbol{x},\boldsymbol{y},\omega) - 2i\overline{u}\omega\frac{\partial g_l(\boldsymbol{x},\boldsymbol{y},\omega)}{\partial y_x} - \overline{u}^2\frac{\partial^2 g_l(\boldsymbol{x},\boldsymbol{y},\omega)}{\partial y_x^2} \tag{6.5}$$

$$\pi_g^1(\boldsymbol{x},\boldsymbol{y},\omega) = -\left(i\omega + \overline{u}\frac{\partial}{\partial y_x}\right)\frac{\partial}{\partial y_x} g_l(\boldsymbol{x},\boldsymbol{y},\omega) \tag{6.6}$$

$$\pi_g^2(\boldsymbol{x},\boldsymbol{y},\omega) = -\left\{3\frac{\partial\overline{u}}{\partial y_r}\frac{\partial}{\partial y_x} - \left(i\omega + \overline{u}\frac{\partial}{\partial y_x}\right)\frac{\partial}{\partial y_r}\right\} g_l(\boldsymbol{x},\boldsymbol{y},\omega) \tag{6.7}$$

$$\pi_g^3(\boldsymbol{x},\boldsymbol{y},\omega) = -\left(i\omega + \overline{u}\frac{\partial}{\partial y_x}\right)\frac{1}{y_r}\frac{\partial}{y_\theta} g_l(\boldsymbol{x},\boldsymbol{y},\omega) \tag{6.8}$$

where the subscript of the source vector $\boldsymbol{y}$ denotes the direction the partial derivative is taken and g_l is the Green's function of Lilley's equation.

Using this solution, the problem is simplified to finding the Green's function of Lilley's equation instead of the full vector Green's function of the LEE. An approximate solution of the Green's function of Lilley's equation is formed by examining the asymptotic solutions of Balsa *et al.*[74] and Goldstein.[75,76,77] The Green's function of the convective Helmholtz equation g, is related g_l,

$$g_l(\boldsymbol{x},\boldsymbol{y},\omega) = \begin{cases} \frac{i}{c_\infty^2 c_0^{c\alpha}\omega}\frac{c_\infty}{\overline{c}}\exp\left[\frac{-i\omega}{c_\infty}\left(x\cos\theta + r\sin\theta\cos\left(\phi_0 - \phi\right)\right)\right] g & \text{if } Re[g_o^*] > 0 \\ \frac{i}{c_\infty^2 c_0^{c\alpha}\omega}\frac{c_\infty}{\overline{c}}\exp\left[\frac{-i\omega}{c_\infty}\left(x\cos\theta + r\sin\theta\cos\left(\phi_0 - \phi\right)\right)\right]\exp\left[-c_\beta\omega/c_\infty\right] g & \text{if } Re[g_o^*] \leq 0 \end{cases} \tag{6.9}$$

where θ is the observer angle from the nozzle downstream axis, c is the local speed of sound,

$c_\beta = 1 \times 10^{-4}$, and,

$$g_o^* = \sqrt{\frac{(1 - u/c_\infty \cos\theta)^2}{(\bar{c}^2/c_\infty^2)} - \cos^2\theta}. \tag{6.10}$$

C_0 is Ribner's convection coefficient,

$$C_0 = \sqrt{(1 - u/c_\infty \cos\theta)^2 + c_{0\alpha}^2 (u/c_\infty)^2} \tag{6.11}$$

where $c_{0\alpha} = (4/25)\sqrt{u_j/c_\infty - 1}$. The convective amplification power coefficient is,

$$c_\alpha = 3 - \tanh\left[f D_j/u_j\right]. \tag{6.12}$$

6.1.2 Tailored Green's Function

The propagation portion of the problem is now simplified to finding the Green's function of the convective Helmholtz equation, g in Eqn. 6.9. Numerical solvers can be used to provide the Green's function of the convective Helmholtz equation. Here, the ray tracing solver, described in Section 5.2, is used to provide the tailored Green's function so that the diffracted field can be accounted for in the jet noise prediction.

For isolated jet predictions the free-field Green's function of the Helmholtz equation is used,

$$g = \frac{e^{[ik\boldsymbol{r}]}}{4\pi\boldsymbol{r}}, \tag{6.13}$$

where $\boldsymbol{r} = \boldsymbol{x} - \boldsymbol{y}$ is the distance from the source to observer. When a scattering geometry such as the airframe is integrated with the jet, the tailored Green's function of the Helmholtz equation is found using the ray tracing solver, following the ray theory methodology described in Section 5.1. Similar to Eq. 5.29 in Section 5.2.6, the tailored Green's function is a sum of components from the free and diffracted field,

$$g = g_I + \sum g_D, \tag{6.14}$$

where g_I is the contribution of any existing incident rays, equivalent to the free-field Green's function in Eq. 6.13 and g_D is the contribution of a single diffracted ray. Following Eqn. 5.15, the value of g_D is,

$$g_D = D g_I(\boldsymbol{V}) \left[\frac{\boldsymbol{\rho}}{\boldsymbol{r}(\boldsymbol{r} + \boldsymbol{\rho})} \right]^{1/2} e^{ik\boldsymbol{r}}, \tag{6.15}$$

where, D is the diffraction coefficient, $g_I(\boldsymbol{V})$ is the free-field component at the point of diffraction, and $\boldsymbol{r}$ and $\boldsymbol{\rho}$ are distances associated with the diffracted ray. Detailed explanations of these parameters are given in Section 5.1.1.

An outline of the acoustic analogy approach in conjunction with a tailored Green's function is illustrated in Figure 6.1. The outline begins with the Euler equations and are linearized and separated in terms of wave propagation and acoustic source. The equations are solved and written in the form of the vector Green's function of the LEE in terms of the Green's function of Lilley's equation. The Green's function of Lilley's equation is represented in terms of the Green's function of the Helmholtz equation that is calculated by the ray tracing solver. The steady RANS solution informs the acoustic source terms with flow-field quantities. A full detailed description of the methodology is given by Miller[16].

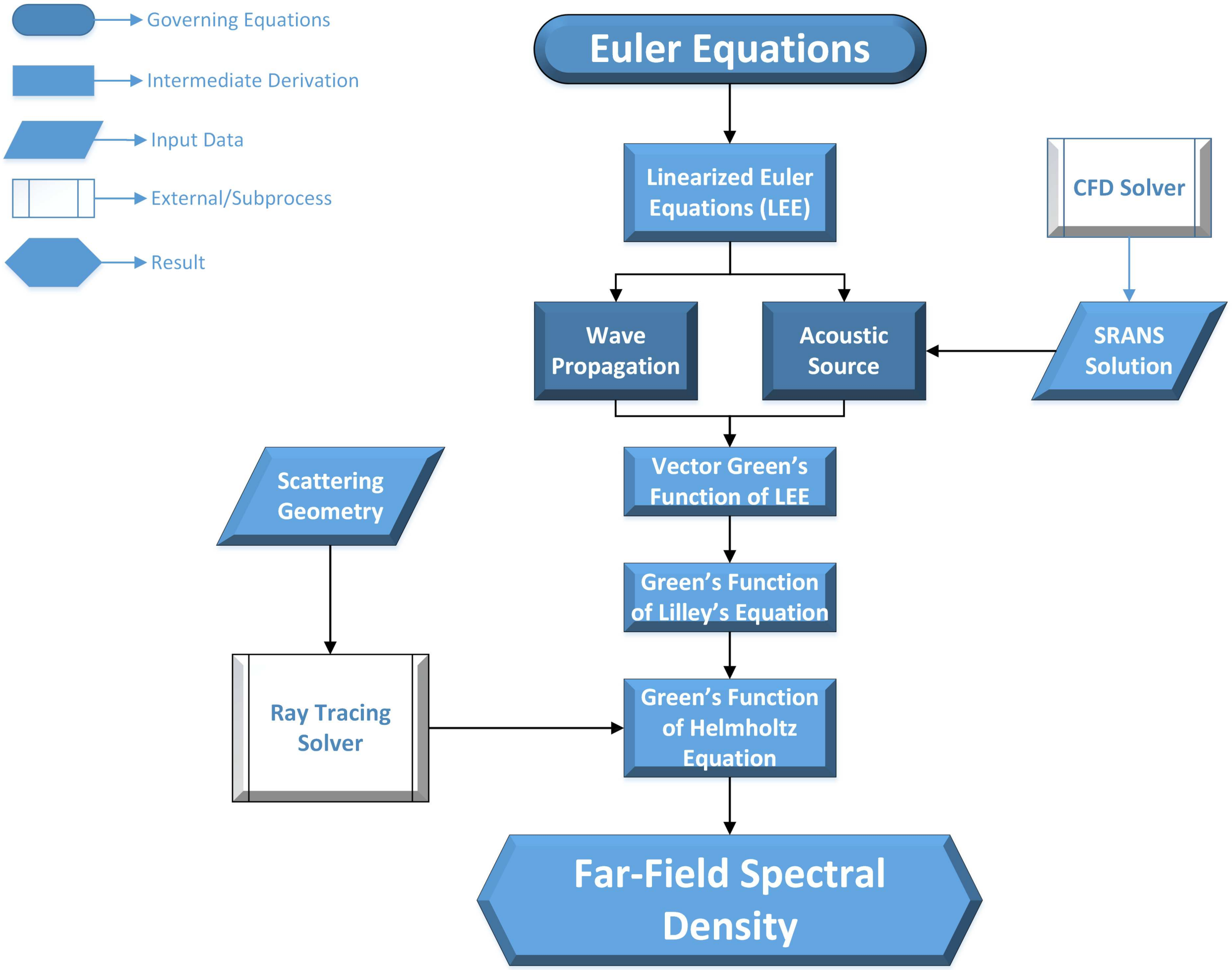

Figure 6.1: An outline of the methodology used in the prediction of jet noise using an acoustic analogy approach with a tailored Green's function. See Miller[16] for the full derivation.

6.2 Jet-Surface Interaction Test

The Jet-Surface Interaction Test (JSIT)of Brown *et al.*[7] was a multi-phase experiment performed at NASA Glenn research center intended to support researchers developing aircraft noise prediction tools by supplying data covering a wide range of surface geometries, positions, and jet flows. The first phase of the experiment involved measuring far-field noise of a jet near a simple planar surface with varying length and location. A flat plate mounted on a two-axis traverse was used to simulate a shield between the jet and the observer and a reflecting surface on the opposite side of the jet from the observer. Comparisons of the shielded configuration are used to validate the developed model. The surface was moved through axial positions $2 < x_p/D < 20$ and radial positions $1 < y_p/D < 20$. x_p is the axial distance from the nozzle exit to the trailing edge and y_p is the distance from the jet centerline and the plate surface. The exit diameter of the SMC nozzles are $D = 0.0508\ m$. The plate positions are illustrated in Figure 6.2. The plate was made using a 1/2" thick aluminum cut with a 1/4" trailing edge angled 39.2° opposite of the jet. The dimensions of the trailing edge of the plate are shown in Figure 6.3. The far-field noise data were acquired from an azimuthal array of 24 microphones centered on the jet exit with a constant radius of 150" ($75D$). The microphones were distributed along the arc at 5 intervals ranging from approximately 50° upstream to 165° downstream from the jet upstream axis. The angles are described in Figure 6.2. A photograph of the experimental test rig is shown in Figure 6.4. To accurately represent the diffracted field, predictions are compared with measured data at angles 50°, 70°, 90°, 110°, 130°, and 150° along the arc array. The range of experimental data used to validate the prediction model includes the plate configurations shown in Table 6.1 and the jet operating conditions shown in Table 6.2. The data processing included transforming the spectra to a lossless condition and scaling the observer to a distance of $100D$ from the nozzle exit by correcting for the atmospheric attenuation and spherical spreading of sound.[74]

Table 6.1: Plate Locations

Axial Distance to Trailing Edge (x_p/D)	Radial Distance to Jet Centerline (y_p/D)
4	2,4,6,8,10
10	2,4,6,8,10
20	2,4,6,8,10

Table 6.2: Jet Operating Conditions

Nozzle	Setpoint	NPR	TTR	M_a	M_j
SMC000	7	1.861	1.000	0.9	0.985
SMC000	27	1.357	1.814	0.9	0.678
SMC016	11606	2.748	0.761	1.128	1.29
SMC016	11610	3.670	0.706	1.31	1.5

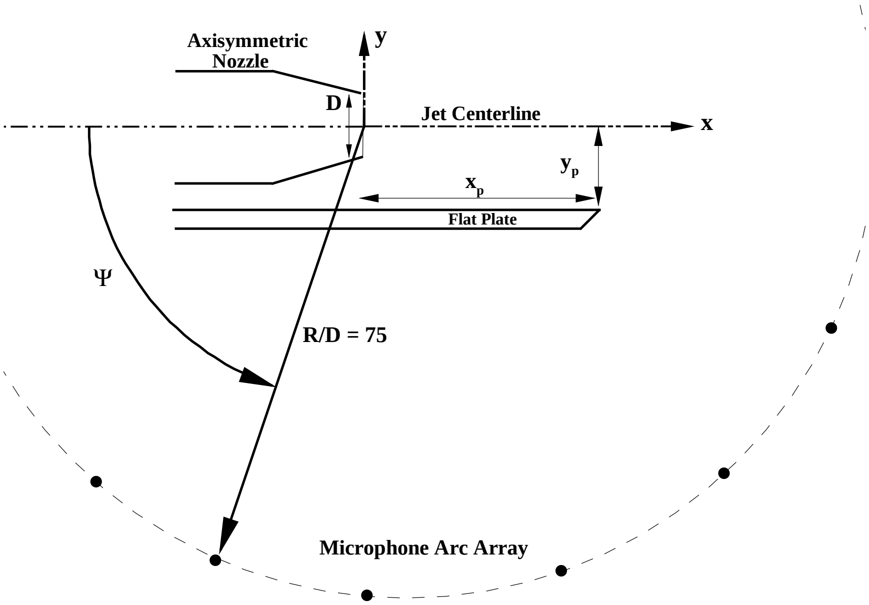

Figure 6.2: Coordinate system and distance parameters based on the JSIT experiment.

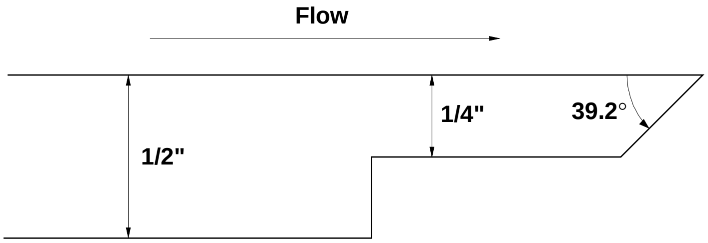

Figure 6.3: Dimensions of the trailing edge of the plate surface.

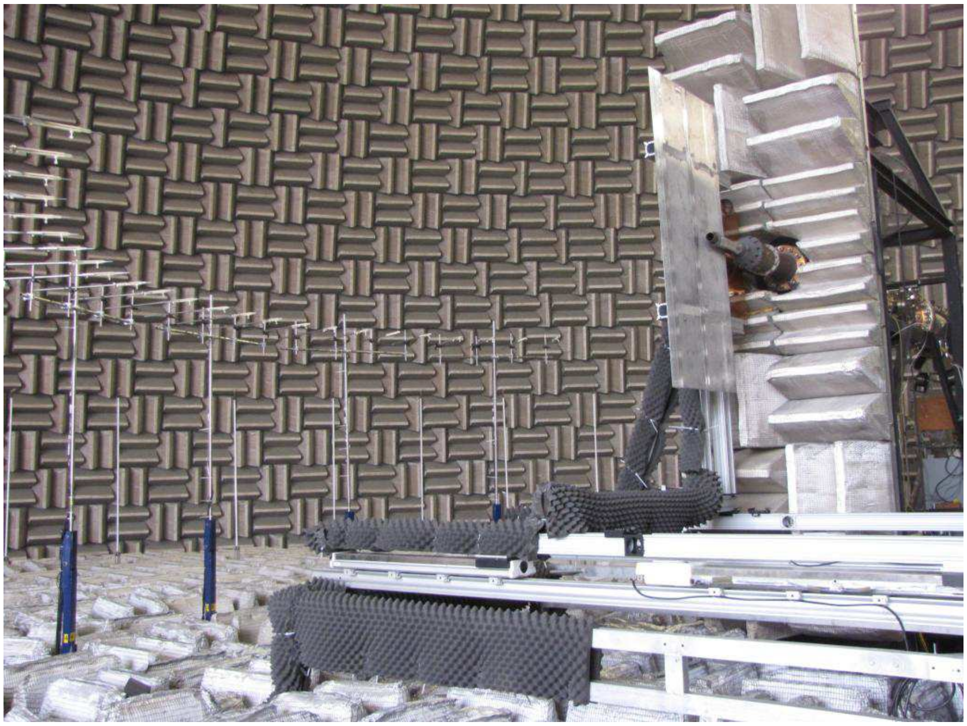

Figure 6.4: The JSIT experimental rig in the shielding configuration. An azimuthal array of 24 microphones centered on the jet exit with a constant radius of 150" ($75D$) is displayed. The photo is from Figure 3 in Podboy[58].

6.3 Jet-Surface Validation

6.3.1 Results

A free-field or isolated jet calculation is required to validate the prediction method. Data from the experiment of Bridges and Brown[56] is used to validate the free-field calculations. For every shielding prediction and experiment comparison, there is also a corresponding static comparison. The results are presented as Sound Pressure Level (SPL) per unit St, where $St = fD_j/u_j$ is the Strouhal number, and D_j and u_j are the fully expanded jet diameter and velocity respectively. The frequency ranges from 20 Hz to 100 kHz in the form of the non-dimensional Strouhal number. In general, the free-field calculations capture the trends of static and jets with forward flight effects with respect to experiment across the range of frequencies and at most angles from the upstream jet axis. Figure 6.5 displays jet noise spectra and associated dominant sources that are observed in the following comparisons. Here, SHJAR represents the free-field experiment and JSIT represents the shielded experiment. The mixing noise is the only jet noise component modeled in the predictions. Descriptions of the multiple sources of jet noise are given in Section 2.1.

Subsonic Jets

The first comparisons consist of the heated subsonic jet operating at $M_j = 0.678$ and $TTR = 1.926$. Results with the plate located at $x_p/D = 4$ and $y_p/D = 2$ are shown in Figure 6.6. The Sound Pressure Level (SPL) per unit St is represented on the y-axis and the non-dimensional frequency St is represented on the x-axis. The Helmholtz number $kx_p = 9$ is also labeled on the x-axis, where k is wave number and x_p is the axial distance from the nozzle exit to the trailing edge of the plate. This value is related to the Helmholtz number,

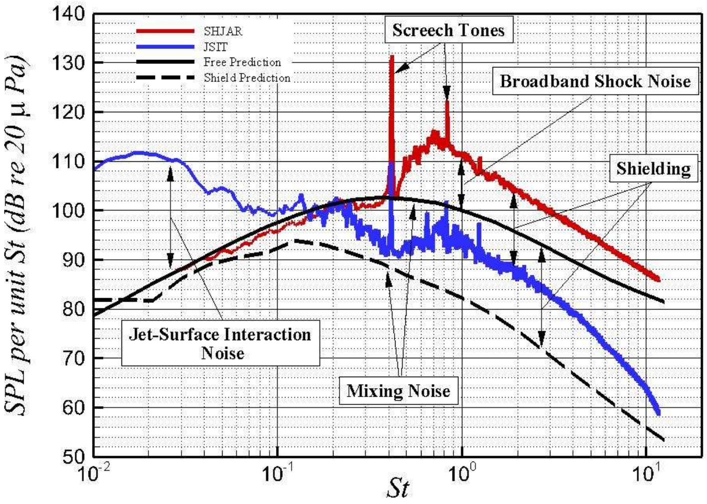

Figure 6.5: The free-field and shielded prediction at $R/D = 100$ and $\Psi = 50°$ compared with experiment. The jet operates at $M_j = 1.29$ and $TTR = 1.00$ from the SMC016 nozzle with $D = 0.0508\ m$ and the plate is located at $x_p/D = 20$ and $y_p/D = 2$.

$kW = 9$, in Section 5.3 that illustrates the low frequency limit of the ray tracing method. The predictions at observer angles $\Psi = 50°$, $70°$, $90°$, $110°$, $130°$, and $150°$ from the upstream jet axis are shown. The last information displayed in Figure 6.6 is the parameter Γ, described in Section 4.1, calculated from the jet-condition and plate configuration. The value of Γ estimates whether additional noise sources from the jet-surface interaction exist. All of the following figures use this convention.

At $\Psi = 50°$ and $\Psi = 70°$ in Figure 6.6, the free-field prediction matches the experiment. The shielding prediction and experiment both have a high frequency decay beginning at $St \approx 0.3$. The shielding is over-predicted as the frequency increases from the initial point of decay at the cutoff frequency. The predicted shielding reaches a maximum decrease of 26 dB and 28 dB at $\Psi = 50°$ and $\Psi = 70°$ and the experiment shows a maximum decrease of 20 dB and 12 dB respectively. The noise is over-predicted in the shielding configuration in the lower frequency range ($< kx_p = 9$) and is attributed to the low frequency limit of the ray tracing method. At $\Psi = 90°$, the free-field calculation deviates from experiment at higher frequencies; however, the relative decrease in SPL from the shielding prediction agrees with the experiment. The shielding experiment and prediction show a maximum decrease of 12 dB relative to the free-field experiment and prediction respectively. At the downstream angle $\Psi = 110°$, the maximum predicted shielding also agrees well with the experiment. The free-field calculation, shows larger deviations at lower frequencies $(6 - 8\ dB)$ and the cutoff frequency is larger than experiment. There is no predicted attenuation at $\Psi = 130°$ and $\Psi = 150°$, but the experiment shows a $4 - 6\ dB$ decrease in SPL across the range of frequencies. For all observer angles, the maximum shielding for both the experiment and prediction occurs at the highest frequency. There is no additional noise sources such as scrubbing or trailing edge noise present in the measurement. This complies with the low value of $\Gamma = 0.199$.

In Figure 6.7, results are shown for a plate position of $y_p/D = 2$ and the trailing edge extended to $x_p/D = 10$. As expected from the larger value of $\Gamma = 0.469$, scrubbing and trailing edge noise created by the jet-surface interaction are apparent in the shielded configuration of the experiment at low frequencies. The prediction method is not designed to account for these additional noise sources. Apart from the deviation in the lower frequency range where the additional noise sources dominate, the shielded predictions agree well with the experiment at all observer angles except downstream at $\Psi = 130°$ and $\Psi = 150°$. At $\Psi = 50°$, $70°$, and $90°$, the predicted shielding is within $\pm 4\ dB$ of the experiment above the peak frequency. The prediction agrees within $\pm 6\ dB$ of the experiment at $\Psi = 110°$ and shows a maximum deviation of $-14\ dB$ at $\Psi = 130°$. Similar to the previous comparison, there is insignificant predicted shielding at the highest downstream angle of $\Psi = 150°$.

The most extreme shielding configuration is shown in Figure 6.8, where the plate is located at $y_p/D = 2$ and the trailing edge extends to $x_p/D = 20$. There is additional noise sources present in the experiment, corresponding to the large value of $\Gamma = 0.994$. However, there is less noise intensity increase at low frequencies compared to the plate length of $x_p/D = 10$. This difference can be explained by a decrease in trailing edge noise resulting due to a decrease in convection velocity at the trailing edge. As shown in Section 3.2, the convection velocity at $x_p/D = 20$, in the fully developed region, is less than at $x_p/D = 10$. As the frequency increases past the region where scrubbing dominates, the prediction agrees within $\pm 2\ dB$ of the experiment at the upstream and sideline observer angles. The prediction is also in better agreement with the experiment at the downstream angles relative to other plate configurations. At $\Psi = 110°$ and $\Psi = 130°$, the prediction is within $\pm 6\ dB$ and $\pm 4\ dB$ of the experiment respectively. In contrast with the previous two plate locations, the shielding is captured by the prediction method at $\Psi = 150°$. The high frequency decay occurs at a higher cutoff frequency, $St \approx 0.2$, relative to experiment, $St \approx 0.1$, but the attenuation is within $\pm 4\ dB$ at frequencies $St > 1$.

In Figure 6.9, comparisons are shown with the trailing edge remaining at the length $x_p/D = 20$ and the surface located further from the nozzle axis at $y_p/D = 6$. The comparisons show similar agreement to the case with the surface located at $y_p/D = 2$, except at $\Psi = 150°$. There is strong agreement at high frequencies, within $\pm 2\ dB$, at $\Psi = 50°$, $70°$, and $90°$. The predicted attenuation rate higher than the peak frequency matches the experiment at all angles except $\Psi = 150°$. There is no predicted shielding at the downstream angle $\Psi = 150°$. In contrast to the $y_p/D = 2$ case, the value of $\Gamma = 0.09$ is low and there is only a small region at low frequencies where there is an increase in noise shown by the experiment.

These comparisons display the trends seen in all plate locations listed in Table 6.1. The predictions of the cold subsonic $M_j = 0.985$ jet also follow the same trends seen with the $M_j = 0.678$ comparisons. The comparisons of all plate locations for both subsonic jets are shown in Appendix B.

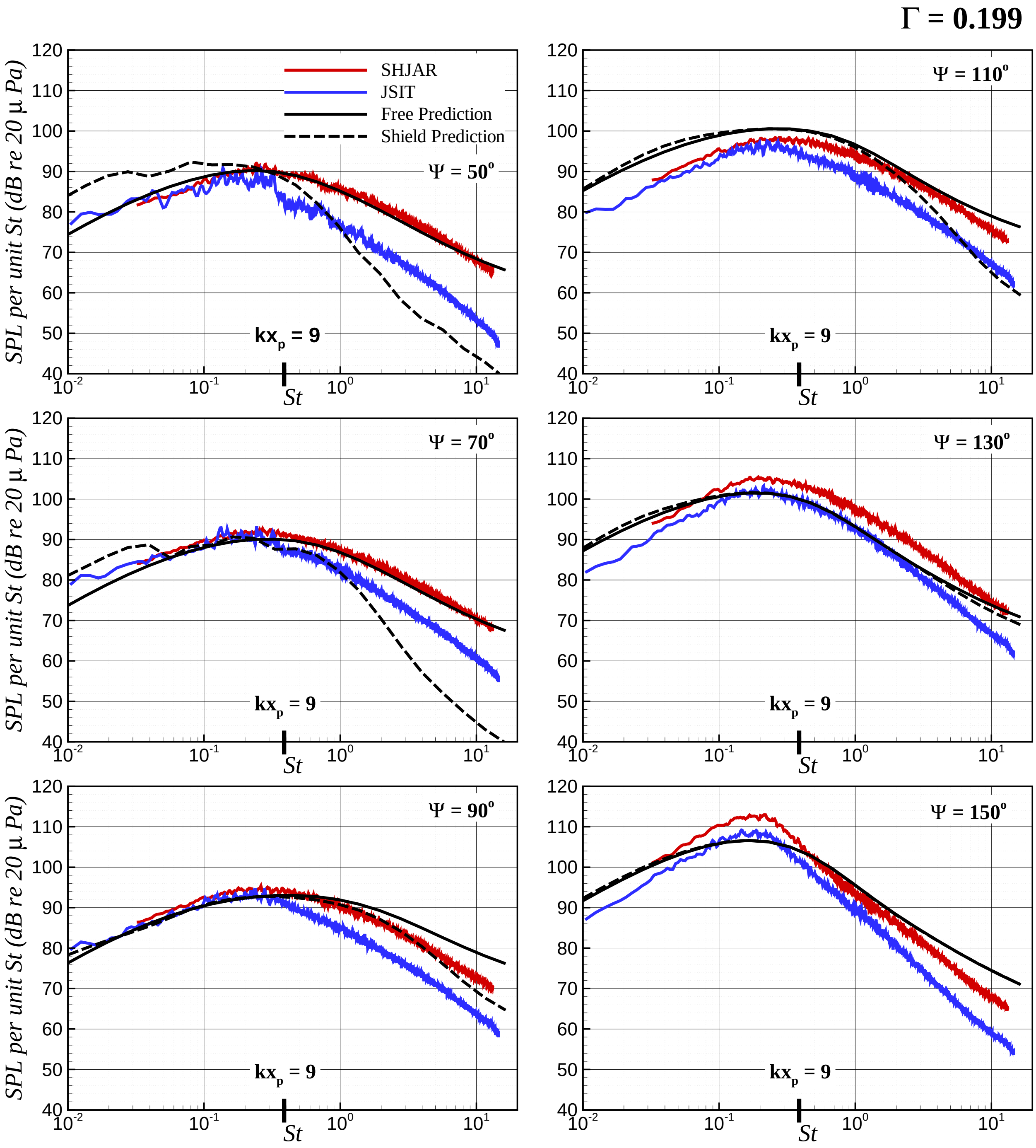

Figure 6.6: The free-field and shielded prediction at $R/D = 100$ compared with experiment. The jet operates at $M_j = 0.678$ and $TTR = 1.926$ from the SMC000 nozzle with $D = 0.0508\ m$ and the plate is located at $x_p/D = 4$ and $y_p/D = 2$.

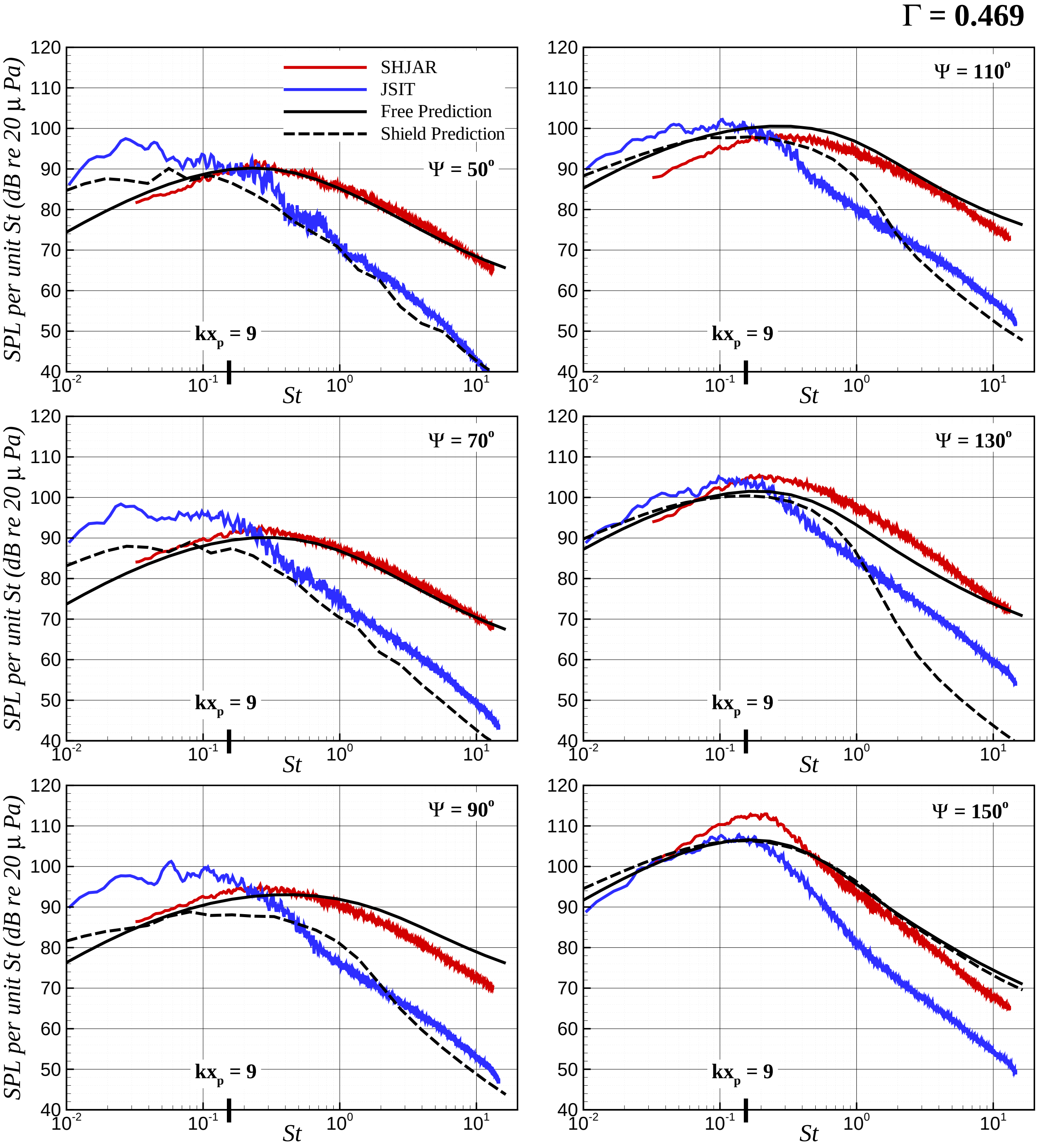

Figure 6.7: The free-field and shielded prediction at $R/D = 100$ compared with experiment. The jet operates at $M_j = 0.678$ and $TTR = 1.926$ from the SMC000 nozzle with $D = 0.0508\ m$ and the plate is located at $x_p/D = 10$ and $y_p/D = 2$.

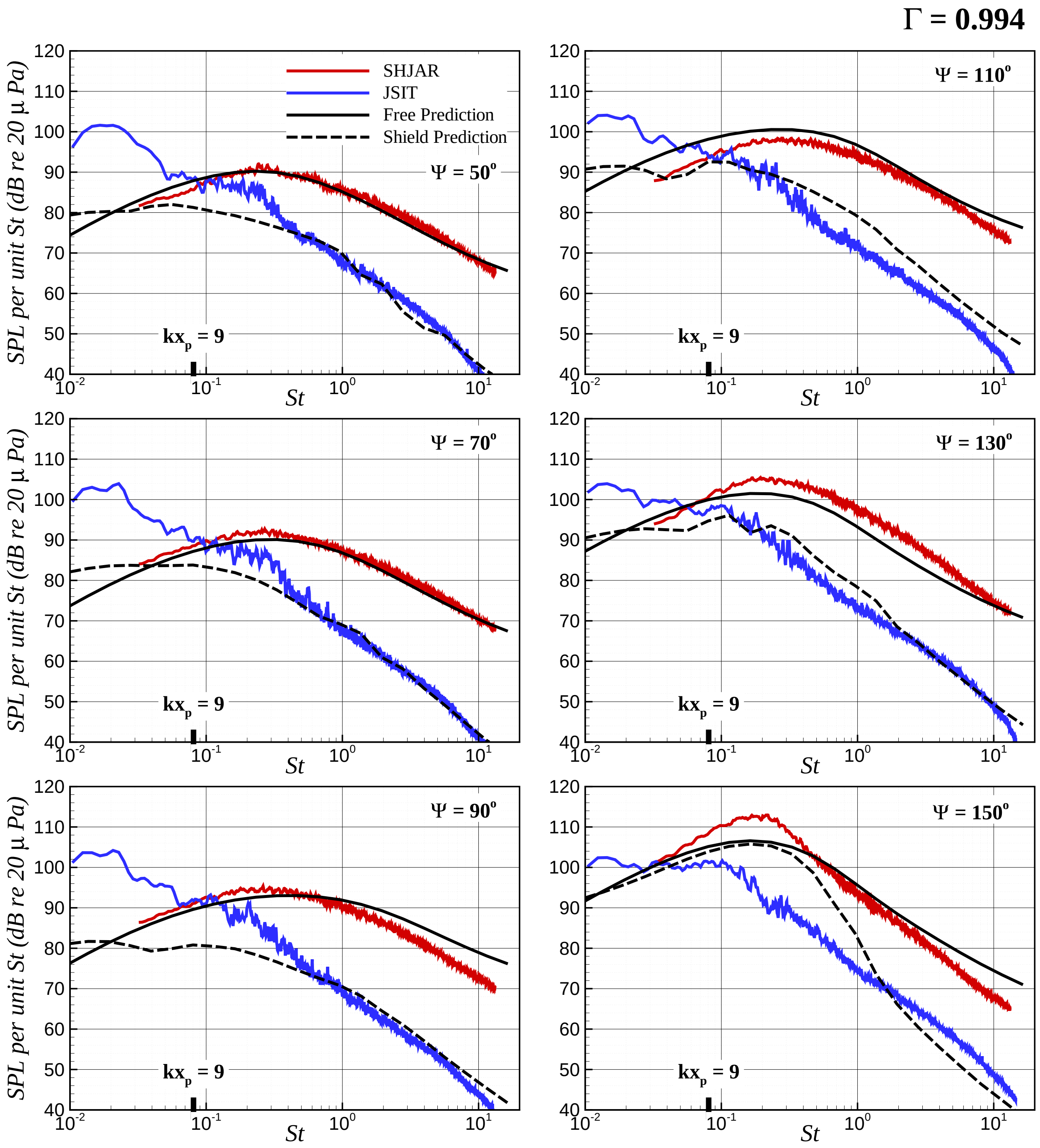

Figure 6.8: The free-field and shielded prediction at $R/D = 100$ compared with experiment. The jet operates at $M_j = 0.678$ and $TTR = 1.926$ from the SMC000 nozzle with $D = 0.0508\ m$ and the plate is located at $x_p/D = 20$ and $y_p/D = 2$.

Γ = 0.090

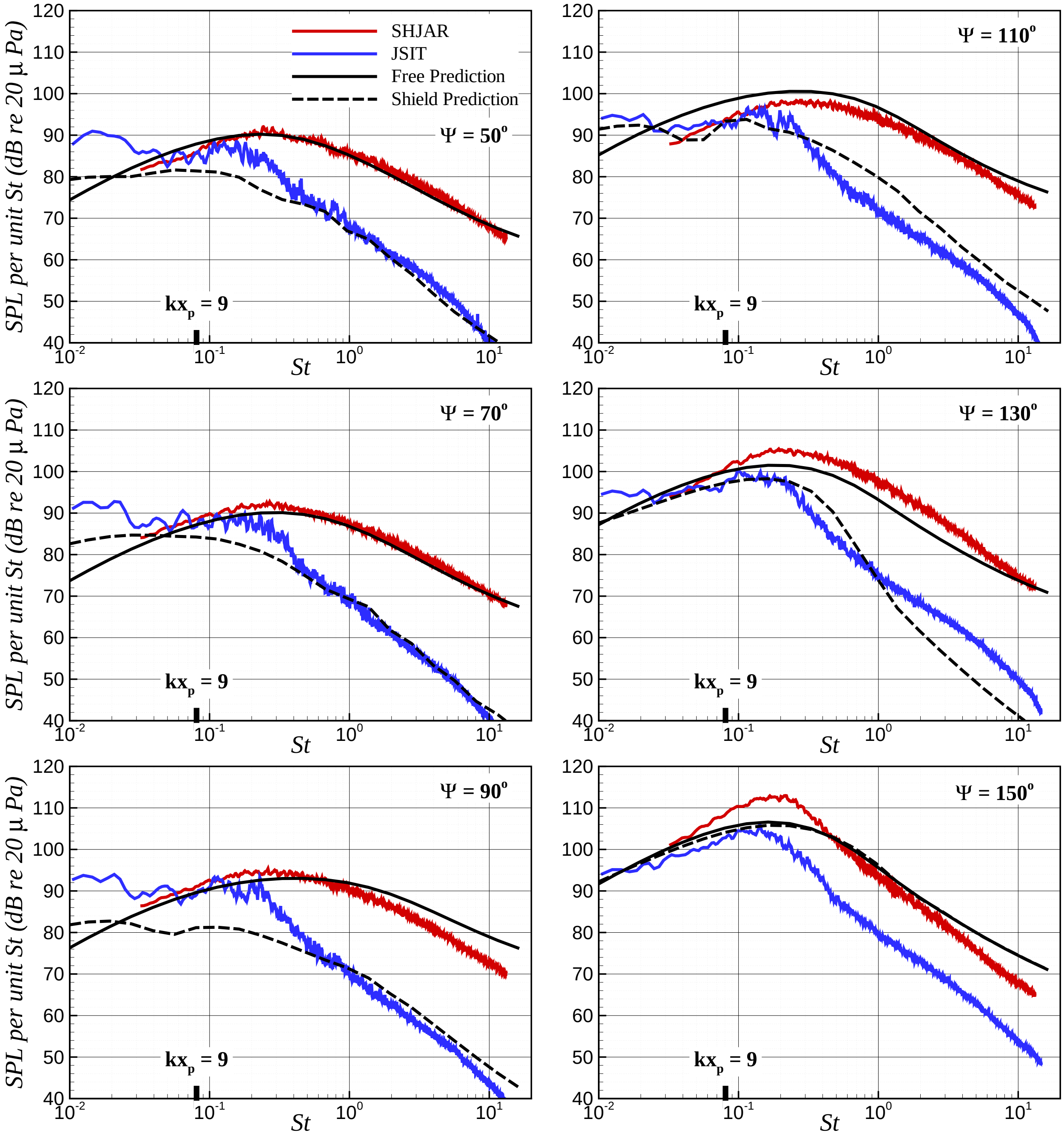

Figure 6.9: The free-field and shielded prediction at $R/D = 100$ compared with experiment. The jet operates at $M_j = 0.678$ and $TTR = 1.185$ from the SMC000 nozzle with $D = 0.0508\ m$ and the plate is located at $x_p/D = 20$ and $y_p/D = 6$.

Supersonic Jets

This section shows comparisons of a series of supersonic jets. The first comparison consist of the cold on-design $M_j = 1.5$ jet. The predictions compared with experiment of the plate located at $x_p/D = 4$ and $y_p/D = 2$ are shown in Figure 6.10. There is significantly less shielding for this plate configuration compared to a subsonic jet with the same plate configuration. There is no significant increase in noise from the surface, which is implied from the low value of $\Gamma = 0.092$. The experiment shows a maximum decrease of 4 dB in the high frequency range for observer angles $\Psi = 50°$ and $\Psi = 150°$. At all other angles, the shielding configuration of the experiment is within ± 2 dB of the isolated jet. The shielding is over-predicted at $\Psi = 50°$ and $\Psi = 70°$ by 14 dB and 9 dB respectively; however, the prediction shows minimal shielding (± 1 dB) for all other angles in compliance with the experiment. Lower shielding effects at this configuration compared to the subsonic jet can be explained by the extended length of the potential core of the supersonic jet, as shown in Section 3.2. With a potential core length extending further downstream from the nozzle exit, there is a larger distribution of equivalent sources past the trailing edge of the plate that are not shielded.

In Figure 6.11, the results are shown for the plate located at $y_p/D = 2$ and the trailing edge extended to $x_p/D = 20$. The jet condition and plate location result in a larger value of $\Gamma = 0.461$, and additional noise from the jet-surface interaction is shown by the experiment at lower frequencies. The predicted SPL of the shielding configuration converges to the SPL of the experiment as the frequency increases and the contribution of surface interaction noise diminishes. The deviation from the experiment decreases with frequency to within ± 1 dB at observer angles $\Psi = 50°$, $70°$, $90°$, and $110°$. At $\Psi = 130°$, the shielding is over-predicted by 6 dB. The maximum attenuation at $\Psi = 150°$ agrees with the experiment, although the high frequency decay occurs at a higher cutoff frequency, $St = 0.4$, than experiment,

$St = 0.1$.

The first comparison of the over-expanded $M_j = 1.29$ jet is shown in Figure 6.12. The plate is located at $y_p/D = 2$ and the trailing edge extends to $x_p/D = 20$. Since the jet is off-design, shocks are present in the jet plume and the resulting screech tones and broadband shock-associated noise (BBSAN) are observed in the measurements. Although the predictions do not take shock noise into account, agreement is seen from the relative attenuation of the turbulent mixing noise. Outside of the shifted increase of BBSAN in the spectra, the predicted shielding follows the same high frequency rate of attenuation at all observer angles except $\Psi = 150°$. At $\Psi = 150°$, the predicted attenuation begins at a higher cutoff frequency and has a larger attenuation rate. The jet condition and plate location result in a value of $\Gamma = 0.602$, and additional noise from the surface interaction is shown by the experiment.

The over-expanded jet is also compared with the plate located at $y_p/D = 10$ and the trailing edge extending to $x_p/D = 20$ in Figure 6.13. The prediction follows the same agreement shown in the previous comparison at $\Psi = 50°$, $70°$, $90°$, and $110°$ but deviates from the experiment at the downstream angles. At $\Psi = 130°$ and $\Psi = 150°$ there is predicted shielding at high frequencies, but the experiment shows a maximum decrease of 20 dB and 5 dB respectively. This comparison is another example in which the prediction shows stronger agreement with experiment at the upstream angles where there is more shielding and shows less agreement at the downstream angles.

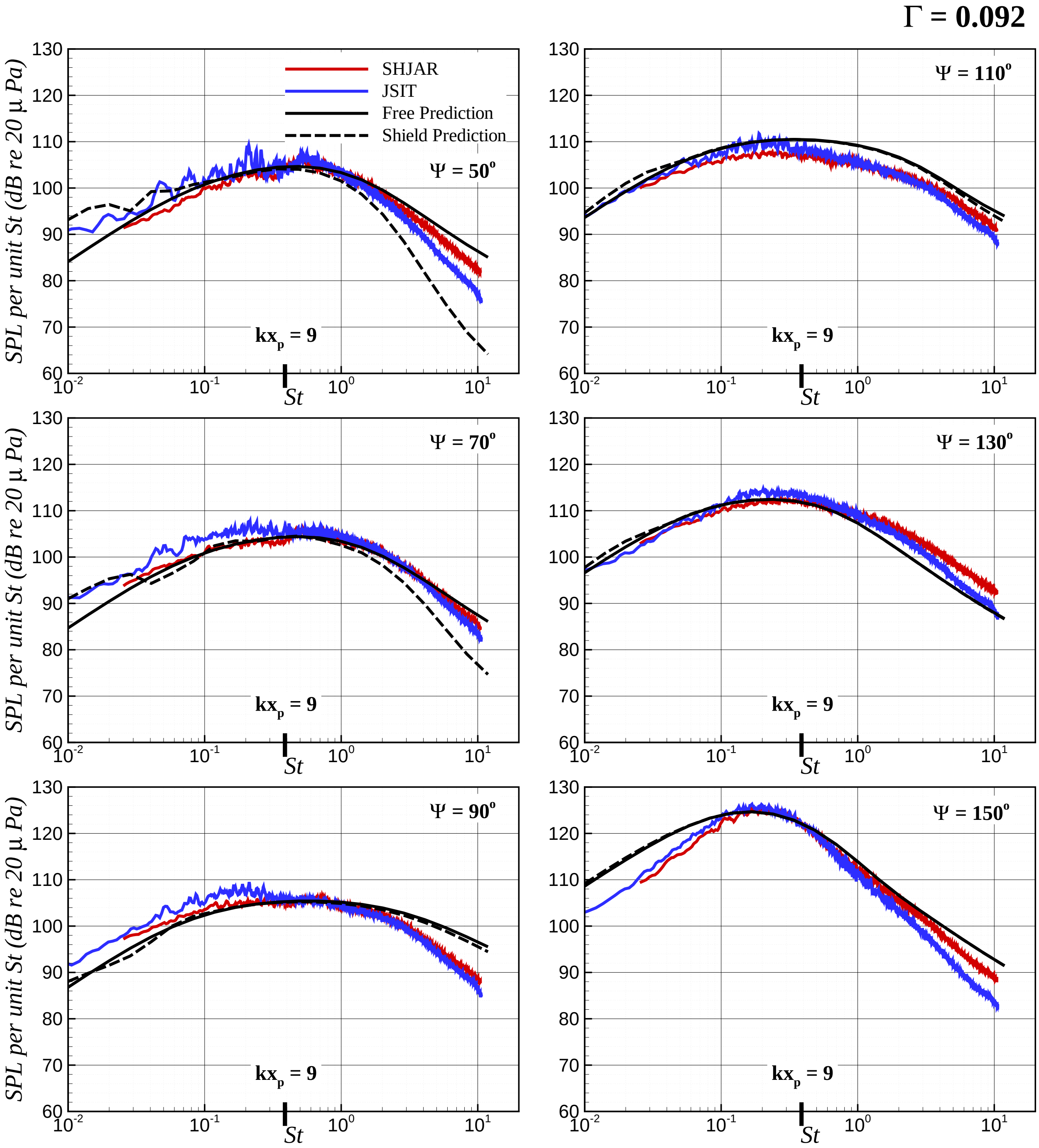

Figure 6.10: The free-field and shielded prediction at $R/D = 100$ compared with experiment. The jet operates at $M_j = 1.50$ and $TTR = 1.00$ from the SMC016 nozzle with $D = 0.0508\ m$ and the plate is located at $x_p/D = 4$ and $y_p/D = 2$.

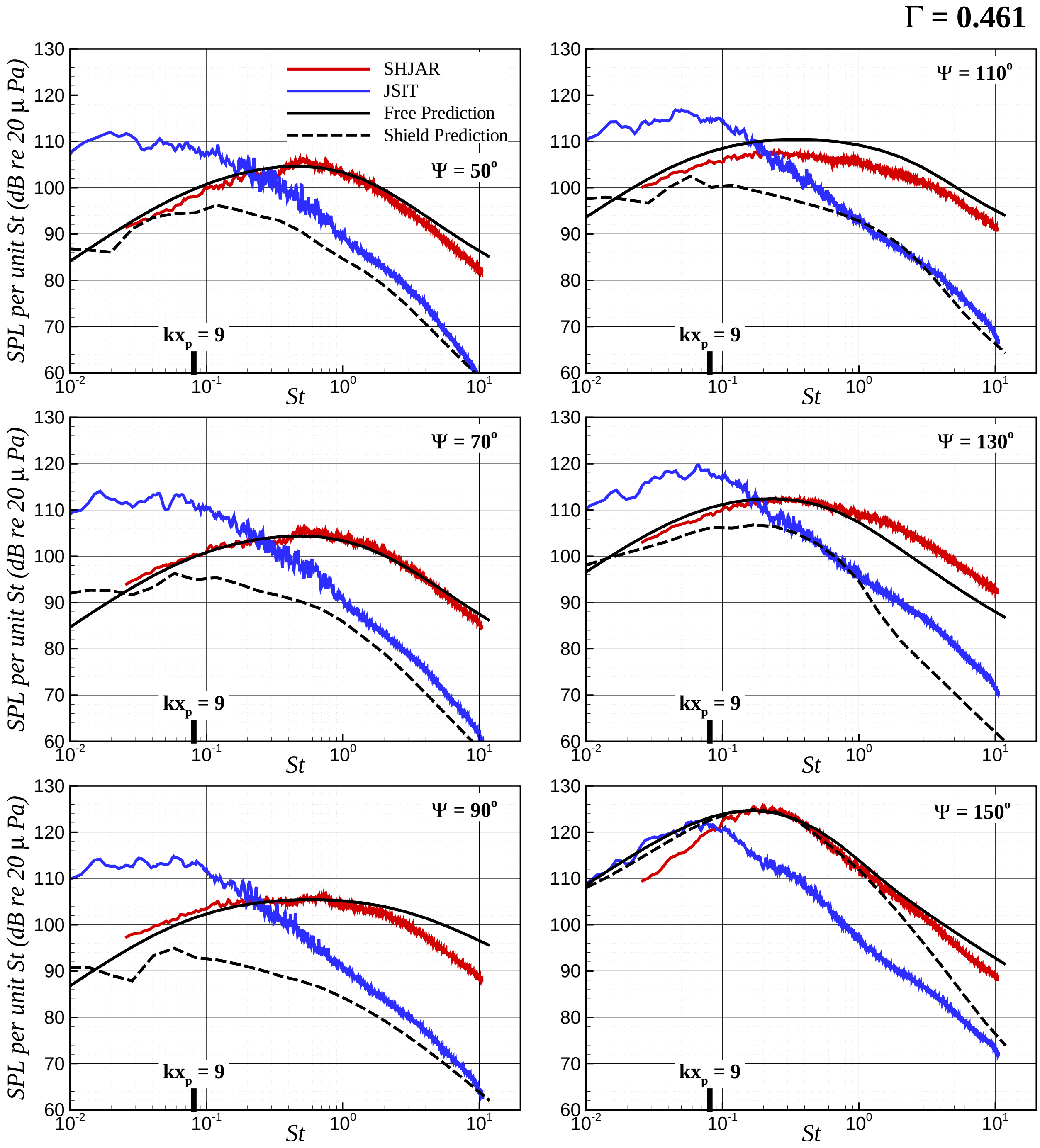

Figure 6.11: The free-field and shielded prediction at $R/D = 100$ compared with experiment. The jet operates at $M_j = 1.50$ and $TTR = 1.00$ from the SMC016 nozzle with $D = 0.0508\ m$ and the plate is located at $x_p/D = 20$ and $y_p/D = 2$.

Γ = 0.602

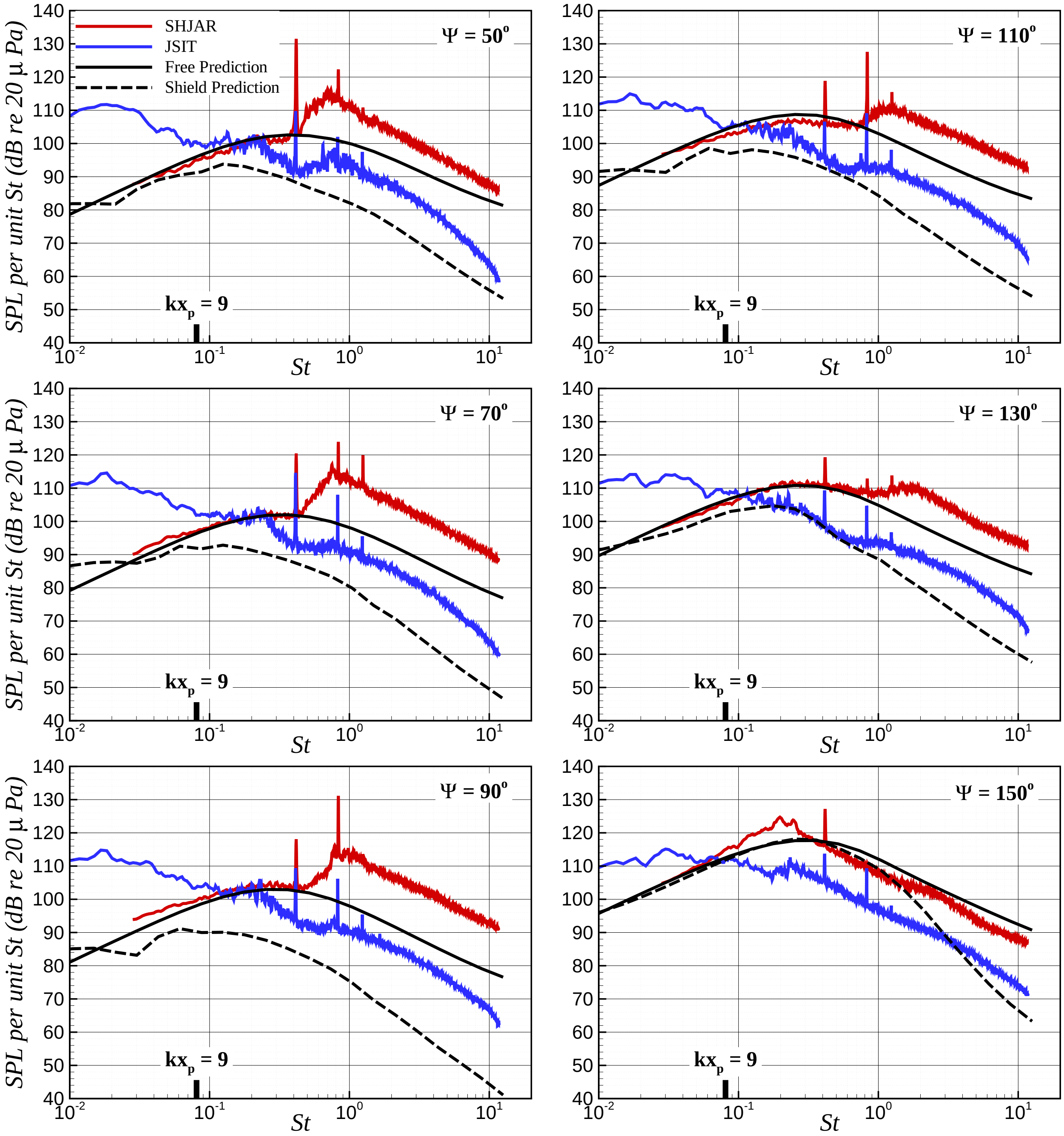

Figure 6.12: The free-field and shielded prediction at $R/D = 100$ compared with experiment. The jet operates at $M_j = 1.29$ and $TTR = 1.00$ from the SMC016 nozzle with $D = 0.0508\,m$ and the plate is located at $x_p/D = 20$ and $y_p/D = 2$.

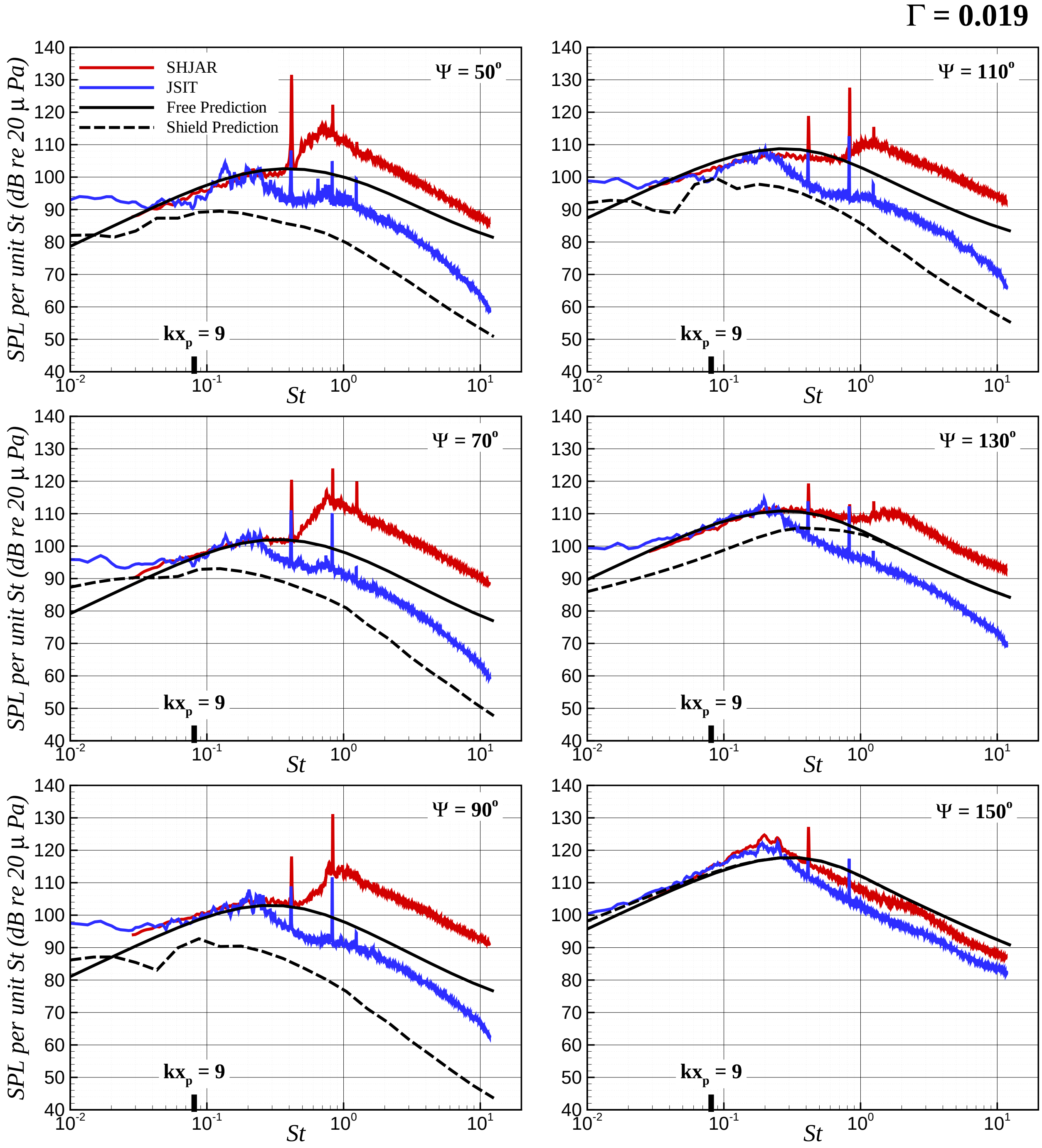

Figure 6.13: The free-field and shielded prediction at $R/D = 100$ compared with experiment. The jet operates at $M_j = 1.29$ and $TTR = 1.00$ from the SMC016 nozzle with $D = 0.0508\,m$ and the plate is located at $x_p/D = 20$ and $y_p/D = 10$.

6.3.2 Summary

In general, the free-field calculations capture the trends of static jets with respect to experiment across the range of frequencies and at most observer angles from the upstream jet axis. Although the free-field calculation matches the experiment in nearly all cases, there still exist areas for continued development, particularly at the downstream angles. Apart from larger deviation from experiment in particular cases, multiple cases display close agreement between the shielding prediction and experiment, and the trends are generally predicted. The comparisons discussed are representative of all plate configurations and jet conditions analyzed. The full set of comparisons are provided in Appendix B. Notable observations based on the shielded comparisons include the following:

1. The validation assessment shows that the acoustic analogy approach and tailored Green's function provided by the ray tracing method are capable of capturing multiple jet shielding characteristics.
2. The analysis suggests that an optimized shielding design includes an airframe located closest to the nozzle axis and extends far downstream with a low value of Γ; High Γ configurations, such as $x_p = 20$ and $y_p = 2$, yield larger shielding effects at lower frequencies, but the jet-surface interaction noise is high.
3. The prediction method shows strong agreement at higher frequencies, where shielding is dominant. The high frequency attenuation rate and the maximum decrease of SPL is captured for most cases. The dominant shielding region occurs past the estimated low frequency limit $kx_p = 9$ of the ray tracing method for all cases.
4. The predicted cutoff frequency of the high frequency decay matches the experiment for most cases. The high frequency decay generally begins at the peak frequency

range ($0.2 \leq St \leq 0.4$). The larger deviations in the predicted cutoff frequency from experiment appear in the downstream observer angles.

5. The predicted peak frequency of the isolated jet matches the experiment for most cases; the largest deviation is with $\pm 4\ dB$ of experiment. For the shielded configuration, the predicted attenuation in peak frequency range generally does not agree with experiment at high downstream angles, especially at $\Psi = 150°$.

6. The shielding predictions show strong agreement at extreme shielding configurations, especially at upstream and sideline observer angles. The lack of agreement in shielding configurations at high angles may be due to the predicted location of the high frequency noise source. Higher frequency noise may be generated further downstream than predicted.

7. The prediction method shows weak agreement at lower frequencies. The Helmholtz number $kx_p = 9$ signifies the frequency limit where the prediction does not compare well with experiment for low values of Γ. The lack of agreement in this region for high values of Γ is attributed to the surface interaction noise. To make a direct comparison, the scrubbing and trailing edge noise needs to be subtracted incoherently from the spectra.

8. The prediction method captured the decrease in shielding as the jet exit velocity increases. An increase in velocity increases the potential core length and produces a larger distribution of equivalent sources past the trailing edge of the plate, where there is less shielding.

9. In general, there is little to no shielding shown by the prediction or experiment at low frequencies through the attenuation cutoff frequencies, where the shielding then increases with increasing frequency.

10. Although the shock noise from the over-expanded jet is not captured by the current prediction, the relative shielding of turbulent mixing noise follows the same trend observed in the shock-free jets.

11. Scrubbing and trailing edge noise is apparent in the experiment for higher values of Γ. Values of $\Gamma \geq 4$ show a significant increase in noise at lower frequencies. The additional noise is generally apparent at frequencies lower than the peak frequency of the isolated jet ($St < 0.2$).

12. The differentiation between scrubbing and trailing edge noise may be apparent in the $x_p = 10$ and $x_p = 20$ cases. The difference in the increase of noise may be due to a larger contribution of trailing edge noise at $x_p = 10$. The trailing edge noise is estimated to increase at $x_p = 10$ because of the higher convection velocity at $x_p = 10$ compared to $x_p = 20$.

6.4 Hybrid Wing Body

The acoustic analogy and ray tracing method are applied to the HWB configuration to demonstrate the compatibility of the methodology with next generation aircraft configurations. As described in Section 1.1, the HWB is an unconventional aircraft concept in which the engines are installed on top of the airframe to shield the noise from the observer. Shielding effects of the HWB are described by Thomas *et al.*[4] and Czech *et al.*[5]

A 5.8% scale model of the HWB aircraft is used to demonstrate the prediction capabilities. The model measures 8.58 ft (2.62 m) long with a span of 12.35 ft (3.76 m) as shown in Figure 6.14. The model geometry corresponds to the parameters used in the 2013 HWB test at NASA Langley Research Center's 14 x 22 Foot Subsonic Wind Tunnel[78]. In the experiment, the jet noise is simulated by two Compact Jet Engine Simulators (CJES) as described by Heath *et al.*[78] The CJES consists of an interior heated core flow and an outer fan flow. The distance from the core nozzle exit to the trailing edge along the jet centerline is $x_p/D_f = 2.17$ and $y_p/D_f = 1.73$ as shown in Figure 6.14, where $D_f = 0.1578$ m is the fan diameter. The jet exit conditions of the two flows are described in Table 6.3. Steady RANS solutions based on the flow conditions of the CJES are used in conjunction with the acoustic analogy and ray scattering methodology previously described in Section 6.1 to predict the mixing noise in the far-field for both the isolated jet and the jet installed into the model airframe.

Table 6.3: CJES Jet Operating Conditions

Stream	D (m)	NPR	TTR	M_j
Core	0.0832	1.378	2.863	0.6920
Fan	0.1578	1.550	1.118	0.8166

6.4.1 Results

The mixing noise produced by one nozzle is calculated, and symmetry is used to calculate the noise produced by the second nozzle. The total acoustic field is determined by incoherently summing the noise generated by both nozzles. The prescribed observer angles are shown relative to the HWB airframe in Figure 6.15. The origin of the coordinate system is located at the center of the trailing edge. The positive x-axis points in the downstream direction along the aircraft centerline, the positive y-axis points points beneath the axis normal to the airframe surface, and the positive z-axis points in the starboard direction following the right hand rule convention. The directivity of the free-field or isolated mixing noise generated by both CJES nozzles at $St = 1.1$ is shown in Figure 6.16. The predictions are shown at observer angles $\Psi = 50°$, $70°$, $90°$, $110°$, $130°$, and $150°$ from the upstream jet axis. Predictions at these angles are also shown in the range $-80° \leq \Phi \leq 80°$, where Φ is the angle from the downward normal axis (positive y-axis). The predictions of all observer angles are displayed as contours of SPL on the surface of a partial hemisphere with radius $R/D_f = 25$ beneath the aircraft. In Figure 6.16, the directivity pattern shows that the free-field noise increases as Ψ increases downstream and remains constant along the lateral angles $-80° \leq \Phi \leq 80°$. A dominant noise band is observed in the region of $\Psi = 130°$ where the SPL reaches a maximum of 115 dB. This dominant noise band is explained by the cardioid directivity pattern of jet noise due to refraction effects. Contours of Mach number are also shown from the steady RANS solutions for each nozzle to give perspective on the region of the equivalent sources within the jet plume. The steady RANS solutions are also shown in the x-z plane at $y = 0.273$ m (jet centerline) in Figure 6.17. The steady RANS solutions demonstrate how far the jet plume extends past the trailing edge of the HWB airframe. The distribution of acoustic sources in the jet plume past the trailing edge is expected to have a crucial role in the predicted shielding of the HWB airframe.

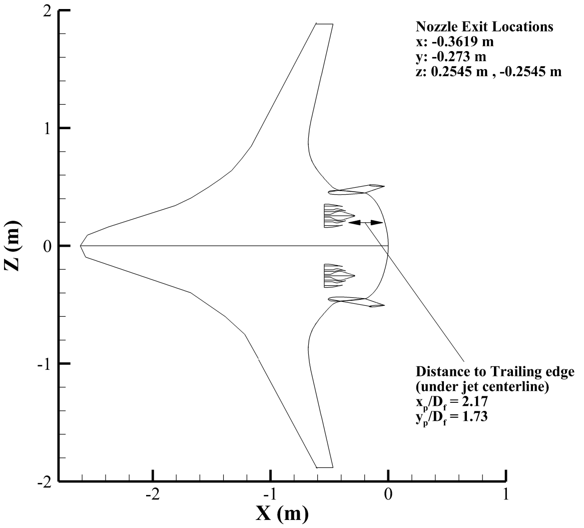

Figure 6.14: The dimensions of the 5.8% model scale HWB configuration. The nozzle fan diameter is $D_f = 0.1578\ m$.

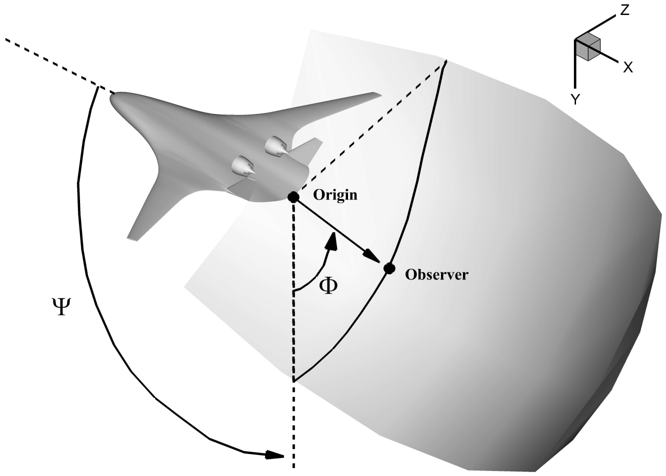

Figure 6.15: The observer angles measured from the HWB airframe. The origin is located at the center of the trailing edge.

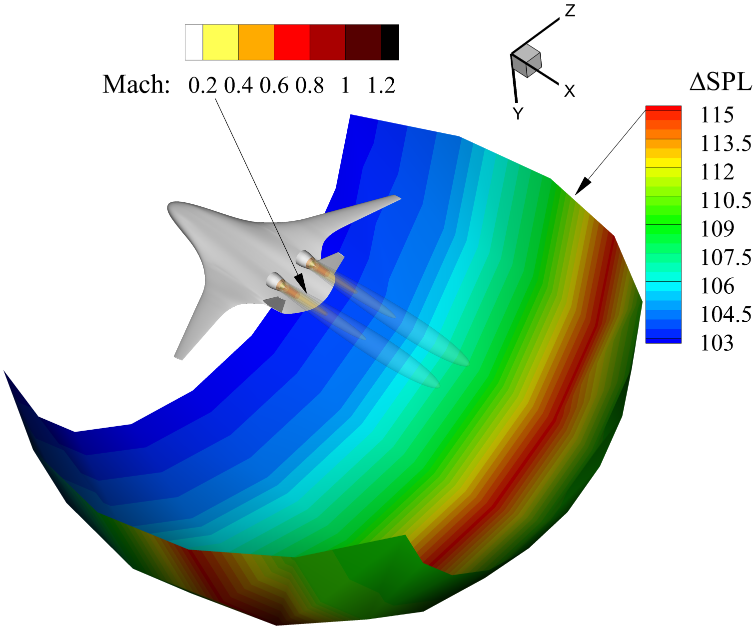

Figure 6.16: Three-dimensional directivity plot of the free-field CJES prediction at $R/D = 25$ and $St = 1.1$. Contours of Mach number are also shown from the steady RANS solutions for each jet plume.

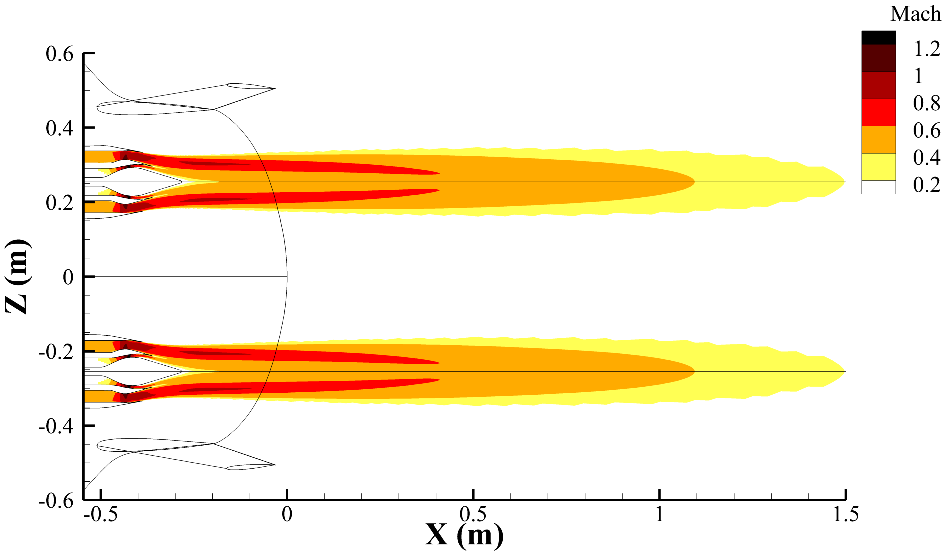

Figure 6.17: Contours of Mach number from the steady RANS solutions based on CJES operating conditions. The core jet operates at $M_j = 0.692$ and $TTR = 2.863$. The fan jet operates at $M_j = 0.8166$ and $TTR = 1.118$.

The installed jet predictions are shown as contours of SPL at $St = 1.1$ in Figure 6.18. The results are displayed at the same observer angles as the free-field predictions. The frequency of $St = 1.1$ is larger than the average cutoff frequency observed in the validation results of Section 6.3. Thus, a noise reduction due to airframe shielding is expected. In Figure 6.18, similar results to the isolated jet are shown at the downstream angles past the trailing edge. The dominant noise band at $\Psi = 130°$ is still observed with a maximum SPL of 115 dB. However, a larger region of reduced noise is observed upstream of the trailing edge.

To better quantify the shielding of the HWB configuration, the isolated jet predictions are subtracted from the installed jet predictions. The results are displayed as contours of ΔSPL in Figure 6.19. An isometric view along with views of the x-y, x-z, and y-z planes are shown. The results show that there is insignificant shielding downstream of the trailing edge. There is a maximum reduction of 1.5 dB in the region directly aft of the trailing edge. Further downstream, there is either no reduction in noise or an increase of $\lesssim 1$ dB. This is explained by the large distribution of equivalent sources in the jet plume extending downstream of the trailing edge that are not shielded. Capturing this effect highlights the importance of representing jet mixing noise as a distributed source. Based on this observation, it is expected that a point source representation of the jet noise located at the nozzle exit would over-predict the shielding effect of the airframe. The results also show a larger region of noise reduction upstream of the trailing edge where more of the equivalent sources distributed in the jet plume are shielded. Directly beneath the center of the trailing edge ($\Phi = 0°$), the magnitude of the noise reduction increases from -1.5 dB to a maximum of -19.6 dB as Ψ approaches 70°. The trend of increased noise reduction beneath the aircraft is also observed in the lateral angles. As Φ approaches 0° or 360°, the magnitude of the noise reduction increases. In the x-z plane shown in Figure 6.19(b), a maximum reduction of -19.6 dB is observed in the shielded region beneath the center of the aircraft at $x = -1.2$ and $z = 0$

($\Psi = 70°$ and $\Phi = 0°$). With increasing frequency, the maximum noise reduction is expected to increase, and the region of noise reduction is expected to grow.

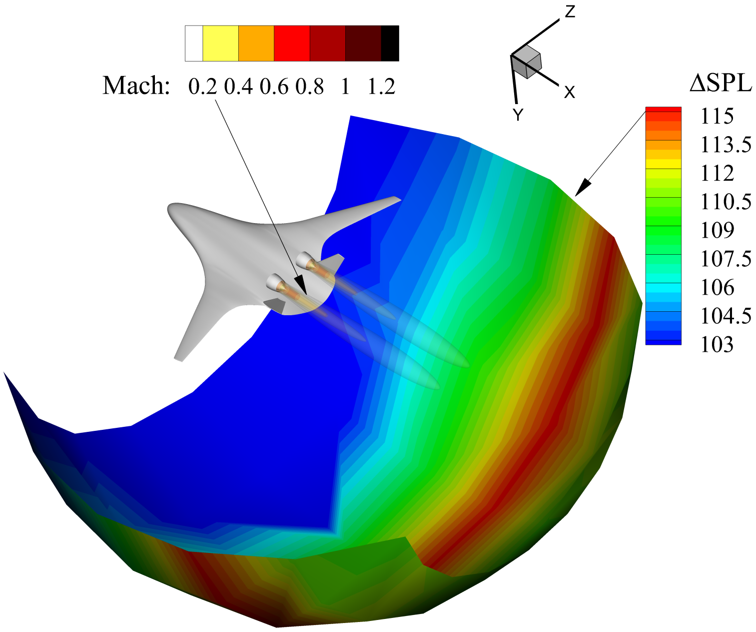

Figure 6.18: Three-dimensional directivity plot of the Hybrid Wing Body configuration at $R/D = 25$ and $St = 1.1$. Contours of Mach number are also shown from the steady RANS solutions for each nozzle.

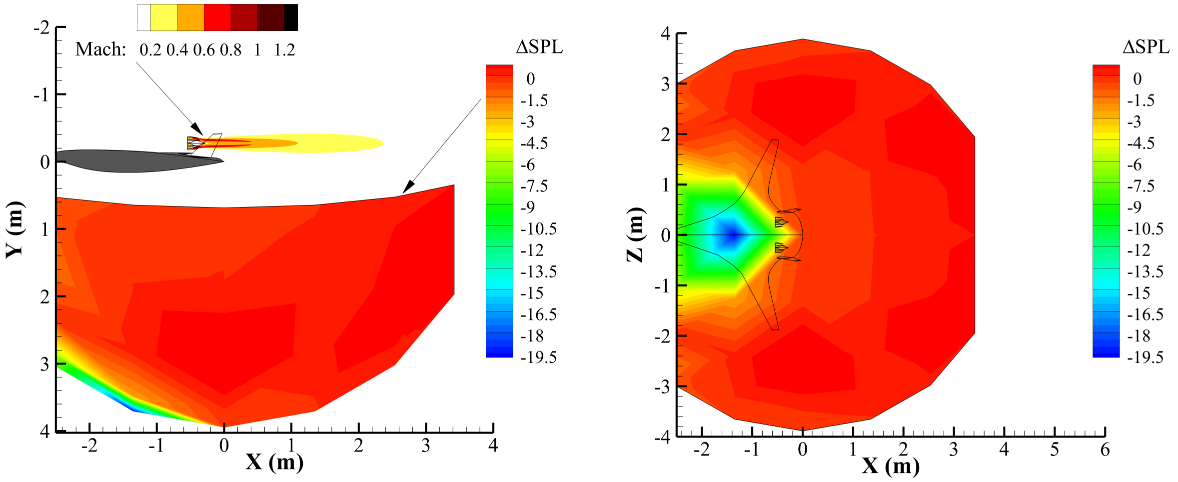

(a) x-y plane

(b) x-y plane

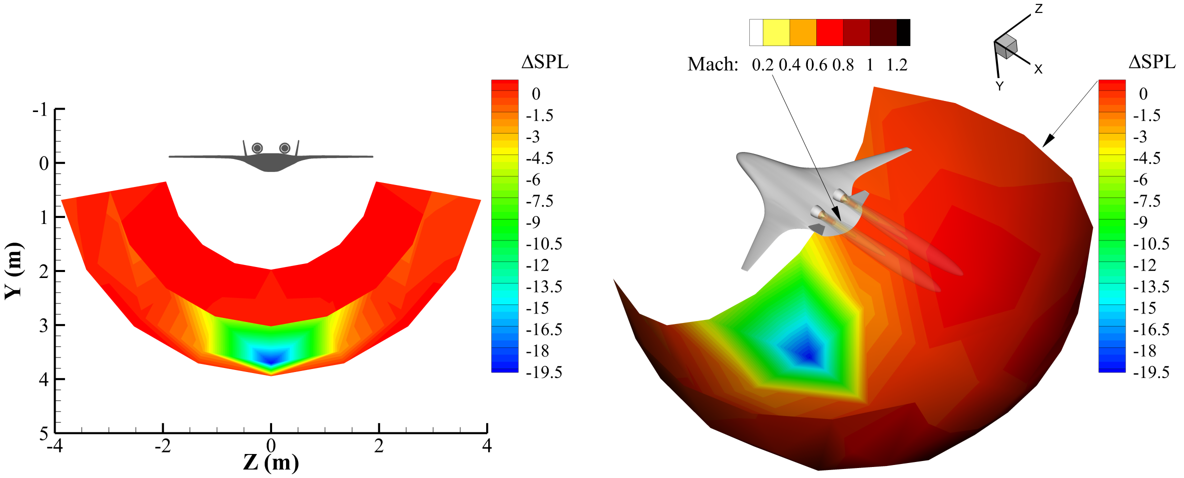

(c) x-y plane

(d) Isometric view

Figure 6.19: The attenuation pattern of the Hybrid Wing Body configuration at $R/D = 25$ and $St = 1.1$. Contours of Mach number are also shown from the steady RANS solutions for each nozzle.

6.4.2 Summary

The results show that the acoustic analogy and ray tracing method are capable of predicting shielding effects of next generation aircraft configurations such as the HWB. In general, the predictions of the HWB configuration show insignificant noise reduction downstream of the trailing edge and a significant reduction of noise in the region beneath the aircraft. Notable observations from the installed jet predictions include the following:

1. There is a maximum reduction of 19.6 dB shown from the predictions at $St = 1.1$ in the shielded region beneath the aircraft.
2. In the region directly below the trailing edge ($\Psi = 90°$) and slightly aft, there is a maximum noise reduction of 1.5 dB. Further downstream, there is either no reduction or a slight increase (0.5 dB) of noise at downstream angles. This can be explained by the large distribution of equivalent sources in the jet plume extending downstream of the trailing edge that are not shielded.
3. The distribution of equivalent sources in the jet plume is critical to an accurate airframe shielding prediction. A point source representation of the jet noise located at the nozzle will over-predict the shielding effect of the airframe.
4. Based on the validation results in Section 6.3, the maximum noise reduction of the HWB configuration is expected to increase, and the region of noise reduction is expected to grow with increasing frequency. There will also be an increase in noise reduction if the nozzles are placed further up stream from the trailing edge. However, scrubbing and trailing edge noise may become significant. The additional noise generated by the airframe surface is not modeled in this thesis.

Chapter 7

Summary

Throughout this study, the variation of the aerodynamic quantities, acoustic source, and far-field acoustic intensity is examined as a large flat plate is positioned relative to the nozzle exit. Predictions from various jet conditions and flat plate configurations are compared with an isolated jet. The aerodynamic models are validated by comparing Steady RANS solutions with PIV data. A non-dimensional number containing the flow-conditions and airframe installation parameters is formed to quantify the propulsion airframe aeroacoustic installation effects on the aerodynamic noise source.

Following the aerodynamic and acoustic source analyses, an assessment of an acoustic analogy for the mixing noise component of jet noise in the presence of a scattering surface is presented. First, a ray tracing approach is derived, implemented, and validated against experimental data of a point source near a flat plate. The ray tracing methodology is then used in conjunction with the acoustic analogy approach to predict far-field mixing noise generated from a jet shielded by a flat plate. The jet noise scattering predictions are validated by comparison with far-field measurements. The prediction approach is then used to demonstrate the shielding capabilities of the HWB concept.

7.1 Conclusions

A summary of the analyses are outlined by the following conclusions.

Aerodynamic Analysis

1. Results of the aerodynamic assessment show that nearby solid surfaces change the aerodynamic characteristics of the jet flow-field, even if the jet centerline is multiple diameters away from a solid surface.
2. The effect of the surface is amplified as it approaches the jet centerline and as the trailing edge extends further downstream.

Acoustic Source Analysis

1. The induced change in the aerodynamic flow-field is shown to have a direct effect on the acoustic source of jet noise.
2. The installed noise predictions relative to the isolated jet show that the acoustic intensity originating from the jet aerodynamic source is decreased as the effective impingement surface area of the plate is increased.
3. The calculation of the parameter Γ can be used as a basic guide to determine if the aerodynamic source is affected by the airframe relative to the equivalent isolated jet aerodynamic source. It is also useful to determine if scrubbing or trailing edge noise is present.

Jet-Surface Shielding Analysis

1. The point source validation demonstrates that the ray tracing method is capable of predicting the correct characteristics and trends of the diffraction pattern in the shadow zone over a wide range of frequencies.
2. The validation assessment shows that the acoustic analogy approach and tailored Green's function provided by the ray tracing method are capable of capturing jet shielding characteristics for multiple shielding configurations and jet exit conditions.
3. The HWB analysis shows that the acoustic analogy and ray tracing method are capable of predicting shielding effects of next generation aircraft configurations.

7.2 Recommendations for Future Work

The understanding of jet noise is directly related to the understanding of turbulence in jet flows; therefore, future work in to increase the physical understanding and enhance the modeling capabilities of turbulence is recommended. Possible future work also includes modeling the surface interaction effects of the BBSAN and screech tones components for supersonic jets. A full jet noise prediction from a PAA configuration includes modeling the shielding of all jet noise components and the additional noise sources generated from the jet-surface interaction. Thus, the addition of scrubbing and trailing edge noise models with the current model is recommended. It would be useful to enhance the abilities of the ray tracing model by including other diffraction effects such as creeping rays and corner-diffracted rays. The current model is also recommended to be integrated into a multi-design optimization code such as NASA's Aircraft Noise Optimization Prediction Program (ANOPP)[79] or (ANOPP2)[80].

Bibliography

[1] Envia, E., "Emerging Community Noise Reduction Approaches," *3rd AIAA Atmospheric Space Environments Conference, June 27-30, Honolulu, Hawaii, AIAA Paper 2011-3532*, 2011.

[2] Hill, G. and Thomas, R. H., "Challenges and Opportunities for Noise Reduction Through Advanced Aircraft Propulsion Airframe Integration and Configurations," *8th CEAS Workshop: Aeroacoustics of New Aircraft and Engine Configurations, November 11-12, Budapest, Hungary*, 2004.

[3] "National Aeronautics Research and Development Plan, Biennial Update," *The National Science and Technology Council*, 2010, URL: http://www.whitehouse.gov/sites/default/files/microsites/ostp/aero-rdplan-2010.pdf.

[4] Thomas, R. H., Burley, C. L., and Olson, E. D., "Hybrid Wing Body Aircraft System Noise Assessment with Propulsion Airframe Aeroacoustic Experiments," *16th AIAA/CEAS Aeroacoustics Conference, Stockholm, Sweden, 7 - 9 June, AIAA Paper 2010-3913*, 2010.

[5] Czech, M. J., Thomas, R. H., and Elkoby, R., "Propulsion Airframe Aeroacoustic Integration Effects for a Hybrid Wing Body Aircraft Configuration," *16th AIAA/CEAS Aeroacoustics Conference, Stockholm, Sweden, 7 - 9 June, AIAA Paper 2010-3912*, 2010.

[6] Horne, W. C. and Burnside, N. J., "AMELIA CESTOL Test: Acoustic Characteristics of Circulation Control Wing and Leading- and Trailing-Edge Slot Blowing," *51st AIAA Aerospace Sciences Meeting, January 7-10, Grapevine, Texas, AIAA Paper 2013-0978*, 2013.

[7] Brown, C., "Jet-Surface Interaction Test: Far-Field Noise Results," *Proceeding of the ASME Turbo Expo, Copenhagen, Denmark, June 15-19, GT2012-69639*, 2011.

[8] Welge, H. R., Nelson, C., and Bonet, J., "Supersonic Vehicle Systems for the 2020 to 2035 Timeframe," *28th AIAA Applied Aerodynamics Conference, Chicago, Illinois, June 28 - July 1, AIAA Paper 2010-4930*, 2010.

[9] Welge, H. R., Bonet, J., Magee, T., Chen, D., Hollowell, S., Kutzmann, A., Mortlock, A., Stengle, J., Nelson, C., Adamson, E., Baughcum, S., Britt, R. T., Miller, G., and Tai, J., "N+2 Supersonic Concept Development and Systems Integration," *NASA/CR 2010-216842*, 2010.

[10] Morgenstern, J. M., Stelmach, M., and Jha, P. D., "Advanced Concept Studies for Supersonic Commercial Transports Entering Service in 2030-35 (N+3)," *28th AIAA Applied Aerodynamics Conference, Chicago, Illinois, June 28 - July 1, AIAA Paper 2010-5144*, 2010.

[11] Sokhey, J. S. and Kube-McDowell, M., "Low Noise Highly Variable Cycle Nozzle for Next Generation Supersonic Aircraft," *NASA ARMD Fundamental Aeronautics Program Technical Conference*, 2008.

[12] Huang, C. and Papamoschou, D., "Numerical Study of Noise Shielding by Airframe Structures," *14th AIAA/CEAS Aeroacoustics Conference, Vancouver, British Columbia Canada, 5 - 7 May, AIAA Paper 2008-2999*, 2008.

[13] Tinetti, A. F., Dunn, M. H., and Pope, S., "Fast Scattering Code (FSC) User's Manual, Version 2.0," *NASA CR 2006-214510*, Oct. 2006.

[14] Agarwal, A., Dowling, A. P., and Graham, W., "A Ray Tracing Approach to Calculate Acoustic Shielding by the Silent Aircraft Airframe," *12th AIAA/CEAS Aeroacoustics Conference, Cambridge, Massachussetts, 8 - 10 May, AIAA Paper 2006-2618*, 2006.

[15] Morris, P. J. and Farassat, F., "Acoustic Analogy and Alternative Theories for Jet Noise Prediction," *AIAA Journal*, Vol. 40, No. 4, 2002, pp. 671–680.

[16] Miller, S. A. E., "The Prediction of Jet Noise Ground Effects using an Acoustic Analogy and a Tailored Green's Function," *19th AIAA/CEAS Aeroacoustics Conference, Berlin, Germany, May 27-29, AIAA Paper 2013-2038, DOI: 10.2514/6.2013-2038*, 2013.

[17] Donaldson, C. D. and Snedeker, R. S., "A Study of Free Jet Impingement. Part 1. Mean Properties of Free and Impinging Jets," *Journal of Fluid Mechanics*, Vol. 45, 1971, pp. 281–319.

[18] Lamont, P. J. and Hunt, B. L., "The Impingement of Underexpanded, Axisymmetric Jets on Perpendicular and Inclined Flat Plates," *Journal of Fluid Mechanics*, Vol. 100, 1980, pp. 471–511.

[19] Sawyer, R. A., "Two-dimensional Reattaching Jet Flows Including the Effects of Curvature on Entrainment," *Journal of Fluid Mechanics*, Vol. 17, 1963, pp. 481–498.

[20] Al-Qutub, A. M. and Budair, M. O., "Experiments on the Flow Over a Flat Surface Impinged by a Supersonic Jet," *31st AIAA/ASME/SAE/ASEE Joint Propulsion Conference and Exhibit, San Diego, California, 10 - 12 July, AIAA Paper 1995-2935*, 1995.

[21] Bridges, J. and Wernet, M. P., "The NASA Subsonic Jet Particle Image Velocimetry (PIV) Dataset," *NASA/TM-2011-216807*, 2011.

[22] Lighthill, M. J., "On Sound Generated Aerodynamically: I. General Theory," *Proceedings of the Royal Society of London*, 1952.

[23] Lighthill, M. J., "On Sound Generated Aerodynamically: II. Turbulence as a Source of Sound," *Proceedings of the Royal Society of London*, 1954.

[24] Tam, K. W., "Jet Noise: Since 1952," *Theoretical and Computational Fluid Dynamics*, Vol. 10, 1998, pp. 393–405.

[25] Ffowcs Williams, J. E., "The Noise from Turbulence Convected at High-Speed," *Philosophical Transactions of the Royal Society A: Mathematical, Physical and Engineering Sciences*, 1963.

[26] Lilley, G. M., "On the Noise from Jets," *AGARD Conference Proceedings In Noise Mechanisms*, 1974.

[27] Pridmore-Brown, D. C., "Sound Propagation in a Fluid Flowing Through an Attenuating Duct," *Journal of Fluid Mechanics*, Vol. 4, 1958, pp. 393–406.

[28] Ribner, H. S., "Perspectives on Jet Noise," *AIAA*, Vol. 19, No. 12, 1981, pp. 1513–1526.

[29] Freund, J. B., Lele, S. K., and Moin, P., "Numerical Simulation of a Mach 1.92 Turbulent Jet and its Sound Field," *AIAA*, Vol. 38, No. 11, 2000, pp. 2023–2031.

[30] Bogey, C., B. C. and Juve, D., "Noise Investigation of a High Subsonic, moderate Reynolds number jet using a compressible LES," *Theoretical and Computational Fluid Dynamics*, Vol. 16, No. 4, 2003, pp. 273297.

[31] Tam, C. K. W. and Auriault, L., "Jet Mixing Noise from Fine-Scale Turbulence," *AIAA Journal*, Vol. 37, No. 2, 1999, pp. 145–153.

[32] Morris, P. J. and Boluriaan, S., "The Prediction of Jet Noise From CFD Data," *10th AIAA/CEAS Aeroacoustics Conference, Manchester, Great Britain, May 10-12, AIAA Paper 2004-2977*, 2004.

[33] Morris, P. J. and Miller, S. A. E., "Prediction of Broadband Shock-Associated Noise Using Reynolds-Averaged Navier-Stokes Computational Fluid Dynamics," *AIAA*, Vol. 48, No. 12, 2010, pp. 2931–2944.

[34] Tam, C. K. W., "Supersonic Jet Noise," *Annual Review of Fluid Mechanics*, Vol. 27, 1995, pp. 17–43.

[35] Tam, C. K. W., G. M. and Seiner, J. M., "On the Two Components of Turbulent Mixing Noise from Supersonic Jets," *2nd AIAA/CEAS Aeroacoustics Conference, State College, Pennsylvania, May 6-8, AIAA Paper 1996-1716*, 1996.

[36] Viswanathan, M., "Analysis of the Two Similarity Components of Turbulent Mixing Noise," *AIAA*, Vol. 40, No. 9, 2002, pp. 1735–1744.

[37] Mollo-Christensen, E., "Physics of Turbulent Flow," *AIAA Journal*, Vol. 9, No. 7, 171, pp. 1217–1228.

[38] Tam, C. K. W. and Chen, K. C., "A Statistical Model of Turbulence in Two-Dimensional Mixing Layers," *Journal of Fluid Mechanics*, Vol. 92, 1979, pp. 303–326.

[39] Harper-Bourne, M. and J., F. M., "The Noise from Shock Waves in Supersonic Jets," *AGARD-CP-131*, 1974.

[40] Curle, G. M., "The Influence of Solid Boundaries upon Aerodynamic Sound," *Proceedings of the Royal Society A: Mathematical, Physical and Engineering Sciences*, 1955.

[41] Ffowcs Williams, J. E. and Hall, L. H., "Aerodynamic Sound Generation by Turbulent Flow in the Vicinity of a Scattering Half Plane," *Journal of Fluid Mechanics*, Vol. 40, 1970, pp. 657–670.

[42] Crighton, D. G. and Lippington, F. G., "Scattering of Aerodynamic Noise by a Semi-infinite Compliant Plate," *Journal of Fluid Mechanics*, Vol. 43, No. 4, 1970, pp. 721–736.

[43] Amiet, R. K., "Noise Radiated from an Edge in Turbulent Flow," *AIAA*, 1975.

[44] Amiet, R. K., "Noise Due to Turbulent Flow Past a Trailing Edge," *Journal of Sound and Vibration*, 1976.

[45] Agarwal, A. and Dowling, A. P., "The Calculation of Acoustic Shielding of Engine Noise by the Silent Aircraft Airframe," *11th AIAA/CEAS Aeroacoustics Conference, Monterey, California, 23 - 25 May, AIAA Paper 2005-2996*, 2005.

[46] Dunn, M. H. and Tinetti, A. F., "Aeroacoustic Scattering Via The Equivalent Source Method," *10th AIAA/CEAS Aeroacoustics Conference, AIAA Paper 2004-2937*, 2004.

[47] Tinetti, A. F. and Dunn, M. H., "The Fast Scattering Code (FSC): Validation Studies and Program Guidelines," *NASA/CR-2011-217158*, 2011.

[48] "Fun3D Manual," *NASA Langley Research Center, Hampton, VA*, Aug. 2012, URL: http://fun3d.larc.nasa.gov/.

[49] Menter, F. R., "Two-Equation Eddy-Viscosity Turbulence Models for Engineering Applications," *AIAA Journal*, Vol. 32, No. 8, 1994, pp. 1598–1605.

[50] Jones, W. P. and Launder, B. E., "The Prediction of Laminarization with a Two-Equation Model of Turbulence," *International Journal of Heat and Mass Transfer*, Vol. 15, 1972, pp. 301–314.

[51] Wilcox, D. C. and Traci, R. M., "A Complete Model of Turbulence," *9th AIAA Fluid and Plasma Dynamics Conference, San Diego, California, 14 - 16 July, AIAA Paper 1976-351*, 1976.

[52] Wilcox, D. C., "A Half Century Historical Review of the k-ω Model," *29th AIAA Aerospace Sciences Meeting, Reno, Nevada, 7 - 10 January, AIAA Paper 1991-0615*, 1991.

[53] Georgiadis, N., Yoder, D. A., and Engblom, W. A., "Evaluation of Modified Two-Equation Turbulence Models for Jet Flow Predictions," *44th AIAA Aerospace Sciences Meeting and Exhibit, AIAA 2006-490*, 2006.

[54] Thomas, R. H., Czech, M. J., and Doty, M. J., "High Bypass Ratio Jet Noise Reduction and Installation Effects Including Shielding Effectiveness," *51st AIAA Aerospace Sciences Meeting, Grapevine, Texas, 7 - 10 January, AIAA Paper 2013-0541*, 2013.

[55] Lau, J. C., "Effects of Exit Mach Number and Temperature on Mean-Flow and Turbulence Characteristics in Round Jets," *Journal of Fluid Mechanics*, Vol. 105, 1981, pp. 193–218.

[56] Bridges, J. and Brown, C. A., "Validation of the Small Hot Jet Acoustic Rig for Aeroacoustic Research," *11th AIAA/CEAS Aeroacoustics Conference, Monterey, California, 23 - 25 May, AIAA Paper 2005-2846*, 2005.

[57] Brooks, T. F., Humphreys, W. M., and Plassman, G. E., "DAMAS Processing for a Phased Array Study in the NASA Langley Jet Noise Laboratory," *16th AIAA/CEAS Aeroacoustics Conference, Stockholm, Sweden, 7 - 9 June, AIAA Paper 2010-3780*, 2010.

[58] Podboy, G. G., "Jet-Surface Interaction Test: Phased Array Noise Source Localization Results," *Proceeding of the ASME Turbo Expo, Copenhagen, Denmark, June 14-18, GT2012-69801*, 2012.

[59] Kinsler, L., Frey, A. R., Coppens, A. B., and Sanders, J. V., *Fundamentals of Acoustics*, John Wiley and Sons, Inc, 4th ed., 2000.

[60] Keller, J. B., "Geometrical Theory of Diffraction," *Journal of the Optical Society of America*, Vol. 52, 1961, pp. 116–130.

[61] Pierce, A. D., *Acoustics: An Introduction to Physical Principles and Applications*, American Institue of Physics, 1994.

[62] Suzuki, T., "High-Frequency Acoustic Fields Solved Based on Geometrical Acoustics: Direct Waves, Reflected Waves, Creeping Waves, Diffracted Waves and Caustics," *16th AIAA/CEAS Aeroacoustics Conference, Stockholm, Sweden, 7 - 9 June, AIAA Paper 2010-3726*, 2010.

[63] van Rens, J. R. P., van Rens, B. J. E., van Holten, T., and Ruijgrok, G. J. J., "Sound Level Prediction using a Ray Tracing Algorithm for a Blended Wing Body," *6th AIAA/CEAS Aeroacoustics Conference, Lahaina, HI, 12 - 14 June, AIAA Paper 2000-2069*, 2000.

[64] Lummer, M., "Maggi-Rubinowicz Diffraction Correction for Ray-Tracing Calculations of Engine Noise Shielding," *14th AIAA/CEAS Aeroacoustics Conference, Vancouver, British Columbia Canada, 5 - 7 May, AIAA Paper 2008-3050*, 2008.

[65] Sommerfeld, A., *Lectures on Theoretical Physics: Optics*, Vol. 4, Academic Press, Inc, 1964.

[66] Levy, B. and Keller, J. B., "Diffraction by a Smooth Object," *Communications on Pure and Applied Mathematics*, Vol. 12, 1959, pp. 159–209.

[67] Agarwal, A., Dowling, A. P., Shin, H.-C., Graham, W., and Sefi, S., "Ray-Tracing Approach to Calculate Acoustic Shielding by a Flying Wing Airframe," *AIAA Journal*, Vol. 45, No. 5, 2007, pp. 1080–1090.

[68] Keller, J. B., "Diffraction by an Aperture," *Journal of Applied Physics*, Vol. 28, No. 4, 1957, pp. 426–444.

[69] Kraus, L. and Levine, L. M., "Diffraction by an Elliptic Cone," *Communications on Pure and Applied Mathematics*, Vol. 14, 1961, pp. 49–68.

[70] Felsen, L. B., "Backscattering from Wide-Angle and Narrow-Angle Cones," *Journal of Applied Physics*, Vol. 26, No. 2, 1955, pp. 136–151.

[71] Siegel, K. M., Crispen, J. W., and Schensted, C. E., "Electromagnetic and Acoustical Scattering from a Semi-Infinite Cone," *Journal of Applied Physics*, Vol. 26, No. 3, 1955, pp. 309–313.

[72] Glassner, A. S., *An Introduction to Ray Tracing*, Academic Press, Inc, 1989.

[73] Ahtye, W. and McCulley, G., "Evaluation of Approximate Methods for the Prediction of Noise Shielding by Airframe Components," *NASA/TP-1980-1004*, 1980.

[74] Balsa, T. F., Gliebe, P. R., Kantola, R. A., Mani, R., and Stringas, E. J., "High Velocity Jet Noise Source Location and Reduction. Task 2. Theoretical Developments and Basic Experiments," *Defense Technical Information Center*, 1978.

[75] Goldstein, M. E., *Aeroacoustics*, McGraw-Hill, New York, 1976.

[76] Goldstein, M. E., "The Low Frequency Sound from Multipole Sources in Axisymmetric Shear Flows - Part II," *Journal of Fluid Mechanics*, Vol. 75, No. 1, 1976, pp. 17–29.

[77] Goldstein, M. E., "The Low Frequency Sound from Multipole Sources in Axisymmetric Shear Flows, with Applications to Jet Noise," *Journal of Fluid Mechanics*, Vol. 70, No. 3, 1975, pp. 595–604.

[78] Heath, S. L., Brooks, T., Hutcheson, F., Doty, M. J., Haskin, H. H., Spalt, T., Bahr, C., Burley, C., Bartram, S., Humphreys, W., Lunsford, C. B., Popernack, T., Colbert, S., Hoad, D., Becker, L., Stead, D., Kuchta, D., and Yeh, L., "Hybrid Wing Body Aircraft Acoustic Test Preparations and Facility Upgrades," *28th AIAA Aerodynamic Measurement Technology, Ground Testing, and Flight Testing Conference, June 24 - 27, San Diego, California, AIAA Paper 2013-2623*, 2013.

[79] Zorumski, W. E., "Aircraft Noise Prediction Program. Theoretical Manual. Parts 1 and 2," *NASA TM 83199*, 1982.

[80] Lopes, L. V. and Burley, C. L., "Design of the Next Generation Aircraft Noise Prediction Program: ANOPP2," *17th AIAA/CEAS Aeroacoustics Conference, AIAA Paper 2011-2854*, 2011.

Appendix A

Aerodynamic Validation Set

This appendix includes steady RANS solutions compared with PIV data from the experiment of Bridges and Wernet[21]. The jet conditions are listed in Table A.1.

Table A.1: Jet Operating Conditions

Nozzle	Setpoint	NPR	TTR	M_a	M_j
SMC000	7	1.861	1.000	0.90	0.985
SMC000	23	1.102	1.814	0.50	0.376
SMC000	27	1.357	1.926	0.90	0.678
SMC000	29	1.888	2.118	1.33	1.00
SMC000	46	1.219	2.862	0.90	0.548
SMC016	11610	3.670	1.00	1.31	1.50
SMC016	11617	4.320	1.00	1.41	1.61

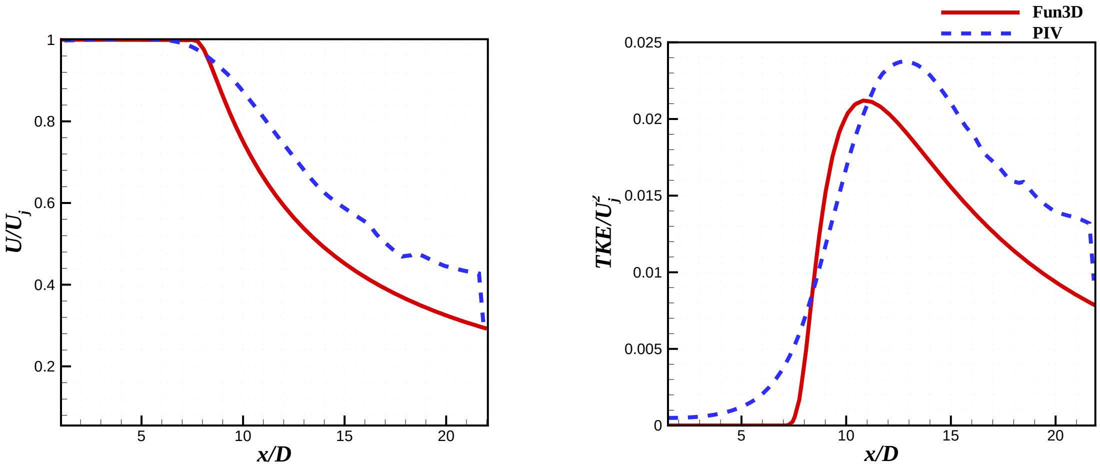

(a) $Velocity - Centerline$ (b) $TKE - Centerline$

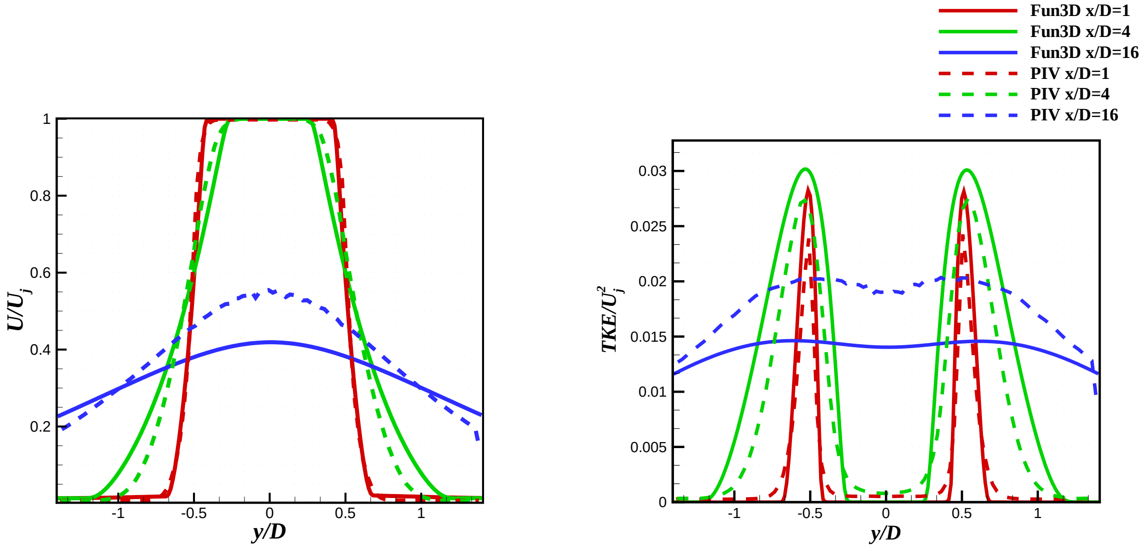

(c) $Velocity - Radial$ (d) $TKE - Radial$

Figure A.1: The (a) steady RANS streamwise velocity component and (b) TKE along the jet centerline ($y/D = 0$ & $z/D = 0$), and the (c) steady RANS streamwise velocity component and (d) TKE at $x/D = 1$, $x/D = 4$, and $x/D = 16$ compared with PIV data from the experiment of Bridges and Wernet[21]. The jet operates at $M_j = 0.985$ and $TTR = 1.00$ from the convergent SMC000 nozzle.

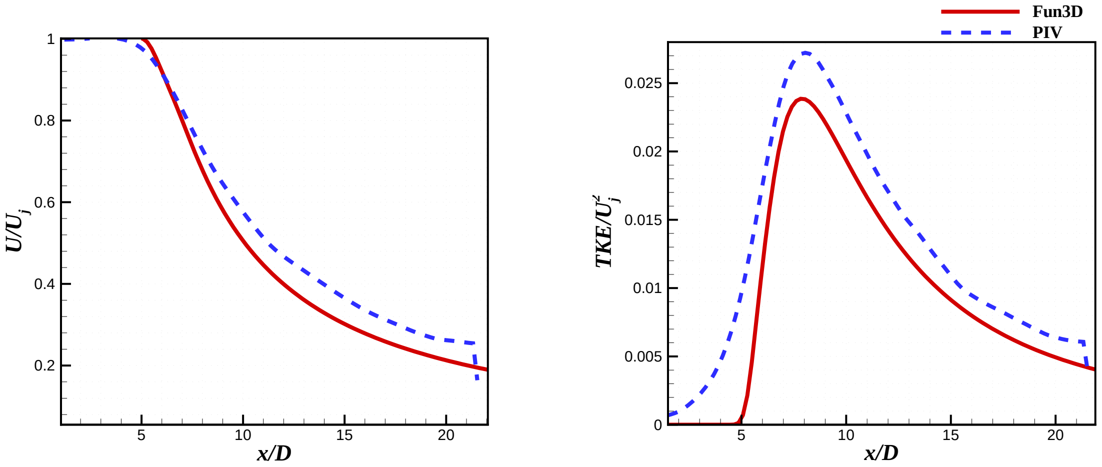

(a) $Velocity - Centerline$ (b) $TKE - Centerline$

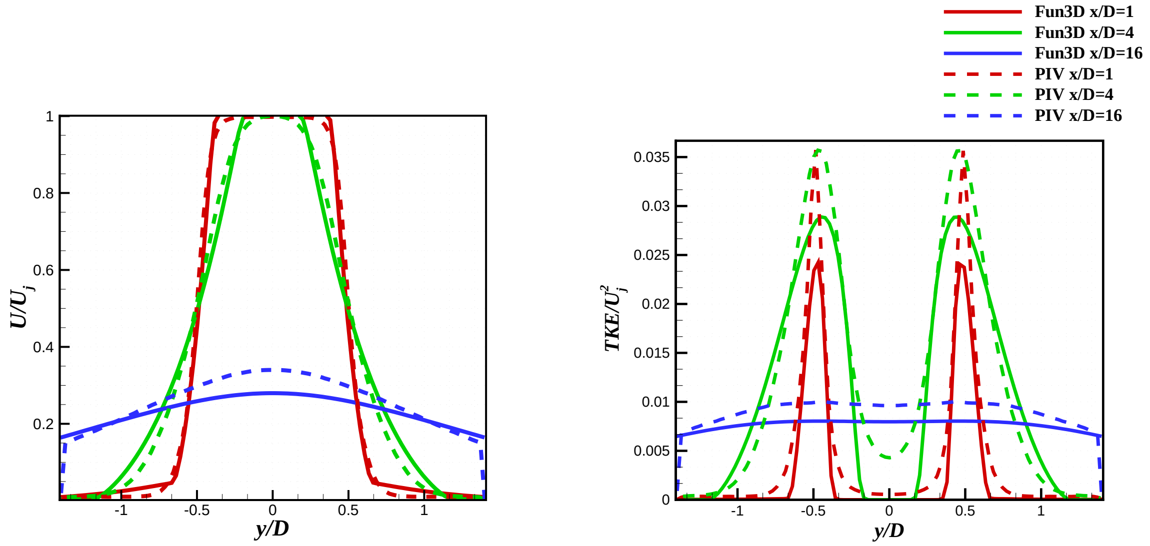

(c) $Velocity - Radial$ (d) $TKE - Radial$

Figure A.2: The (a) steady RANS streamwise velocity component and (b) TKE along the jet centerline ($y/D = 0$ & $z/D = 0$), and the (c) steady RANS streamwise velocity component and (d) TKE at $x/D = 1$, $x/D = 4$, and $x/D = 16$ compared with PIV data from the experiment of Bridges and Wernet[21]. The jet operates at $M_j = 0.376$ and $TTR = 1.814$ from the convergent SMC000 nozzle.

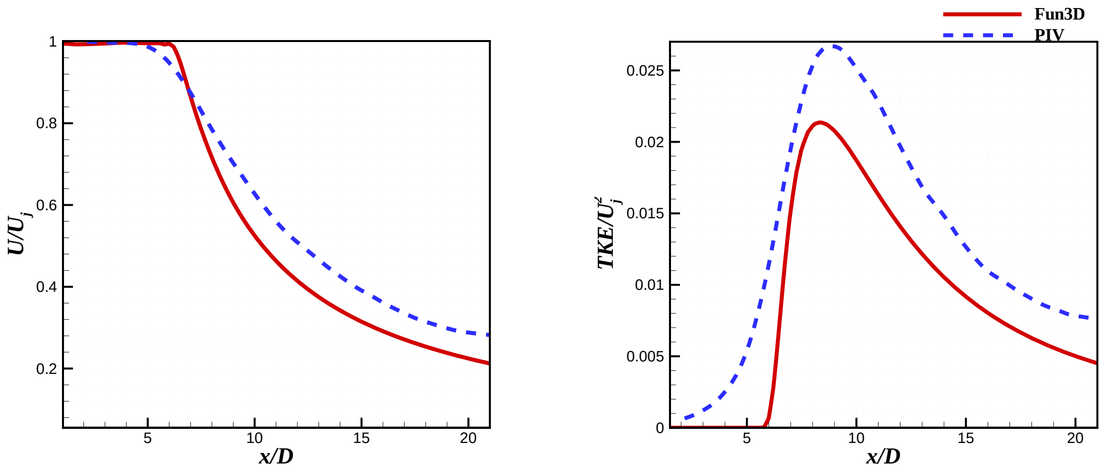

(a) $Velocity - Centerline$ (b) $TKE - Centerline$

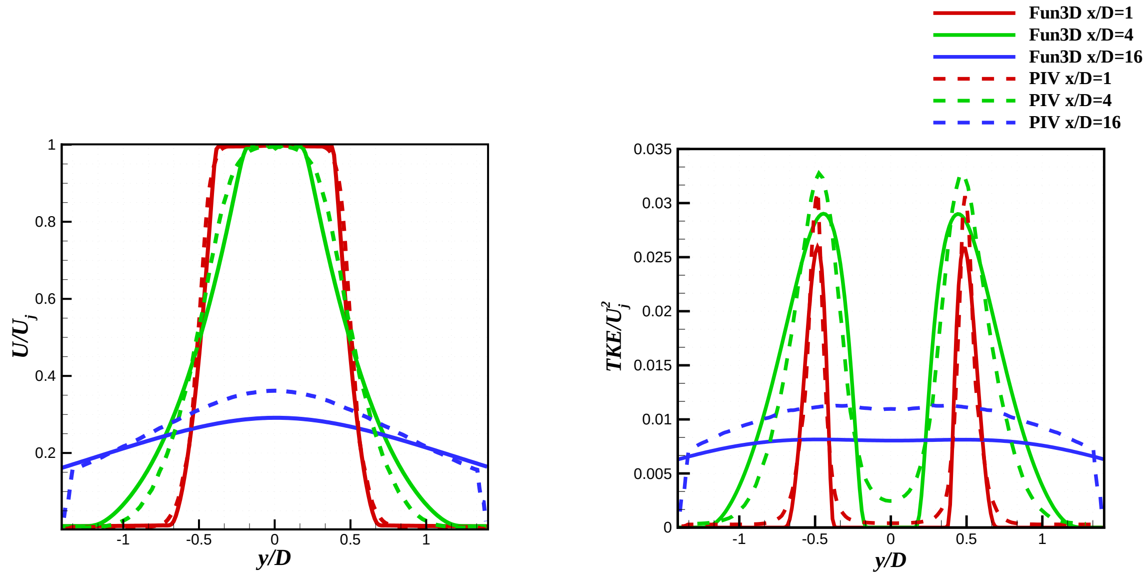

(c) $Velocity - Radial$ (d) $TKE - Radial$

Figure A.3: The (a) steady RANS streamwise velocity component and (b) TKE along the jet centerline ($y/D = 0$ & $z/D = 0$), and the (c) steady RANS streamwise velocity component and (d) TKE at $x/D = 1$, $x/D = 4$, and $x/D = 16$ compared with PIV data from the experiment of Bridges and Wernet[21]. The jet operates at $M_j = 0.678$ and $TTR = 1.926$ from the convergent SMC000 nozzle.

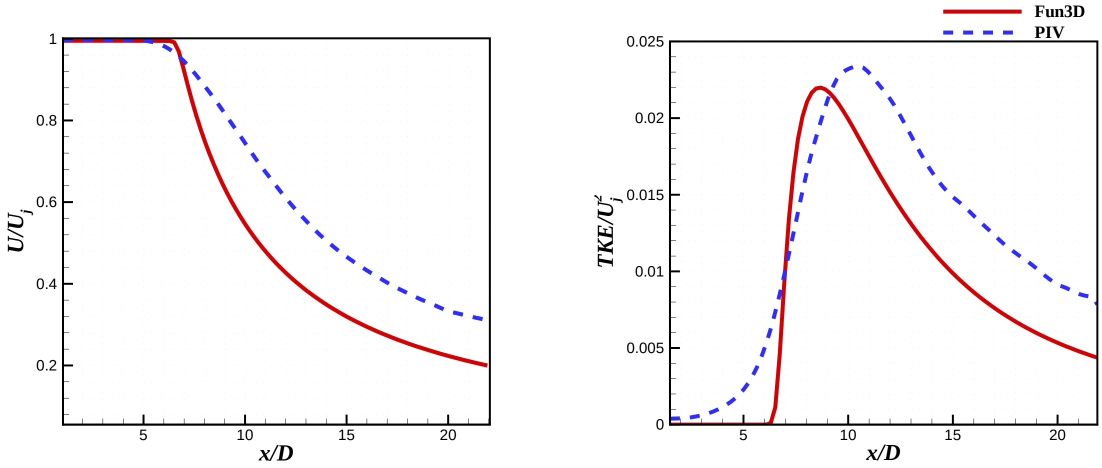

(a) $Velocity - Centerline$ (b) $TKE - Centerline$

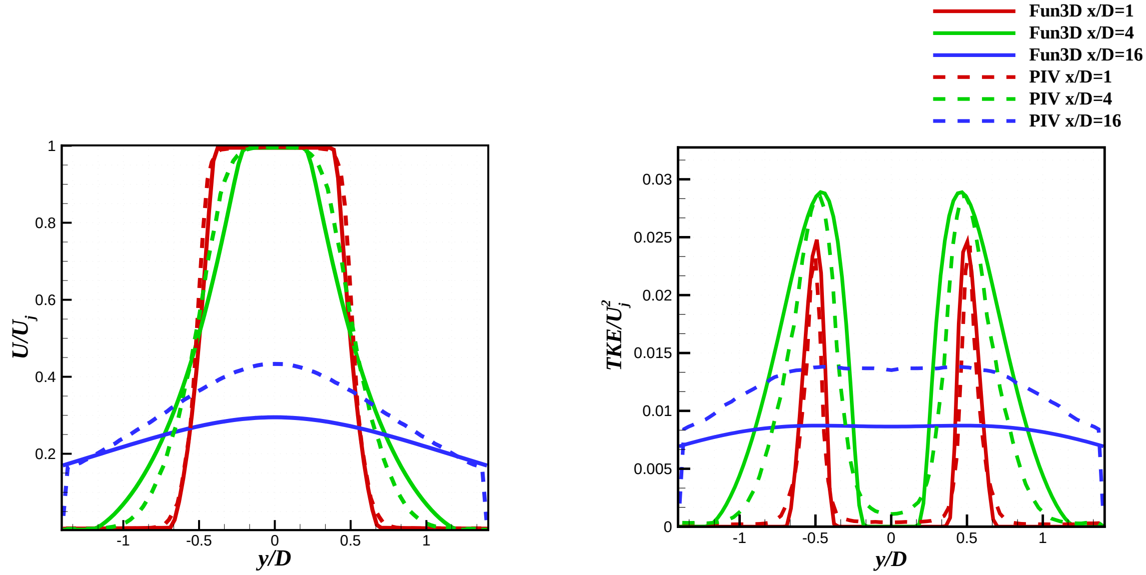

(c) $Velocity - Radial$ (d) $TKE - Radial$

Figure A.4: The (a) steady RANS streamwise velocity component and (b) TKE along the jet centerline ($y/D = 0$ & $z/D = 0$), and the (c) steady RANS streamwise velocity component and (d) TKE at $x/D = 1$, $x/D = 4$, and $x/D = 16$ compared with PIV data from the experiment of Bridges and Wernet[21]. The jet operates at $M_j = 1.00$ and $TTR = 2.118$ from the convergent SMC000 nozzle.

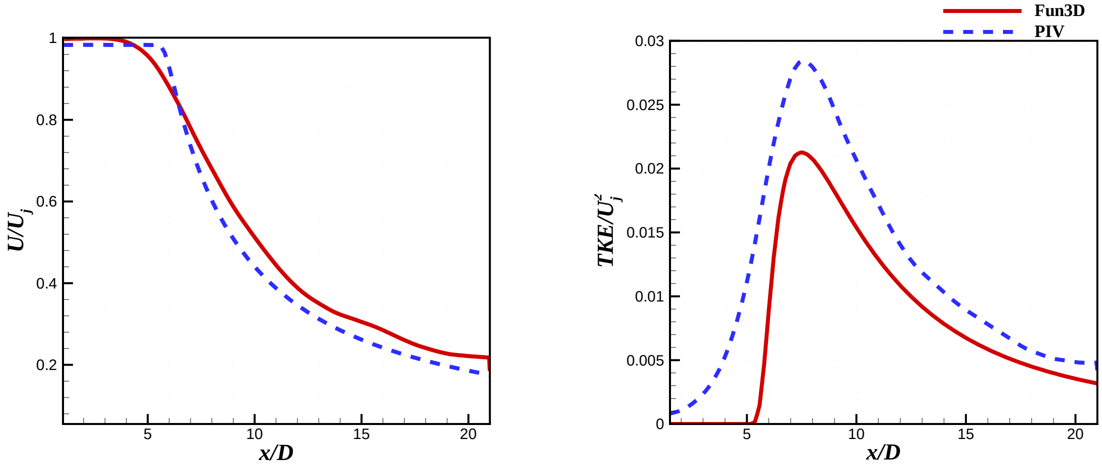

(a) $Velocity - Centerline$ (b) $TKE - Centerline$

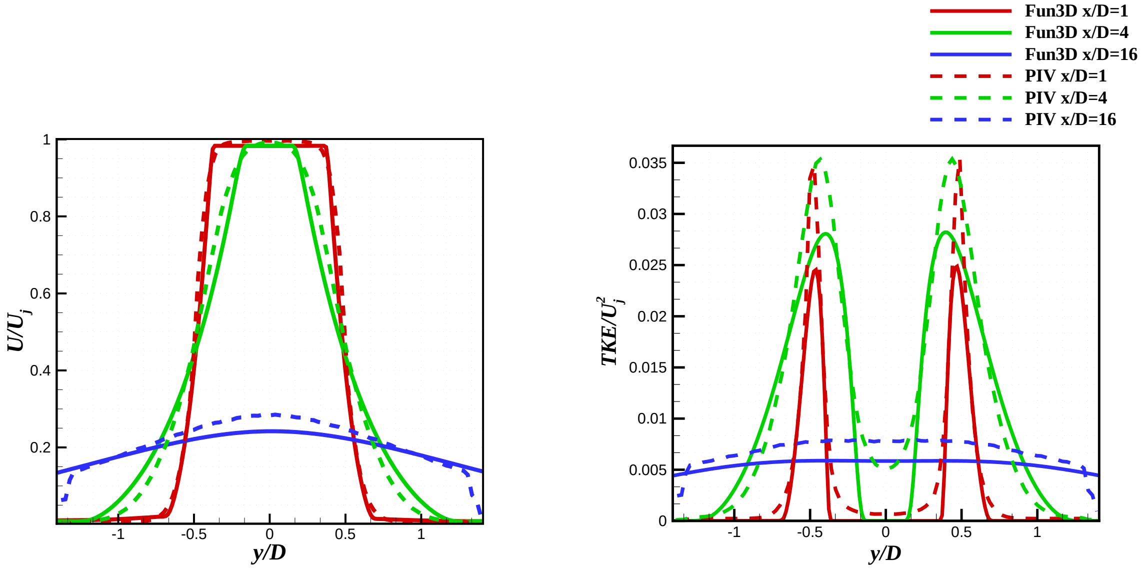

(c) $Velocity - Radial$ (d) $TKE - Radial$

Figure A.5: The (a) steady RANS streamwise velocity component and (b) TKE along the jet centerline ($y/D = 0$ & $z/D = 0$), and the (c) steady RANS streamwise velocity component and (d) TKE at $x/D = 1$, $x/D = 4$, and $x/D = 16$ compared with PIV data from the experiment of Bridges and Wernet[21]. The jet operates at $M_j = 0.548$ and $TTR = 2.862$ from the convergent SMC000 nozzle.

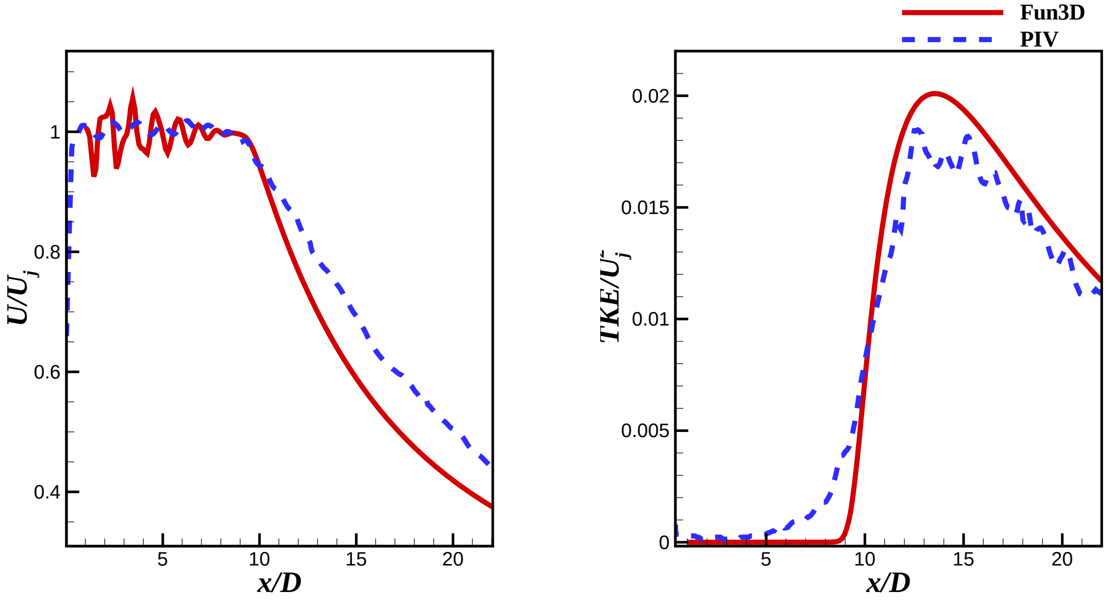

(a) $Velocity - Centerline$ (b) $TKE - Centerline$

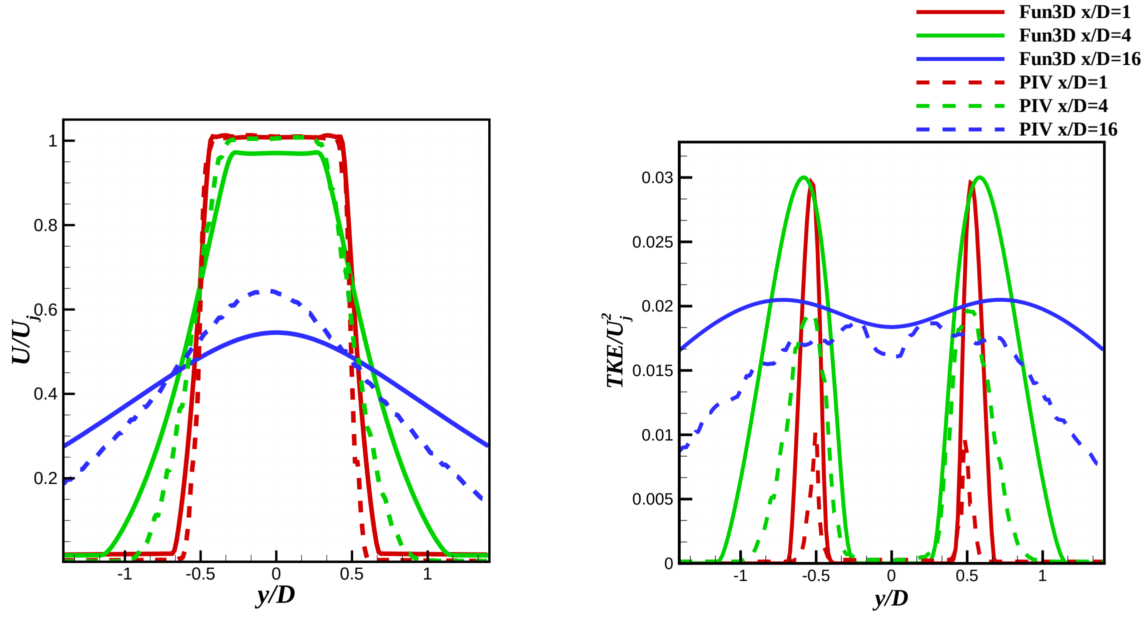

(c) $Velocity - Radial$ (d) $TKE - Radial$

Figure A.6: The (a) steady RANS streamwise velocity component and (b) TKE along the jet centerline ($y/D = 0$ & $z/D = 0$), and the (c) steady RANS streamwise velocity component and (d) TKE at $x/D = 1$, $x/D = 4$, and $x/D = 16$ compared with PIV data from the experiment of Bridges and Wernet[21]. The jet operates at $M_j = 1.50$ and $TTR = 1.00$ from the convergent SMC016 nozzle.

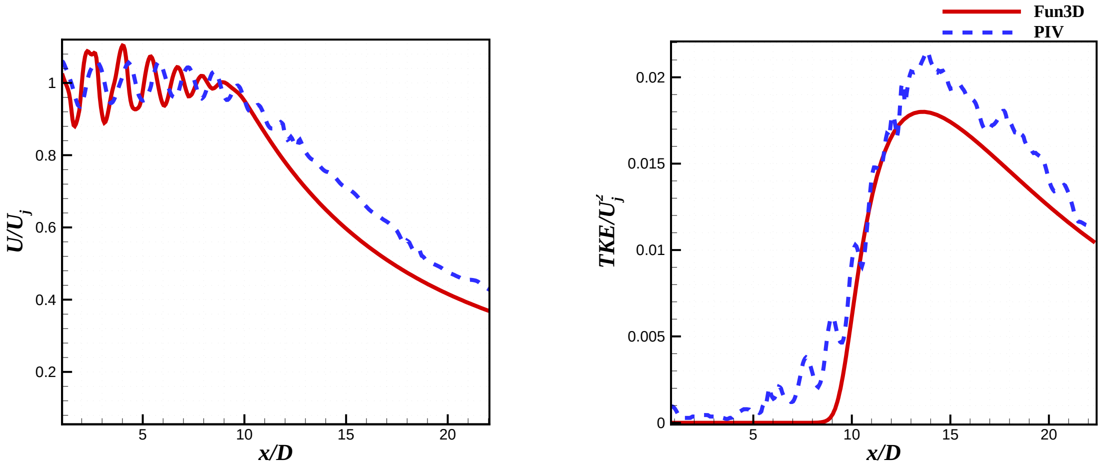

(a) $Velocity - Centerline$ (b) $TKE - Centerline$

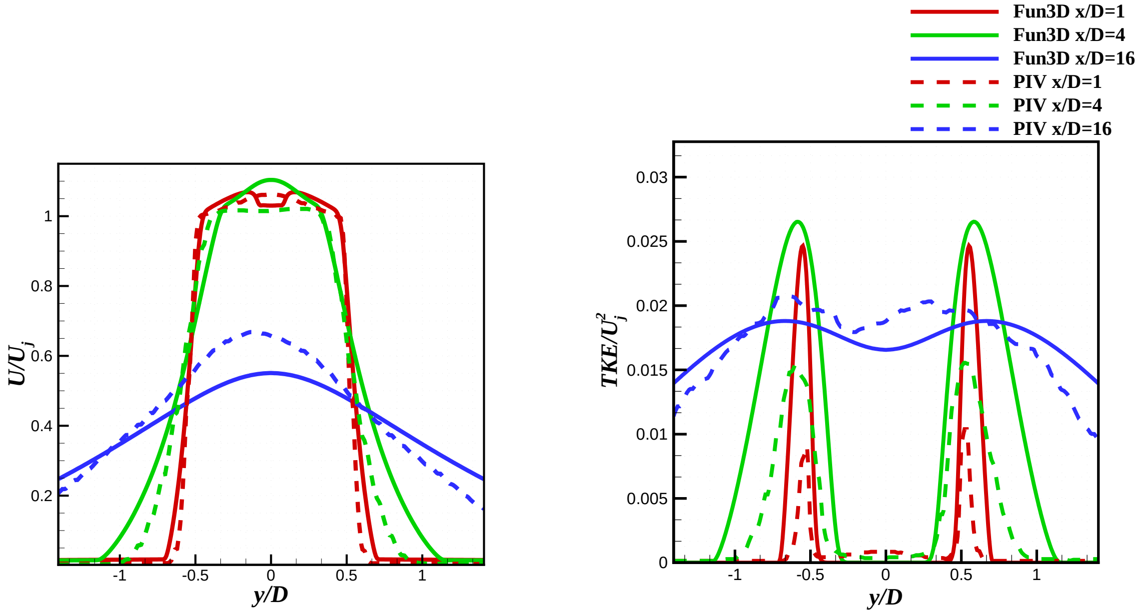

(c) $Velocity - Radial$ (d) $TKE - Radial$

Figure A.7: The (a) steady RANS streamwise velocity component and (b) TKE along the jet centerline ($y/D = 0$ & $z/D = 0$), and the (c) steady RANS streamwise velocity component and (d) TKE at $x/D = 1$, $x/D = 4$, and $x/D = 16$ compared with PIV data from the experiment of Bridges and Wernet[21]. The jet operates at $M_j = 1.61$ and $TTR = 1.00$ from the convergent SMC016 nozzle.

Appendix B

Jet Noise Validation Set

This appendix includes all jet noise predictions compared with experimental data from the JSIT experiment of Brown *et al.*[7]. The plate configurations and jet operating conditions are listed in Table B.1 and B.2.

Table B.1: Plate Locations

Axial Distance to Trailing Edge (x_p/D)	Radial Distance to Jet Centerline (y_p/D)
4	2,4,6,8,10
10	2,4,6,8,10
20	2,4,6,8,10

Table B.2: Jet Operating Conditions

Nozzle	Setpoint	NPR	TTR	M_a	M_j
SMC000	7	1.861	1.000	0.9	0.985
SMC000	27	1.357	1.814	0.9	0.678
SMC016	11606	2.748	1.000	1.128	1.29
SMC016	11610	3.670	1.000	1.31	1.5

B.1 Subsonic Heated Jet

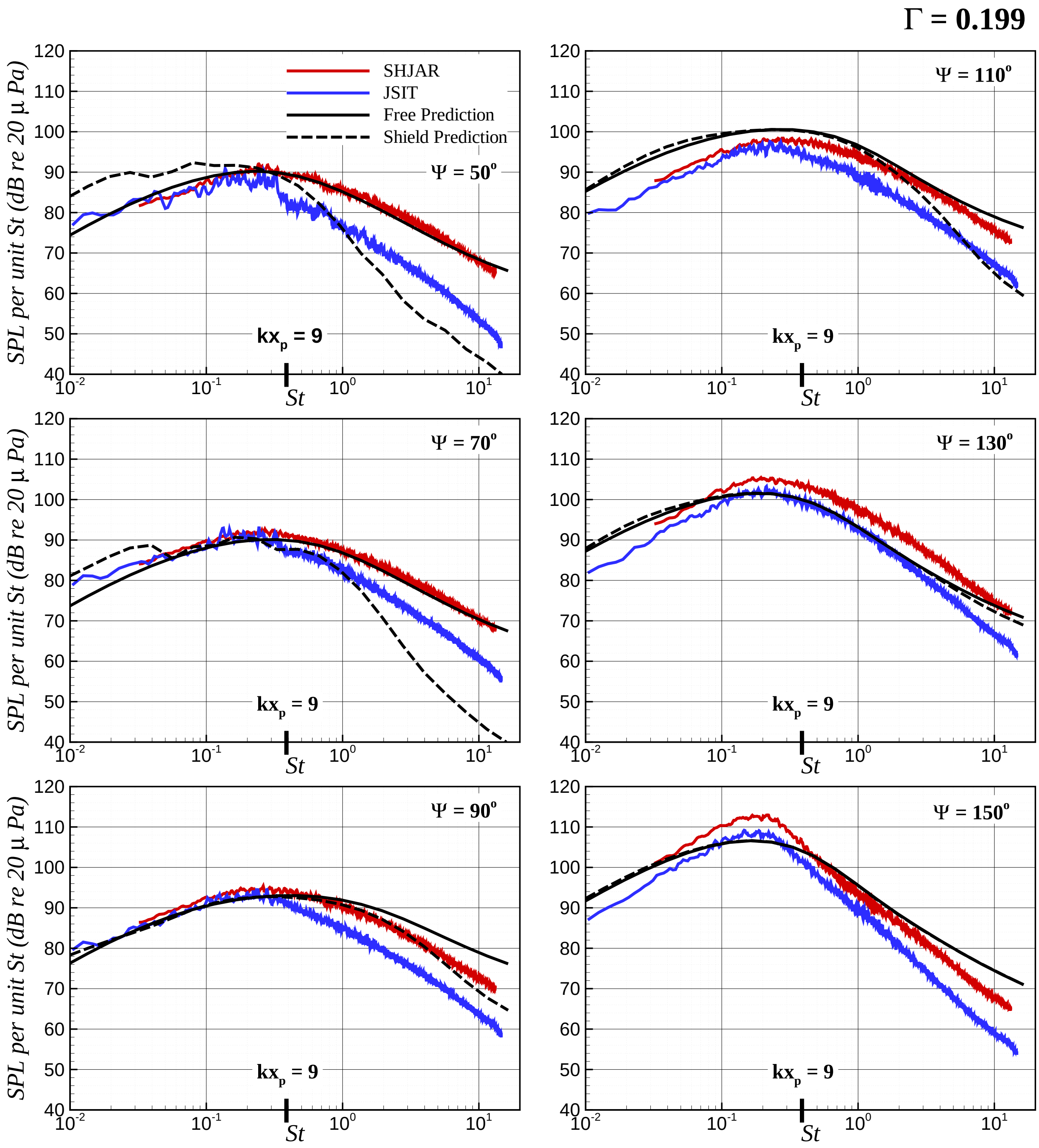

Figure B.1: The free-field and shielded prediction at $R/D = 100$ compared with experiment. The jet operates at $M_j = 0.678$ and $TTR = 1.814$ from the SMC000 nozzle with $D = 0.0508\ m$ and the plate is located at $x_p/D = 4$ and $y_p/D = 2$.

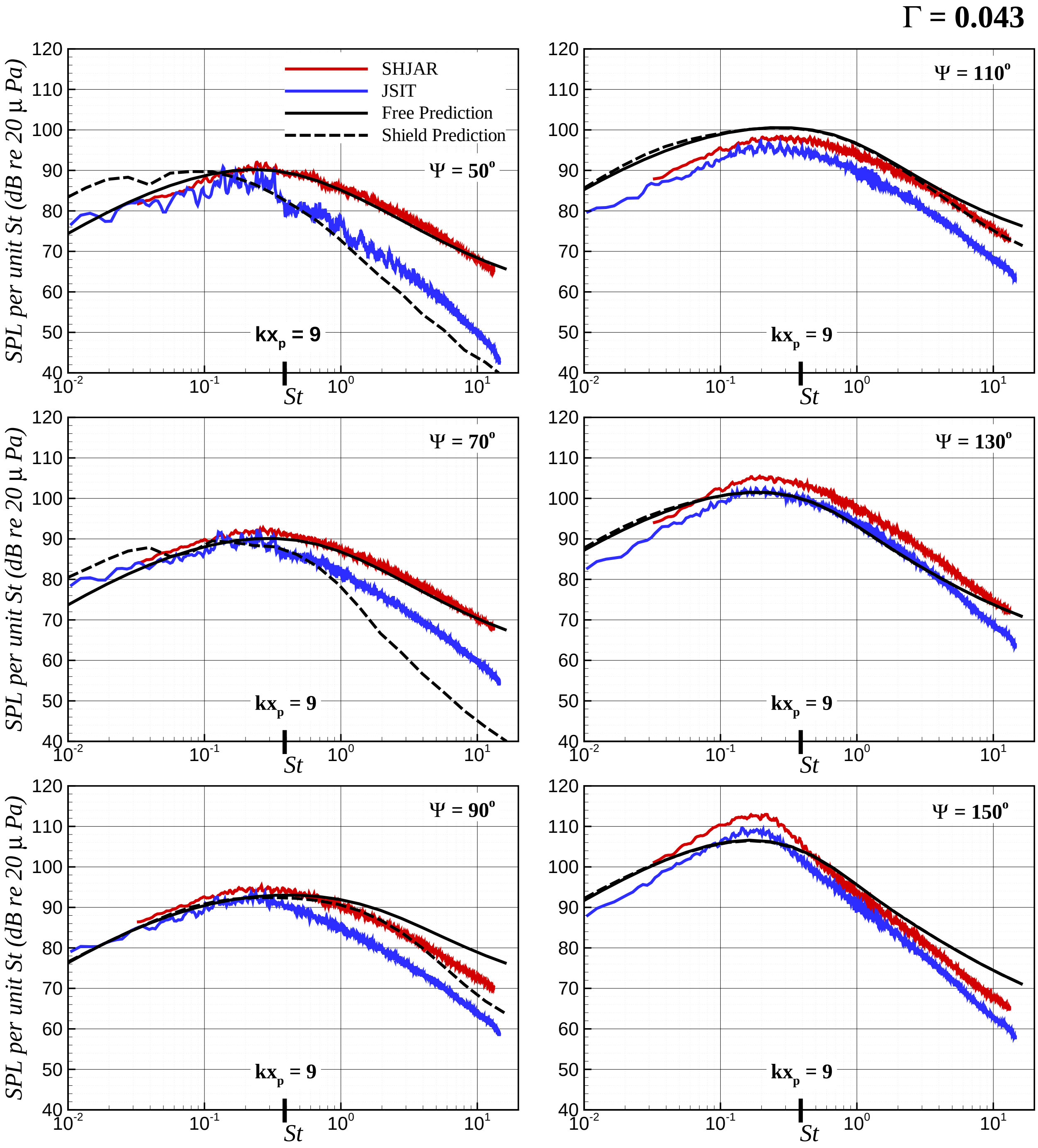

Figure B.2: The free-field and shielded prediction at $R/D = 100$ compared with experiment. The jet operates at $M_j = 0.678$ and $TTR = 1.926$ from the SMC000 nozzle with $D = 0.0508\ m$ and the plate is located at $x_p/D = 4$ and $y_p/D = 4$.

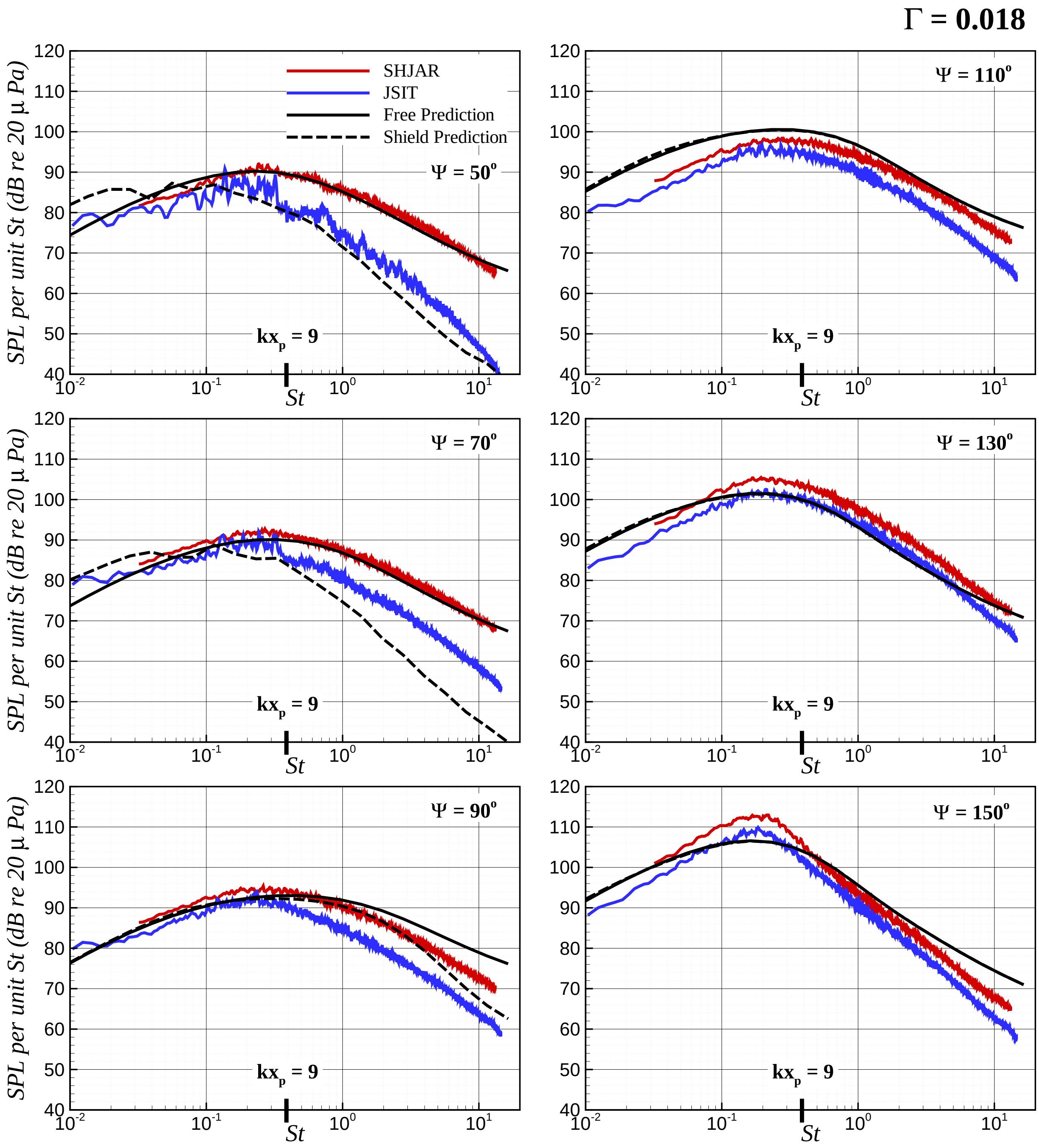

Figure B.3: The free-field and shielded prediction at $R/D = 100$ compared with experiment. The jet operates at $M_j = 0.678$ and $TTR = 1.926$ from the SMC000 nozzle with $D = 0.0508\ m$ and the plate is located at $x_p/D = 4$ and $y_p/D = 6$.

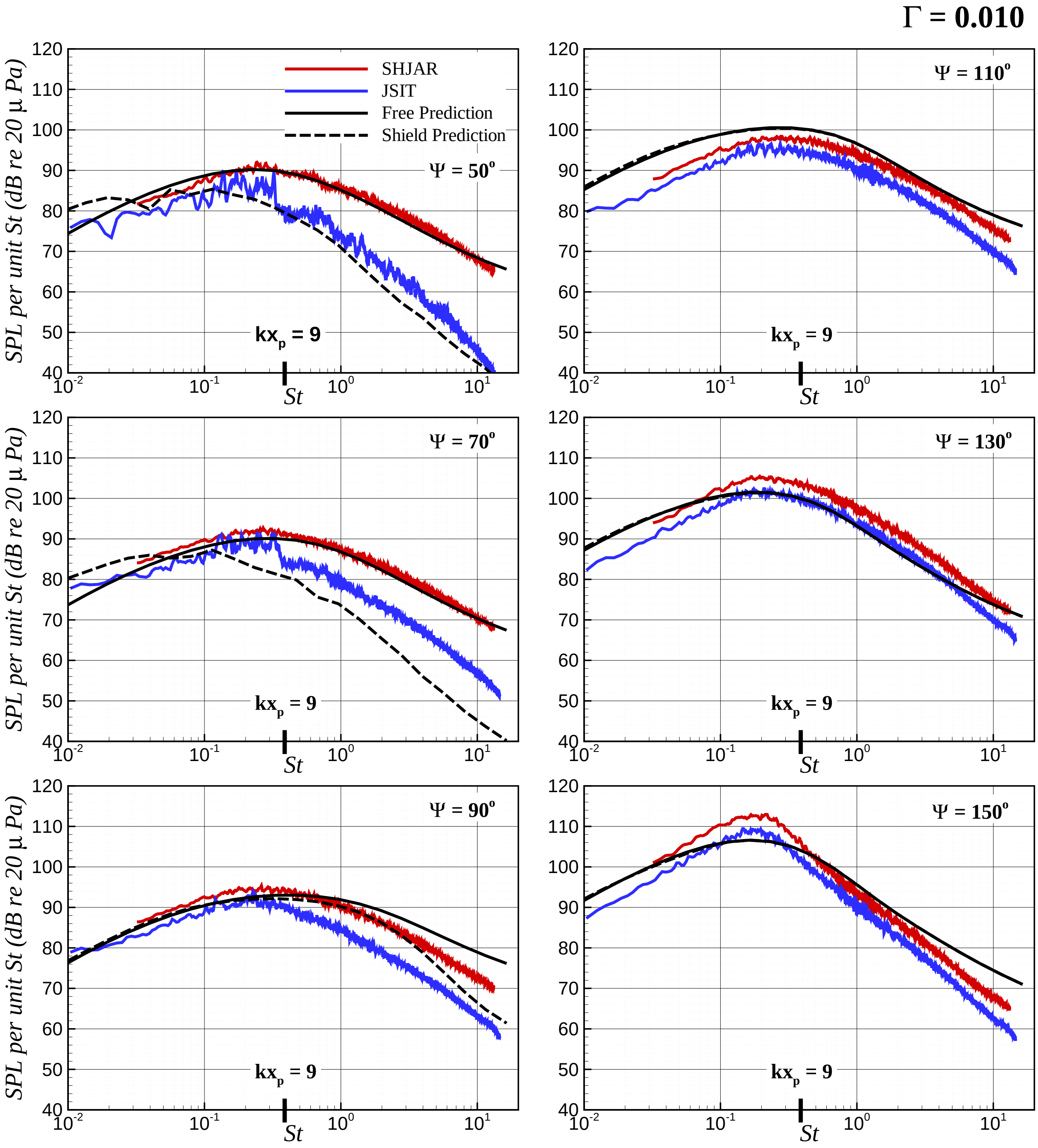

Figure B.4: The free-field and shielded prediction at $R/D = 100$ compared with experiment. The jet operates at $M_j = 0.678$ and $TTR = 1.926$ from the SMC000 nozzle with $D = 0.0508\ m$ and the plate is located at $x_p/D = 4$ and $y_p/D = 8$.

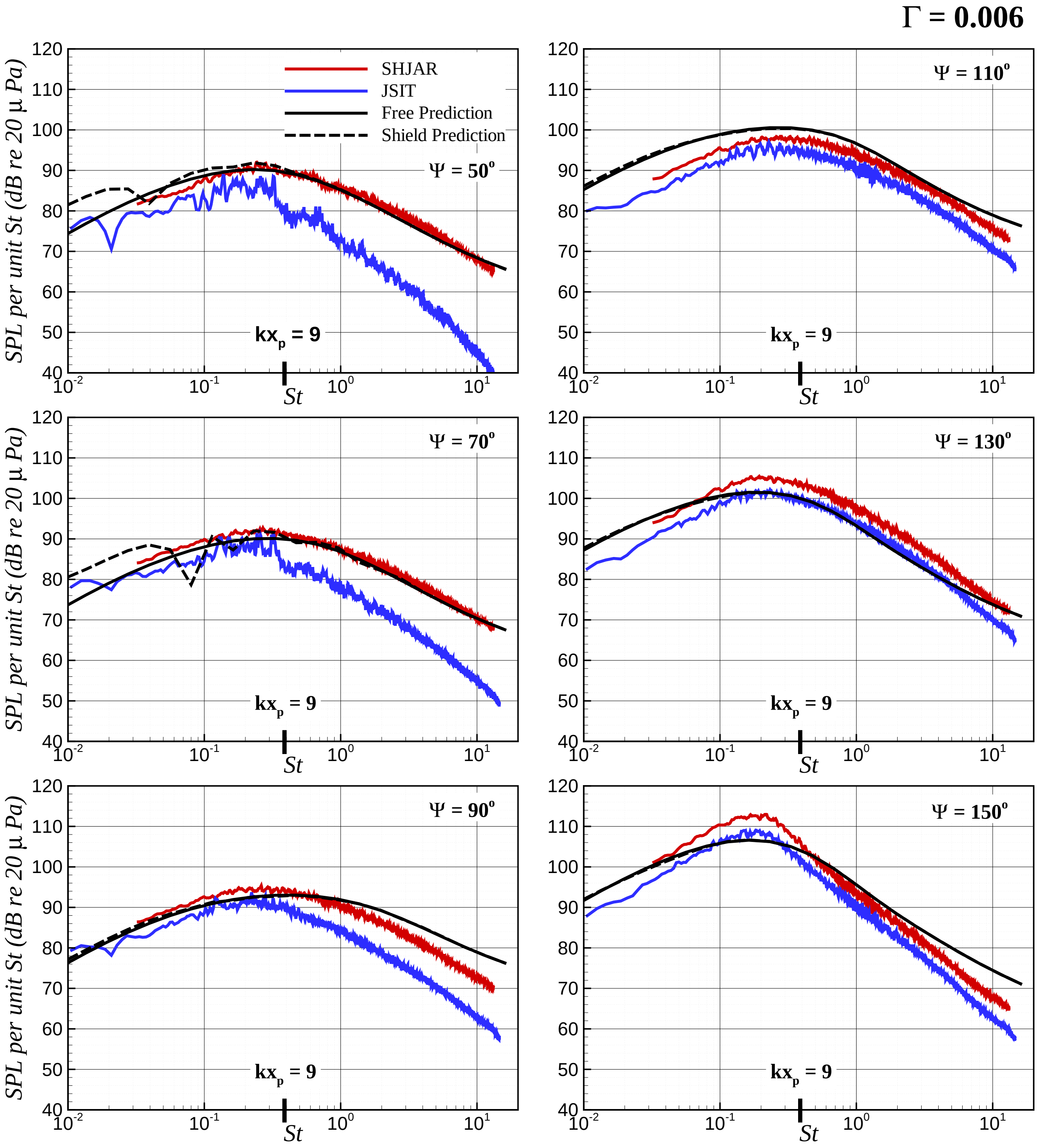

Figure B.5: The free-field and shielded prediction at $R/D = 100$ compared with experiment. The jet operates at $M_j = 0.678$ and $TTR = 1.926$ from the SMC000 nozzle with $D = 0.0508\ m$ and the plate is located at $x_p/D = 4$ and $y_p/D = 10$.

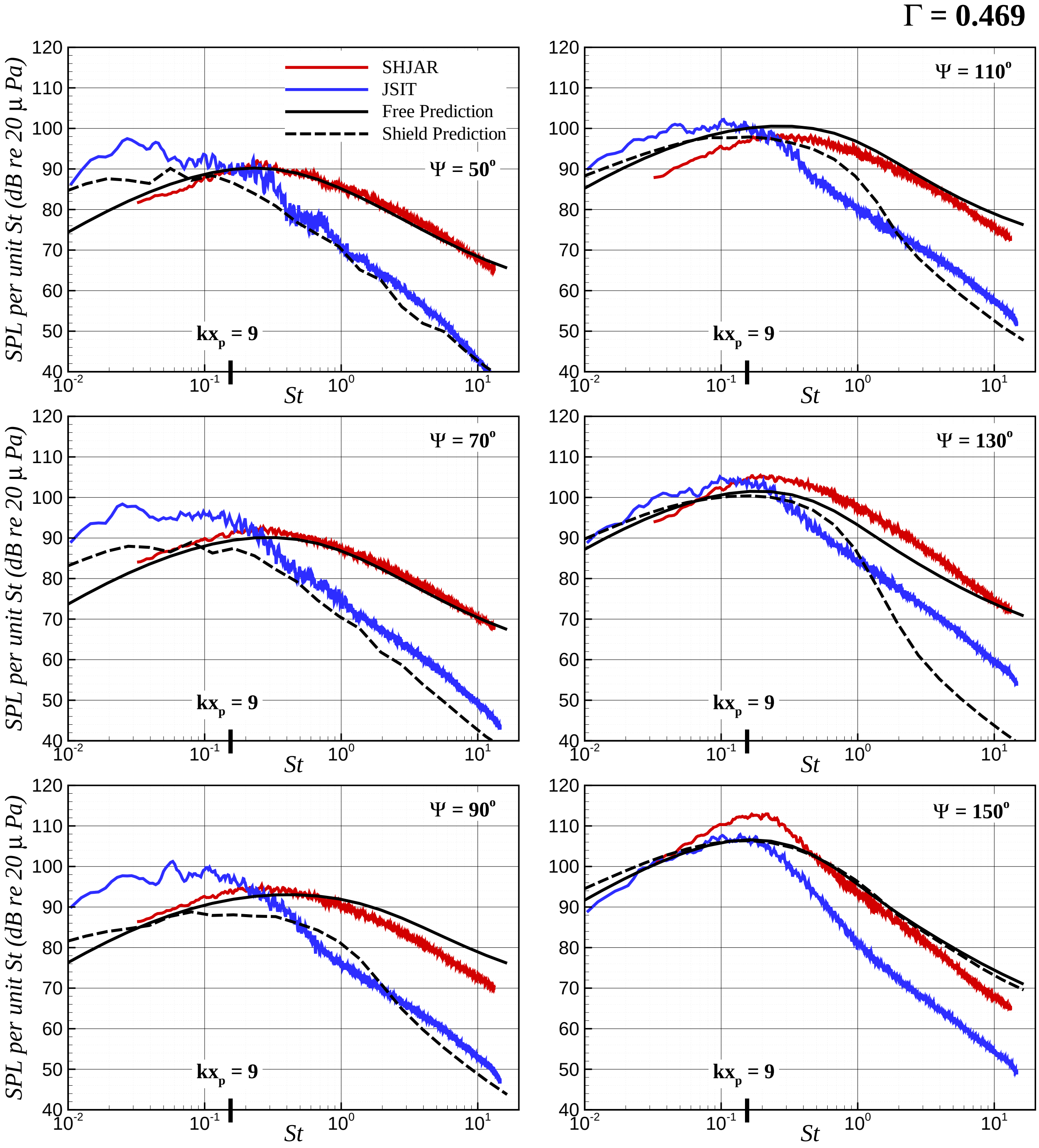

Figure B.6: The free-field and shielded prediction at $R/D = 100$ compared with experiment. The jet operates at $M_j = 0.678$ and $TTR = 1.926$ from the SMC000 nozzle with $D = 0.0508\ m$ and the plate is located at $x_p/D = 10$ and $y_p/D = 2$.

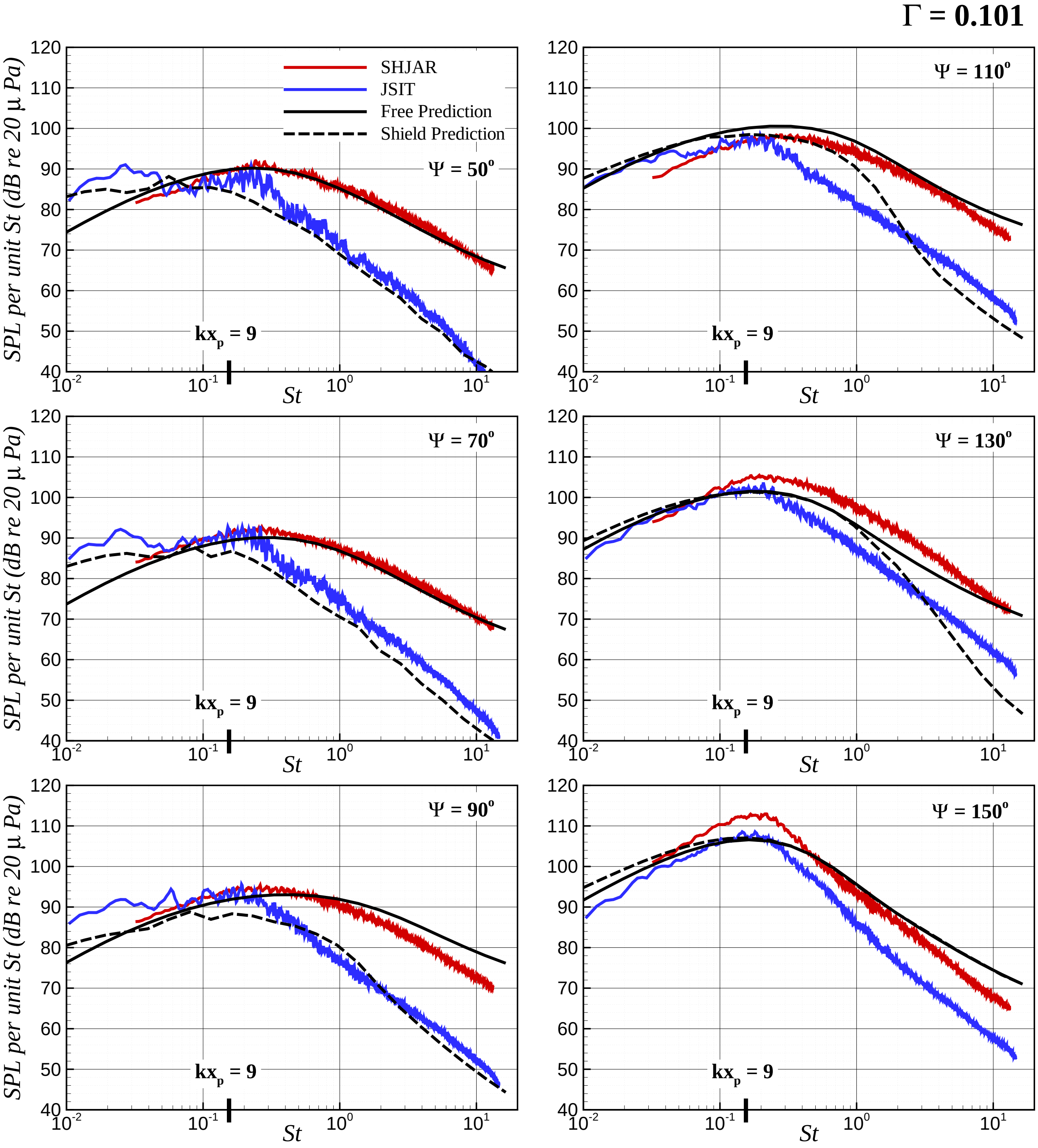

Figure B.7: The free-field and shielded prediction at $R/D = 100$ compared with experiment. The jet operates at $M_j = 0.678$ and $TTR = 1.926$ from the SMC000 nozzle with $D = 0.0508\ m$ and the plate is located at $x_p/D = 10$ and $y_p/D = 4$.

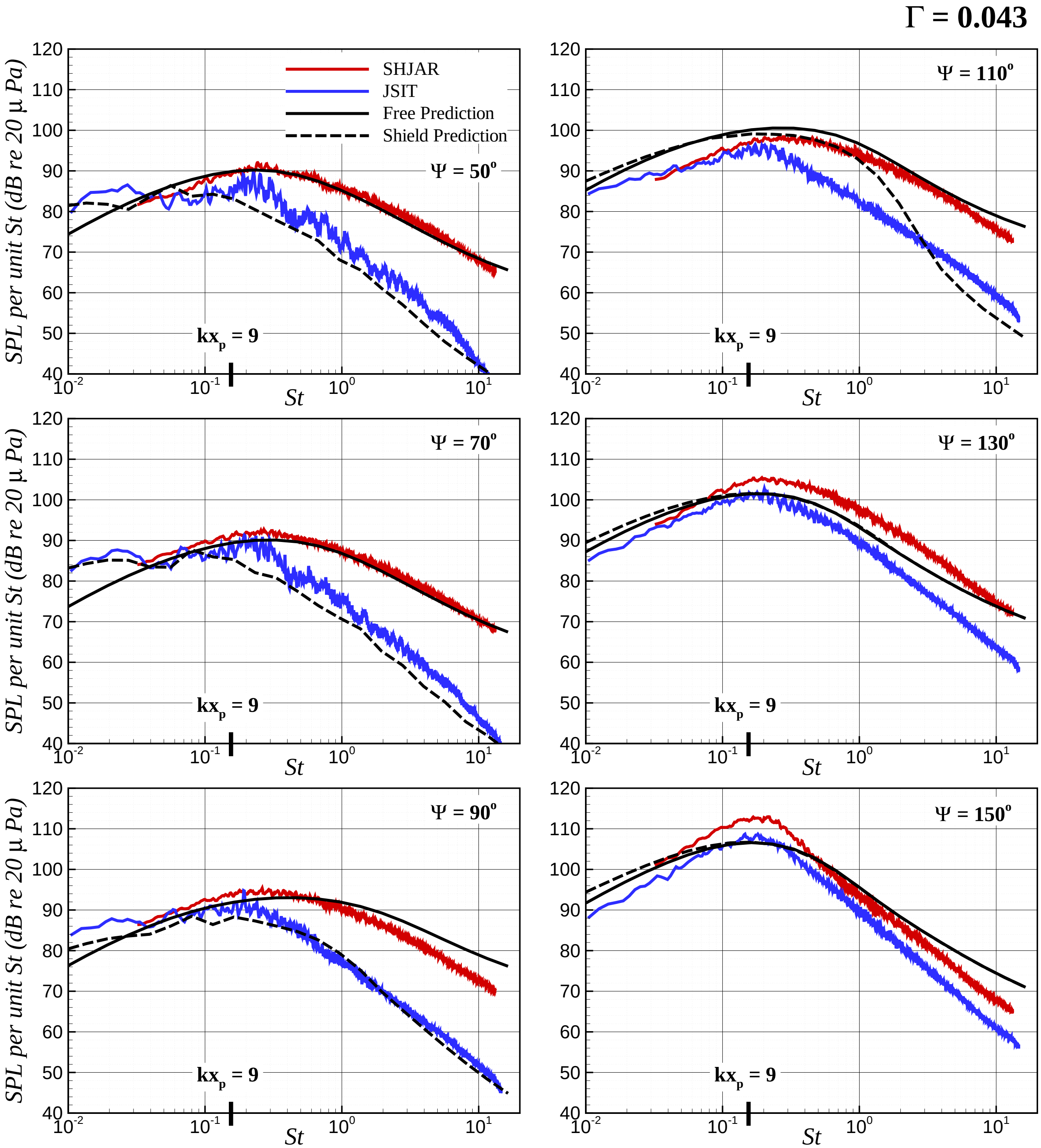

Figure B.8: The free-field and shielded prediction at $R/D = 100$ compared with experiment. The jet operates at $M_j = 0.678$ and $TTR = 1.926$ from the SMC000 nozzle with $D = 0.0508\ m$ and the plate is located at $x_p/D = 10$ and $y_p/D = 6$.

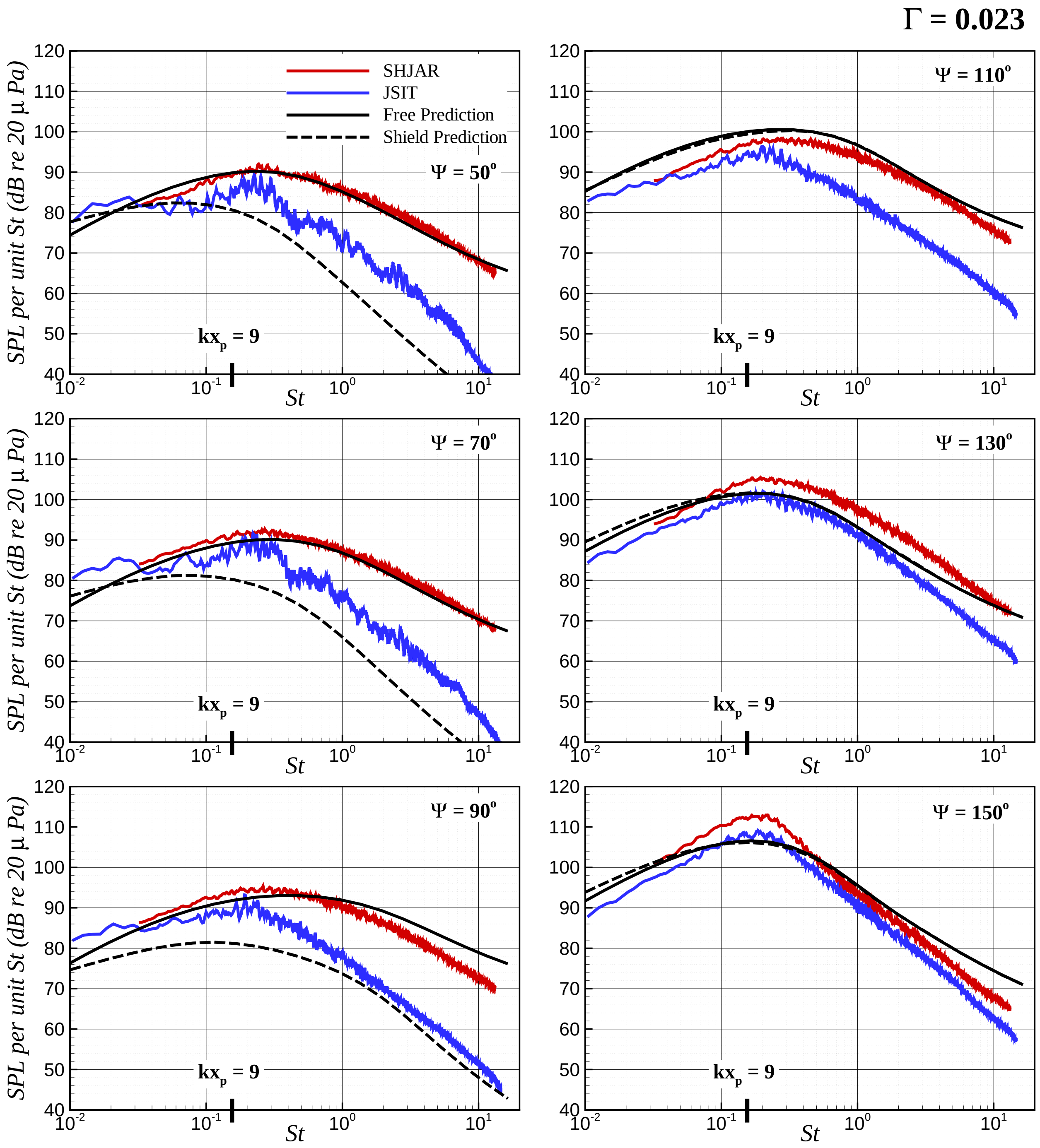

Figure B.9: The free-field and shielded prediction at $R/D = 100$ compared with experiment. The jet operates at $M_j = 0.678$ and $TTR = 1.926$ from the SMC000 nozzle with $D = 0.0508\ m$ and the plate is located at $x_p/D = 10$ and $y_p/D = 8$.

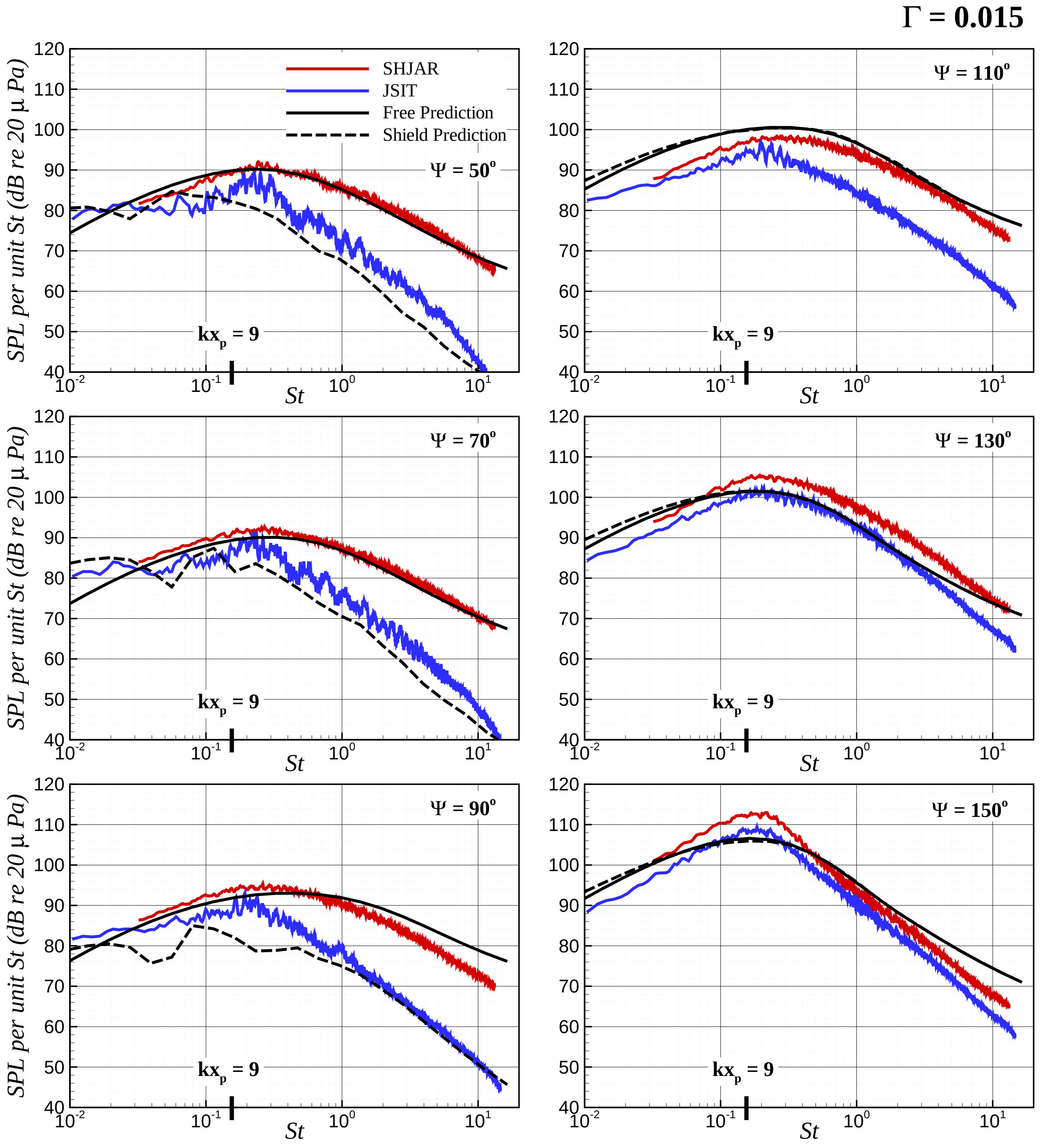

Figure B.10: The free-field and shielded prediction at $R/D = 100$ compared with experiment. The jet operates at $M_j = 0.678$ and $TTR = 1.926$ from the SMC000 nozzle with $D = 0.0508\ m$ and the plate is located at $x_p/D = 10$ and $y_p/D = 10$.

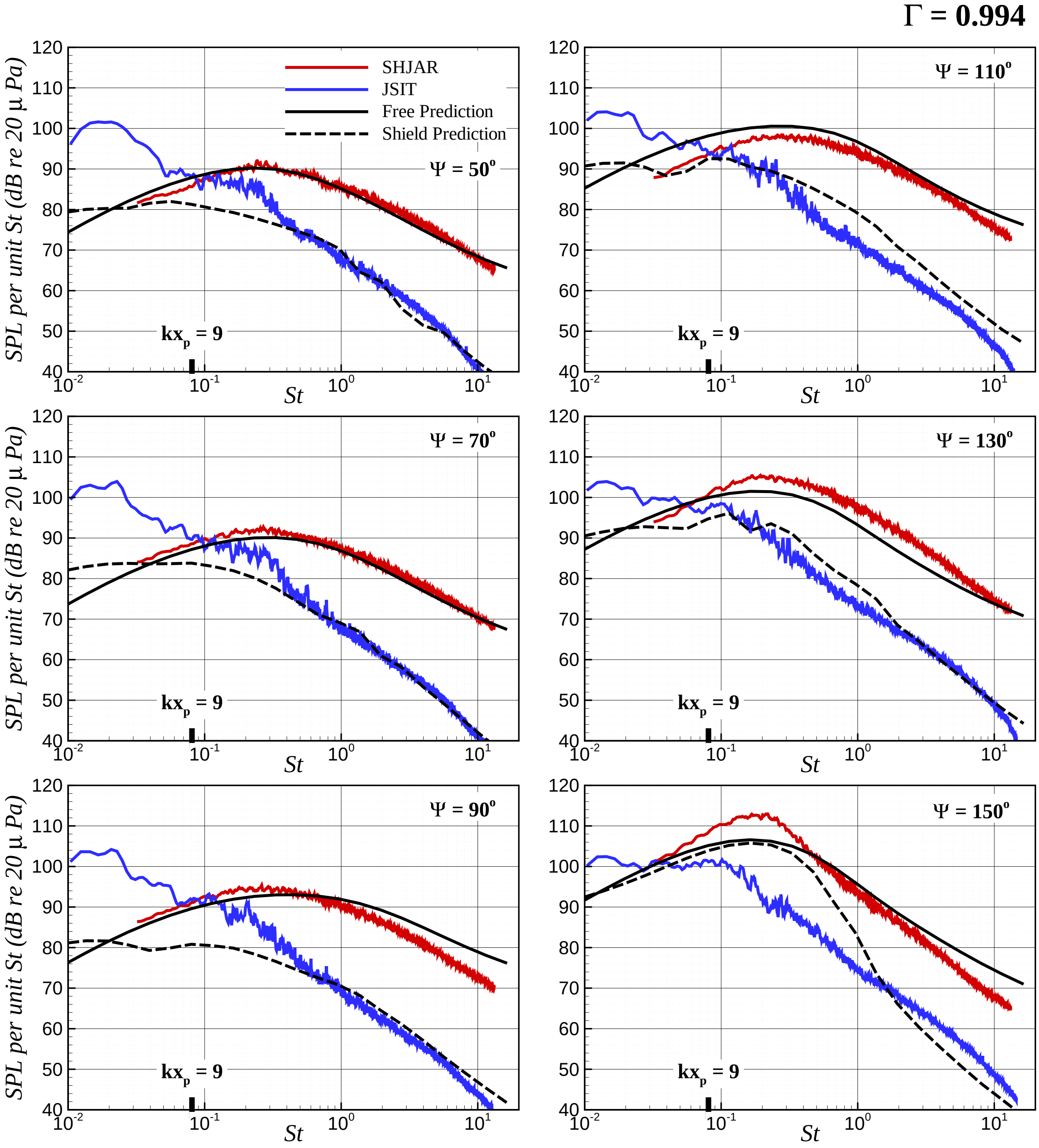

Figure B.11: The free-field and shielded prediction at $R/D = 100$ compared with experiment. The jet operates at $M_j = 0.678$ and $TTR = 1.926$ from the SMC000 nozzle with $D = 0.0508\ m$ and the plate is located at $x_p/D = 20$ and $y_p/D = 2$.

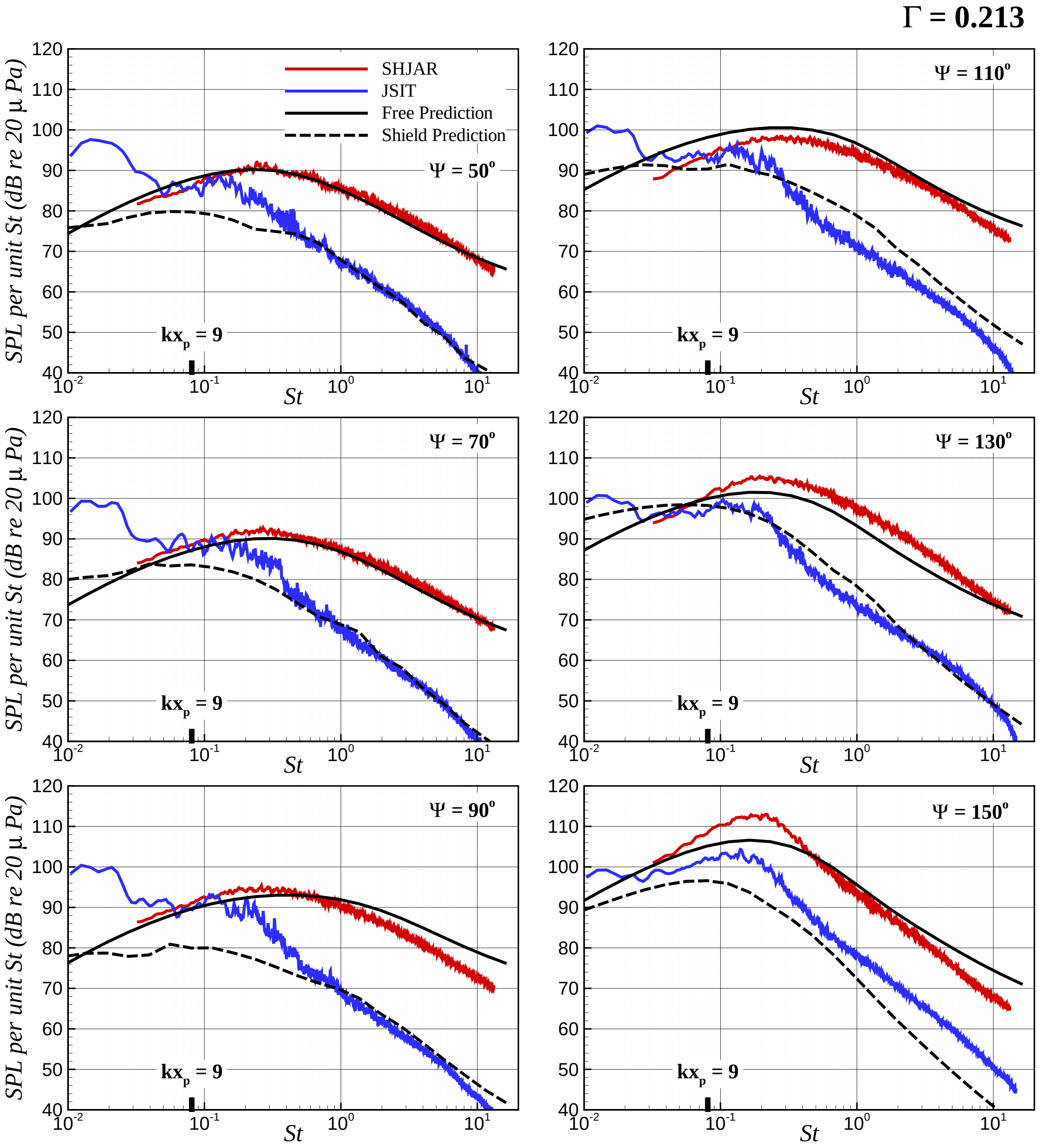

Figure B.12: The free-field and shielded prediction at $R/D = 100$ compared with experiment. The jet operates at $M_j = 0.678$ and $TTR = 1.926$ from the SMC000 nozzle with $D = 0.0508\ m$ and the plate is located at $x_p/D = 20$ and $y_p/D = 4$.

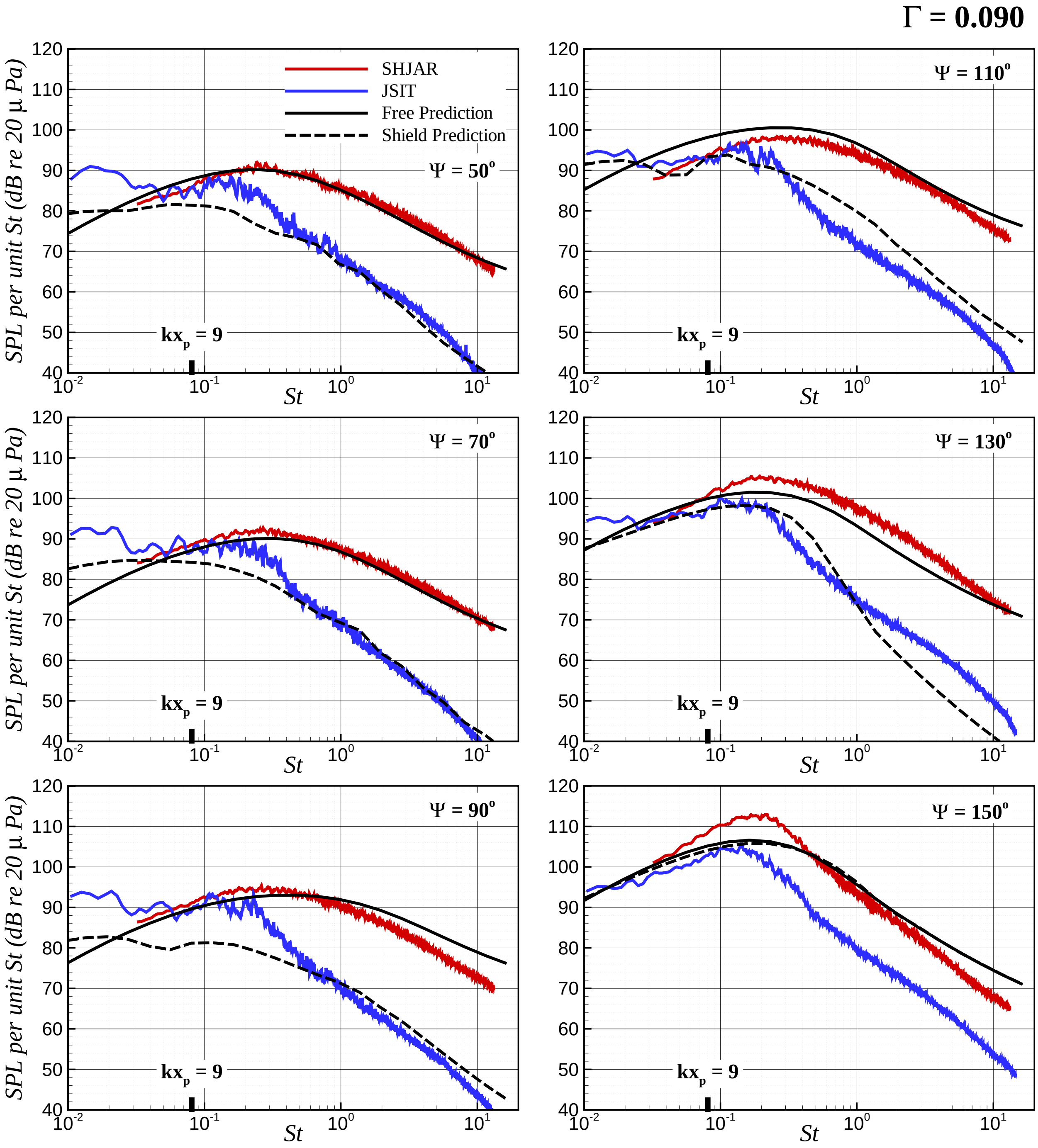

Figure B.13: The free-field and shielded prediction at $R/D = 100$ compared with experiment. The jet operates at $M_j = 0.678$ and $TTR = 1.926$ from the SMC000 nozzle with $D = 0.0508\ m$ and the plate is located at $x_p/D = 20$ and $y_p/D = 6$.

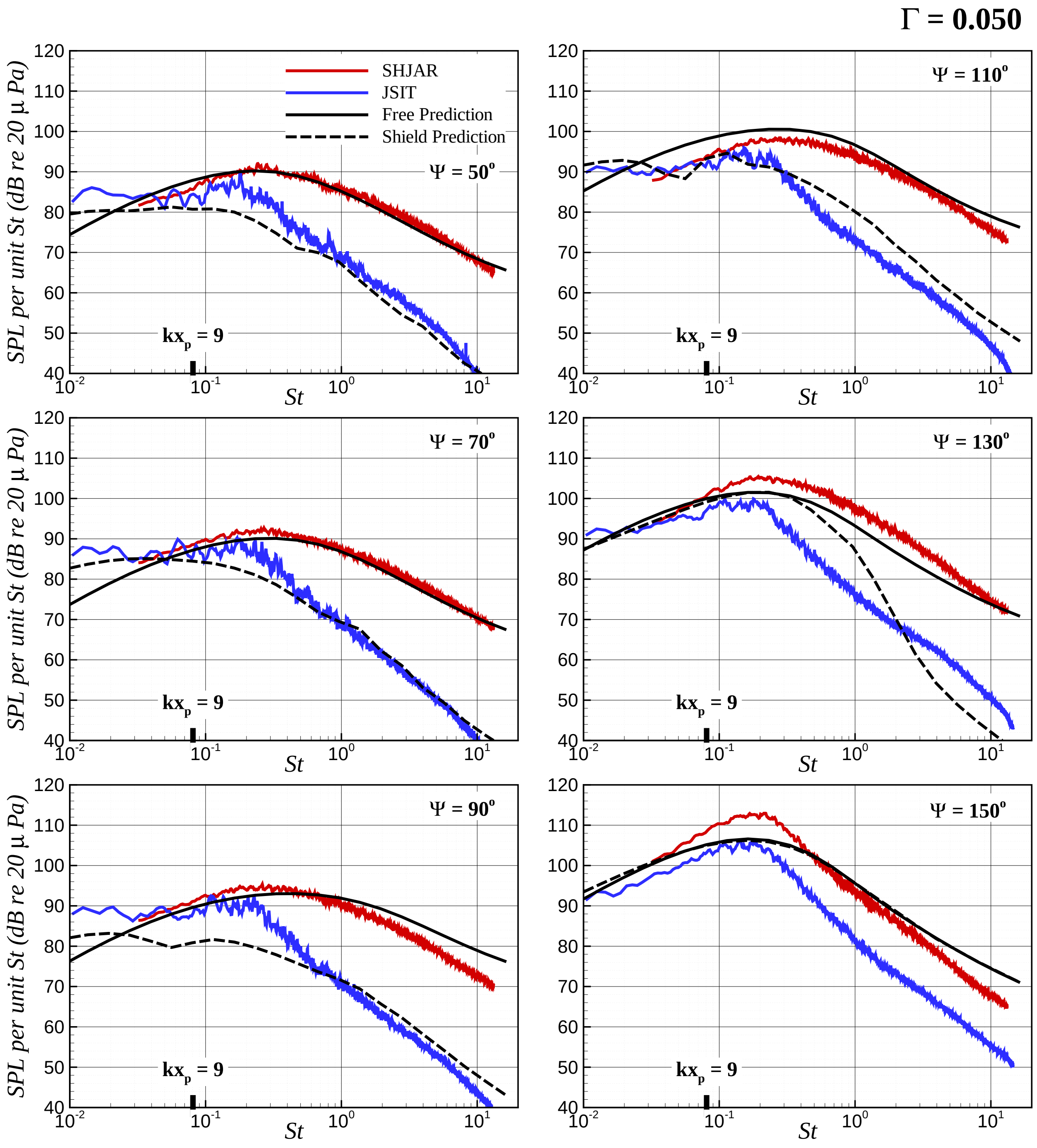

Figure B.14: The free-field and shielded prediction at $R/D = 100$ compared with experiment. The jet operates at $M_j = 0.678$ and $TTR = 1.926$ from the SMC000 nozzle with $D = 0.0508\ m$ and the plate is located at $x_p/D = 20$ and $y_p/D = 8$.

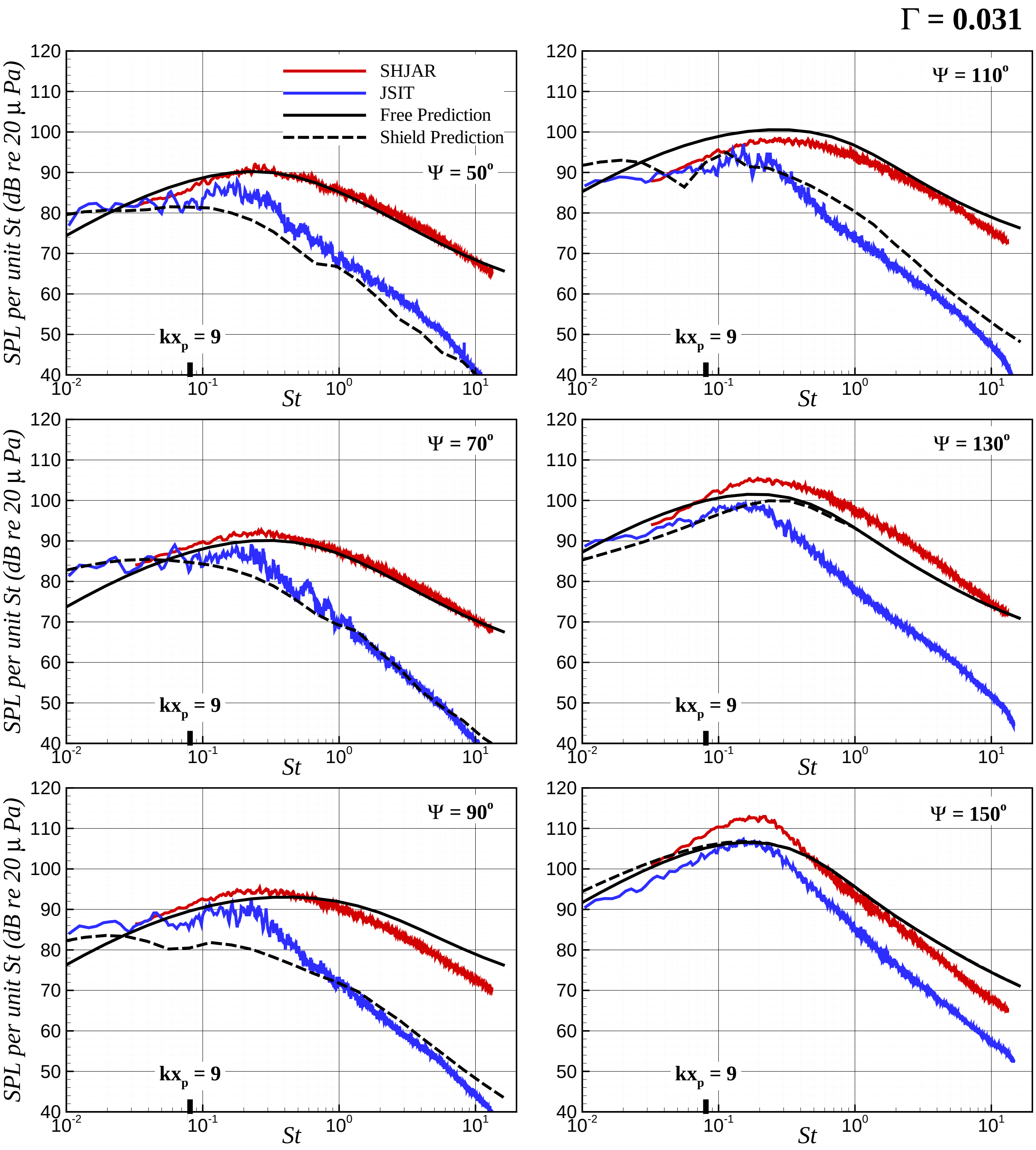

Figure B.15: The free-field and shielded prediction at $R/D = 100$ compared with experiment. The jet operates at $M_j = 0.678$ and $TTR = 1.926$ from the SMC000 nozzle with $D = 0.0508\ m$ and the plate is located at $x_p/D = 20$ and $y_p/D = 10$.

B.2 Subsonic Cold Jet

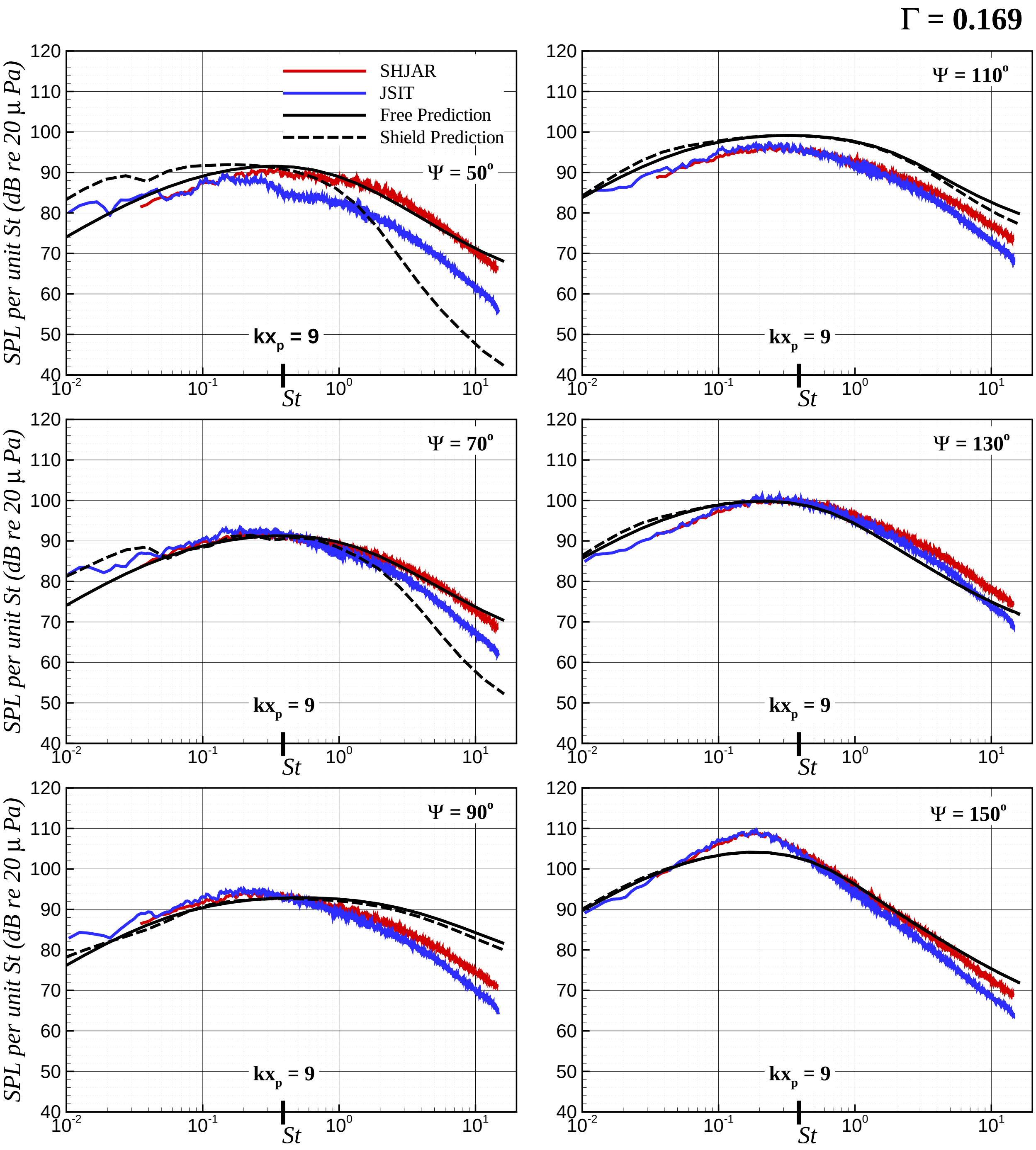

Figure B.16: The free-field and shielded prediction at $R/D = 100$ compared with experiment. The jet operates at $M_j = 0.985$ and $TTR = 1.00$ from the SMC000 nozzle with $D = 0.0508\,m$ and the plate is located at $x_p/D = 4$ and $y_p/D = 2$.

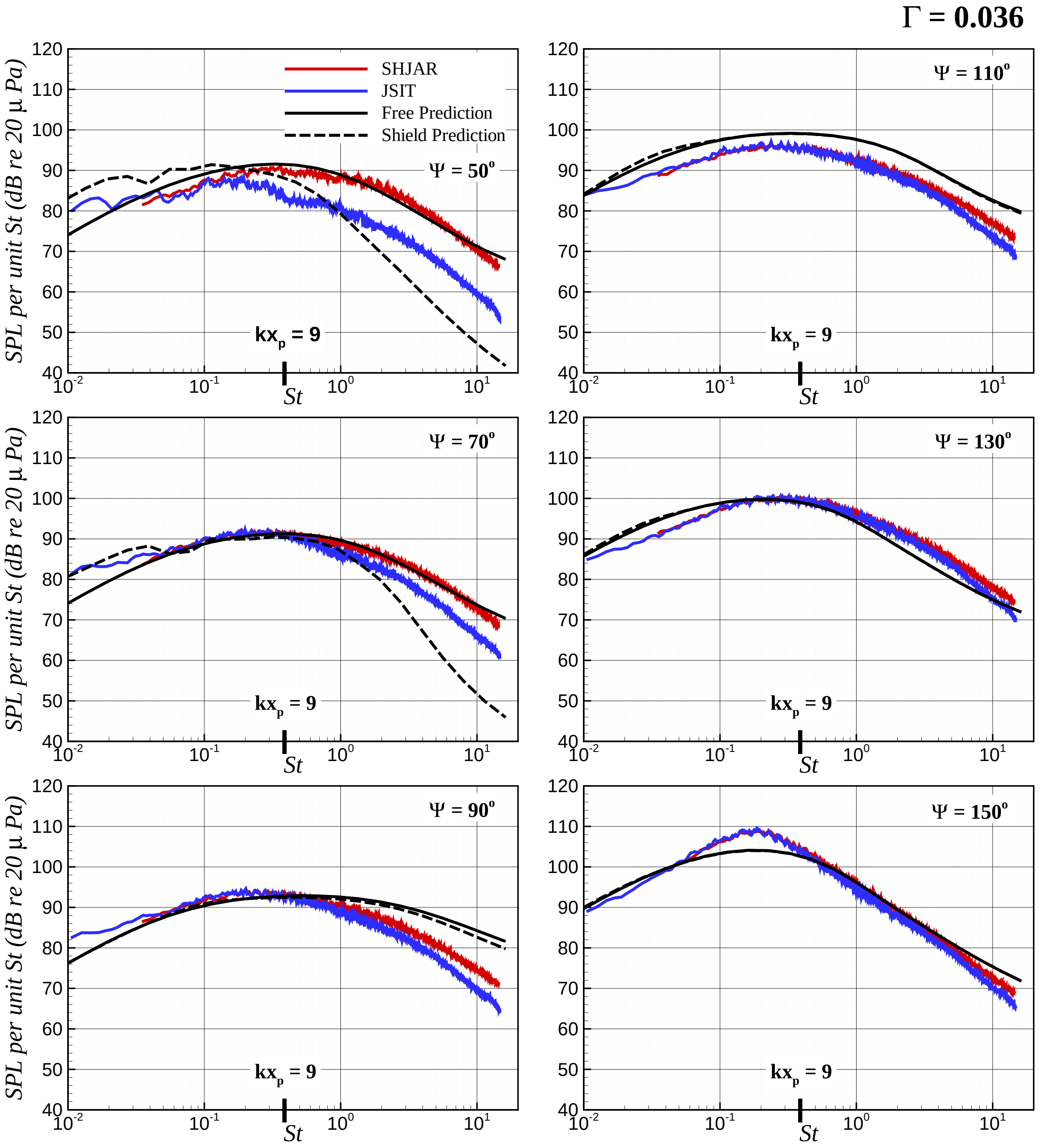

Figure B.17: The free-field and shielded prediction at $R/D = 100$ compared with experiment. The jet operates at $M_j = 0.985$ and $TTR = 1.00$ from the SMC000 nozzle with $D = 0.0508\,m$ and the plate is located at $x_p/D = 4$ and $y_p/D = 4$.

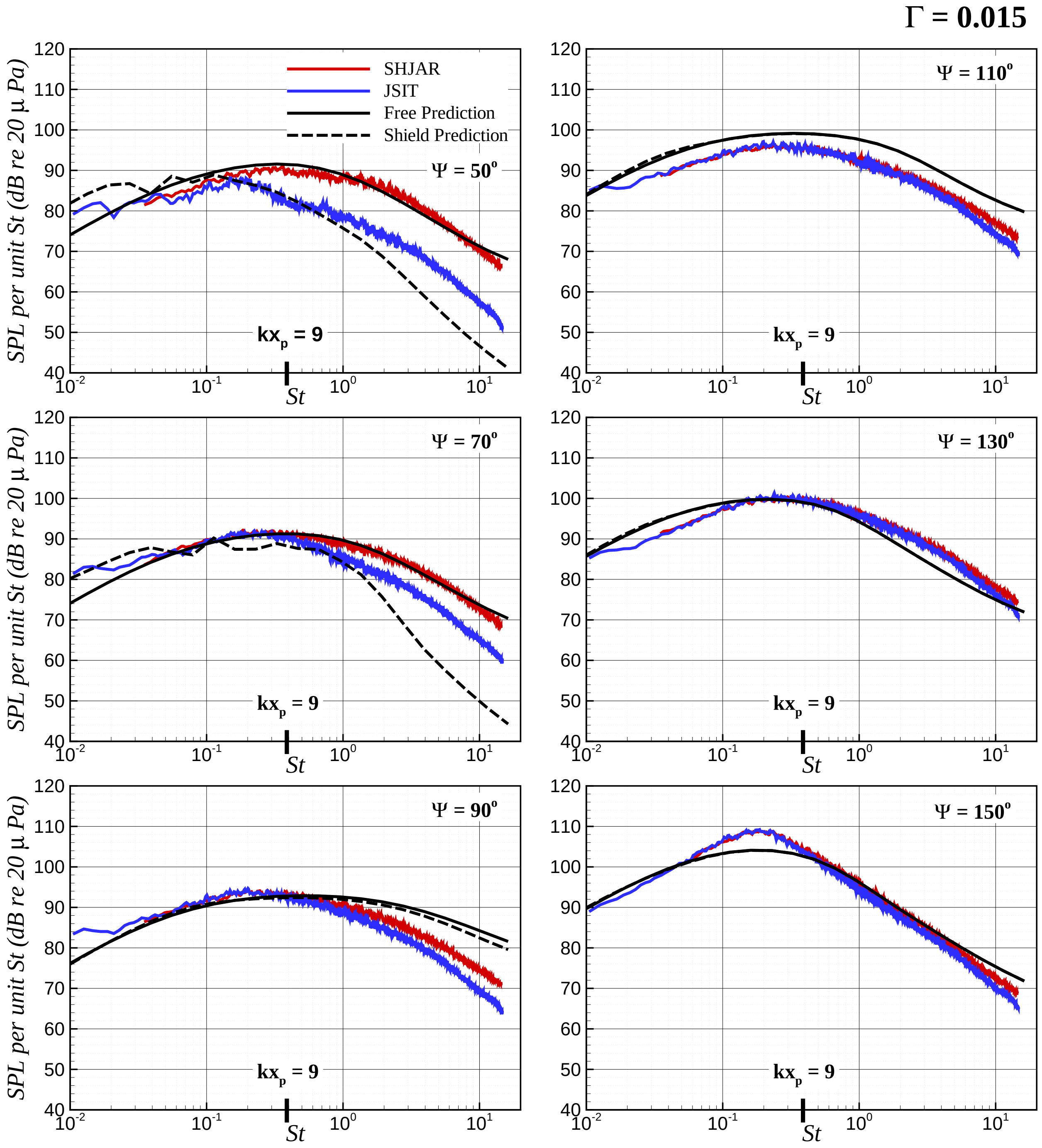

Figure B.18: The free-field and shielded prediction at $R/D = 100$ compared with experiment. The jet operates at $M_j = 0.985$ and $TTR = 1.00$ from the SMC000 nozzle with $D = 0.0508\,m$ and the plate is located at $x_p/D = 4$ and $y_p/D = 6$.

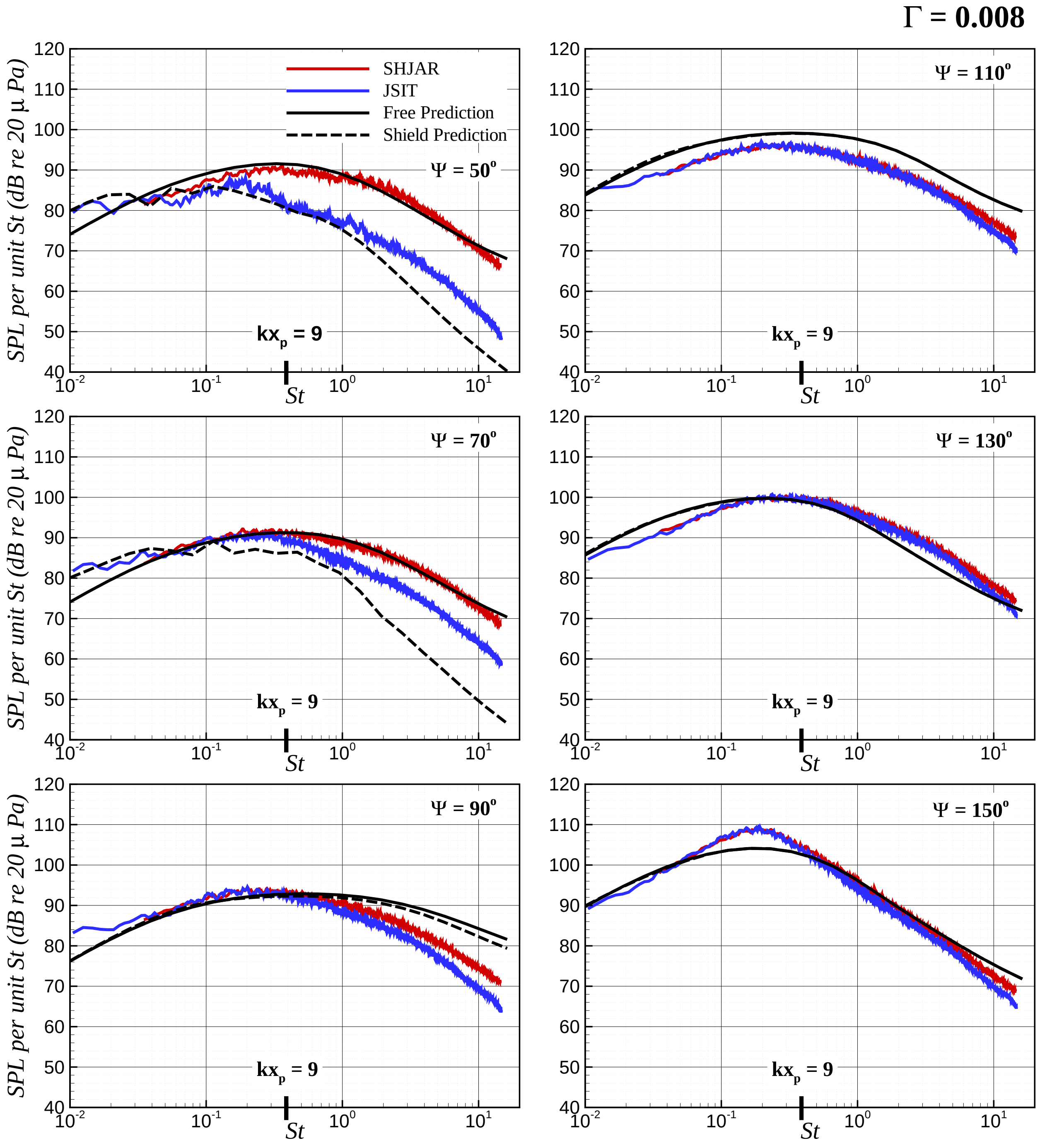

Figure B.19: The free-field and shielded prediction at $R/D = 100$ compared with experiment. The jet operates at $M_j = 0.985$ and $TTR = 1.00$ from the SMC000 nozzle with $D = 0.0508\,m$ and the plate is located at $x_p/D = 4$ and $y_p/D = 8$.

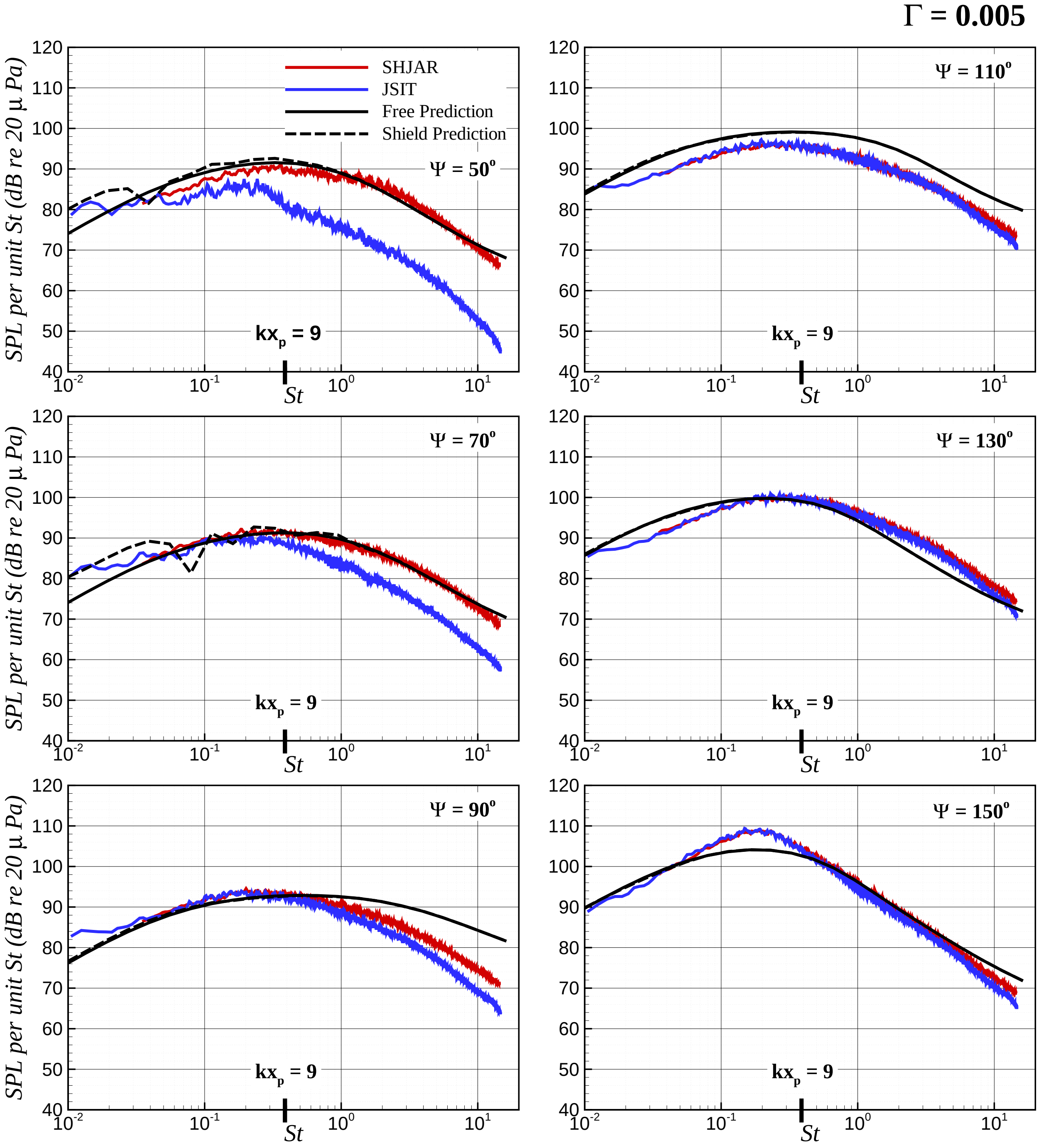

Figure B.20: The free-field and shielded prediction at $R/D = 100$ compared with experiment. The jet operates at $M_j = 0.985$ and $TTR = 1.00$ from the SMC000 nozzle with $D = 0.0508\,m$ and the plate is located at $x_p/D = 4$ and $y_p/D = 10$.

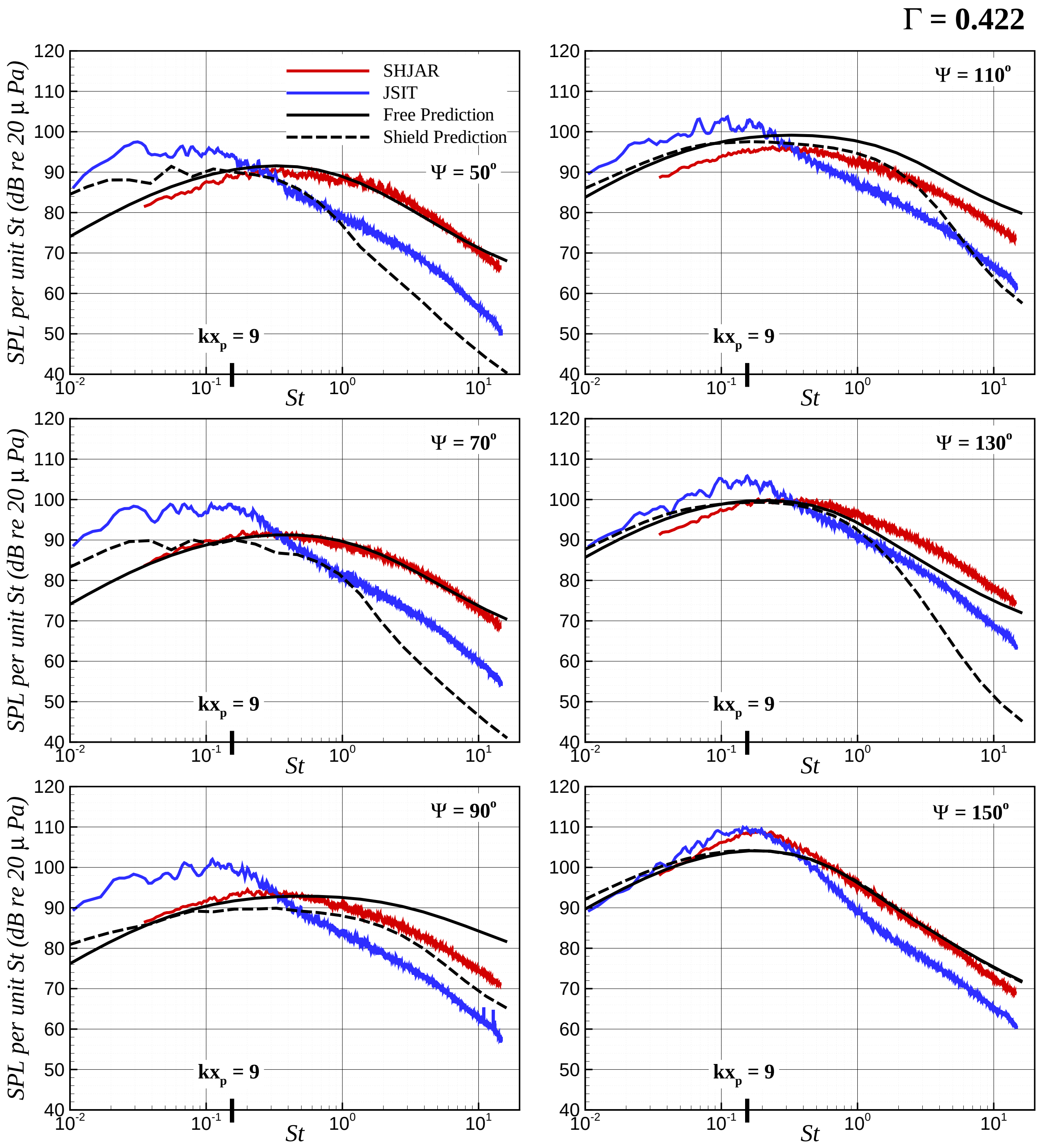

Figure B.21: The free-field and shielded prediction at $R/D = 100$ compared with experiment. The jet operates at $M_j = 0.985$ and $TTR = 1.00$ from the SMC000 nozzle with $D = 0.0508\,m$ and the plate is located at $x_p/D = 10$ and $y_p/D = 2$.

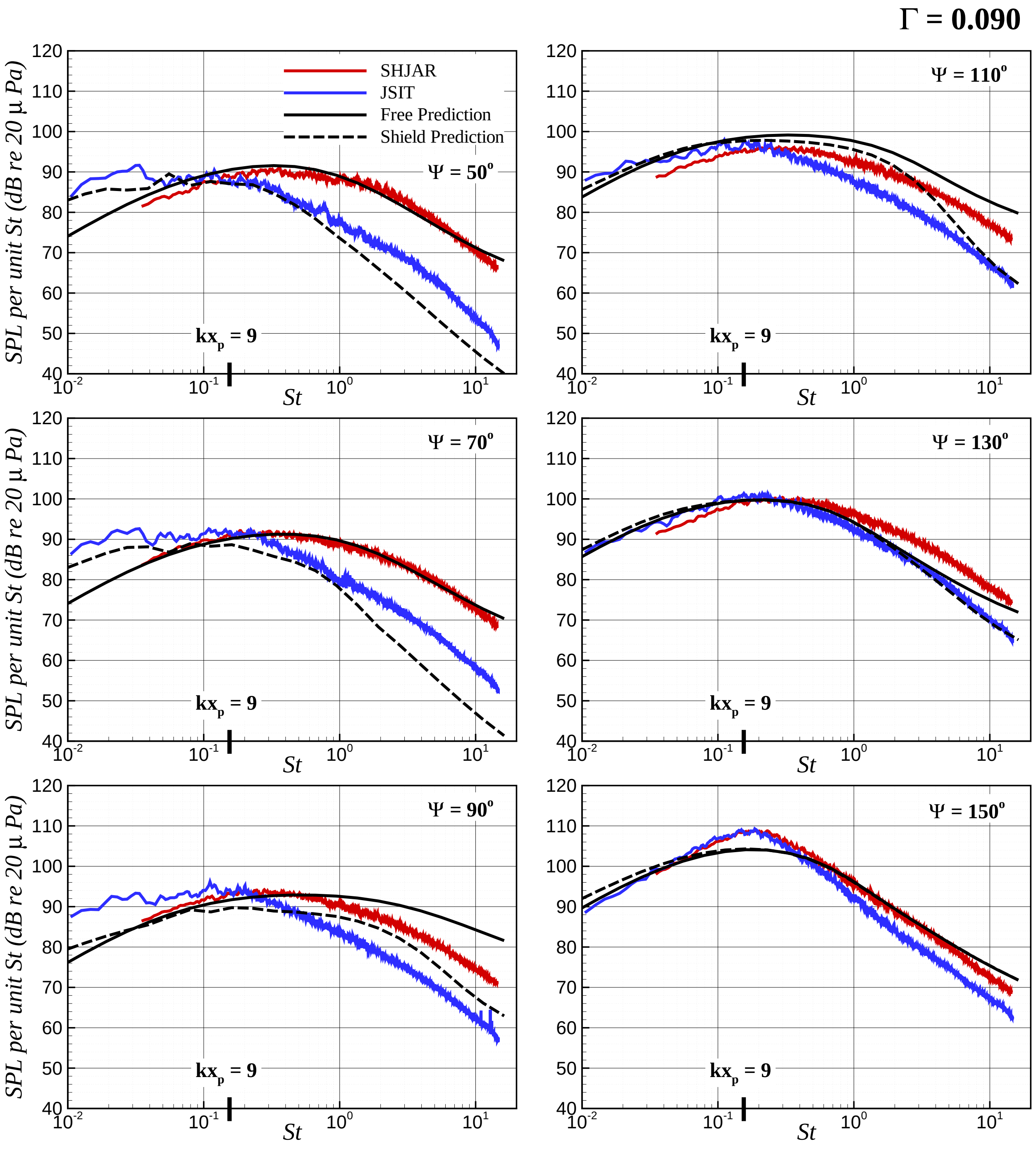

Figure B.22: The free-field and shielded prediction at $R/D = 100$ compared with experiment. The jet operates at $M_j = 0.985$ and $TTR = 1.00$ from the SMC000 nozzle with $D = 0.0508\,m$ and the plate is located at $x_p/D = 10$ and $y_p/D = 4$.

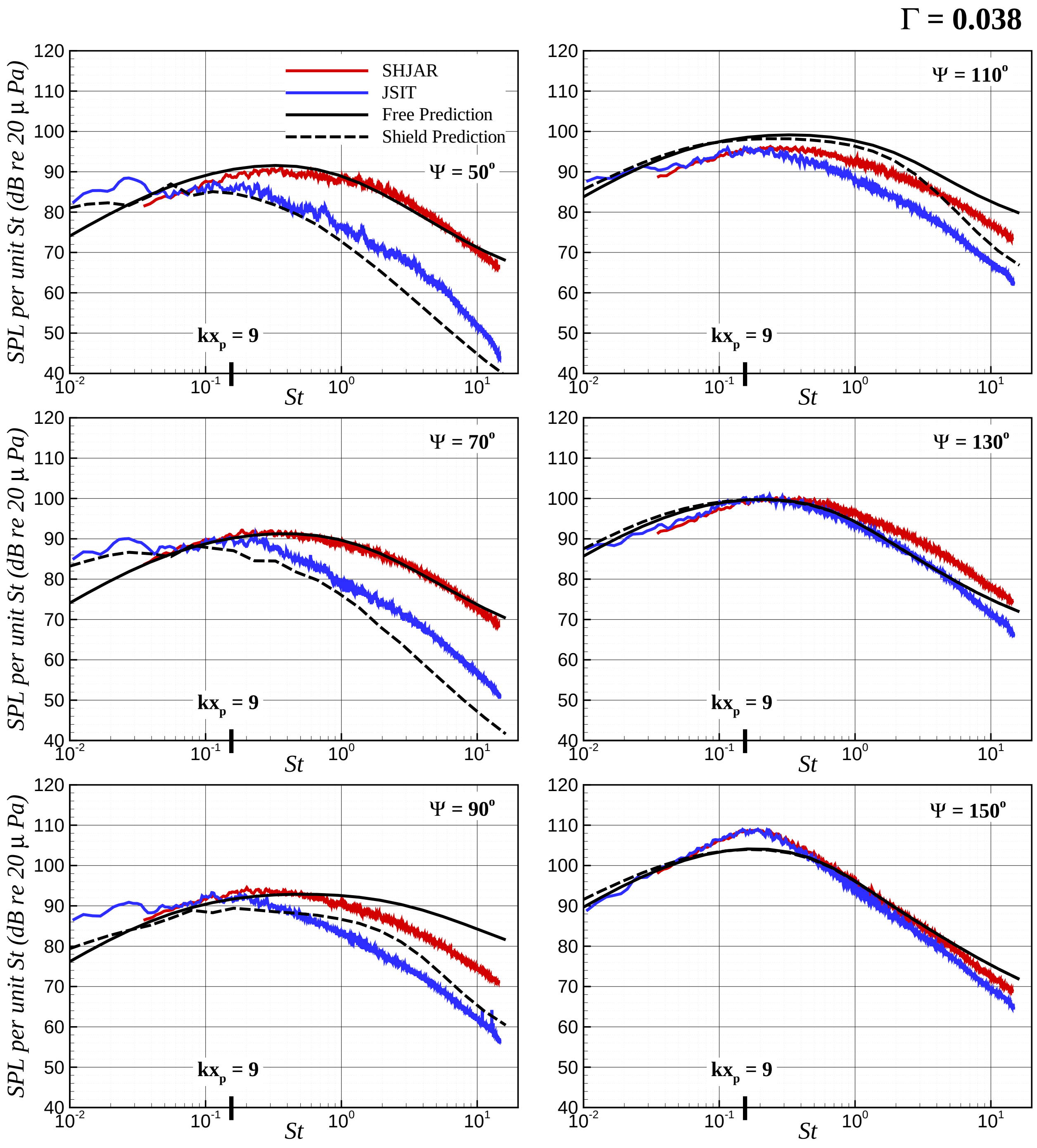

Figure B.23: The free-field and shielded prediction at $R/D = 100$ compared with experiment. The jet operates at $M_j = 0.985$ and $TTR = 1.00$ from the SMC000 nozzle with $D = 0.0508\,m$ and the plate is located at $x_p/D = 10$ and $y_p/D = 6$.

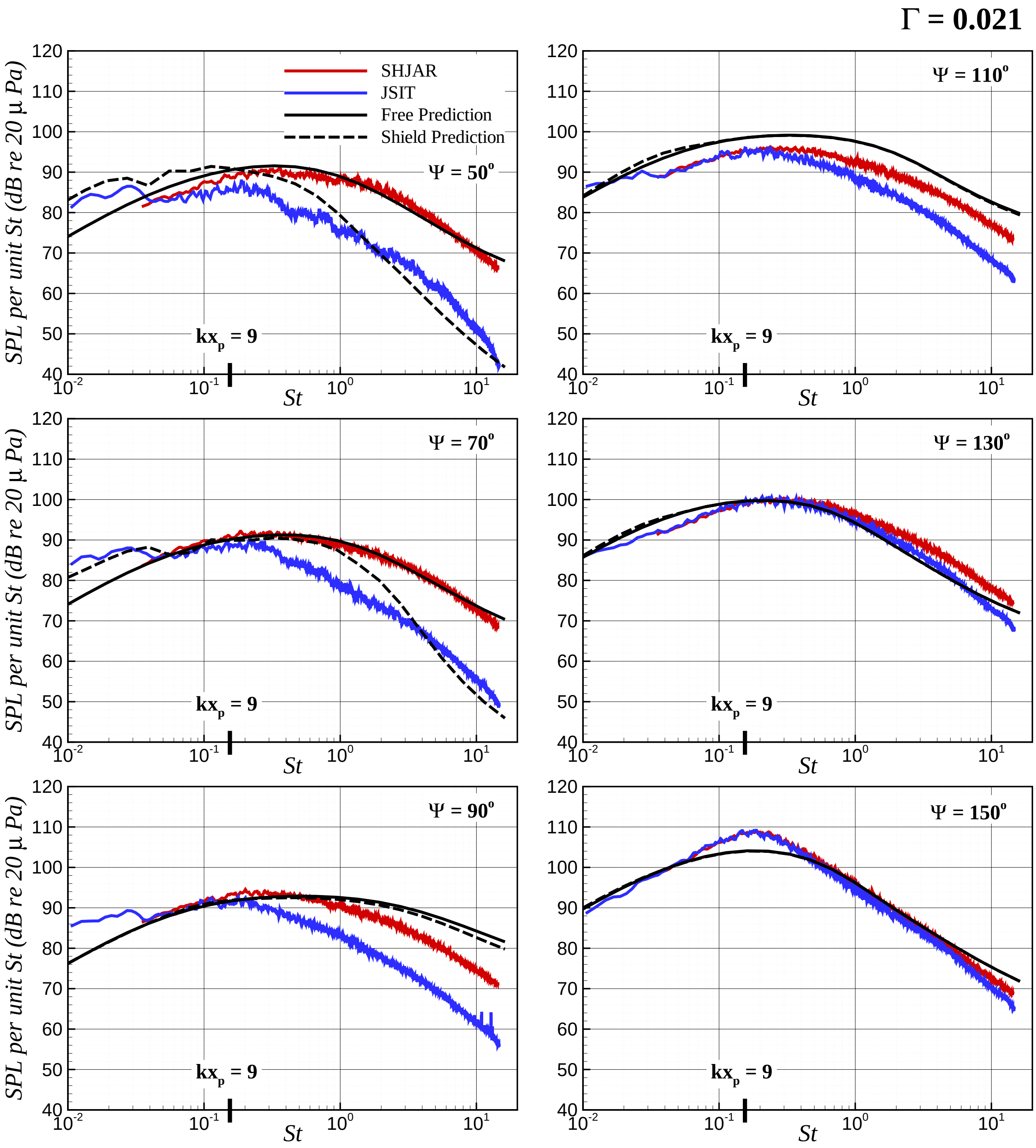

Figure B.24: The free-field and shielded prediction at $R/D = 100$ compared with experiment. The jet operates at $M_j = 0.985$ and $TTR = 1.00$ from the SMC000 nozzle with $D = 0.0508\,m$ and the plate is located at $x_p/D = 10$ and $y_p/D = 8$.

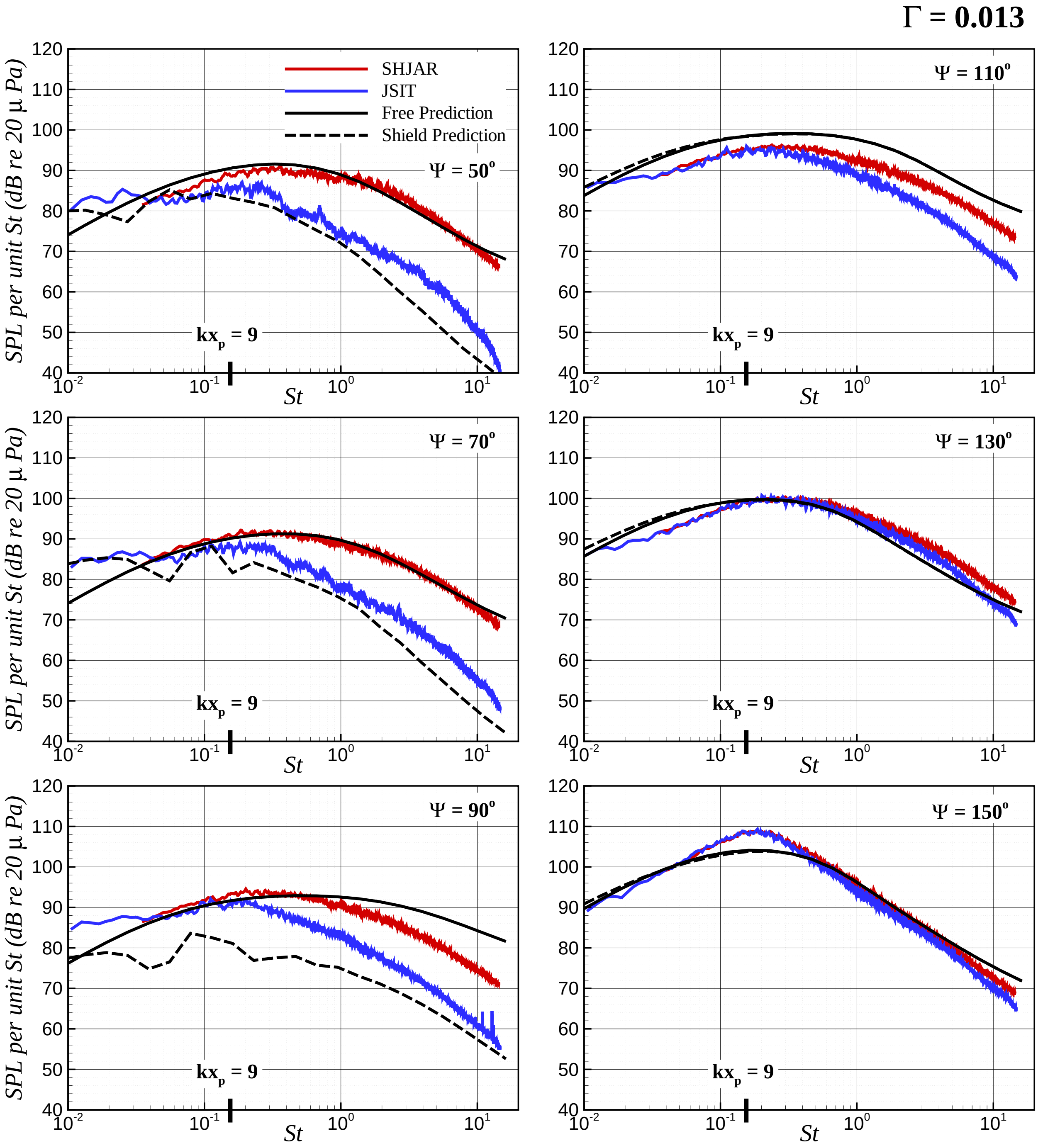

Figure B.25: The free-field and shielded prediction at $R/D = 100$ compared with experiment. The jet operates at $M_j = 0.985$ and $TTR = 1.00$ from the SMC000 nozzle with $D = 0.0508\,m$ and the plate is located at $x_p/D = 10$ and $y_p/D = 10$.

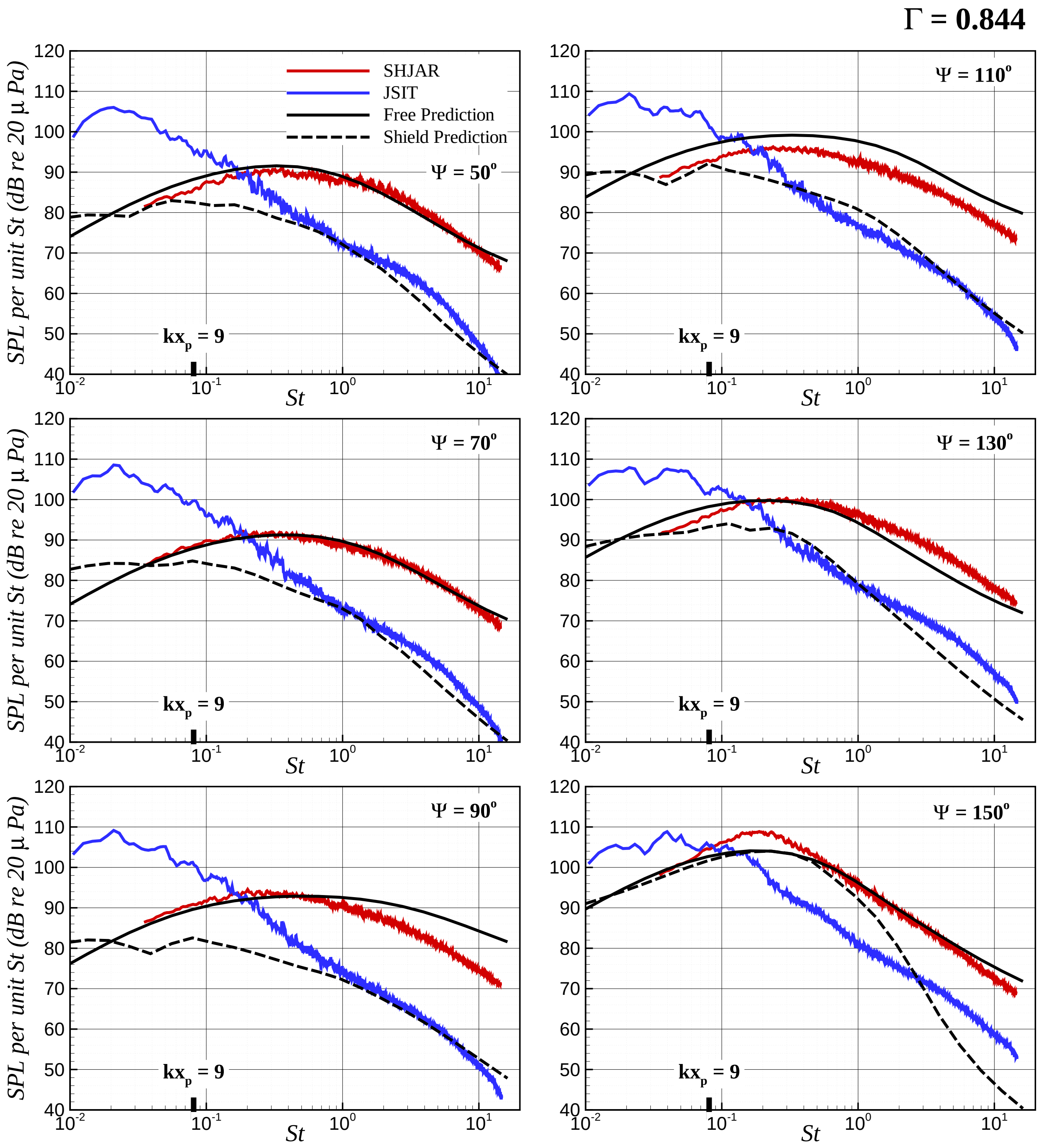

Figure B.26: The free-field and shielded prediction at $R/D = 100$ compared with experiment. The jet operates at $M_j = 0.985$ and $TTR = 1.00$ from the SMC000 nozzle with $D = 0.0508\ m$ and the plate is located at $x_p/D = 20$ and $y_p/D = 2$.

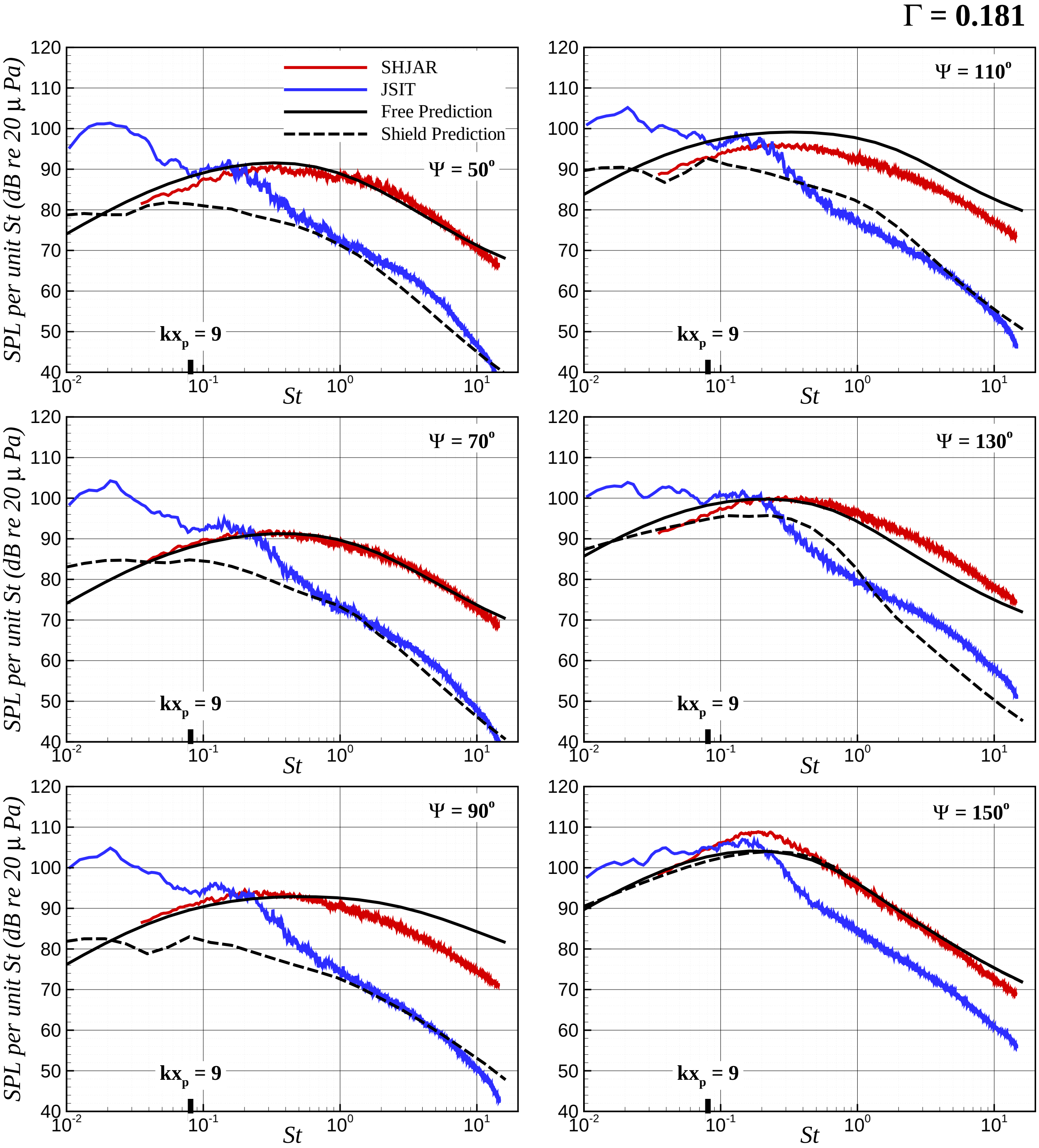

Figure B.27: The free-field and shielded prediction at $R/D = 100$ compared with experiment. The jet operates at $M_j = 0.985$ and $TTR = 1.00$ from the SMC000 nozzle with $D = 0.0508\,m$ and the plate is located at $x_p/D = 20$ and $y_p/D = 4$.

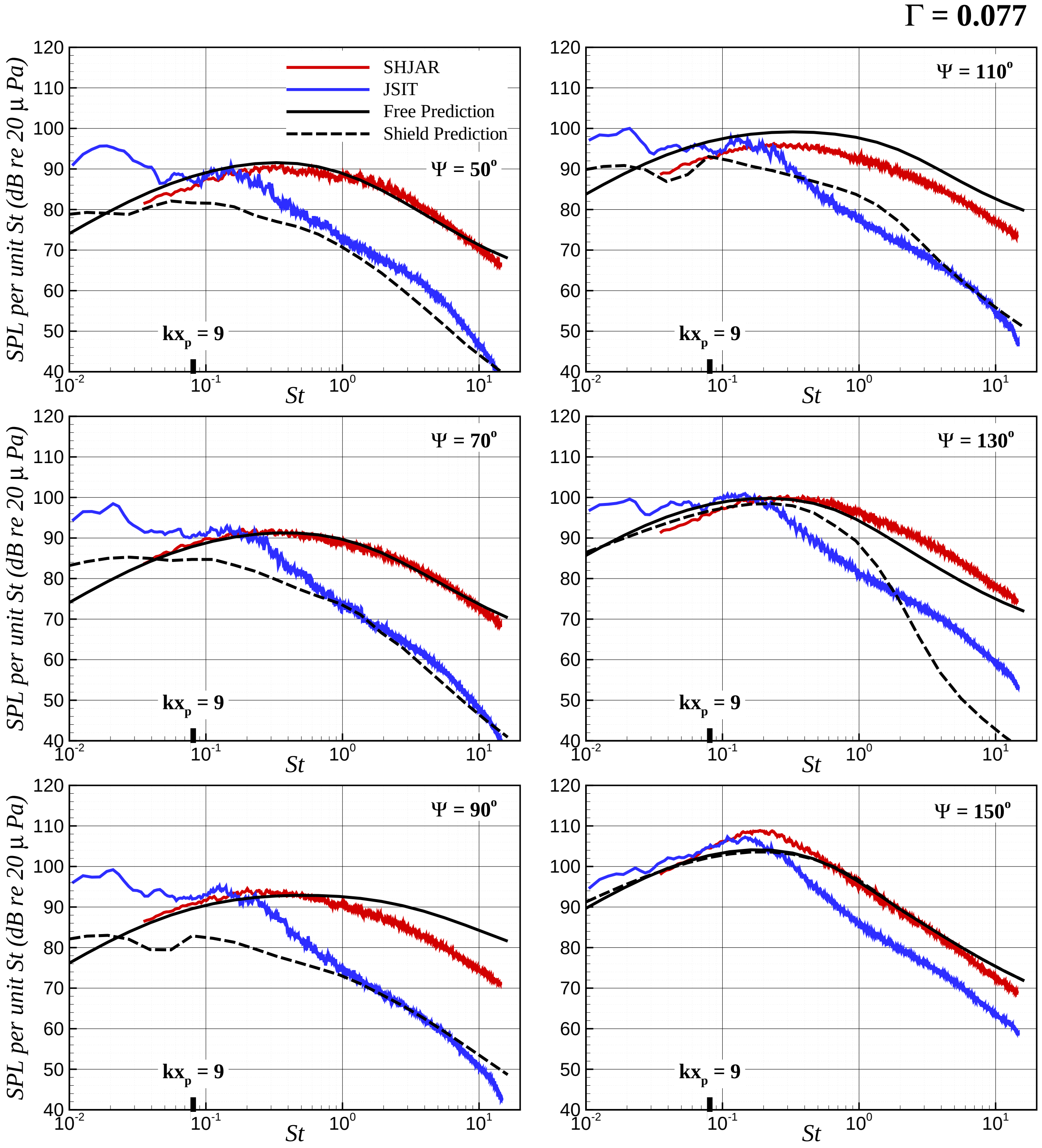

Figure B.28: The free-field and shielded prediction at $R/D = 100$ compared with experiment. The jet operates at $M_j = 0.985$ and $TTR = 1.00$ from the SMC000 nozzle with $D = 0.0508\,m$ and the plate is located at $x_p/D = 20$ and $y_p/D = 6$.

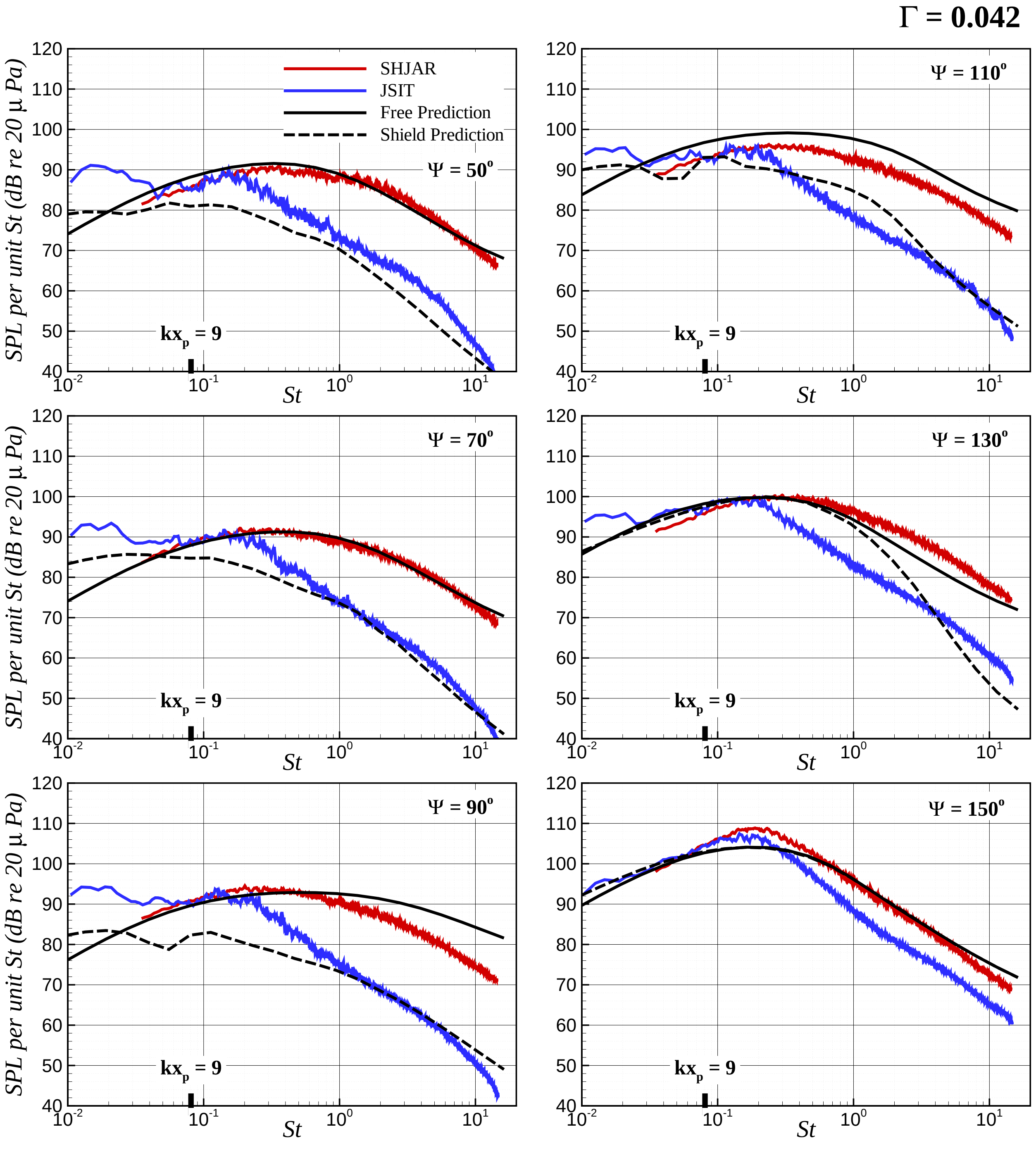

Figure B.29: The free-field and shielded prediction at $R/D = 100$ compared with experiment. The jet operates at $M_j = 0.985$ and $TTR = 1.00$ from the SMC000 nozzle with $D = 0.0508\ m$ and the plate is located at $x_p/D = 20$ and $y_p/D = 8$.

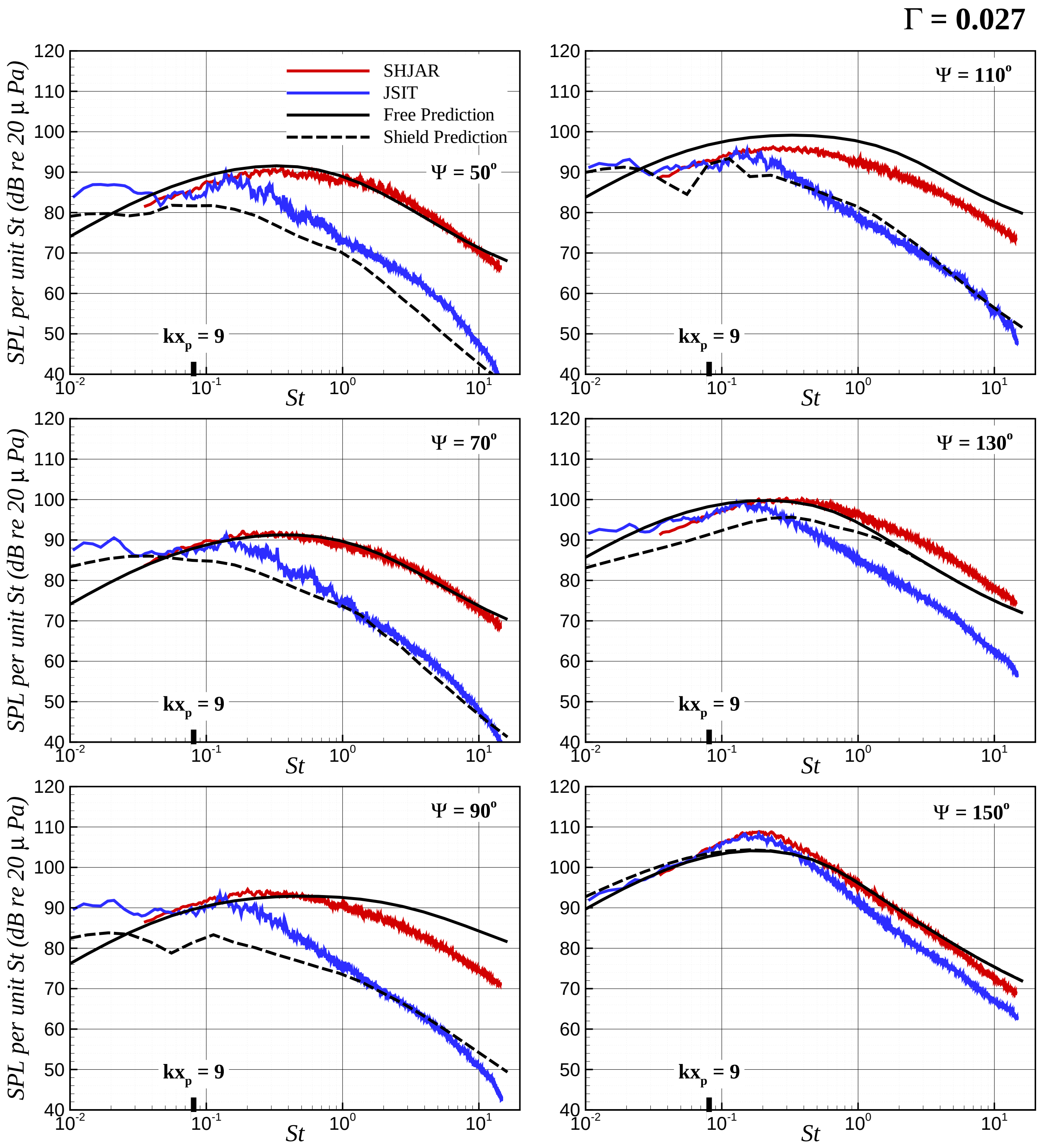

Figure B.30: The free-field and shielded prediction at $R/D = 100$ compared with experiment. The jet operates at $M_j = 0.985$ and $TTR = 1.00$ from the SMC000 nozzle with $D = 0.0508\,m$ and the plate is located at $x_p/D = 20$ and $y_p/D = 10$.

B.3 Supersonic On-Design Jet

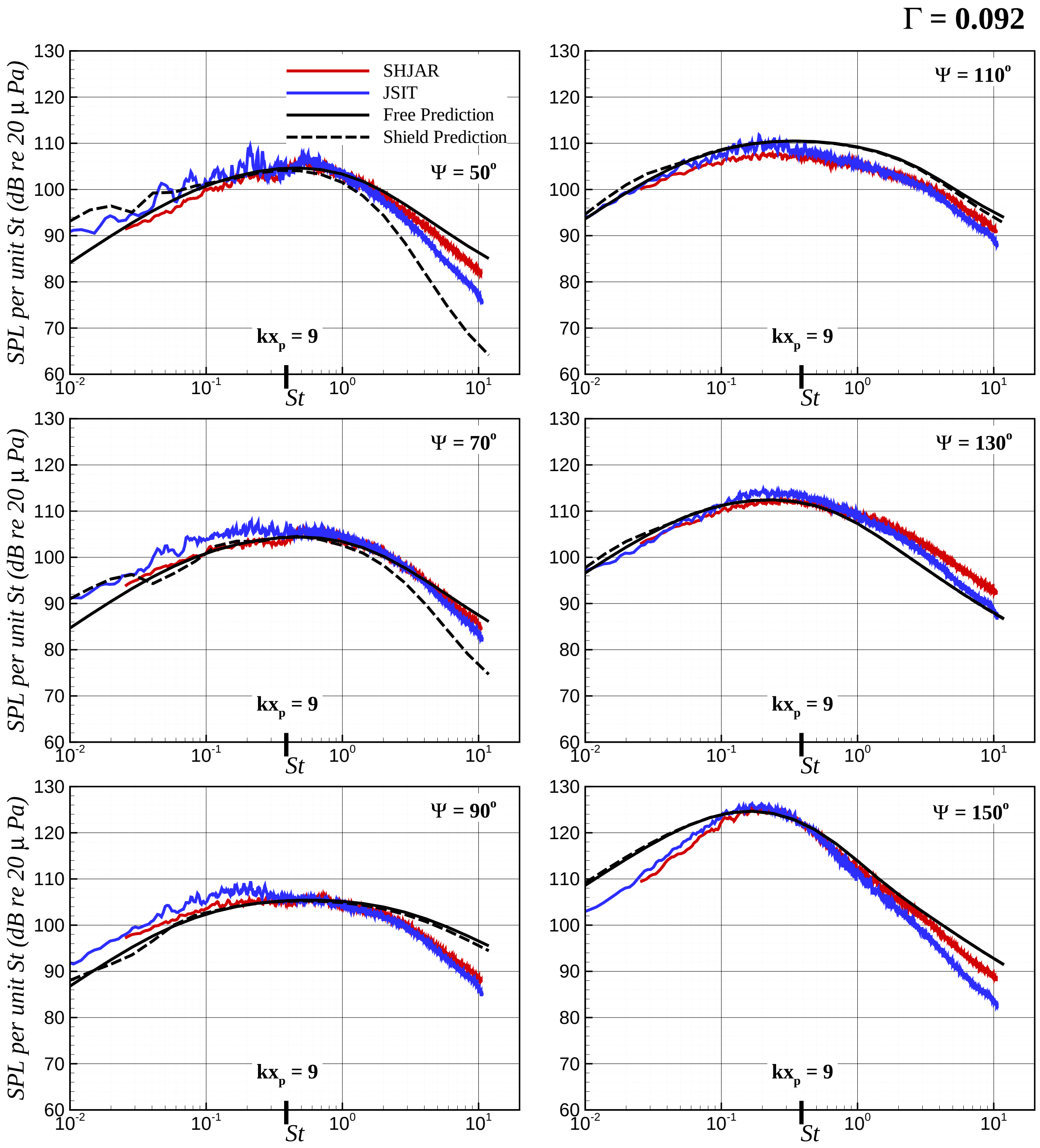

Figure B.31: The free-field and shielded prediction at $R/D = 100$ compared with experiment. The jet operates at $M_j = 1.50$ and $TTR = 1.00$ from the SMC000 nozzle with $D = 0.0508\ m$ and the plate is located at $x_p/D = 4$ and $y_p/D = 2$.

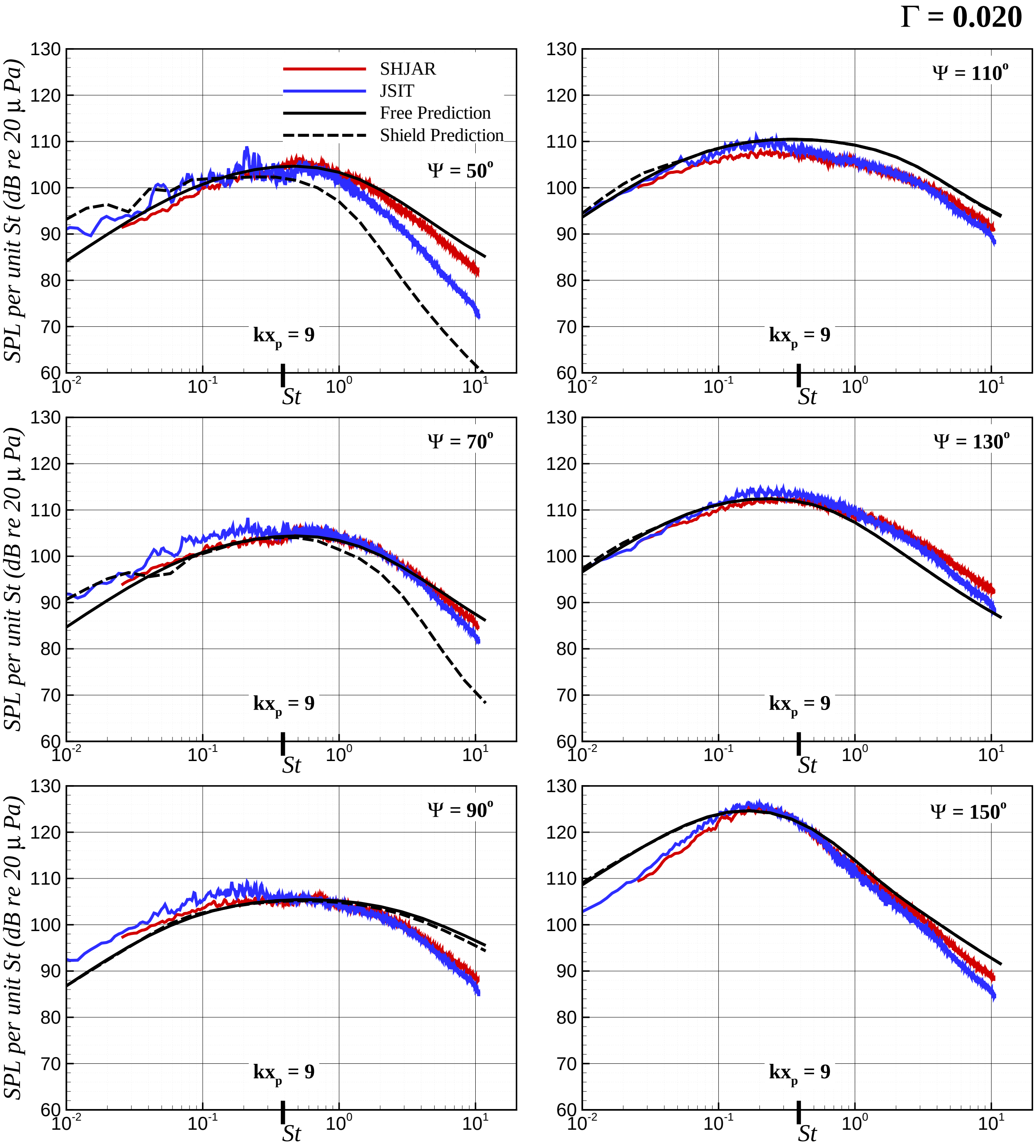

Figure B.32: The free-field and shielded prediction at $R/D = 100$ compared with experiment. The jet operates at $M_j = 1.50$ and $TTR = 1.00$ from the SMC000 nozzle with $D = 0.0508\ m$ and the plate is located at $x_p/D = 4$ and $y_p/D = 4$.

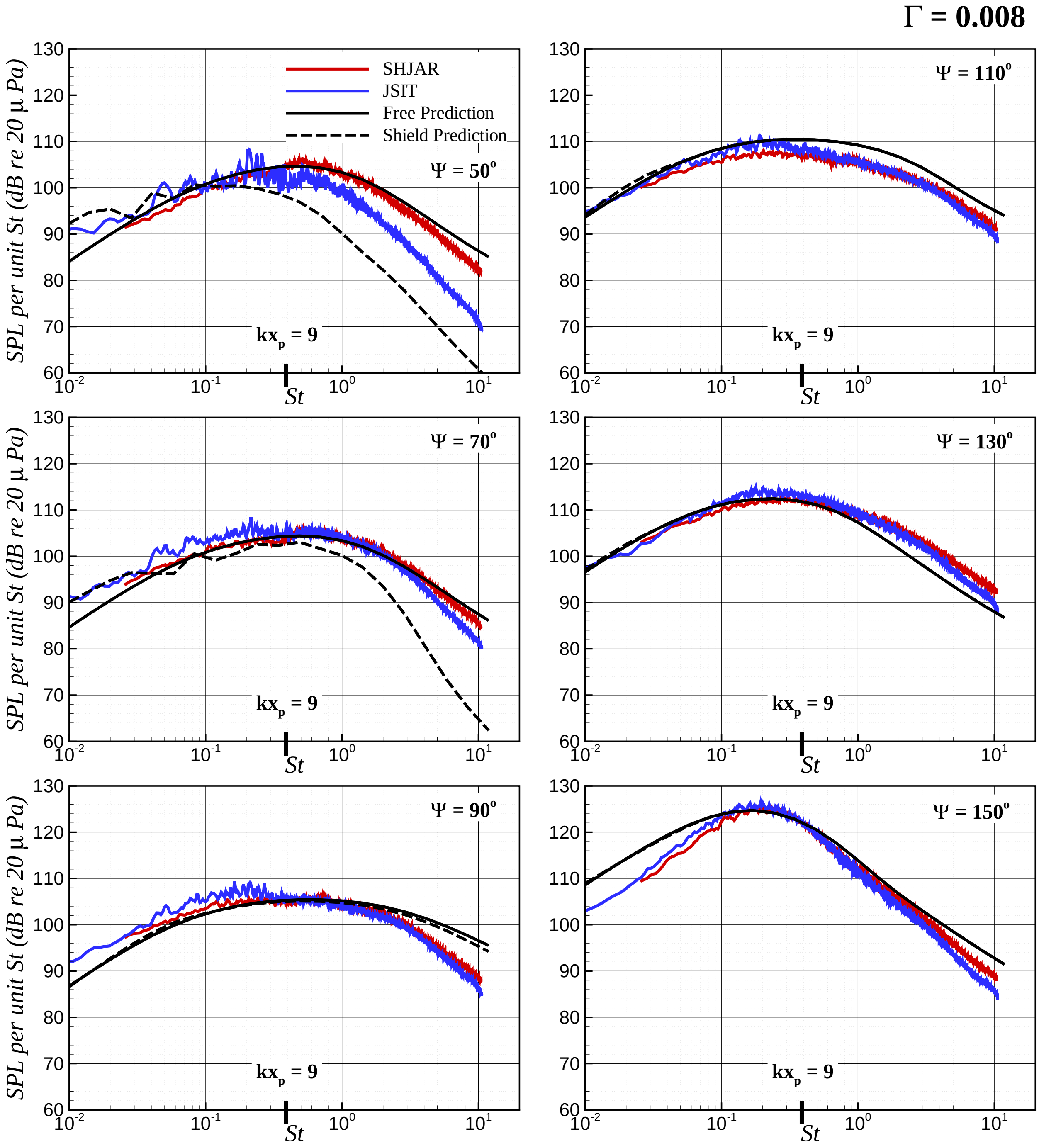

Figure B.33: The free-field and shielded prediction at $R/D = 100$ compared with experiment. The jet operates at $M_j = 1.50$ and $TTR = 1.00$ from the SMC000 nozzle with $D = 0.0508\ m$ and the plate is located at $x_p/D = 4$ and $y_p/D = 6$.

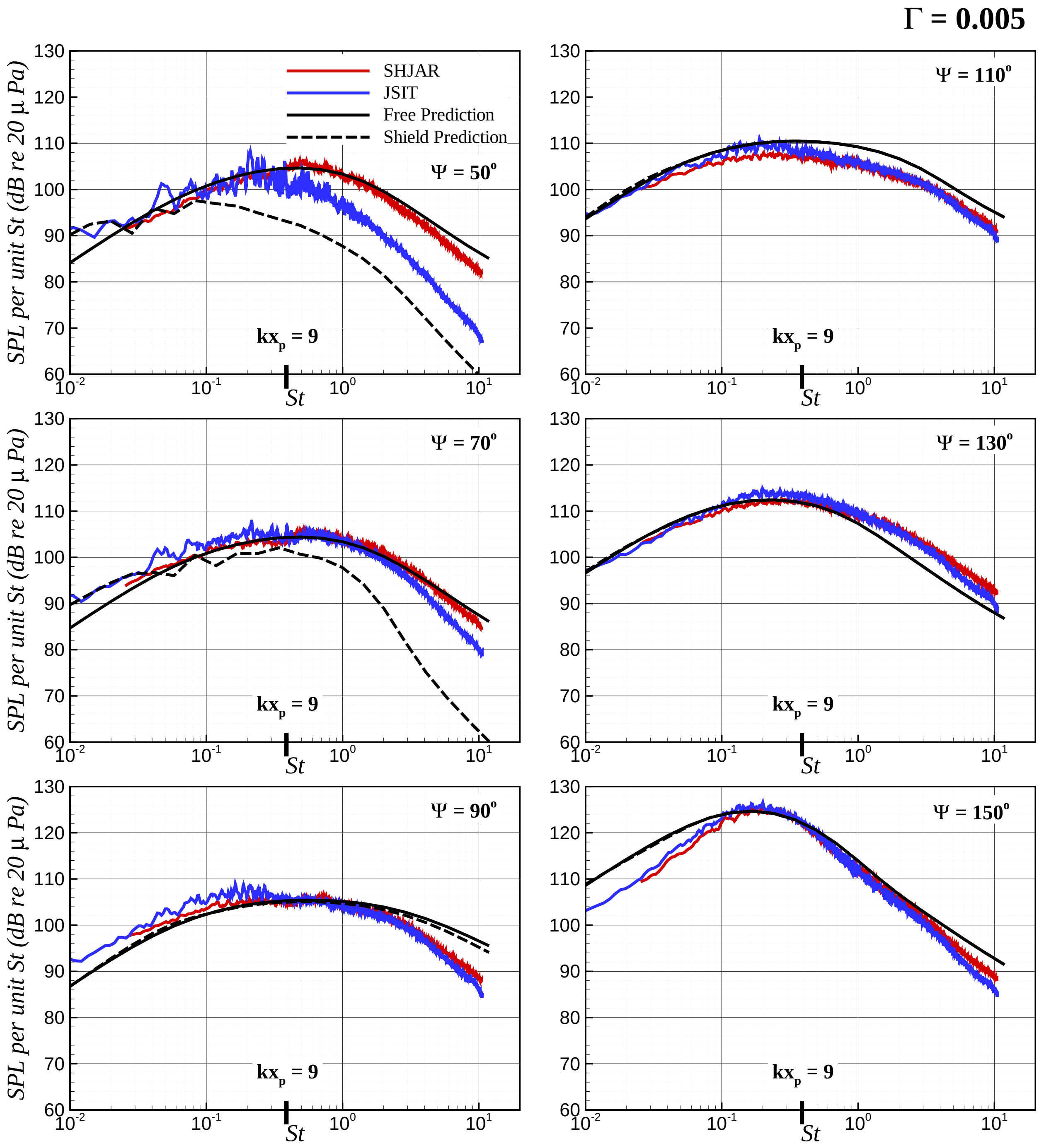

Figure B.34: The free-field and shielded prediction at $R/D = 100$ compared with experiment. The jet operates at $M_j = 1.50$ and $TTR = 1.00$ from the SMC000 nozzle with $D = 0.0508\ m$ and the plate is located at $x_p/D = 4$ and $y_p/D = 8$.

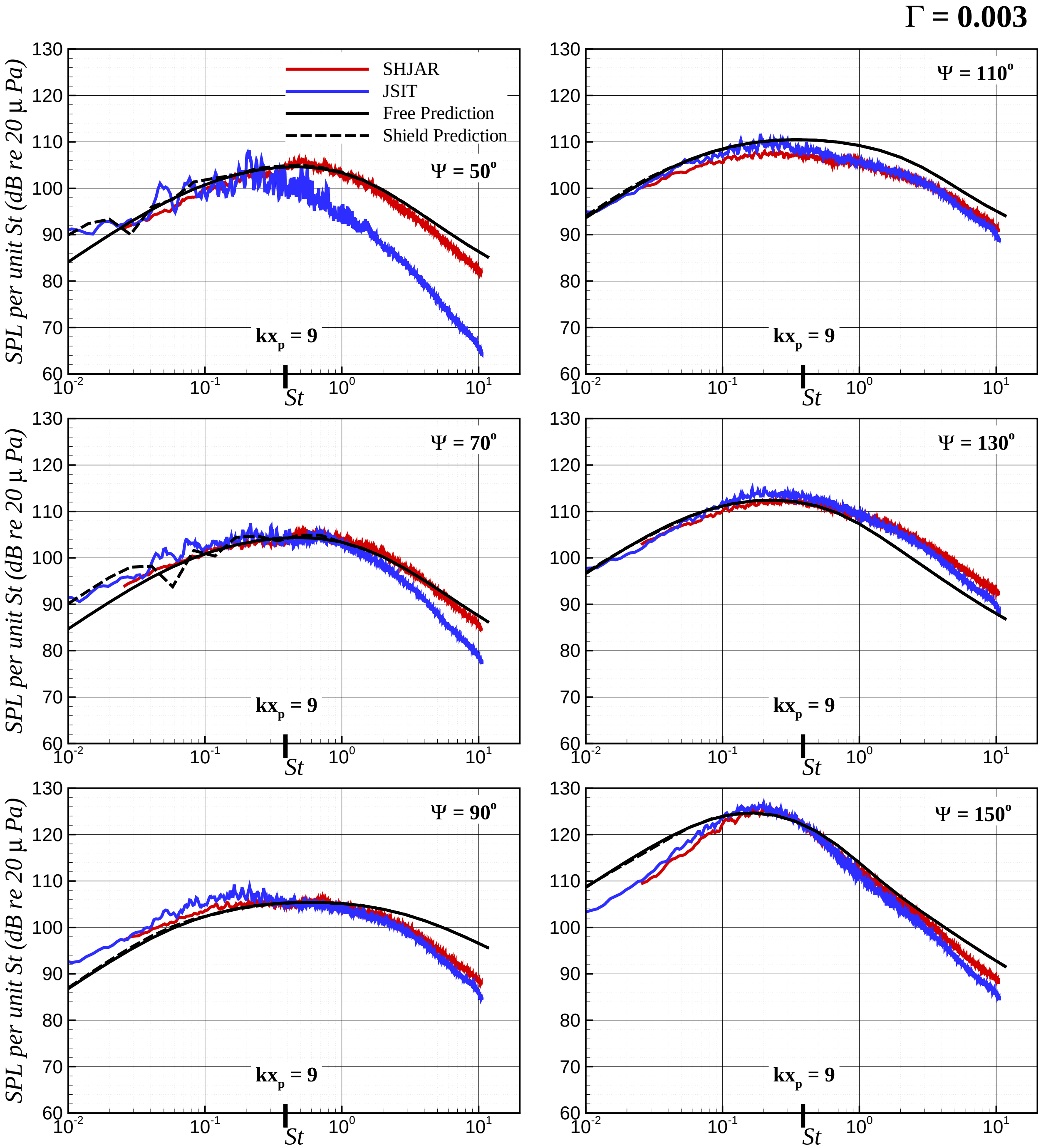

Figure B.35: The free-field and shielded prediction at $R/D = 100$ compared with experiment. The jet operates at $M_j = 1.50$ and $TTR = 1.00$ from the SMC000 nozzle with $D = 0.0508\ m$ and the plate is located at $x_p/D = 4$ and $y_p/D = 10$.

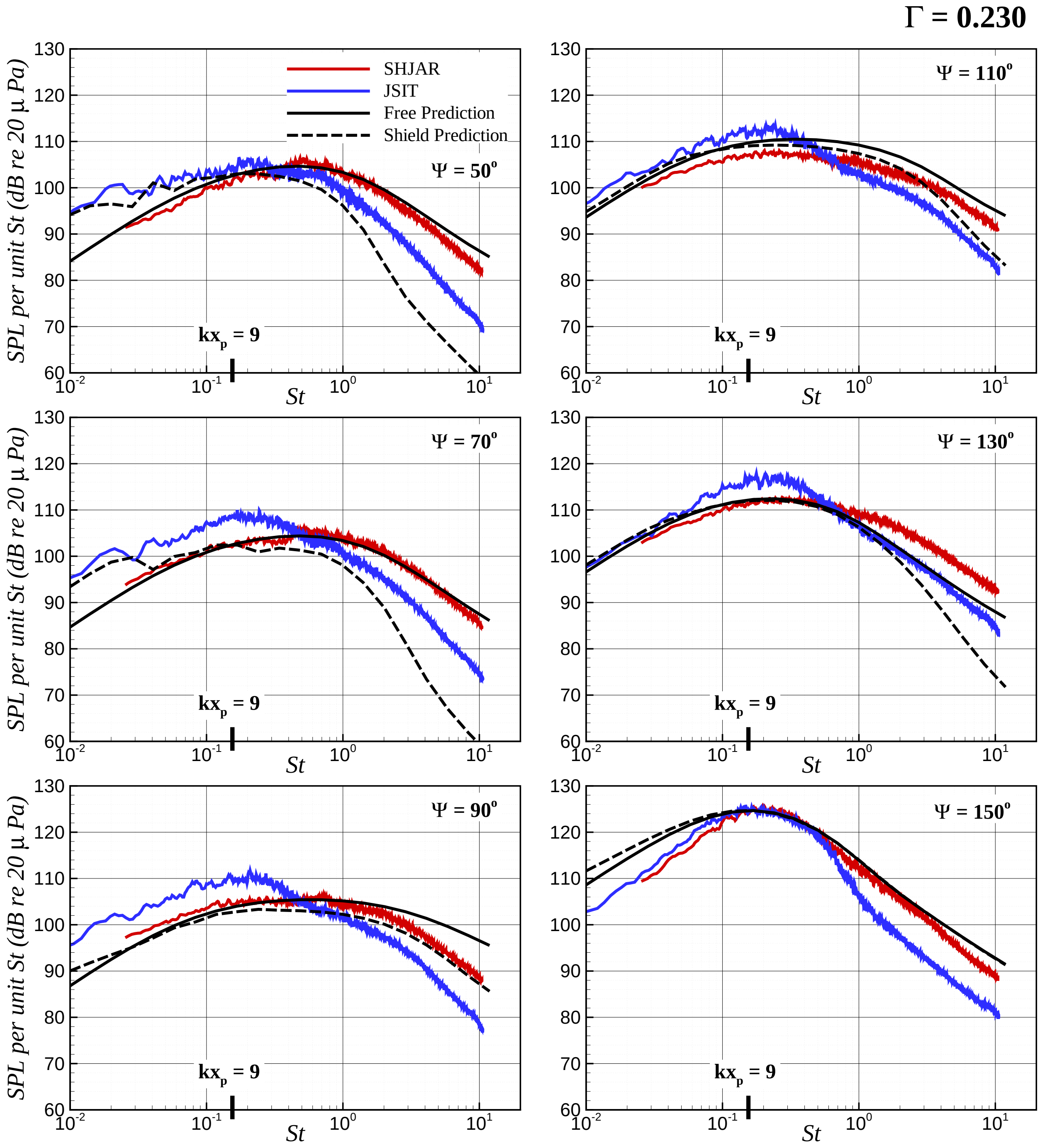

Figure B.36: The free-field and shielded prediction at $R/D = 100$ compared with experiment. The jet operates at $M_j = 1.50$ and $TTR = 1.00$ from the SMC000 nozzle with $D = 0.0508\ m$ and the plate is located at $x_p/D = 10$ and $y_p/D = 2$.

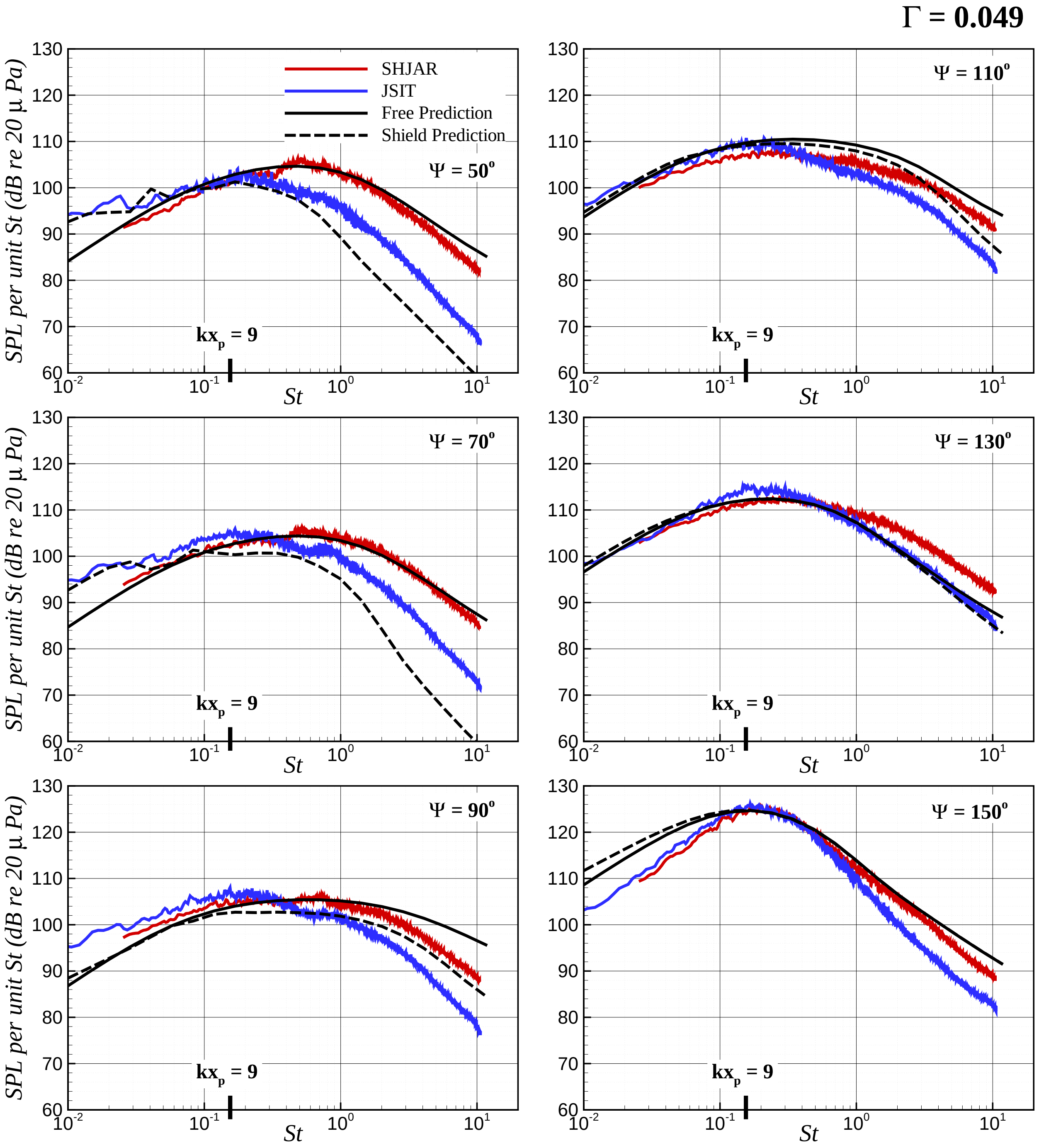

Figure B.37: The free-field and shielded prediction at $R/D = 100$ compared with experiment. The jet operates at $M_j = 1.50$ and $TTR = 1.00$ from the SMC000 nozzle with $D = 0.0508\ m$ and the plate is located at $x_p/D = 10$ and $y_p/D = 4$.

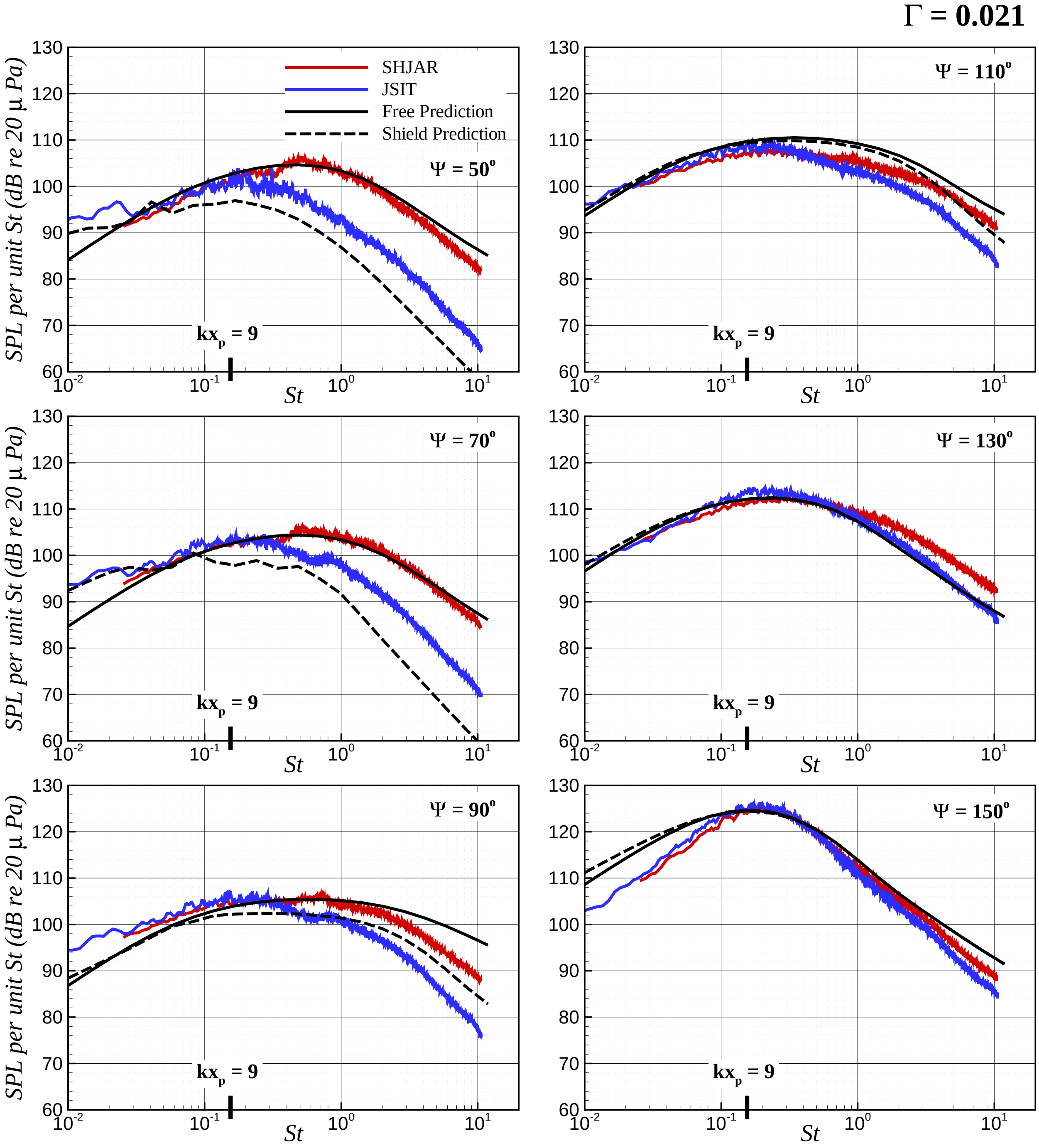

Figure B.38: The free-field and shielded prediction at $R/D = 100$ compared with experiment. The jet operates at $M_j = 1.50$ and $TTR = 1.00$ from the SMC000 nozzle with $D = 0.0508\ m$ and the plate is located at $x_p/D = 10$ and $y_p/D = 6$.

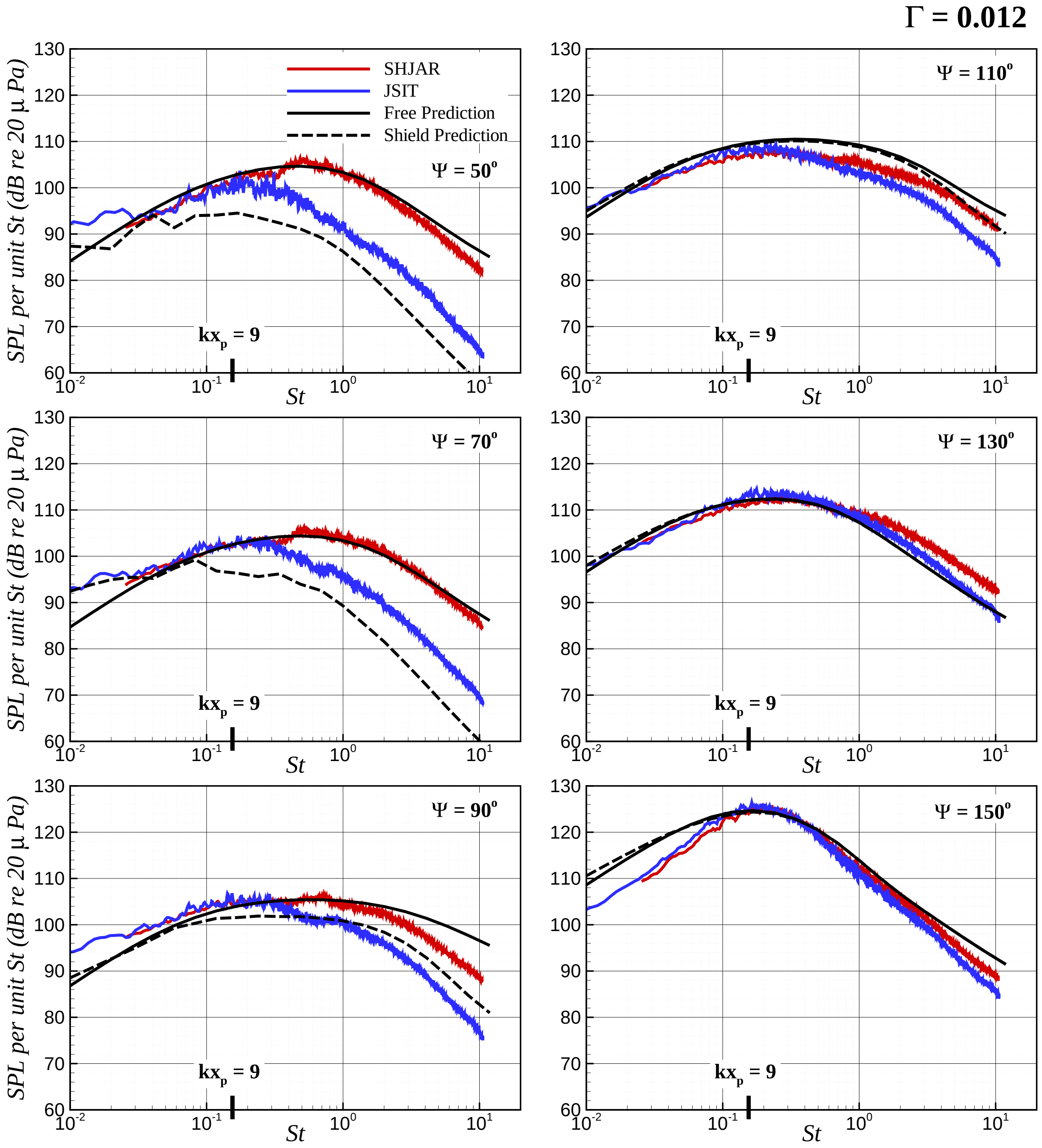

Figure B.39: The free-field and shielded prediction at $R/D = 100$ compared with experiment. The jet operates at $M_j = 1.50$ and $TTR = 1.00$ from the SMC000 nozzle with $D = 0.0508\ m$ and the plate is located at $x_p/D = 10$ and $y_p/D = 8$.

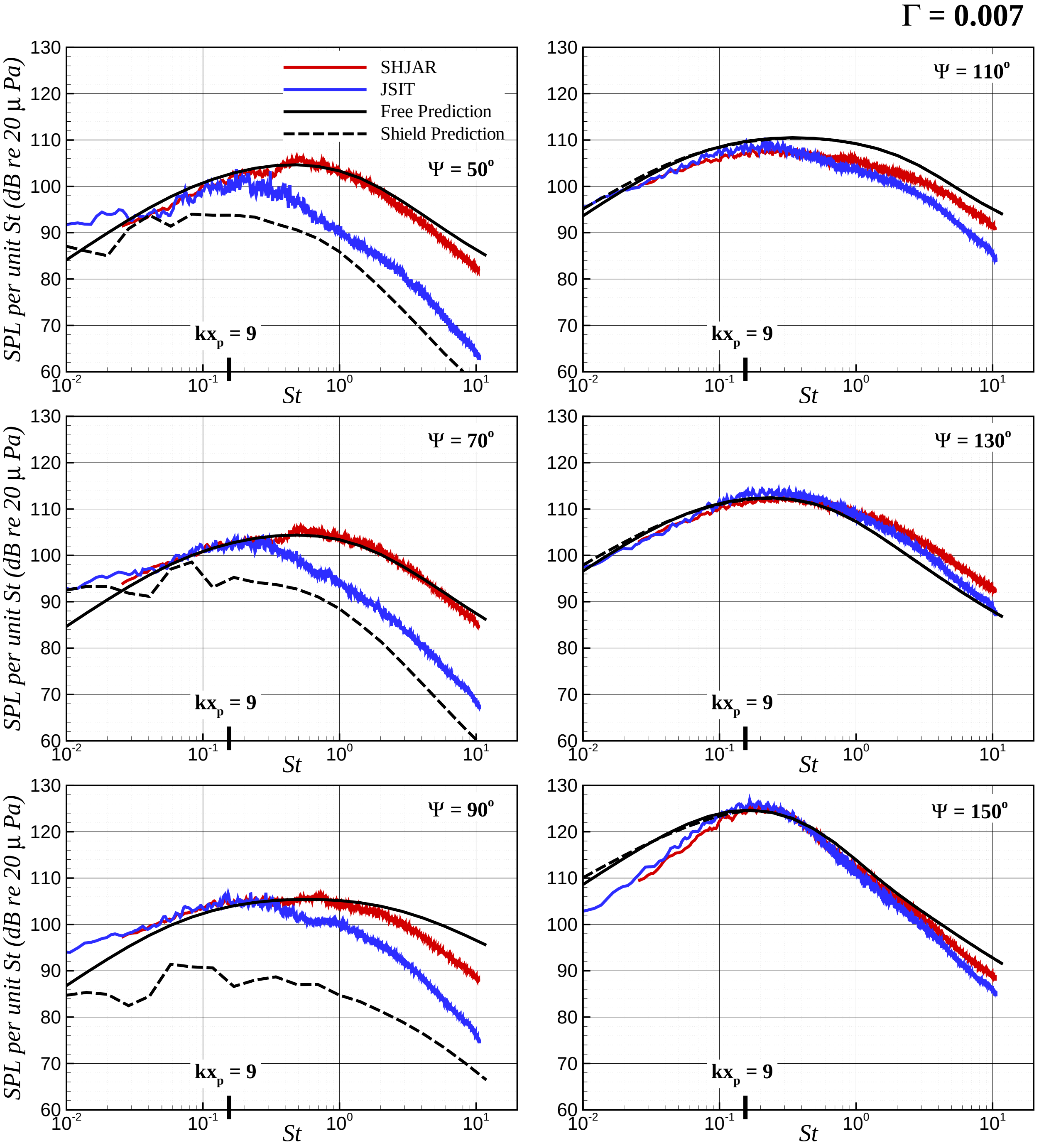

Figure B.40: The free-field and shielded prediction at $R/D = 100$ compared with experiment. The jet operates at $M_j = 1.50$ and $TTR = 1.00$ from the SMC000 nozzle with $D = 0.0508\ m$ and the plate is located at $x_p/D = 10$ and $y_p/D = 10$.

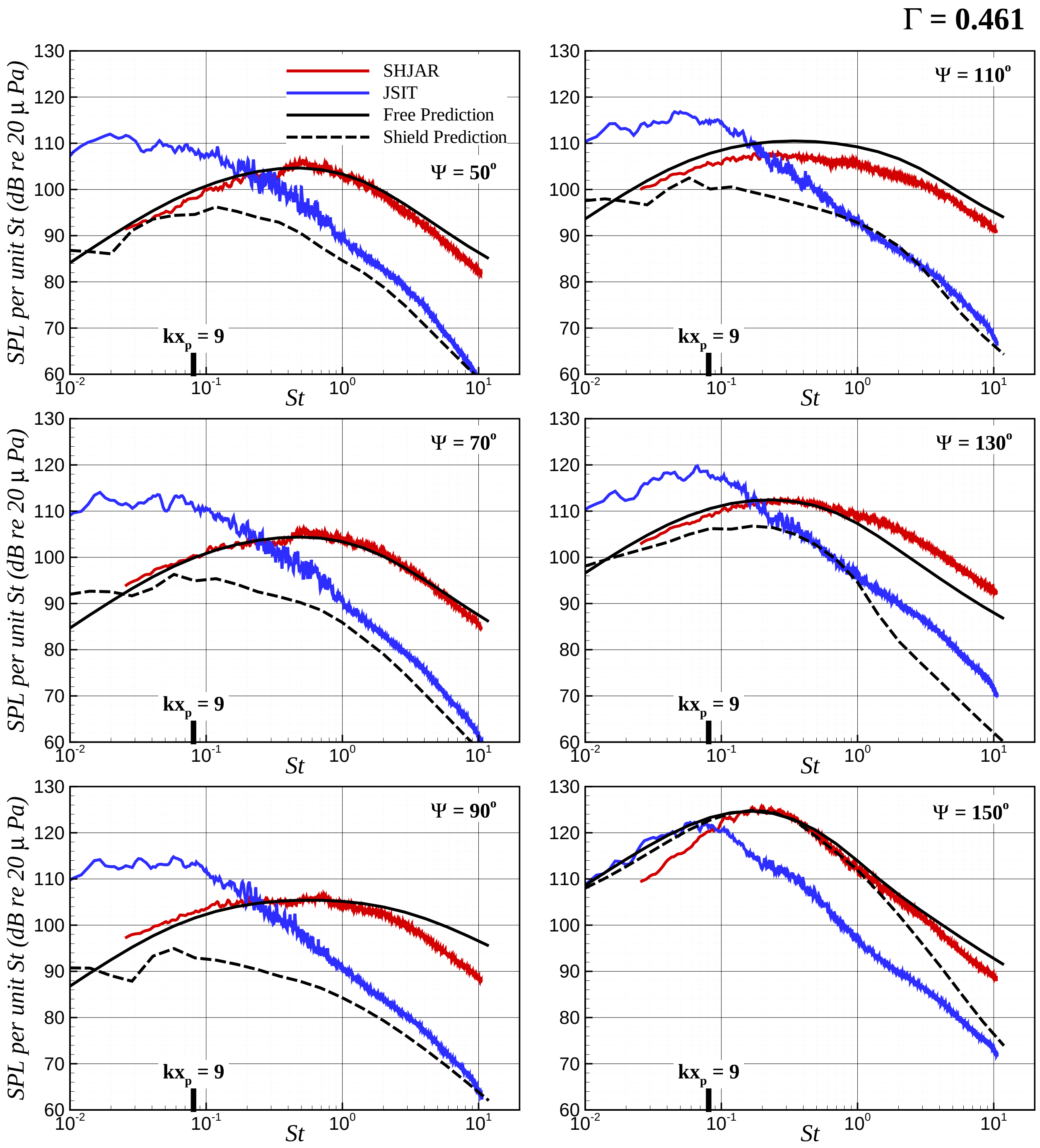

Figure B.41: The free-field and shielded prediction at $R/D = 100$ compared with experiment. The jet operates at $M_j = 1.50$ and $TTR = 1.00$ from the SMC000 nozzle with $D = 0.0508\,m$ and the plate is located at $x_p/D = 20$ and $y_p/D = 2$.

Γ = 0.099

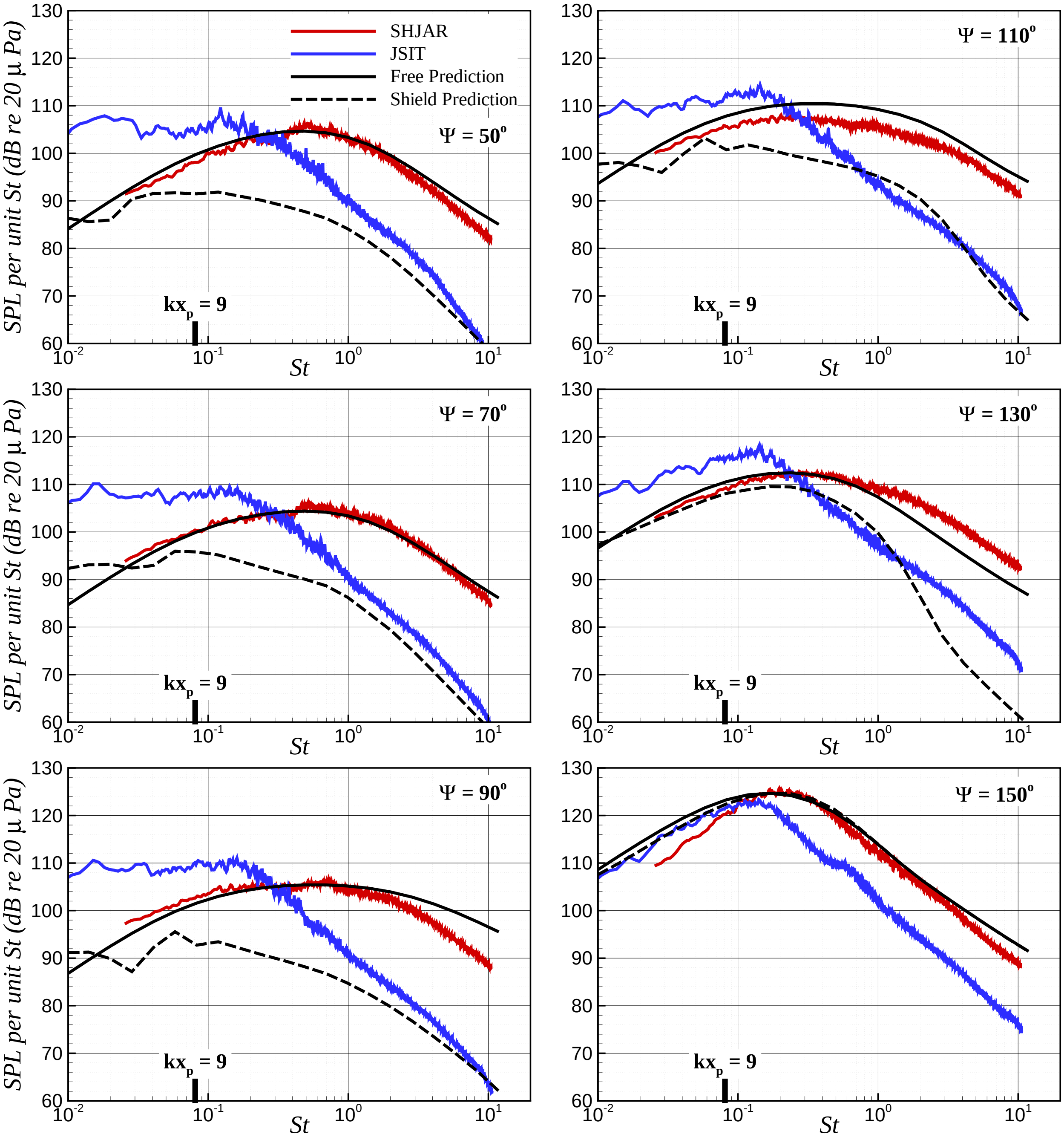

Figure B.42: The free-field and shielded prediction at $R/D = 100$ compared with experiment. The jet operates at $M_j = 1.50$ and $TTR = 1.00$ from the SMC000 nozzle with $D = 0.0508\ m$ and the plate is located at $x_p/D = 20$ and $y_p/D = 4$.

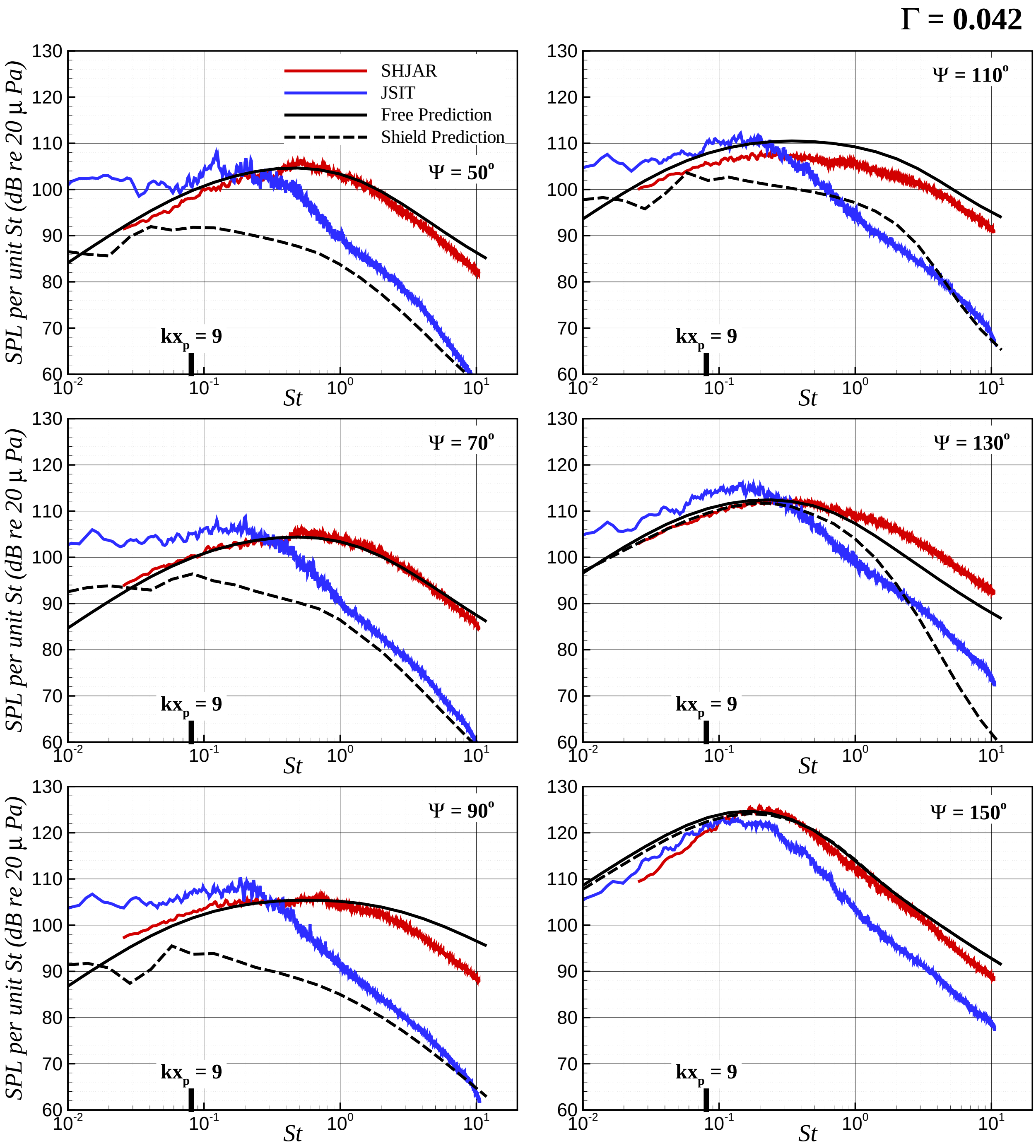

Figure B.43: The free-field and shielded prediction at $R/D = 100$ compared with experiment. The jet operates at $M_j = 1.50$ and $TTR = 1.00$ from the SMC000 nozzle with $D = 0.0508\ m$ and the plate is located at $x_p/D = 20$ and $y_p/D = 6$.

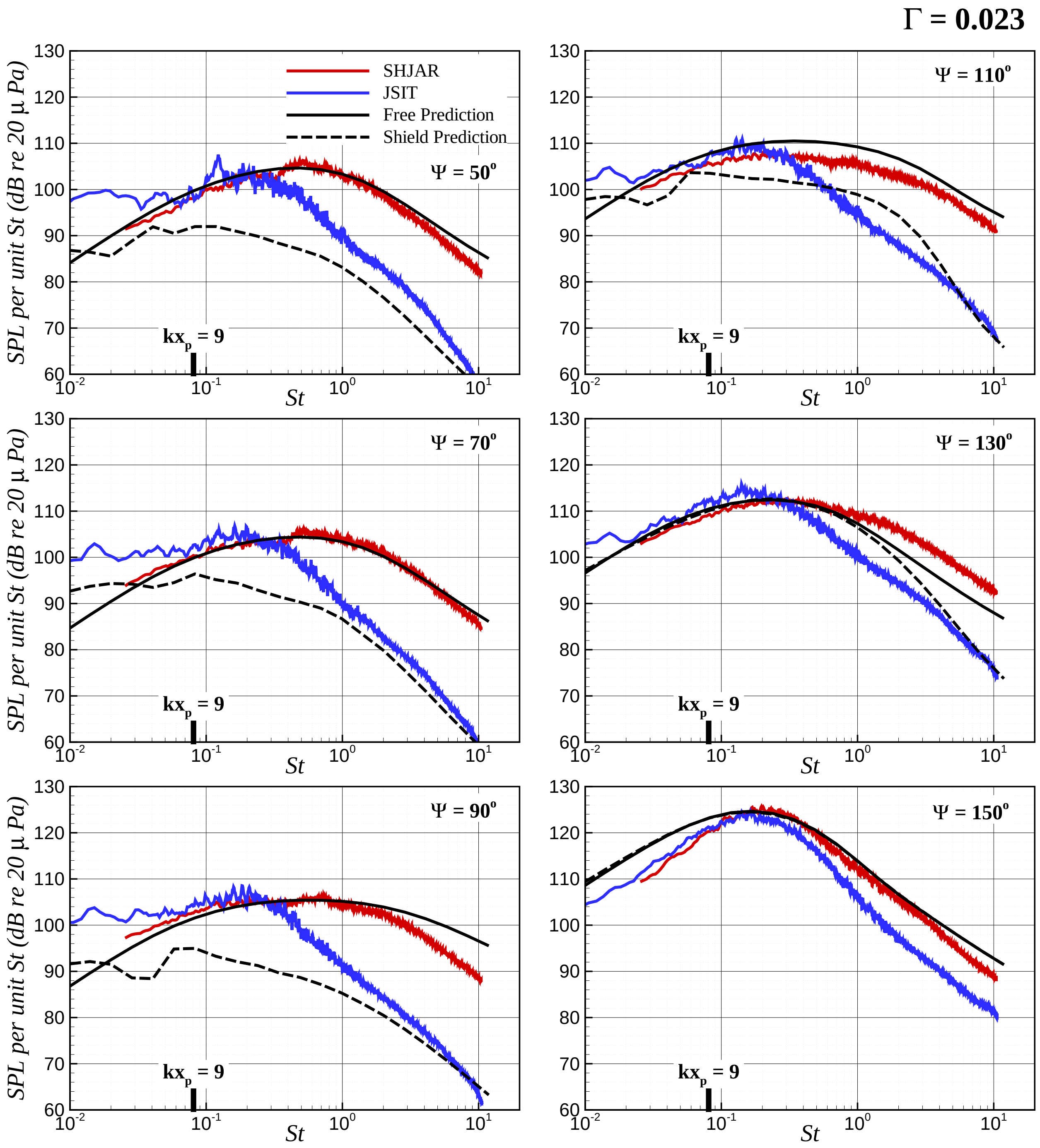

Figure B.44: The free-field and shielded prediction at $R/D = 100$ compared with experiment. The jet operates at $M_j = 1.50$ and $TTR = 1.00$ from the SMC000 nozzle with $D = 0.0508\ m$ and the plate is located at $x_p/D = 20$ and $y_p/D = 8$.

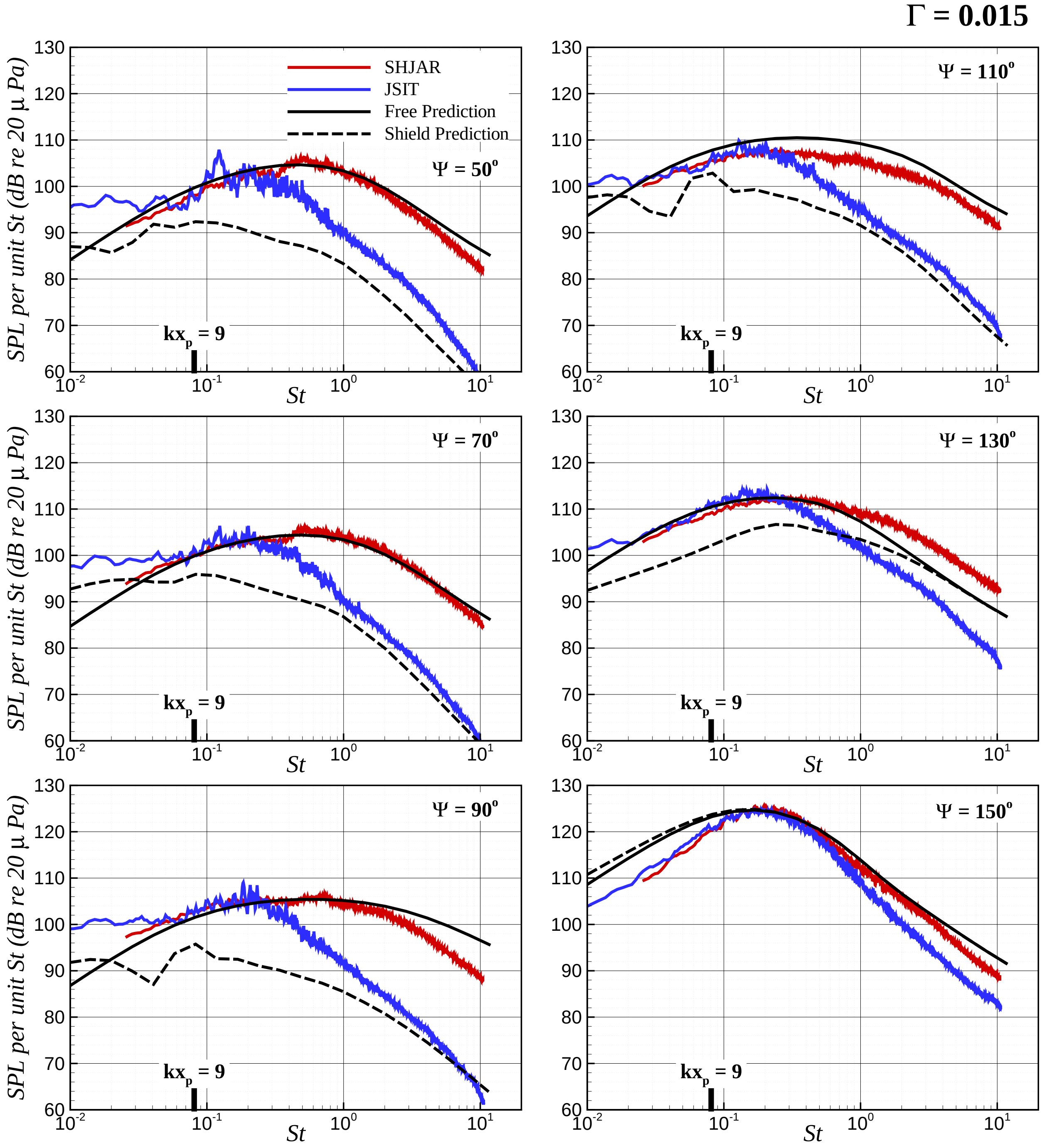

Figure B.45: The free-field and shielded prediction at $R/D = 100$ compared with experiment. The jet operates at $M_j = 1.50$ and $TTR = 1.00$ from the SMC000 nozzle with $D = 0.0508\ m$ and the plate is located at $x_p/D = 20$ and $y_p/D = 10$.

B.4 Supersonic Over-Expanded Jet

Γ = 0.120

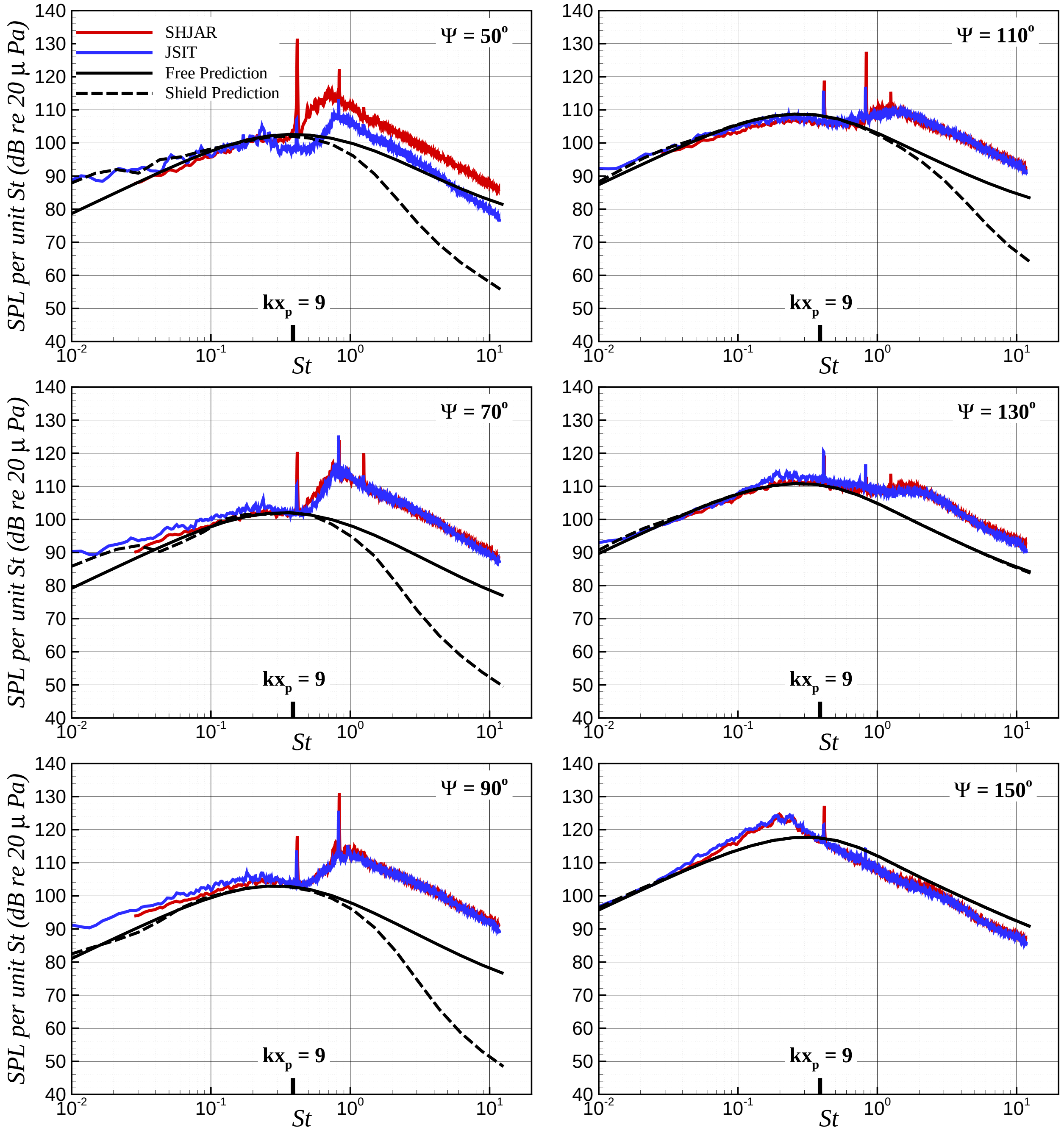

Figure B.46: The free-field and shielded prediction at $R/D = 100$ compared with experiment. The jet operates at $M_j = 1.290$ and $TTR = 1.00$ from the SMC000 nozzle with $D = 0.0508\,m$ and the plate is located at $x_p/D = 4$ and $y_p/D = 2$.

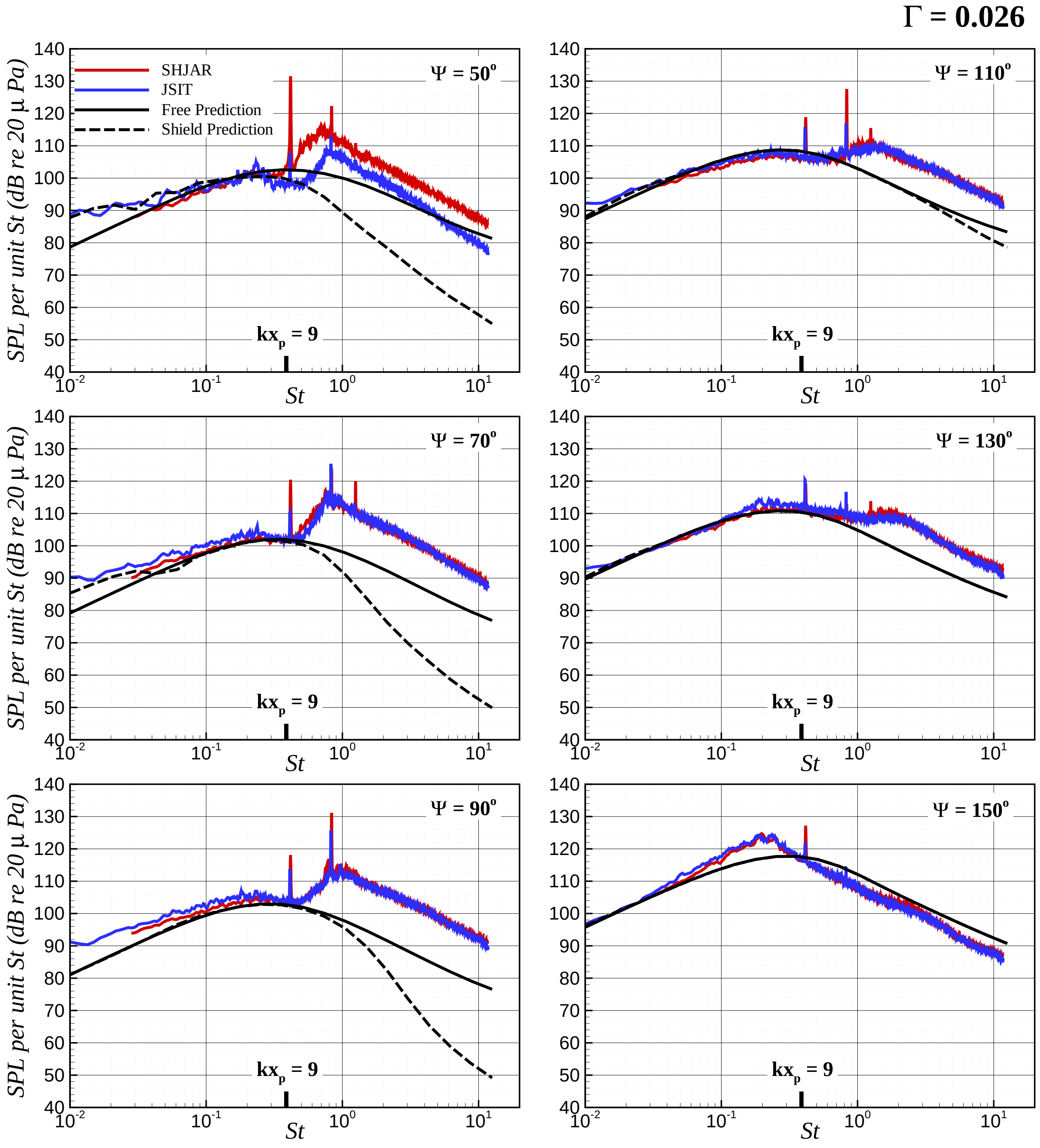

Figure B.47: The free-field and shielded prediction at $R/D = 100$ compared with experiment. The jet operates at $M_j = 1.290$ and $TTR = 1.00$ from the SMC000 nozzle with $D = 0.0508\,m$ and the plate is located at $x_p/D = 4$ and $y_p/D = 4$.

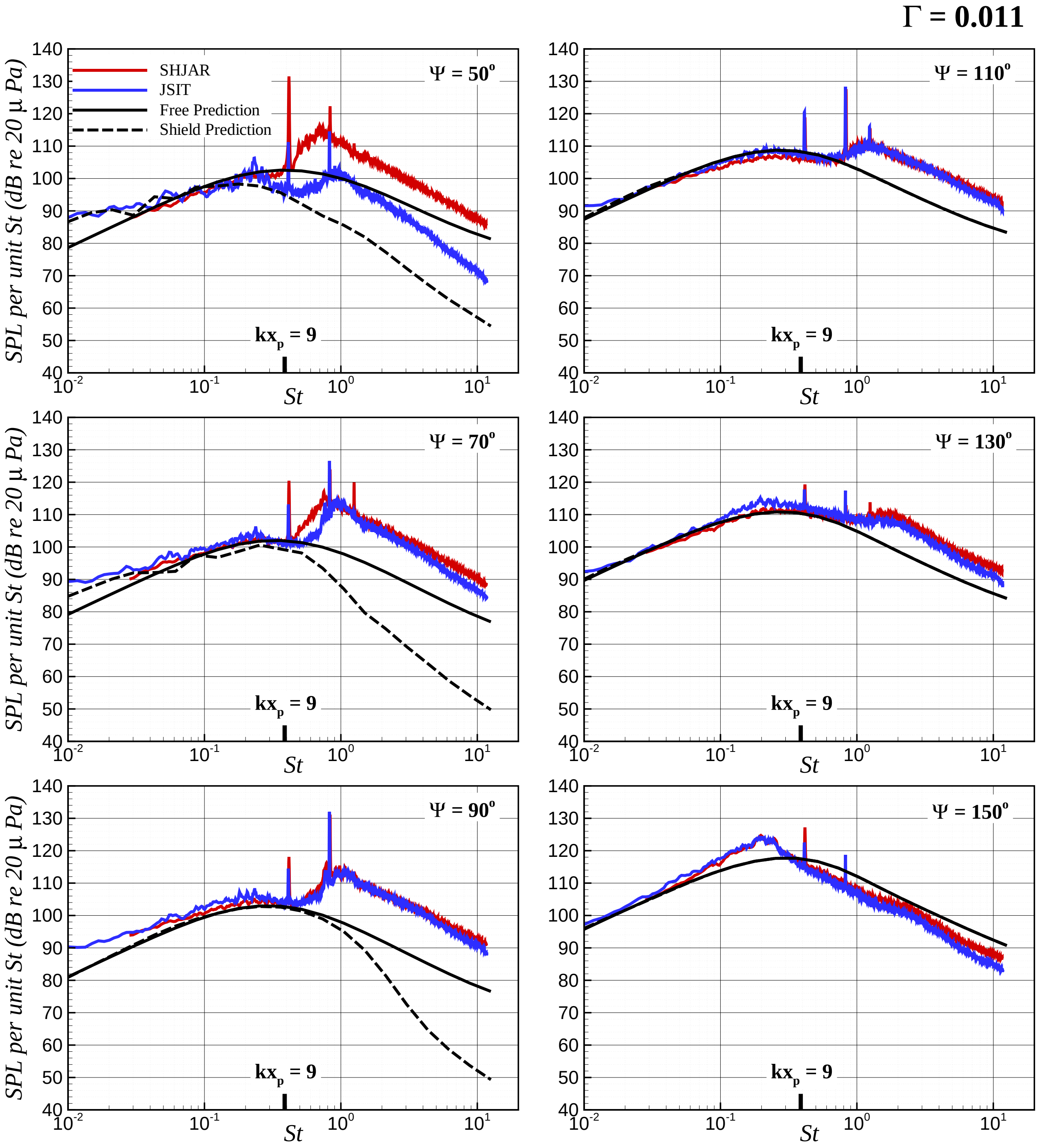

Figure B.48: The free-field and shielded prediction at $R/D = 100$ compared with experiment. The jet operates at $M_j = 1.290$ and $TTR = 1.00$ from the SMC000 nozzle with $D = 0.0508\,m$ and the plate is located at $x_p/D = 4$ and $y_p/D = 6$.

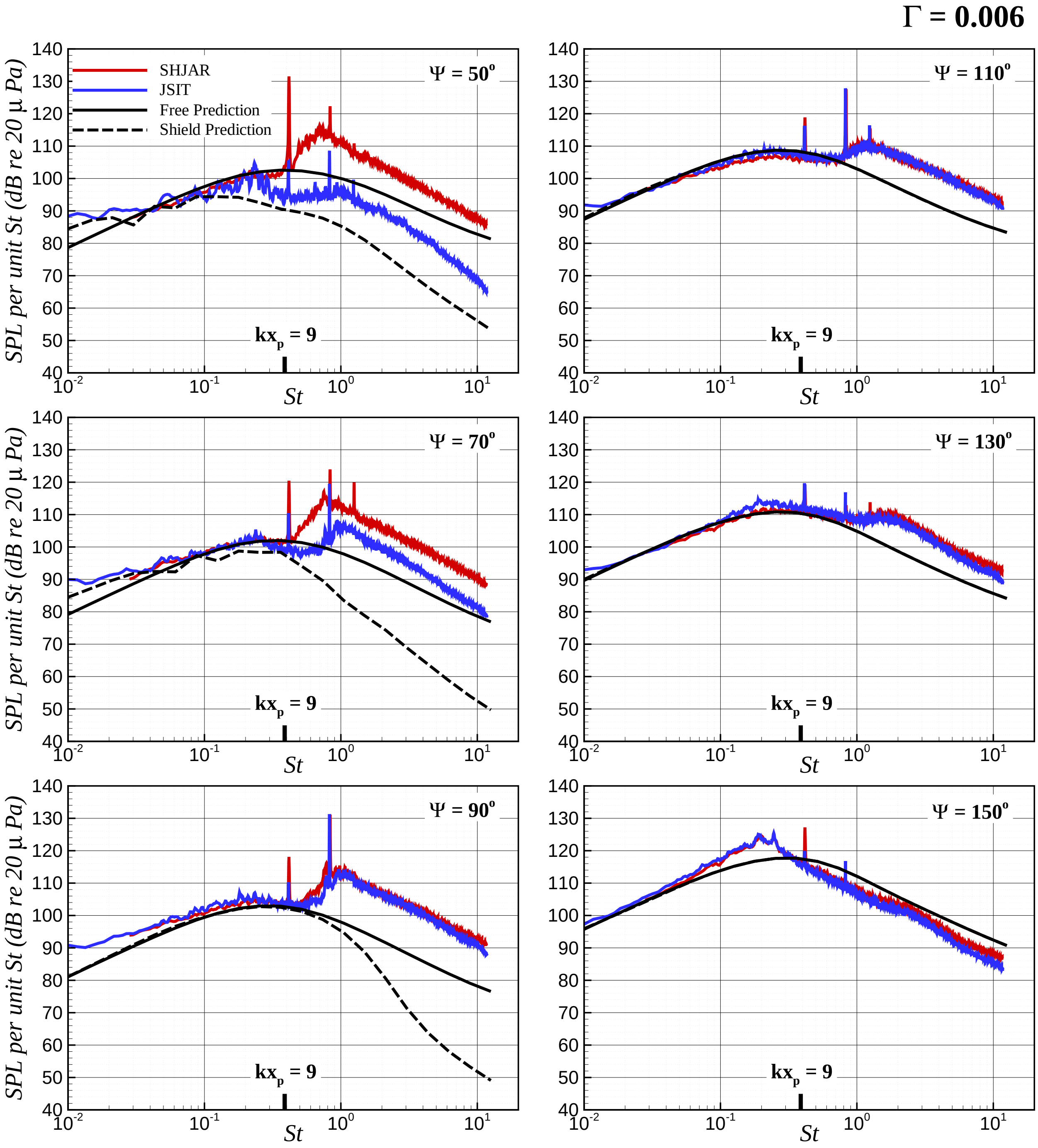

Figure B.49: The free-field and shielded prediction at $R/D = 100$ compared with experiment. The jet operates at $M_j = 1.290$ and $TTR = 1.00$ from the SMC000 nozzle with $D = 0.0508\,m$ and the plate is located at $x_p/D = 4$ and $y_p/D = 8$.

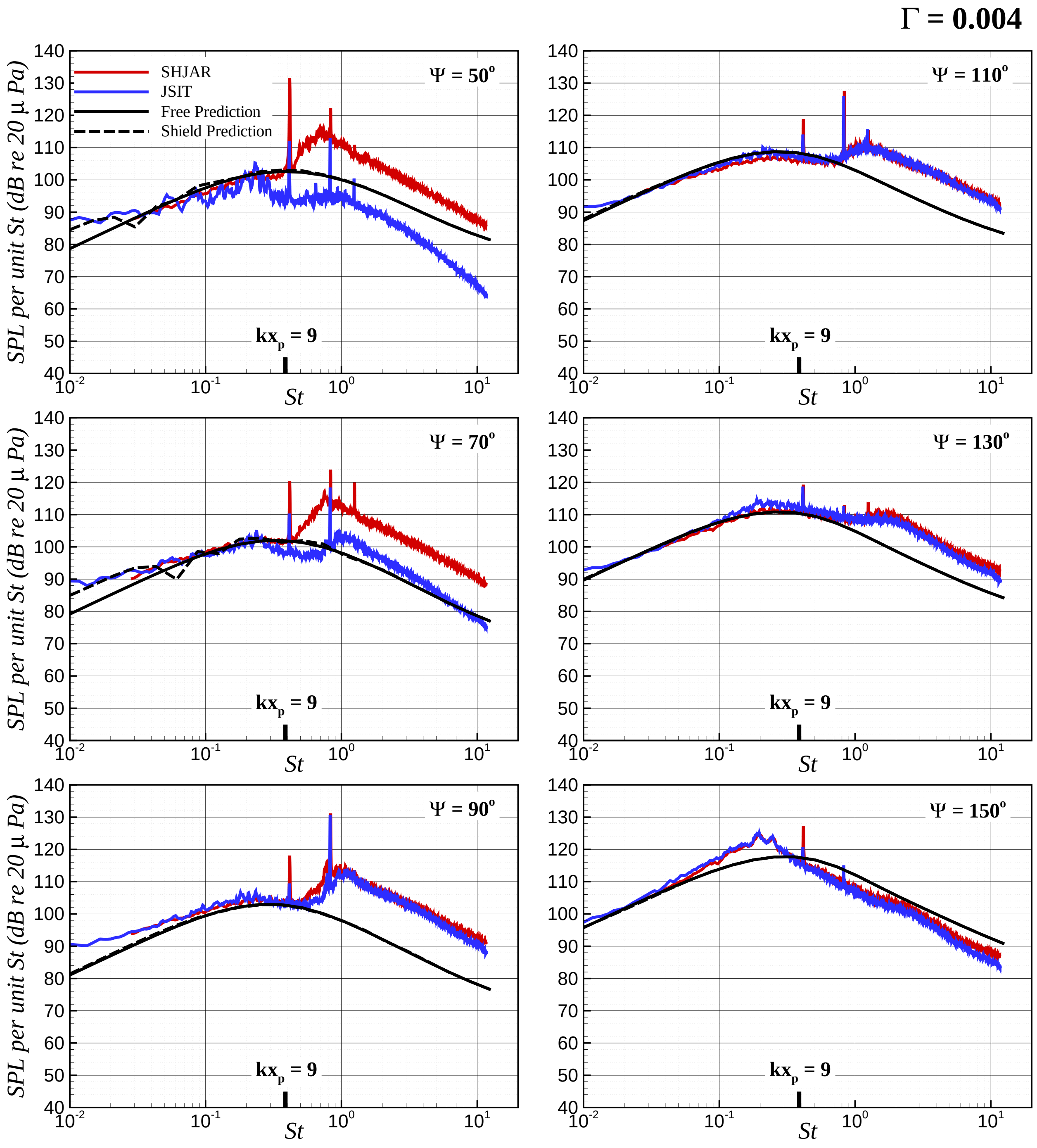

Figure B.50: The free-field and shielded prediction at $R/D = 100$ compared with experiment. The jet operates at $M_j = 1.290$ and $TTR = 1.00$ from the SMC000 nozzle with $D = 0.0508\,m$ and the plate is located at $x_p/D = 4$ and $y_p/D = 10$.

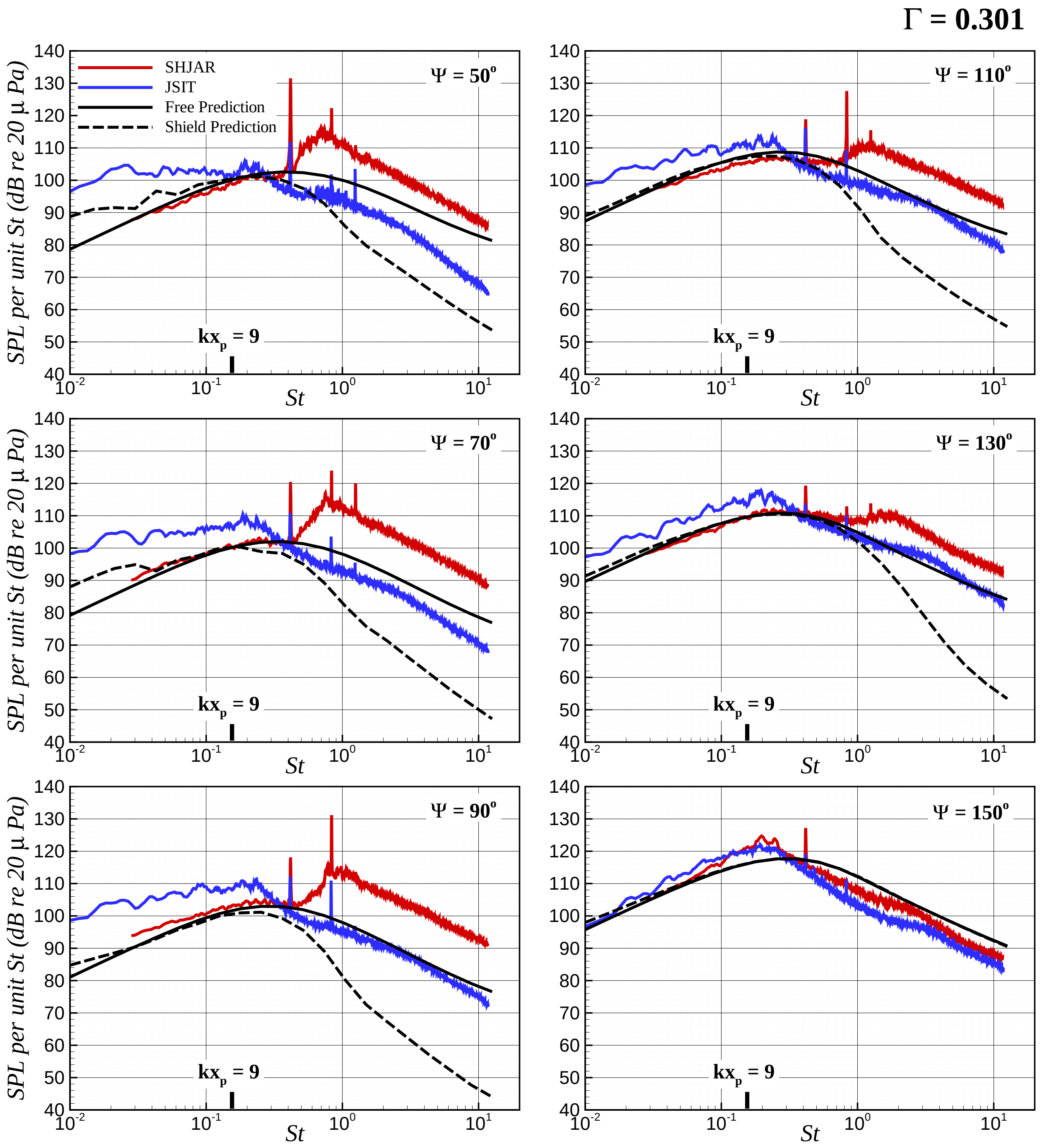

Figure B.51: The free-field and shielded prediction at $R/D = 100$ compared with experiment. The jet operates at $M_j = 1.290$ and $TTR = 1.00$ from the SMC000 nozzle with $D = 0.0508\,m$ and the plate is located at $x_p/D = 10$ and $y_p/D = 2$.

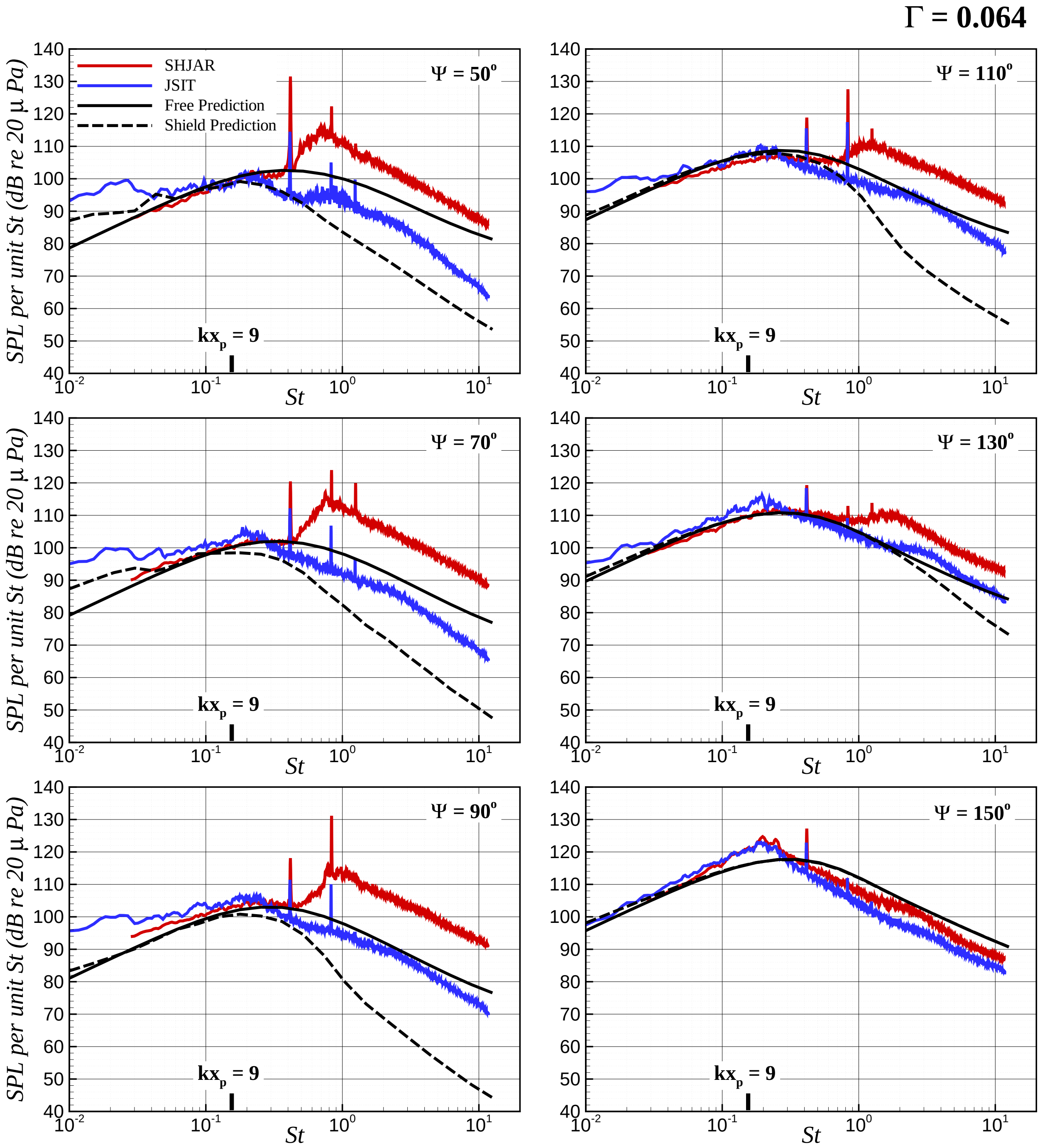

Figure B.52: The free-field and shielded prediction at $R/D = 100$ compared with experiment. The jet operates at $M_j = 1.290$ and $TTR = 1.00$ from the SMC000 nozzle with $D = 0.0508\,m$ and the plate is located at $x_p/D = 10$ and $y_p/D = 4$.

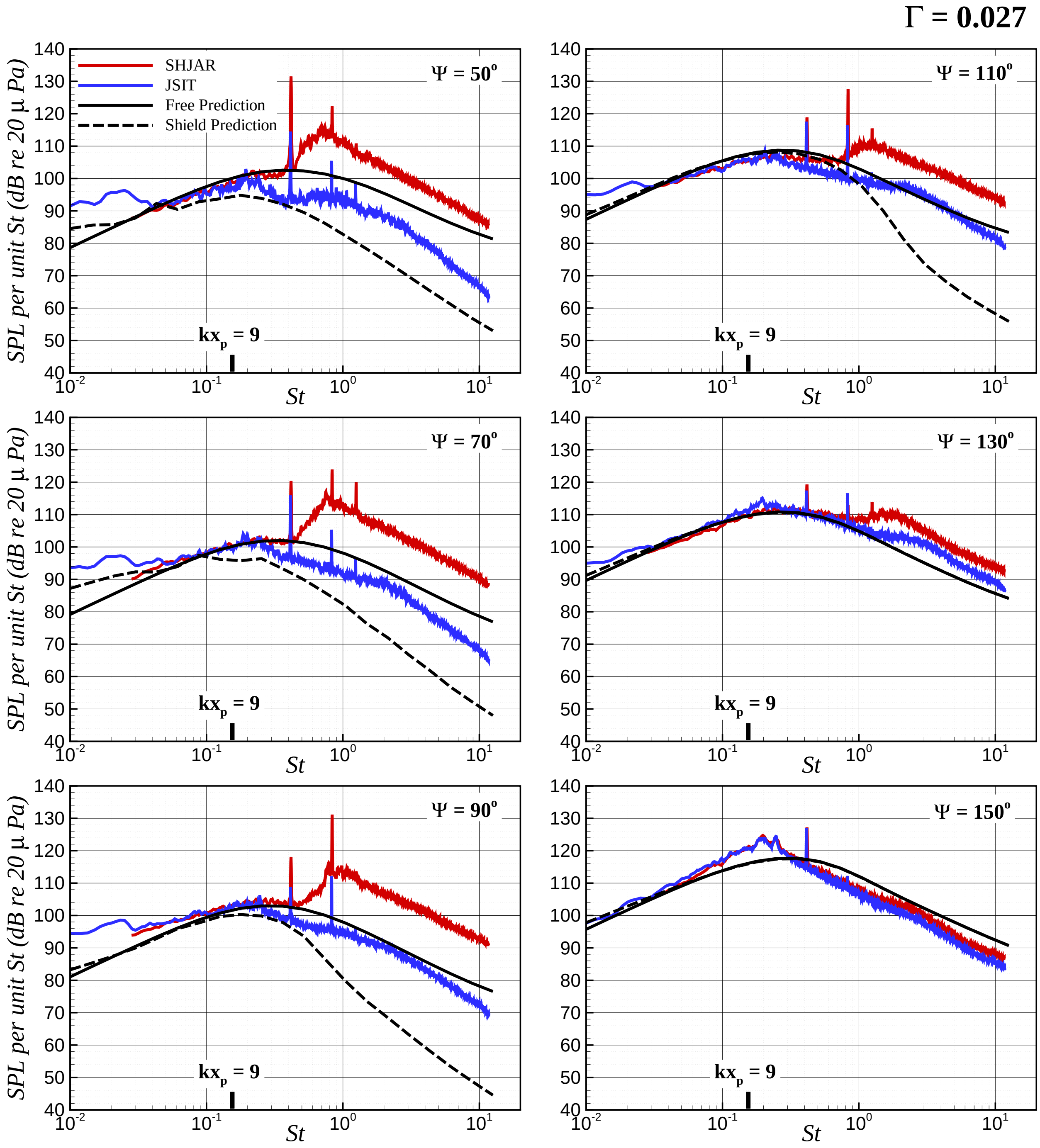

Figure B.53: The free-field and shielded prediction at $R/D = 100$ compared with experiment. The jet operates at $M_j = 1.290$ and $TTR = 1.00$ from the SMC000 nozzle with $D = 0.0508\,m$ and the plate is located at $x_p/D = 10$ and $y_p/D = 6$.

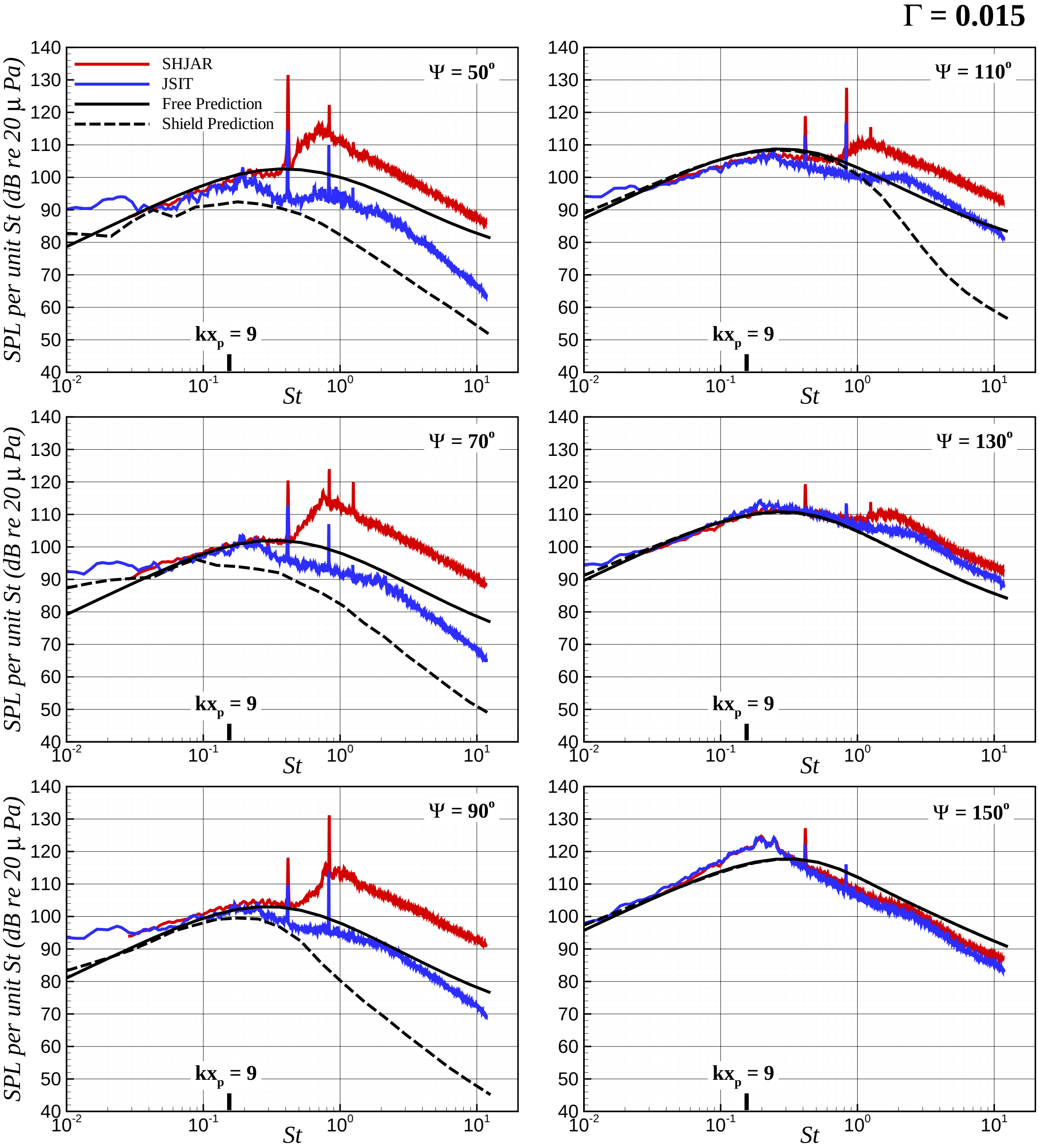

Figure B.54: The free-field and shielded prediction at $R/D = 100$ compared with experiment. The jet operates at $M_j = 1.290$ and $TTR = 1.00$ from the SMC000 nozzle with $D = 0.0508\,m$ and the plate is located at $x_p/D = 10$ and $y_p/D = 8$.

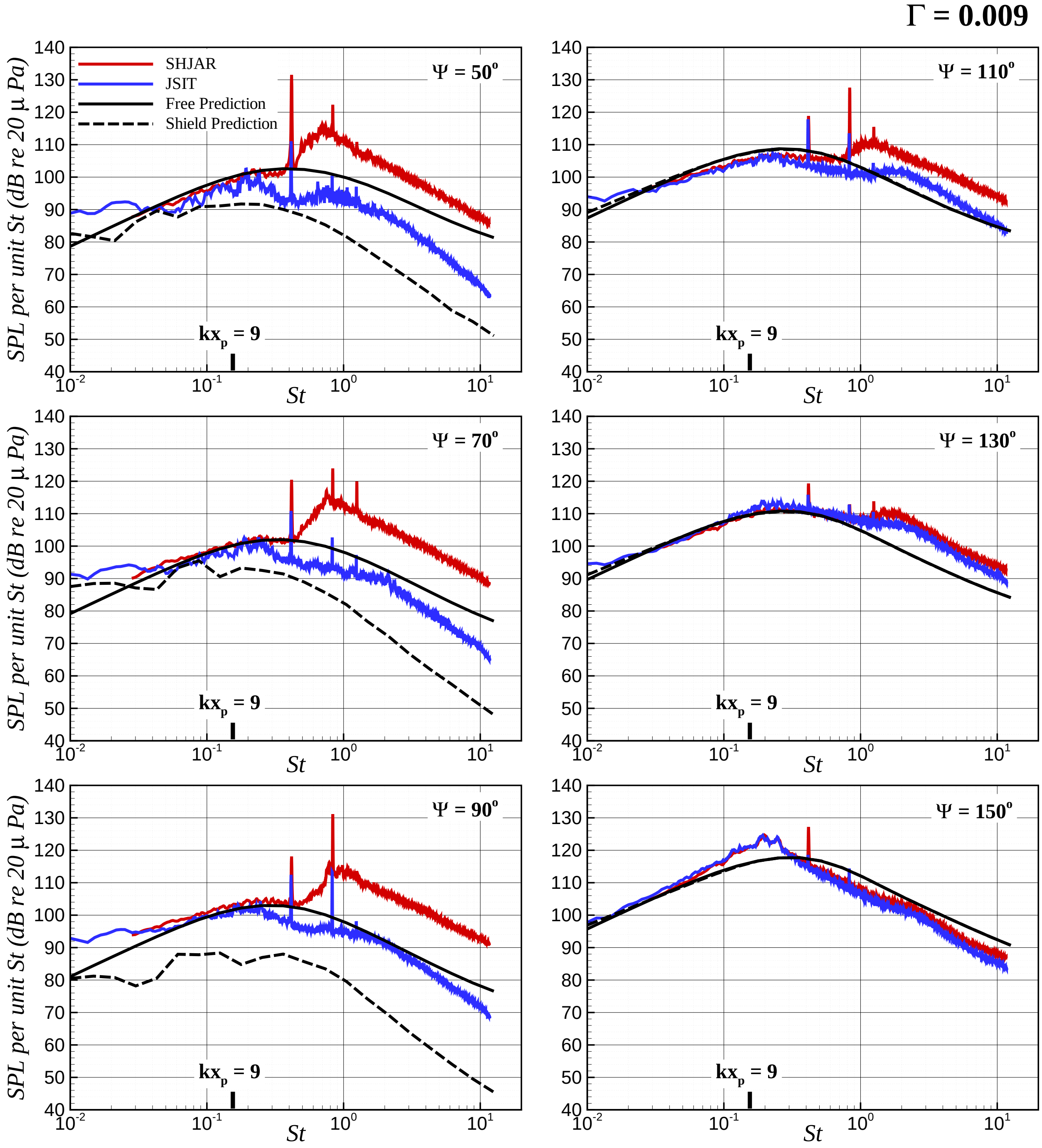

Figure B.55: The free-field and shielded prediction at $R/D = 100$ compared with experiment. The jet operates at $M_j = 1.290$ and $TTR = 1.00$ from the SMC000 nozzle with $D = 0.0508\,m$ and the plate is located at $x_p/D = 10$ and $y_p/D = 10$.

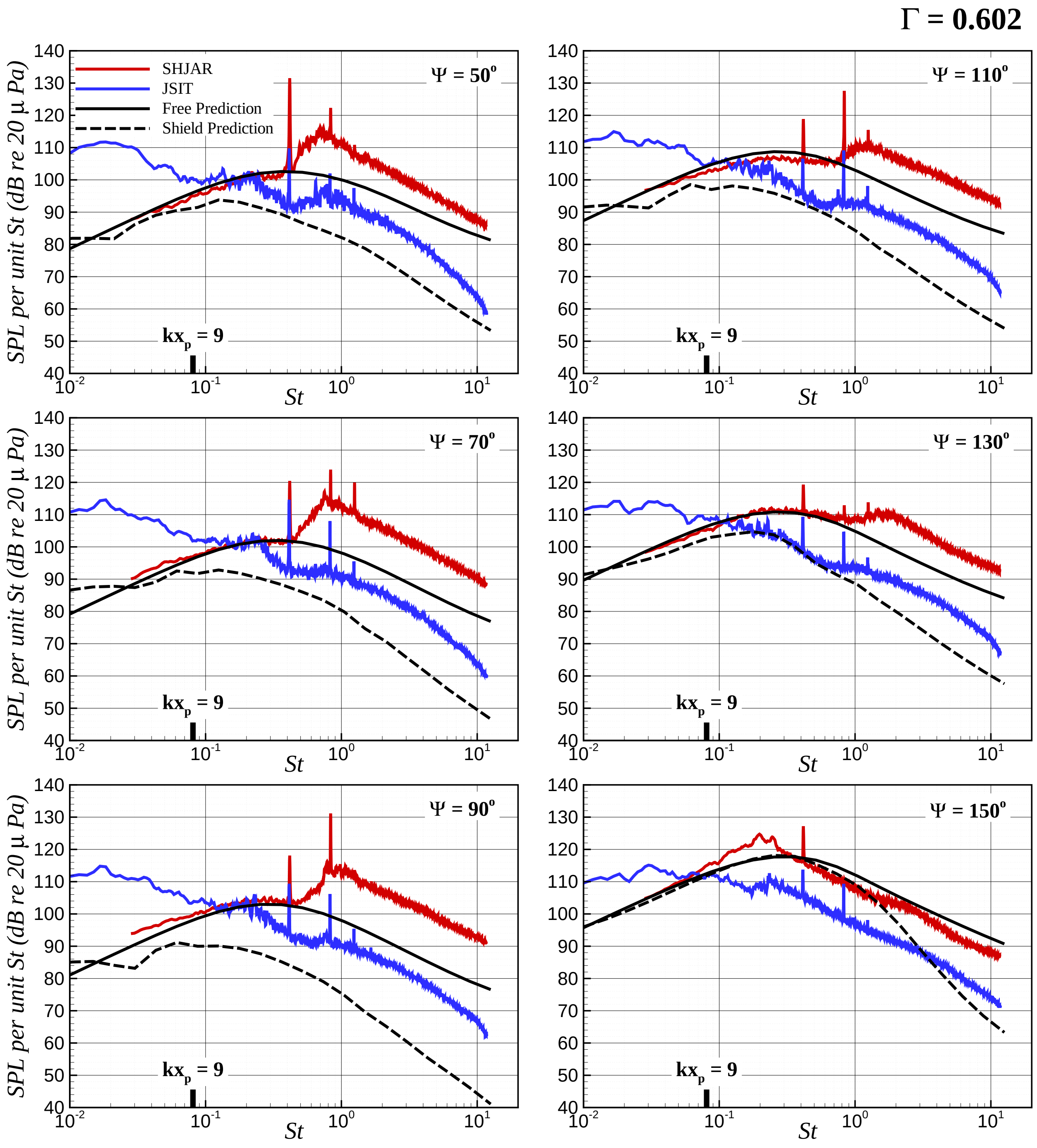

Figure B.56: The free-field and shielded prediction at $R/D = 100$ compared with experiment. The jet operates at $M_j = 1.290$ and $TTR = 1.00$ from the SMC000 nozzle with $D = 0.0508\,m$ and the plate is located at $x_p/D = 20$ and $y_p/D = 2$.

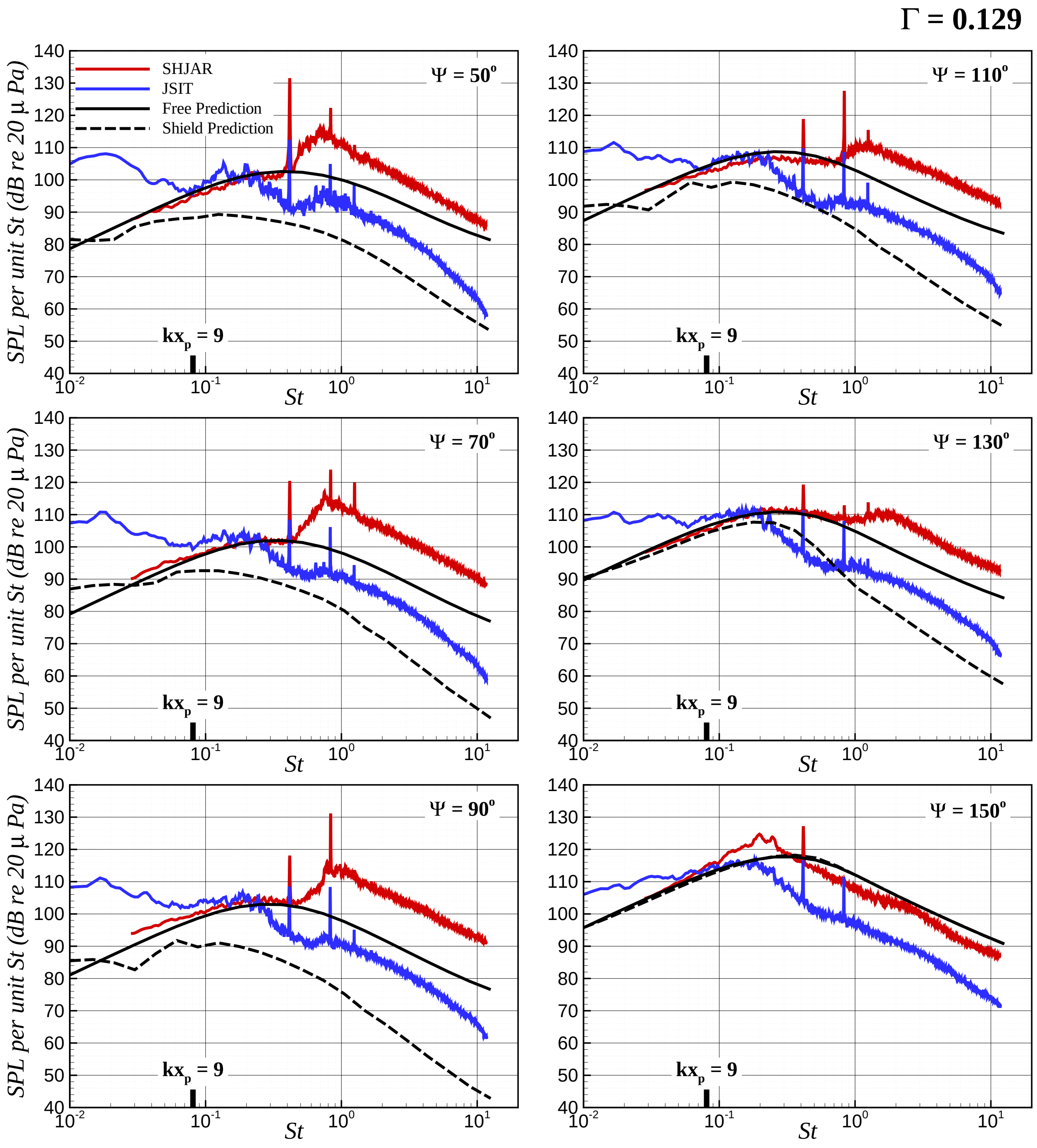

Figure B.57: The free-field and shielded prediction at $R/D = 100$ compared with experiment. The jet operates at $M_j = 1.290$ and $TTR = 1.00$ from the SMC000 nozzle with $D = 0.0508\,m$ and the plate is located at $x_p/D = 20$ and $y_p/D = 4$.

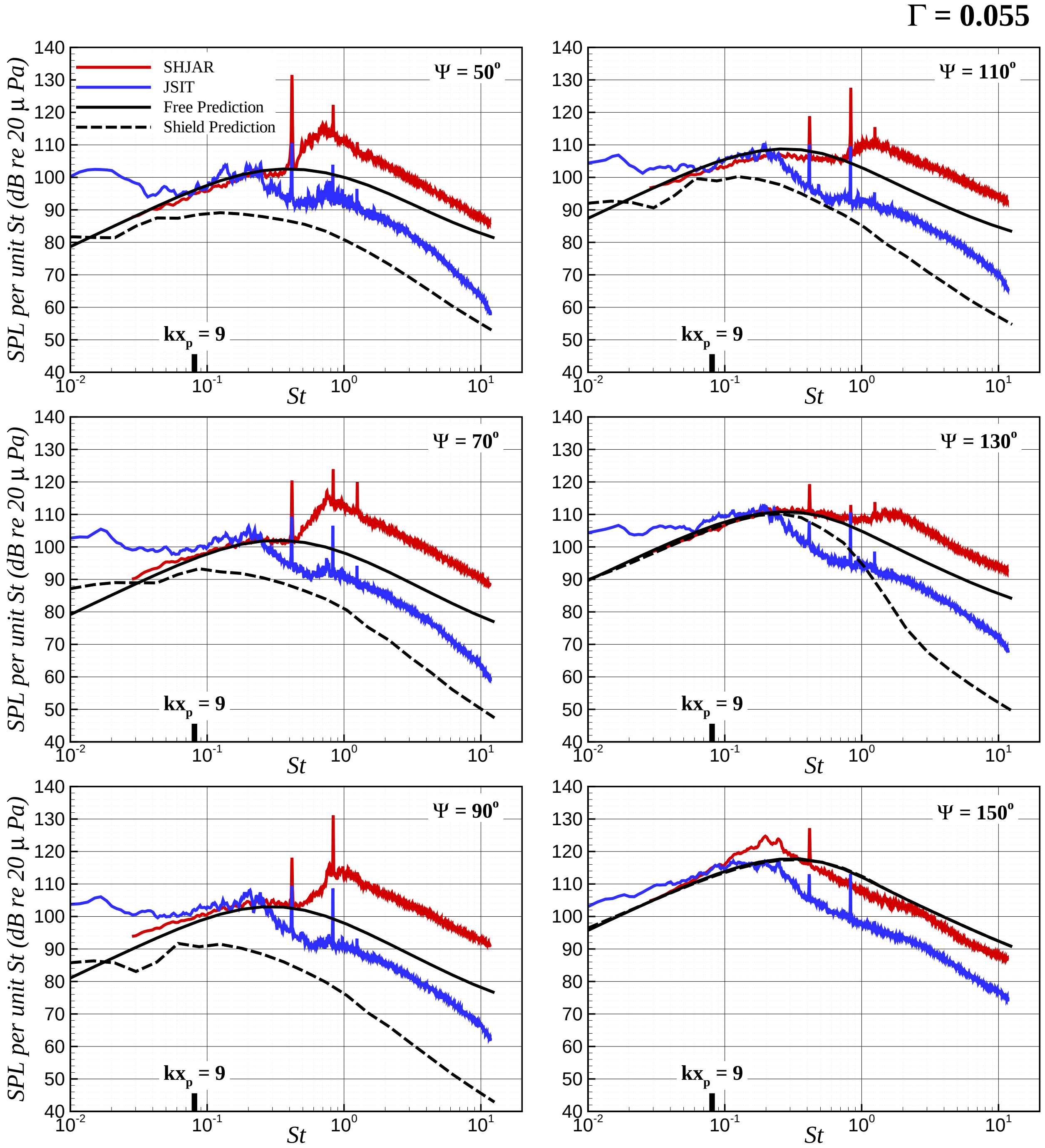

Figure B.58: The free-field and shielded prediction at $R/D = 100$ compared with experiment. The jet operates at $M_j = 1.290$ and $TTR = 1.00$ from the SMC000 nozzle with $D = 0.0508\,m$ and the plate is located at $x_p/D = 20$ and $y_p/D = 6$.

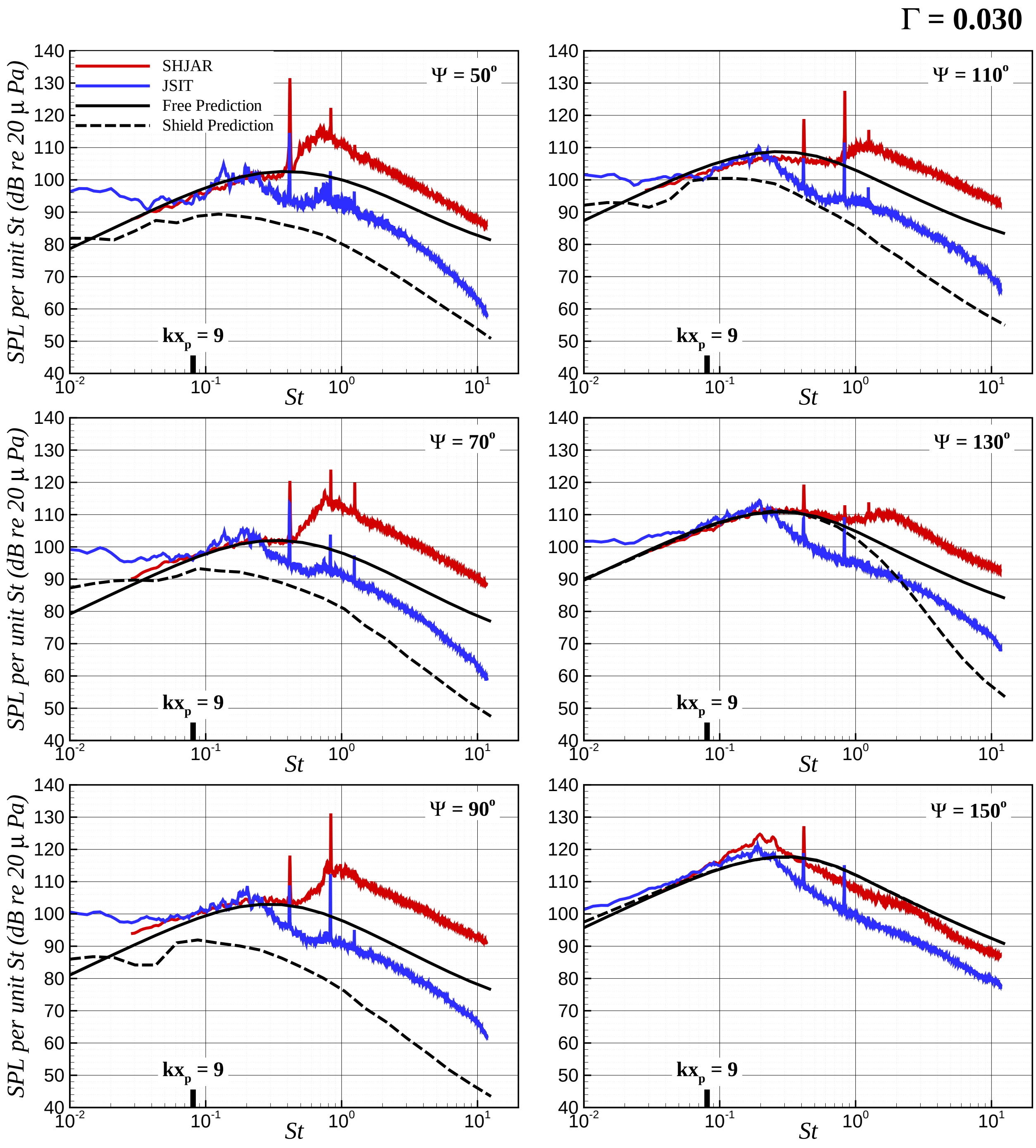

Figure B.59: The free-field and shielded prediction at $R/D = 100$ compared with experiment. The jet operates at $M_j = 1.290$ and $TTR = 1.00$ from the SMC000 nozzle with $D = 0.0508\,m$ and the plate is located at $x_p/D = 20$ and $y_p/D = 8$.

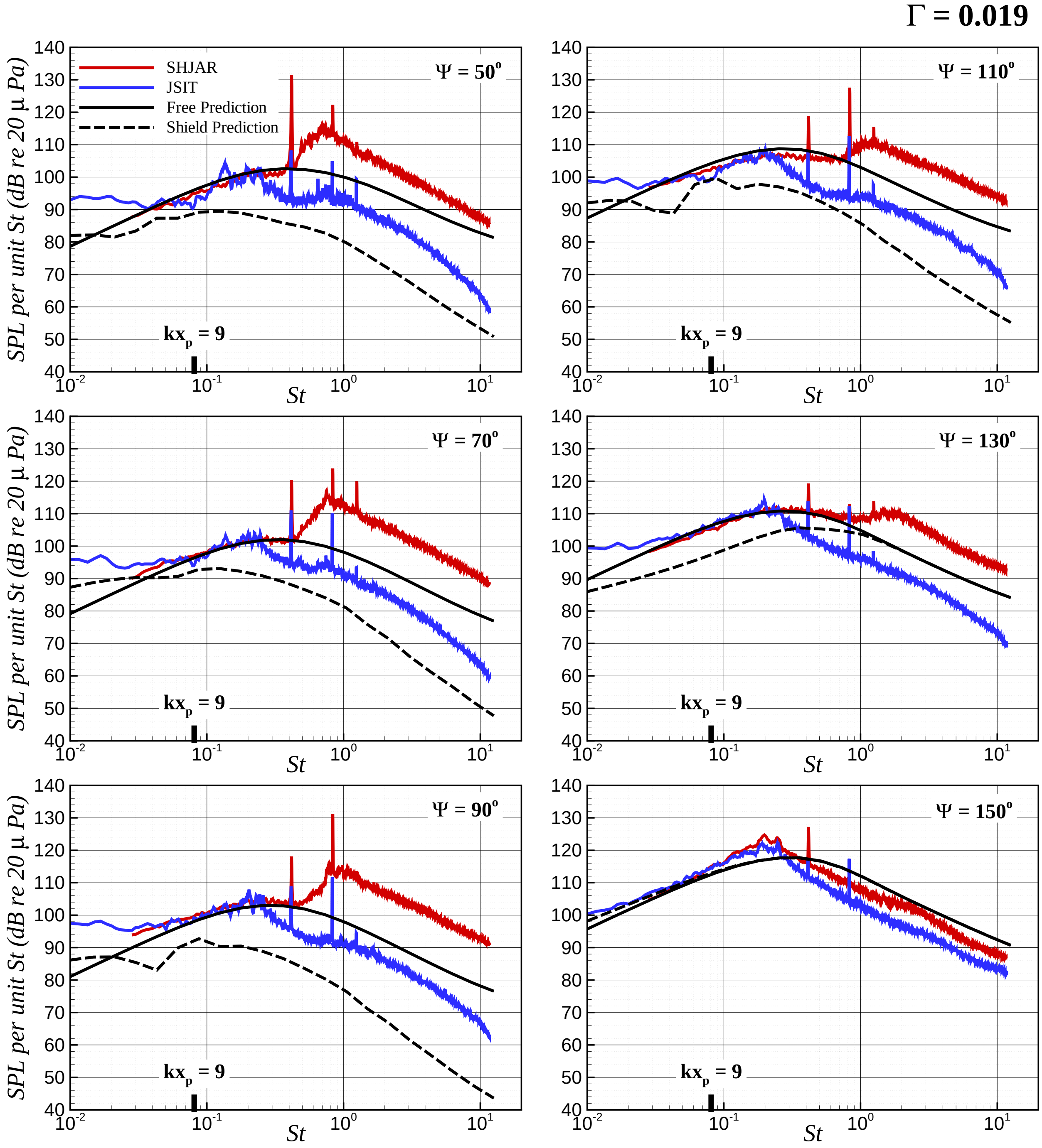

Figure B.60: The free-field and shielded prediction at $R/D = 100$ compared with experiment. The jet operates at $M_j = 1.290$ and $TTR = 1.00$ from the SMC000 nozzle with $D = 0.0508\,m$ and the plate is located at $x_p/D = 20$ and $y_p/D = 10$.